Solid-State Molecular OrganoMetallic Chemistry (SMOM):

Synthesis, Alkane Dehydrogenation and Surface Modification of Crystalline σ-Alkane Complexes

Alexander J. Bukvic

A thesis submitted in partial fulfilment of the requirements for the degree of Doctor of Philosophy at the University of Oxford

Magdalen College

August 2020

Declaration

The work presented in this thesis was carried out between September 2016 and June 2020 under the supervision of Professor Andrew S. Weller. All of the work, unless otherwise stated, is my own and has not been submitted previously for any degree at this, or any other, University.

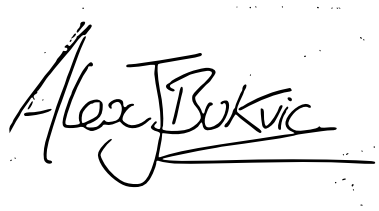

Alexander J. Bukvic
August 2020

Acknowledgments

Andrew: First and foremost, thank you for everything over the last 4 years. You've gone above and beyond what anyone might expect from a PhD supervisor. I couldn't recommend you more. Not only have you helped me academically but personally too, to which I can't thank you enough (even if Katie decided York would be a nice place to live just at the wrong time). I hope you find a new PhD student who you can fire as regularly for googly-eyeing your office, following Female Wrestlers on Instagram and cutting the odd peak or two out of an NMR spectrum. Hopefully see you on an Alp sometime soon.

Thank you for to all the wonderful members of the Weller group too. I'm eternally grateful for all your help in making me the scientist and person I am today. In particular, to the post-docs of Dr Alasdair McKay and Dr Antonio J. Martínez-Martínez (Team Alkane), may the words 'alkane dehydrogenation', 'polySMOM' or 'octahedron' never enter our lives again. Dr Samantha Furfari, Dr Laurence Doyle & Dr Claire Brodie – best of luck in your Weller group (SMOM) adventures, can't wait to read all about them. It's been a pleasure working with you as colleagues and as friends.

PhD Students Past and Present – Most of you already know how I feel about you after many nights out together featuring too much alcohol. May your future endeavours into town be filled with all the colours of WKDs. Thank you for the laughs, help scientifically and help annoying the post-docs (and not forgetting the odd WCC ride as well). Best of luck for all your write ups; I'm only an e-mail away if you want anything reading. Big thank you to Dr Gemma Adams as well, for helping me in not only my PhD but during the toughest time I've faced in my life so far. It's never forgotten.

To all the other fantastic undergrad students I've had the pleasure of working with, thank you for being the lives and souls of the group throughout your times. Special shoutout to Danny 'Firestarter' Sheldon and Hollie Garwood for writing a couple of these chapters. Honk.

A huge shout out to all the Weller group collaborators throughout my time – including Dr Bengt Tener, Arron Burnage and Prof. Stuart Macgreller for your beautiful calculations. As well to Dr Graham Tizzard (Southampton University) and Dr Mark Warren (Diamond Light Source) for enabling some of these complexes to be proven.

Importantly, this thesis would be even worse if it wasn't for all the fantastic support staff helping myself and the group over these 4 years. Dr Nick Rees, Dr Amber Thompson and Dr Dana Georgiana Crivoi for all your technical and chemical assistance throughout this thesis. To Ron Terry and Team also, thank you for helping with everything problem we've had lab (and Atrium) related. Thank you as well to all support staff at the University of York also, for making everything so smooth in our landing. This thesis would have been still ongoing today if it wasn't for all your help.

A big shout out to everyone non-academic for keeping me somewhat sane during these years too. To all the big boys and girls at Cardiff, I owe you all a pint or two. Thanks to Mum and Paul too – most of the experiments presented herein were fuelled on some tasty cakes and the odd quiche made by you, thank you again.

Abbreviations

Å	Angstrom
$[BAr^F{}_4]^-$	$[B((3,5\text{-}C_6H_3)(CF_3)_2)_4]^-$
BCP	bi-capped pyramid
br	broad
calc.	calculated
Cy	cyclohexyl
d.	doublet
δ	chemical shift
DFT	Density Functional Theory
ΔG	change in Gibbs free energy
ΔH	change in enthalpy
ΔS	change in entropy
EDX	Energy Dispersive X-ray
EI	electron ionisation
ESI	electrospray ionisation
Et	ethyl
Eq	equivalents
FSLG	Frequency Switch Lee-Goldberg
GC	Gas Chromatography
GPC	Gel Permutation Chromatography
η	hapticity
Hz	Hertz
HECTOR	Heteronuclear Correlation
I	nuclear spin
J	coupling constant
K	Kelvin
kcal mol^{-1}	kilocalorie per mole
kJ mol^{-1}	kilojoule per mole
M	mol dm^{-3}
Me	methyl
mL	millilitre
M_n	number average molecular number
MOF	Metal Organic Framework
MS	Mass Spectrometry
M_w	number average molecular weight
m/z	mass to charge ratio
NBA	norbornane
NBO	Natural Bond Order
NBD	norbornadiene
NCI	Non-Covalent Interactions
NMR	Nuclear Magnetic Resonance
NQS	Non-Quaternary Suppression
O_h	octahedral
ppm	parts per million
σ-CAM	sigma-Complex Assisted Metathesis
SEM	Scanning Electron Microscopy
SMOM	Solid-State Molecular OrganoMetallic
SOMC	Surface OrganoMetallic Catalysts
SHC	Supported Homogeneous Catalysts
SSNMR	Solid-State Nuclear Magnetic Resonance
^{t}Bu	tertbutyl
t	triplet
°C	degrees Celsius

Abstract

This thesis reports the synthesis of single-crystalline σ-alkane complexes of rhodium. These are synthesised by the hydrogenation of precursor alkene or diene complexes in solid/gas single-crystal to single-crystal (SC-SC) transformations, using the Solid-State Molecular OrganoMetallic (SMOM) methodology developed by the Weller group. *Chapter 1* Introduces the general field and *Chapter 6* provides experimental details.

Chapter 2 reports the synthesis of the alkene precursors **[Rh($Cy_2P(CH_2)_2PCy_2$)(L)][BAr^F_4]** [Ar^F = 3,5-$(CF_3)_2C_6H_3$, L = propene, butadiene, *iso*butene, 2-methyl-1,3-butadiene, 3-methyl-1,3-pentadiene, *n*-hexadiene] which all undergo hydrogenation in SC-SC reactions to form the corresponding σ-alkane complexes **[Rh($Cy_2P(CH_2)_2PCy_2$)(η-L)][BAr^F_4]** [L = propane, *n*-butane, *iso*butane, *iso*pentane, 3-methylpentane, *n*-hexane]. These complexes are characterised by solid-state NMR spectroscopy and single-crystal x-ray diffraction. The bonding in **[Rh($Cy_2P(CH_2)_2PCy_2$)(*iso*butane)][BAr^F_4]** is probed using a DFT computational analysis conducted by Aaron Burnage and Prof. Stuart Macgregor of Heriot-Watt University.

Chapter 3 explores the onwards evolution (under a dynamic vacuum or a flow of Ar) of the *iso*butane and *iso*pentane σ-alkane complexes reported in *Chapter 2*, that results in an acceptorless dehydrogenation to reform alkene complexes: **[Rh($Cy_2P(CH_2)_2PCy_2$)(L)][BAr^F_4]**, L= *iso*butene and *iso*pentane respectively. Crystallinity is retained during this process, and the products are analysed by single-crystal x-ray diffraction directly. The temporal evolution of these SC-SC dehydrogenation reactions were modelled against either a classical kinetics or a modified JMAK expression. The latter is found to give the best fit. The mechanism for this process is further probed DFT calculations (Prof. Stuart Macgregor group).

Chapter 4 explores the solid/gas reactivity of all of the σ-alkane complexes reported in *Chapter 2* when placed under a D_2 atmosphere. H/D exchange is shown to occur in the alkane ligand, to form partially-deuterated σ-alkane complexes, which compete with decomposition. These reactions were followed using solid-state NMR spectroscopy as well as analysis of the isolated alkane ligands using solution NMR spectroscopy. The combination of H/D exchange and dehydrogenation is explored with **[Rh($Cy_2P(CH_2)_2PCy_2$)(*iso*butane)][BAr^F_4]**, resulting in a deuterium-enriched **[Rh($Cy_2P(CH_2)_2PCy_2$)(*iso*butene-d_x)][BAr^F_4]** (x = 10 - 7).

Chapter 5 details the surface-based reactivity of the crystalline σ-alkane complex **[Rh($Cy_2P(CH_2)_2PCy_2$)(norbornane)][BAr^F_4]**. When exposed to a vapour of ethylvinyl ether (EVE) a surface cationic polymerisation occurs to coat the crystals in poly(ethylvinylether). This coating layer of polymer was shown to significantly increase the stability of the crystalline σ-alkane complex when exposed to air. As a structural model for an EVE-coordinated intermediate, the diethylether-coordinated complex is synthesised **[Rh($Cy_2P(CH_2)_2PCy_2$)($H_3CH_2COCH_2CH_3$)][BAr^F_4]** using SC-SC techniques.

Thesis Contents

Chapter 1:

Introduction

1.1. Upgrading Alkanes

Fossil derived, low molecular weight, alkanes such as ethane (C_2H_6) to hexane (C_6H_{14}) are abundant, cheap and are often seen as side products in shale oil purification.[1] They typically have limited applications, as their low energy density and high volatility makes them unsuitable for transportation fuels. This is unlike their higher molecular weight counterparts of heptane to nonane. The primary use of these lower molecular weight alkanes is in their calorific value, e.g., propane / butane in stove-gas. Additionally, more niche reagents such as pentane is used in polystyrene manufacture as a blowing agent as well as hexane as a solvent in adhesives and for extraction processes.[1,2]

Their potential as feedstock materials towards commodity compounds of higher chemical and economical value is often disregarded. Industrially, upgrading these alkanes can be achieved by cracking, steam-reforming or oxidative carbonylation,[3] where require the use of heterogenous catalysts. These operate at high temperature, where this large energy input reduces the overall economy of the process, and can also lead to poor product selectivity.[4]

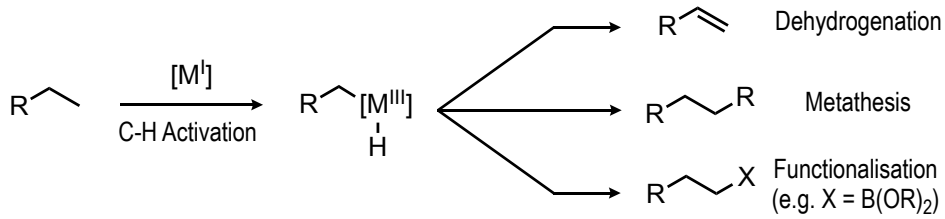

Scheme 1.1: Examples of C-H Activation and functionalisation.[3]

The use of homogeneous, transition metal organometallic catalysts can offer a lower energy pathway with increased selectivity. Since the 1980s,[5] it's been shown that alkanes can be valorised in reactions such as alkane metathesis, dehydrogenation, and functionalisation using a range of reagents (Scheme 1.1).[6] Late transition metals in low oxidation states are typically employed in these systems, as they encourage oxidative addition of C–H bonds.[7] Rhodium is an example of a late transition metal often used in processes shown in Scheme 1.1. The 4d-metal can readily undergo the oxidative addition / reductive elimination steps required in these reaction pathways. This is aided by the ability of rhodium to change its oxidation state, typically between Rh^{I}/Rh^{III}.

A key step in all the pathways presented is in the formation of a σ-alkane complex. This involves the direct coordination of an alkane ligand to a metal centre, before undergoing any further reactivity. Their role within low valent, electron-rich, late transition metal complexes towards C–H activation is well established.[8] Prior to their formation however, the alkane ligand must overcome a pre-equilibrium, outcompeting ligand and solvents alike. This is shown by the first equilibrium step in Scheme 1.2.

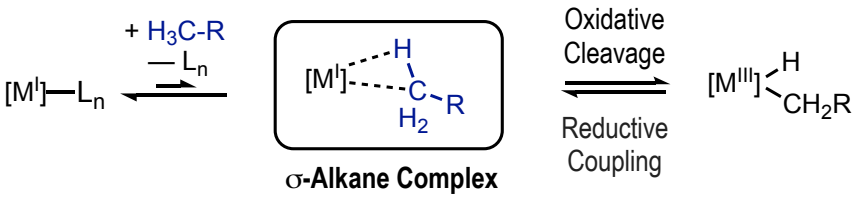

Scheme 1.2: Pre-equilibrium towards σ-alkane complex formation.

This pre-equilibrium often lies far to the left, with the σ-alkane complex not formed. Once this complex has been formed however, subsequent bond breaking and making steps are energetically accessible, leading to rapid further reactivity.[9–11] This results in σ-alkane complexes only appearing as transient species, either being not observed or seen as fleeting intermediates at best. This makes the isolation, and therefore, characterisation of these complexes extremely challenging, and they have been historically elusive to observe. Overcoming this pre-equilibrium problem and enhancing the relative concentration of the σ-alkane complex is key in all reaction pathways towards upgrading alkanes.

1.2. σ-Complexes

To fully understand the bonding within σ-alkane complexes, they can be compared to previously, well studied σ-complexes. Transition metal-ligand complex formation is typically achieved by donation of electrons from regions of local, high electron density, such as π-bonds or lone pairs, towards a suitble empty orbital located on the metal centre. These are formally 2-center 2-electron interactions.

If no lone pairs or π-bonds are present, weaker bonding interations by donation of electrons from σ-bonds can occur,[12] forming 3-centre 2-electron interactions.[13] The Dewar-Chatt-Duncanason model for the bonding of alkenes can be adpted to compare the two bonding models, shown in Figure 1.1. These so-called σ-complexes have been well documented in a range of E–H compounds, including, but not limited to, E = H[14], C,[15,16] B[17] and Si[18].

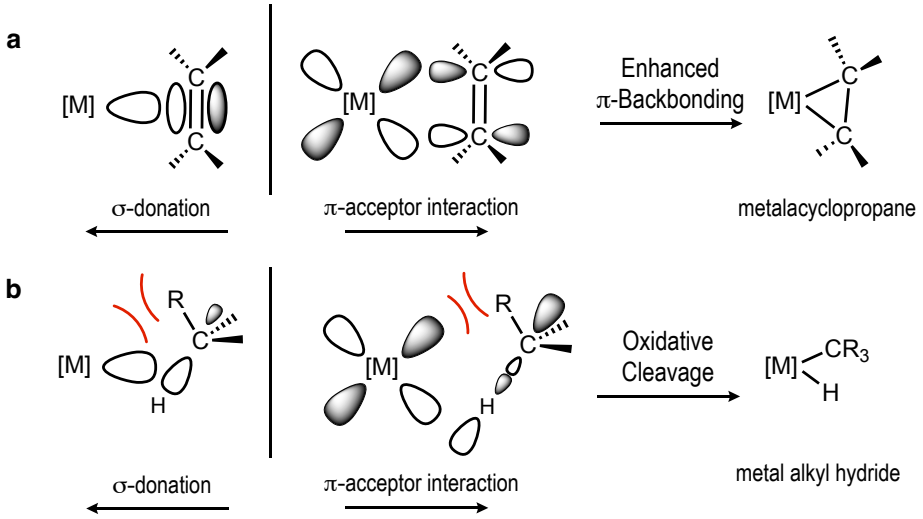

Figure 1.1: **a**) Dewar-Chatt-Duncanason model for alkene coordination to a transisition metal centre and **b**) adapted Dewar-Duncanson-Chatt model for C–H coordination to metal centre.

In σ-alkane complexes, the weak nature of [M]•••C–H interactions arise from the very poor nucleophilic nature of the C–H bond. As carbon and hydrogen are of similar electronegativities, 2.55 and 2.20 respectively,[19] the C–H interaction is essentially non-polar. This combined with the low polarizability, high pKa values and strong C–H bond (~400 kJ mol^{-1}) results in metal-catalysed C–H functionalisation being kinetically challenging. Local steric bulk around the C–H bond can further inhibit coordination.

The nature of alkane coordination to a metal centre has many similarities to that of well-studied metal-dihydrogen interactions. C–H and H–H interactions are both π-basic, accepting electron density from the metal centre into the respective C–H / H–H σ*-orbital,

and both are typically weak, ~60 kJ mol^{-1} and 80-100 kJ mol^{-1} respectively.[14,20,21] The extent of the backbonding will determine the population of the σ*-orbital, and therefore if further oxidative cleavage occurs to form a methyl hydride or dihydride complex respectiviely.[22,23] The high energy and poor directional overlap of the corresponding σ*-orbital in a C–H bond however can inhibit this cleavage step.

The bonding model of σ-alkane coordination can also be compared with the very similar [M]•••C–H interactions that arise in agostic complexes. In agostic complexes, the C–H σ-bond is on an intramolecular chelating group, which is tethered to the metal centre in primary interactions, such as alkyl phosphine or alkyl (Scheme 1.2).[24] σ-Alkane complexes do not have this pendant group. In agostic complexes, this [M]•••C–H interaction results in typically longer C–H bond lengths (1.8 to 2.4 Å) and an upfield shift in the ^{1}H NMR spectrum compared to that of the uncoordinated C–H environment.

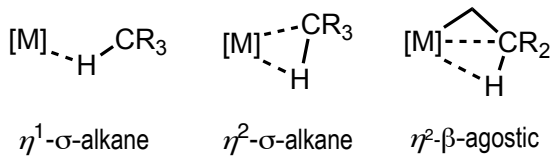

Scheme 1.3: Overview of η^{x}-σ-alkane and η^{2}-agostic complexes.

The [M]•••C distance and angle formed by the [M]•••H–C interaction can give insight into the precise nature of the σ-interaction in both agostic and σ-alkane complexes. Relatively obtuse M–C–H bond angles, large [M]•••C and small [M]•••H distances are suggestive of η^{1}-interactions, where smaller [M]•••C distances and acute [M]–C–H bond angles suggest η^{2}-interactions. These distances and angles differ from anagostic complexes, which are electrostatic interactions and are comparable to regular hydrogen bonds. Computational methods such as Quantum Theory of Atoms in Molecules (QTAIM)[25] and Natural Bond Orders (NBO)[26] have been applied to give detailed analysis of these interactions.

1.3. σ-Alkane Complexes Synthesis

1.3.1. Neutral σ-Alkane Complex Synthesis: Photolytic Routes

Attempts to isolate σ-alkane complexes began in the 1970s. Since then, many examples have been presented and this area extensively reviewed.[27–29] As such, only key milestones highlighted here.

Initially, work by the Turner group reported that *in situ* UV-photolysis of $Cr(CO)_6$ or $Fe(CO)_5$ at 20 K in a CH_4/Ar matrix resulted in the dissociation of a CO ligand which enabled CH_4 coordination (Complex **[i]**, Scheme 1.4a).[30] Characterisation of this σ-methane complex came from the changing CO stretching frequencies in the infra-red spectra and electronic transitions in UV/visible spectrum. These spectral changes could be assigned to the short lived σ-complexes, often occuring with halflives of only ~20 ps upon warming.[15,31] The development of *time resolved infra-red* (TRIR) spectroscopy allowed for higher temperature studies, although these were still well below room temperature,[32] producing the analogous complexes of $M(CO)_5$(alkane) following similar experimental procedures, where M = Cr, Mo, W and alkane = pentane, cyclohexane and heptane.[33–35]

The first example of a late transition metal σ-alkane complexes was reported by Bergman *et al.*. $Rh(\eta^5\text{-}C_5Me_5)(CO)$(*neo*pentane) could be synthesised from the flash photolysis of $Rh(\eta^5\text{-}C_5Me_5)(CO)_2$ in the presence of *neo*pentane.[10] Expanding from this, the George group reported the analogous rhenium complex of $Re(\eta^5\text{-}C_5H_5)(CO)_2$(cyclopentane) (Complex **[ii]**, Scheme 1.4b).[36] Synthesised through the low temperature photolysis of $Re(\eta^5\text{-}C_5H_5)(CO)_3$ within cyclopentane solvent, this particular σ-complex showed stability at room temperature with a half-life of ~ 125 ns, the longest persisiting σ-alkane complex at the time.

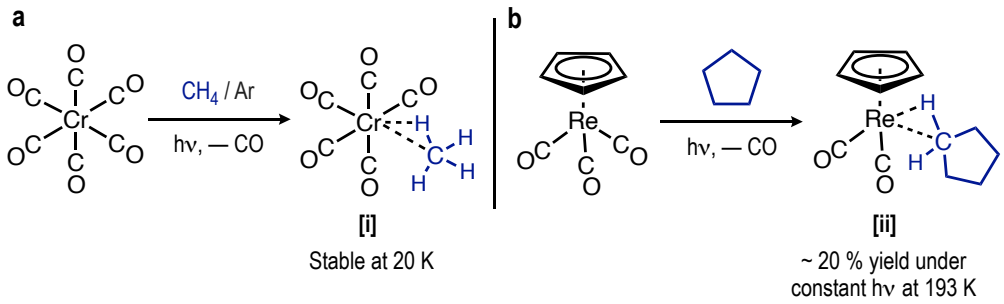

Scheme 1.4: Methodology towards **a**) $Cr(CO)_5(CH_4)$ **[i]** complex and **b**) $Re(Cp)(CO)_2(C_5H_{10})$ **[ii]**.

This led to Ball *et al.* in 1998 reporting **[ii]** as the first charaterisable σ-alkane complex using NMR spectroscopy.[37] The increased lifetime of **[ii]** allowed it to be analysed by the relatively slow timescale of NMR spectroscopic experiments, compared to TRIR. Resonances observed at δ –2.3 in the ^{1}H NMR spectrum (where only one signal is seen from the rapidly exchanging proton environments) and δ –31.2 in the ^{13}C{^{1}H} NMR spectrum were assigned to the CH_2 group of the σ-interaction. Even under constant irradiation however, the maximum yield of this σ-alkane complex was only ~ 20% and when considering this experiment was carried out on a 2 mg scale, meant large-scale σ-alkane complex synthesis was not possible.

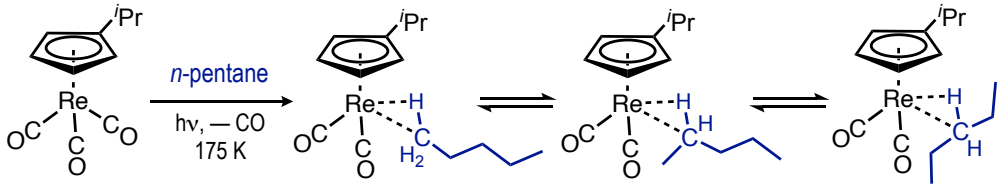

[iii]

Scheme 1.5: Interconverting *n*-pentane binding modes in Re(^{i}PrCp)(CO)$_2$(*n*-pentane) **[iii]**.

This new NMR spectroscopy methodology led to a further range of solution characterised σ-alkane complexes.[38–40] For example, the photolysis of Re(^{i}PrCp)(CO)$_3$, (^{i}PrCp = η^5-(isopropyl)cyclopentadienyl), at 173 K in *n*-pentane resulted in the complex of Re(^{i}PrCp)(CO)$_2$(*n*-pentane), **[iii]**, confirmed by ^{1}H and ROESY (Rotating frame Overhause Effect SpectroscopY) NMR spectroscopy. These experiments also showed that the three coordinating environments of pentane were interconverting slowly (Scheme 1.5) but a slight preference of binding at the CH_2 sites *versus* the -CH_3 environment was observed.[41] This favourability was also shown in computational studies,[42,43] which is in contrast to historic experimental observations that terminal C–H bonds are typically preferentially activated in linear alkanes.

More relevant to the themes of this thesis, σ-alkane complexes from *in situ* UV irradiation within an NMR probe have revealed complexes of propane/butane[44] coordinated to manganese or rhenium metal centres (Scheme 1.6a). Further to these, complexes of ethane and *iso*pentane coordinated to a manganese metal centre (**[iv]** and **[v]**, Scheme 1.6b) were also reported,[45] all of which are synthesised from the respective M(Cp)(CO)$_3$ complex. Much like the previously discussed solution σ-alkane complexes, none of these were stable for any appreciable timescale at room temperature, all with half-lives on the second timescale.

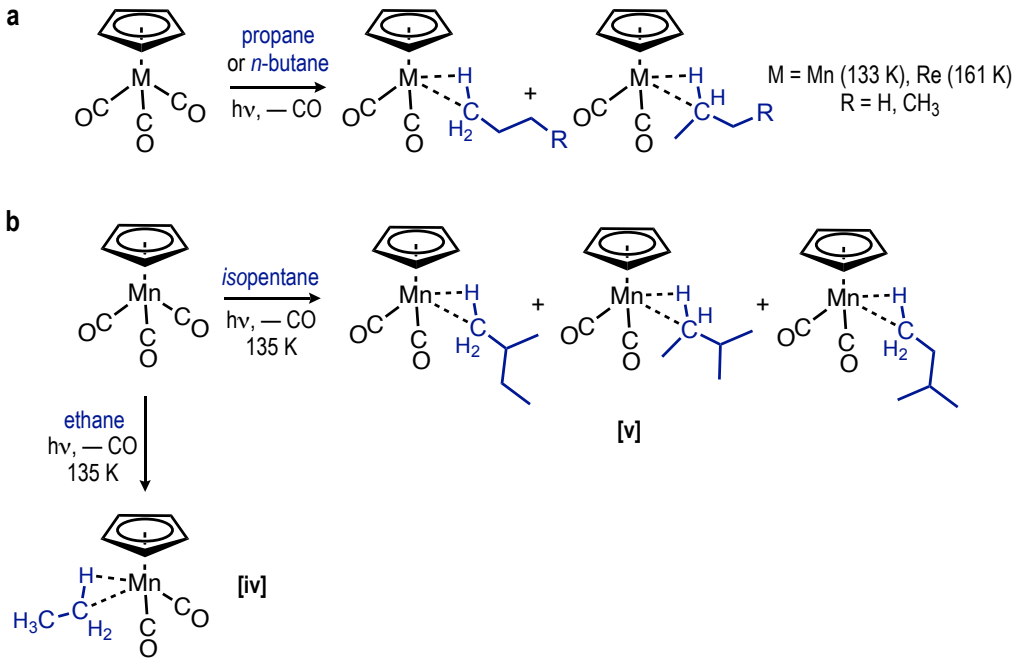

Scheme 1.6: Fomation of σ-alkane complexes of **a**) propane, butane and **b**) ethane and *iso*pentane.

Notably, no preference in C–H binding site was observed for the alkanes of propane or butane yet was for *iso*pentane (Complex **[v]**). No evidence for the coordination to the tertiary C–H group was found by NMR or TR-IR spectroscopy, proposed to be due to steric inhibition around this site, preventing such coordination.

1.3.2. σ-Alkane Complex Synthesis: Solution Phase Protonation

1.3.2.1. Synthetic Routes

An alternative route to solution σ-alkane complexes was published by Brookhart in 2009.[46] The low temperature (163 K) protonation of a Rh(PONOP)(CH_3) complex with [$H(OEt_2)_2$)][$BAr^F{}_4$], where PONOP = 2,6-(^{t}$Bu_2PO)_2C_5H_3N$ and Ar^F = 3,5-$(CF_3)_2C_6H_3$. This generated a stoichiometric amount of CH_4 *in situ*, which remained bound to the rhodium(I) centre, isolating the cationic complex of [Rh(PONOP)(CH_4)][$BAr^F{}_4$], **[vi]**, Scheme 1.7. Additionally, the [Rh]–ethane complex, **[vii]**, was also reported using the same methodology starting from a [Rh]–Et complex.[47]

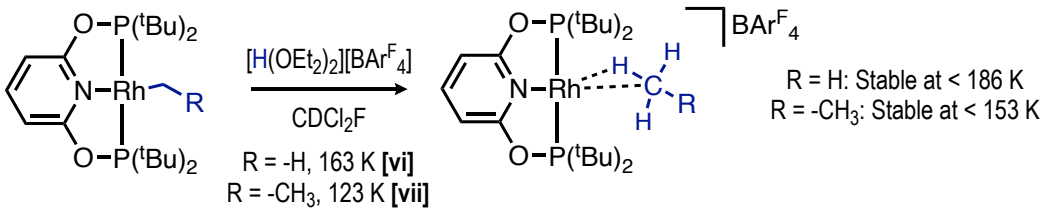

Scheme 1.7: The synthesis of [Rh(PONOP)(CH_4)][BAr^F_4].

Evidence for the formation of **[vi]** was presented by the observation of new signal in the ^{1}H NMR spectrum (δ –0.86, J_{RhH} = 6.3 Hz), assigned to the rapidly exchanging CH_4 protons. A quintet at δ –41.7 was observed in the ^{13}C NMR spectrum, assigned to the bound methane, significantly upfield from free methane [δ –4.9]. Further evidence was also collected from isotopic labelling studies, by protonation of the sister [Rh]-CD_3 complex under the same conditions. This resulted in bound CHD_3, shown by the ^{2}H{^{1}H} NMR spectrum. A slight downfield shift in signal (δ –1.02) can be explained by isotopic perturbation of equilibrium (IPE),[48] where the C–H, rather than C–D, bond is favoured to be in the bridging, bonding position.

The same methodology was also used in the formation of the ethane analogue, through the protonation of the corresponding [Rh]-ethyl complex at 123 K to form [Rh(PONOP)(C_2H_6)][BAr^F_4], **[vii]**. The lower temperature of 123 K was required due to the even lower stability of this complex, in part due to the increased steric interactions of the ethane ligand with bulky ^{t}Bu arms on the PONOP ligand. Upon warming to 153 K (or 186 K for the Rh-methane complex), free alkane was observed in the ^{1}H NMR spectrum and formation of the solvent coordinated complex of [Rh]–$CDCl_2F$. It was noted the steric bulk around the rhodium centre also prevented the formation of a zwitterionic [Rh]–BAr^F_4 decomposition product for both complexes.

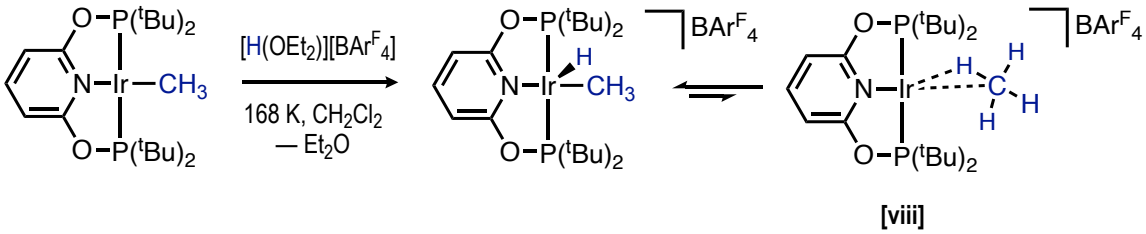

Scheme 1.8: The synthesis of [Ir(PONOP)(CH_3)(H)][BAr^F_4].

Attempts were also made by the Brookhart group to isolate the analogous iridium(I) σ-methane complex. These were unsuccessful, as an iridium(III) methyl hydride complex is isolated, rather than the σ-methane ligated complex (Complex **[viii]**, Scheme 1.8).[49] This is explained by the tendency for 5d-metals to activate of C–H bonds, and the

thermodynamic preference for iridium(III) hydride complexes over the iridium(I) σ-complex. The formation of a transient, intermediate iridium(I) σ-methane complex was confirmed, however, where a fluxional process is observed by the solution 168 K EXSY (EXchange SpectroscopY) NMR spectrum, showing the exchange between the hydride and methyl protons.

The complexes of **[vi]**, **[vii]** and **[viii]** are all cationic, and so require counter anions and polar solvents compared to their neutral counterparts (e.g., **[iii]**). Brookhart utilised Freon ($CDFCl_2$),[47] a polar hydrofluorocarbon (HFC) solvent known for its weakly coordinating nature. Although the fluorine atoms contain lone pairs, the high electronegativity of fluorine makes it a reluctant donor. It has been shown in similar systems that alkanes coordinate to metal centres favourably over that of HFCs.[50] These poorly coordinating solvents, along with weakly coordinating anions (see Section 1.2.2.2.), are used to help supress the decomposition pathway of σ-alkane complexes shown in Scheme 1.9.

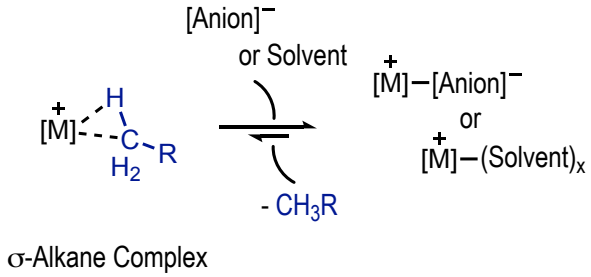

Scheme 1.9: Common decompositon pathways of σ-alkane complexes in solution.

1.2.2.2. Weakly Coordinating Anions

Weakly coordinating anions are pivotal in the synthesis of low-coordinate organometallic complexes and any catalytic applications.[51,52] They are designed so that the negative charge is delocalised over large, non-nucleophilic, chemically robust groups.[53,54] The addition of steric bulk to these anions also helps prevent coordination to metal centres. Common examples of weakly coordinating anions are shown in Figure 1.2.

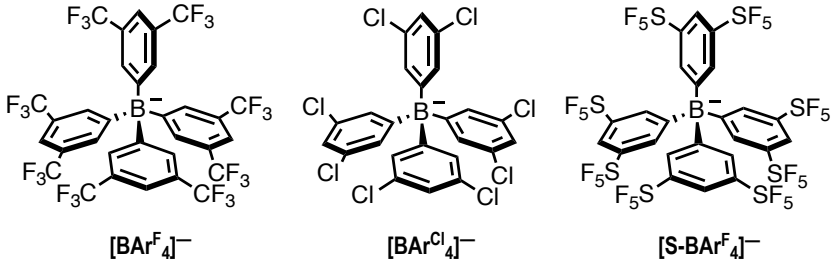

Figure 1.2: The weakly cooridnation anions of $[BAr^{F}{}_4]^-$, $[BAr^{Cl}{}_4]^-$ and $[S\text{-}BAr^{F}{}_4]^-$.

Brookhart successful utilised $[BAr^{F}{}_4]^-$ in the formation of the σ-alkane complexes of **[vi]** and **[vii]** (Scheme 1.7).[47] The $-CF_3$ groups are ideal for their electron withdrawing capabilities, further reducing the anion nucleophilicity. These also provide additional steric hindrance, further preventing coordination to a metal centre. Analogues of $[BAr^{F}{}_4]^-$ include $[BAr^{Cl}{}_4]^-$ (Ar^{Cl} = 3,5-$(Cl)_2C_6H_3$)[55] and $[S\text{-}BAr^{F}{}_4]^-$ (Ar^{F} = 3,5-$(SF_5)_2C_6H_3$),[56] shown in Figure 1.2, where substitution of the $-CF_3$ groups with -Cl and $-SF_5$ has been achieved. While these are weakly coordinating, they are not non-coordinating and still can undergo η^6-coordination of the aryl groups to the metal centre. This results in a zwitterionic, anion-coordinated complex, where examples of these are shown in Figure 1.3.[57,58]

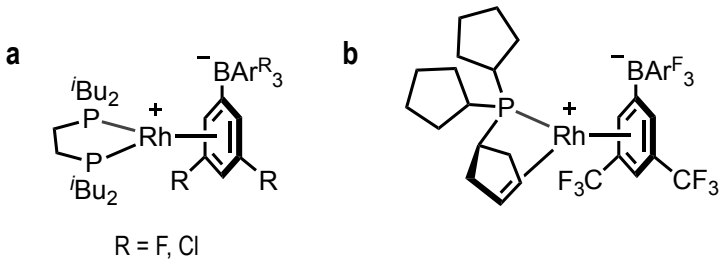

Figure 1.3: Examples of η^6-coordinated $[BAr^{X}{}_4]^-$ complexes. **a**) = $[Rh(^{i}Bu_2PCH_2CH_2P^{i}Bu_2)\{(\eta^6\text{-}C_6H_3R_2)BArR_3\}]$[59] where R = F, Cl and **b**) = $[Rh\{P(Cyp_2)(\eta^2\text{-}C_5H_7)\}\{\eta^6\text{-}(C_6H_3(CF_3)_2)BAr^{F}{}_3\}]$.[58]

1.3.3. Cationic σ-Alkane Complex Synthesis: Photolytic Routes

Anions to even further minimise coordination with a transition metal centre have been developed by the Krossing group.[60] On example is the perfluoroalkoxyaluminate anion of $[Al(OC(CF_3)_3)_4]^-$, shown in Scheme 1.10a, where Ball *et al.* utilised this anion in the synthesis of the cationic σ-cyclopentane complex (Complex **[ix]**, Scheme 1.10b).[50] This was conducted by the photolysis of [Re(hexaethylbenzene)$(CO)_3$][$Al(OC(CF_3)_3)_4$] at 193 K in a mixture of HFC (1,1,1,3,3,3-hexafluoropropane, $F_3CCH_3CF_3$) and cyclopentane solvents, that lead to the formation of [Re(hexaethylbenzene)$(CO)_2$(η^2-cyclopentane)][$Al(OC(CF_3)_3)_4$], **[ix]**.

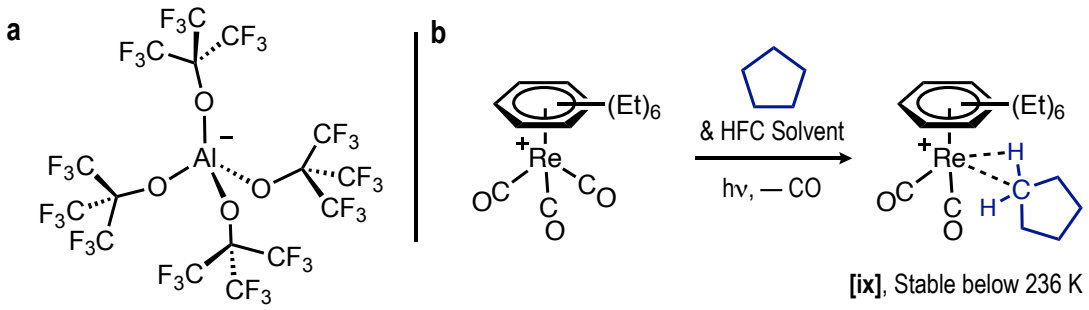

Scheme 1.10: The synthesis of [Re$(Cp(Et)_6)(C_5H_{10})$][$Al(OC(CF_3)_3)_4$], **[ix]**.

This σ-cyclopentane complex is reported to be stable for hours below 213 K, however, rapid decomposition occurs at 236 K to form a range of unidentified products. As no anion coordinated decomposition products could be directly isolated, this highlights the extremely poorly coordinating nature of the $[Al(OC(CF_3)_3)_4]^-$ anion.

1.3.4. Solution σ-Alkane Complex Synthesis: Summary

Overall, similarities can be drawn between the photochemical and protonation methods in σ-alkane complex synthesis in solution. The complexes were shown with short lifetimes (ps to hours), synthesised at low temperatures (20 to 212 K) in small quantities (1 to 20 mgs) and at often less than 100 % efficiencies. This overall results in sub-optimal conditions for the isolation of σ-alkane complexes.

The lack of isolation of the σ-alkane complexes means that full characterisation and any exploration of any further reactivity, such as kinetics studies, is difficult. The short lifetimes of these complexes also meant that growth of any single-crystals for single-crystal x-ray diffraction – seen as the 'gold-standard' in structural characterisation – is challenging. Alternative methodologies were needed to be developed to allow for this method of characterisation.

1.3.5. σ-Alkane Complex Synthesis: Alkane Incorporation

The first reported solid-state characterisation of a σ-alkane complex resulted from the introduction of an alkane ligand to a pre-organised structure. In 1997, Boyd *et al.* reported that recrystallisation of an iron(II) porphyrin complex from C_6H_5F / *n*-heptane solvent combination resulted in an iron(II) heptane complex (**[x]**, Scheme 1.11).[61] This relied on the extended structure being already equipped with vacant sites, which are able to support the σ-alkane interaction.

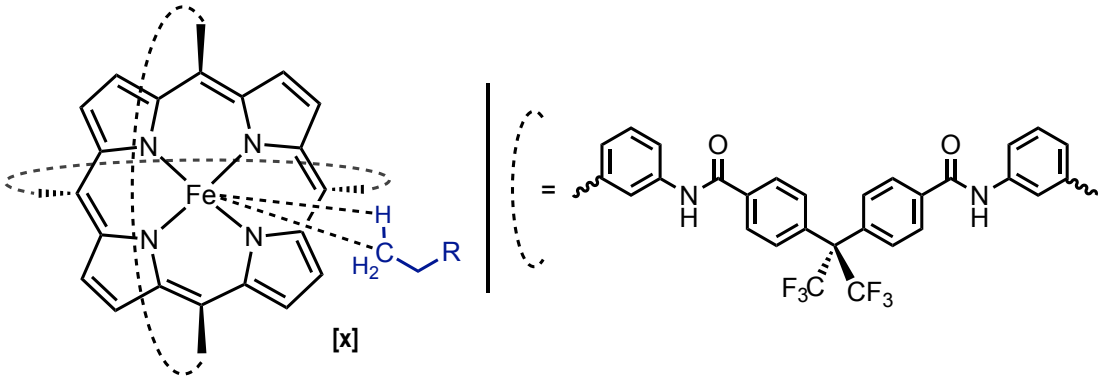

Scheme 1.11: a) The solid-state characterised iron(II) porphyrin σ-heptane complex **[x]**. R = $-(CH_2)_4CH_3$.

The recrystallised product was of sufficient quality to be examined by single crystal x-ray diffraction, which revealed a close-encounter of each methyl group on the heptane towards an iron site, where only one of these interactions is shown in Scheme 1.11. These two sites revealed Fe•••C distances of 2.5 and 2.8 Å. As these distances are comparable to the sum of the covalent radii of Fe and C (2.28 Å),[62] this is suggestive of a long, but significant σ-interaction. The stability of these complexes can be linked to the surrounding solid-state environment, providing a support network of non-covalent interactions to encourage the metal-alkane interactions. This idea is further explored in Chapter 2.

A further example of a close metal-alkane interaction is of the unsaturated uranium complex $[U(ArO)_3tacn]$, where tacn = 1,4,7-tris(3,5-di-^{t}butyl-2-hydroxybenzyl)-1,4,7-triazacyclononane. This work by the Meyer group[63] showed C_5 and C_6 cyclic-hydrocarbons, which are derived from the solvent, could be incorporated into this framework upon dissolution and recrystallisation. This is shown with methylcyclohexane as complex **[xi]** in Scheme 1.12. Single crystal x-ray diffraction was used to characterise these complexes, which suggest a metal-alkane interaction.

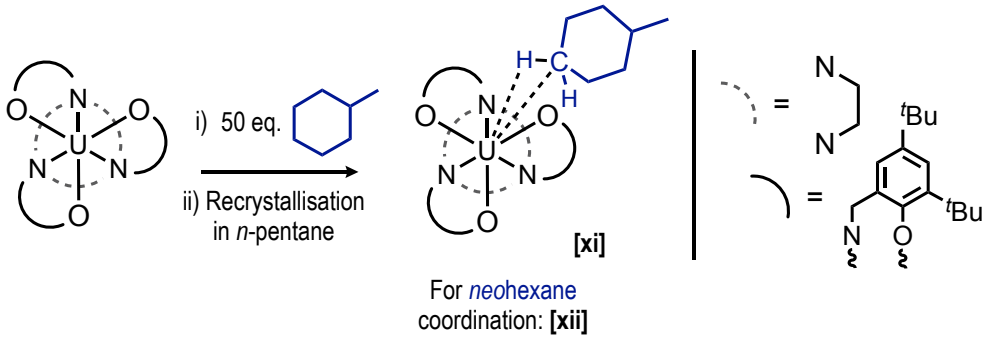

Scheme 1.12: A proposed solid-state characterised uranium σ-alkane complex.

The U•••C distances however were reported as 3.731(8) and 3.864(7) Å for *neo*hexane and methylcyclohexane respectively. As these distances are longer than the sum of the covalent radii of U and C (2.72 Å),[62] this is probably best described as a host/guest complex, supported by non-covalent, dispersion interactions, rather than σ-alkane complexes.[64] There is a high amount of disorder of the alkane fragment present within the crystal structure, which hinders any hapticity discussions. Similar host/guest interactions towards the formation of σ-alkane complexes have been also reported towards K^+ metal centres,[65] as well as alkane binding to Fe centres in metal-organic frameworks (MOFs).[66]

For the complexes of **[xi]** and **[xii]**, no solution-based spectroscopic data was available. Rapid displacement of alkane fragment occurs upon dissolution so they cannot be compared directly to the complexes presented in Section 1.1.1. No solid-state spectroscopic techniques, such as solid-state NMR spectroscopy, were reported either. This, along with the debateable metal alkane distances, meant the search for a well-defined σ-alkane complex in the solid-state continued. One methodology to achieve this is to by-pass the use of solutions altogether and undergo reactions directly in the solid-state, which would remove any detrimental solvent coordination completely. This idea is discussed in Section 1.4.

1.4. Solid-State Reactivity

1.4.1. Surface Organometallic Chemistry

The capability to take well-established, homogeneous organometallic catalysts/reagents and convert them for use in heterogeneous reactions has a wide range of fundamental and technological applications.[47] This approach combines the benefits of homogeneous reactions, such as control over selectivity and activity as determined by the metal/ligand environment, with the benefits of heterogeneous systems of durability, product separation and catalytic recovery.

Single-Site Heterogenous Catalysts (SSHC) are the example of this approach. Here, spatially isolated, organometallic complexes can be integrated over thin films or, more commonly, into three-dimensional supports.[67] Examples of these 3D supports include zeolites, metal oxides or microporous aluminates,[68] which all contain large surface areas where specific, organometallic active sites can be attached.

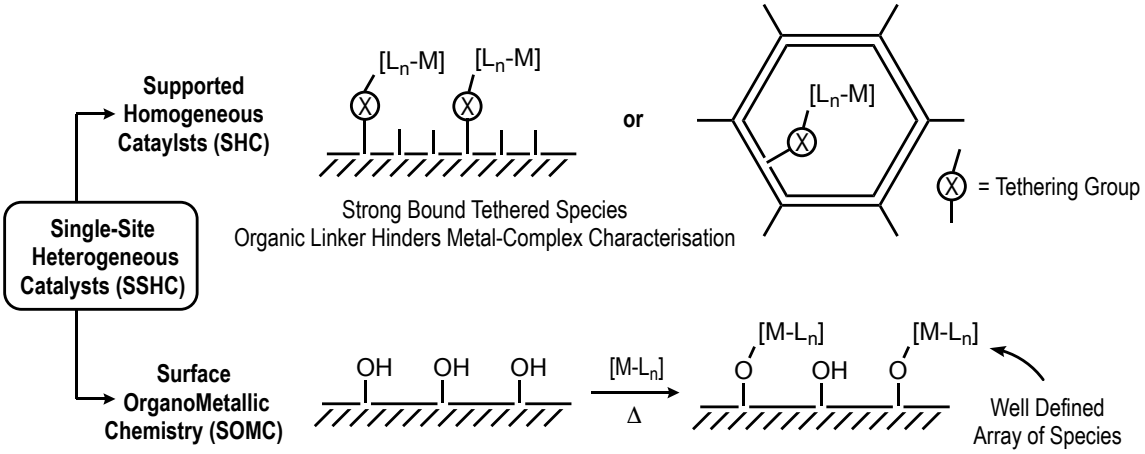

Scheme 1.13: Overview of Single-Site Heterogeneous Catalysts (SSHCs).

The term SSHCs can be split into two specific types: Supported Homogeneous Catalysts (SHCs) and Surface OrganoMetallic Catalysts (SOMC) (Scheme 1.13). SHCs are where the metal complex is attached to the platform support *via* a tethering-group, whilst SOMC directly anchors the metal complexes to the support's surface. SOMC systems allow for a greater surface covering of active sites to the support platform and are often chemically comparable to the species present in their homogeneous counterparts. SHC systems however allow for a greater dispersion of species throughout the support material, and the covalently bonded tethers reduce catalyst leaching. SOMC systems have been applied to a wide range of selective catalytic reactions including Zeiger-Natta olefin polymerisation,[69]

olefin metathesis[70] and light-alkane dehydrogenation.[71] SHCs are also comparable to MOF-functionalized materials with organometallic species.[72–75]

The structural characterisation of the coordination spheres in SOMC and MOF systems can be studied by a range of techniques. These include powder x-ray diffraction, microscopy and gas adsorption, which focus on the morphology and surface area of the bulk support. Additionally, when using a range of x-ray techniques, IR/Raman and UV spectroscopies, this can probe the metal's oxidation state and coordination sphere.

In both cases however, probing the nature of the active sites can be challenging at the molecular level, and these are often ill-defined.[76] This characterisation is essential in any structure-activity relationship studies. It takes the combination of all these techniques however to build up a model of the overall SOMC material,[76] which can be used to either characterise the active catalyst or probe catalytic species during reactions. Although SSNMR spectroscopy methods are widely used, the poor sensitivity from typically low loadings of the catalysts limits this spectroscopic technique.

1.4.2. Single-Crystal to Single-Crystal Reactions

A single-crystal to single-crystal (SC-SC) transformation is one where a solid, crystalline material is directly reacted upon, resulting in structurally transformed products and retains crystallinity (Scheme 1.14).[77,78] Within the crystalline solid-state, molecular packing and long-range order is determined within a set of limits which are defined by the array of bonding forces such as van der Waals, ionic and covalent interactions. These intramolecular forces create a confined nature, which can restrict certain molecular movements. This is opposed to a homogeneous solution, where freely moving molecules can orient themselves randomly.

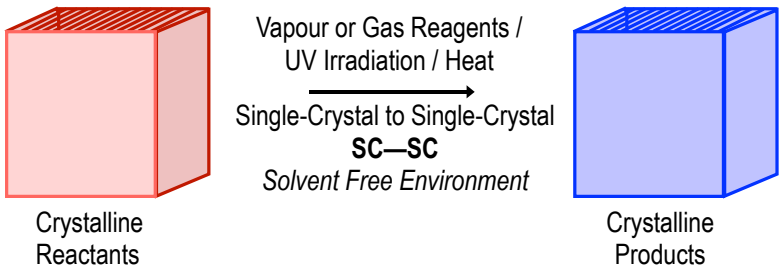

Scheme 1.14: Overview of Single-Crystal to Single-Crystal reactivity.

SC-SC reactions in a range of materials have been reported, for example, in platform supported materials such as MOFs[72,79] and coordination polymers (CP).[80,81] Discrete molecular systems can also undergo SC-SC reactivity,[82–84] which can be initiated by external stimulus agents such as solvent vapours,[85] gaseous reagents,[86] heat and irradiation by UV light.[87] Single-crystal or powder diffraction techniques can then be used to determine the product's structure directly in the solid-state. When conducted in tandem with orthogonal spectroscopic techniques, such as solid-state UV, FT-IR and NMR spectroscopies, complimentary information at the atomic and molecular level is collected.

In discrete molecular systems, only small structural changes are typically tolerated, with typical unit cell volume changes of ~4 %, where more complex structural rearrangements tend to lead to a loss of long-range order of the material and amorphous solid-state products.[88] The retention of crystallinity is pivotal for the isolation and characterisation of products from solid-state reactions. When the analysis of such products from solid-state reactions are conducted in solvent, this may lead to further reactivity upon dissolution, and are not indicative of the solid-state products.[88] Furthermore, these products may differ from those when the reaction is conducted in solvent altogether.

One such example of a discrete molecular system was reported by Powers *et al.*[89] Upon UV irradiation, single-crystals of a Rh_2 alkylazide, undergoes N_2 elimination, resulting in a Rh_2 nitrenoid product, shown in Scheme 1.15.

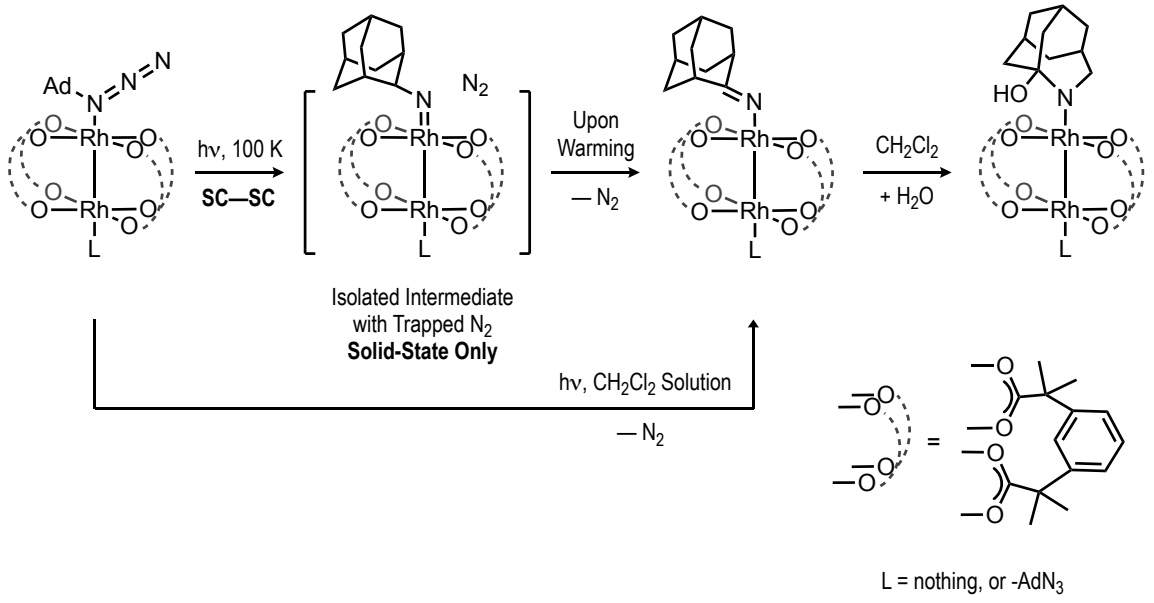

Scheme 1.15: SC-SC reaction pathway towards a Rh_2 nitrenoid.

Although it was shown this reaction proceeds in both the solution and solid-state when conducted in the solid-state an, unseen in solution, intermediate complex can be assigned. The SC-SC nature of this reaction allows for the intermediate Rh_2 nitrenoid product to be isolated and characterised by single-crystal x-ray diffraction at 100 K. Key crystallographic metrics, such as Rh–N / N–C distances and C–Rh–N angles were used to confirm these structural changes. Notably, the collected structure also showed that the eliminated N_2 was trapped within the crystal lattice, located within a close, yet non-coordinating, distance to the Rh centre. This again, is not observed in solution, due to the rapid loss of N_2.

Upon warming from 100 K however, rapid isomerisation and N_2 loss in the solid-state occurs to form the same product as from the solution route. It was also further shown that this Rh_2 nitrenoid undergoes a rapid reaction with H_2O in solution to reach the final alcohol product. Overall, this solid-state matrix, combined with a SC-SC reaction, has allowed for the isolation and characterisation of this species, which is not observed in solution. The solid-state environment has directly stabilised the product for elongated periods of time. This idea is taken further throughout this thesis.

1.5. Solid-State Molecular OrganoMetallic (SMOM) Chemistry

1.5.1. SMOM Concept

The use of discrete, crystalline organometallic complexes in solid/gas reactions, without being supported upon a platform material, is the foundation of the Solid-State Molecular OrganoMetallic (SMOM) methodology. This still establishes a heterogeneous system yet has the benefit of being able to be straightforwardly studied at the molecular level. This is unlike SOMC/SSHC heterogeneous systems presented in Section 1.3.

This so-called SMOM methodology is readily applied in combination with single-crystal to single-crystal (SC-SC) reactions. This allows for single-crystal x-ray diffraction to be used to directly visualise the solid-state structures of the intermediate and product complexes. Spectroscopic techniques, such as such as solid-state NMR (SSNMR) spectroscopy is also available due to the high concentration of spin active nuclei. As these systems are precisely defined, computational methods such as periodic DFT can also be readily applied. The SMOM concept was introduced by the Weller group for σ-alkane complex synthesis in the solid-state,[83] and is the subject of this thesis.

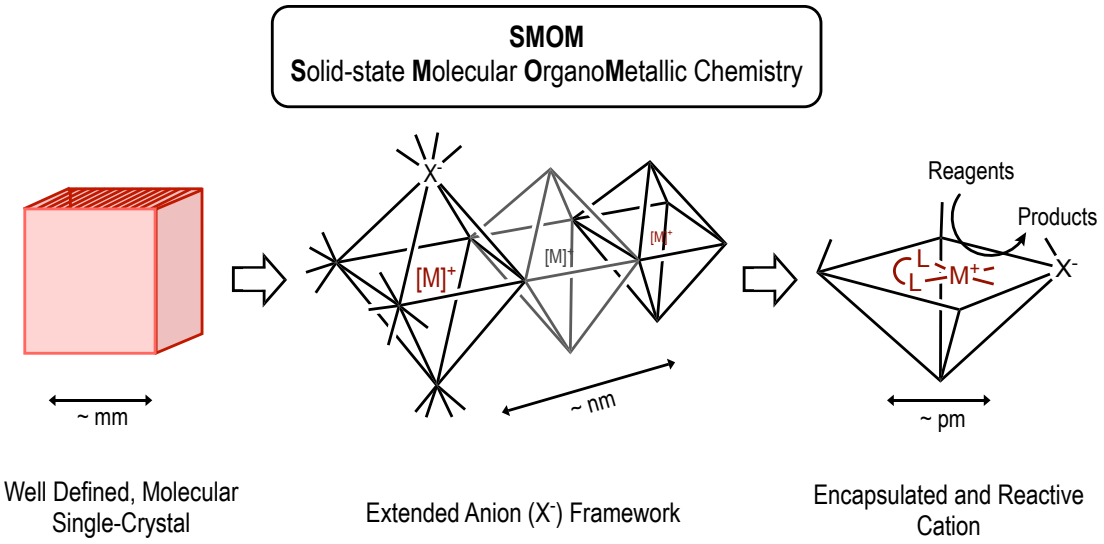

Figure 1.4: Overview of the SMOM concept.

The SMOM concept has been successfully applied towards the synthesis of cationic, rhodium σ-alkane complexes. By taking single-crystals of a cationic rhodium diene complex and reacting them with dihydrogen gas, this results in the direct formation of a σ-alkane complex in the solid-state. This follows a SC-SC reaction where the product can be determined directly by single-crystal x-ray diffraction.

Notably, the SC-SC reaction is supported by the anion framework, noted as vital towards providing a robust, crystalline microenvironment that can withstand the rearrangement of the cation whilst retaining the overall single crystalline structure (Figure 1.4). It also acts as a support, stabilising the σ-alkane complex and thus allowing for the isolation, characterisation and further reactivity of these systems to be reliably studied.

Three systems of notable stability and further reactivity are highlighted within Section 1.5.2. Detailed analysis of these systems are also further discussed in the following sub-sections.

1.5.2. σ-Alkane Complex Synthesis: Solid-State Alkene Hydrogenation

1.5.2.1. A σ-norbornane Complex, [1-NBA][BAr$^F_4$]

The first solid-state σ-alkane complex discussed is a σ-noroborane (NBA) complex. When single-crystalline material of the precursor diene complex of [Rh($Cy_2PCH_2CH_2PCy_2$)(C_7H_8)][BAr$^F_4$], **[1-NBD][BAr$^F_4$]** (NBD = norbornadiene) was reacted directly with H_2 gas, this resulted in hydrogen addition across the alkene bonds of the NBD ligand, in a Schrock-Osborn like hydrogenation.[90] The resultant complex was that of the saturated alkane of noroborane coordinated to the rhodium(I) centre, using two 3c-2e$^-$ interactions, of [Rh($Cy_2PCH_2CH_2PCy_2$)(C_7H_{12})][BAr$^F_4$], **[1-NBA][BAr$^F_4$]** (Scheme 1.16, Figure 1.5).

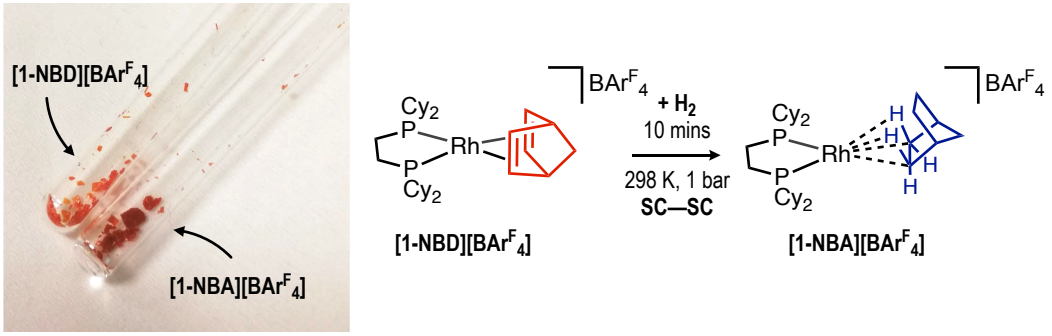

Scheme 1.16: Images of crystals of **[1-NBD][BAr$^F_4$]** and **[1-NBA][BAr$^F_4$]** and synthetic procedure to **[1-NBA][BAr$^F_4$]**.

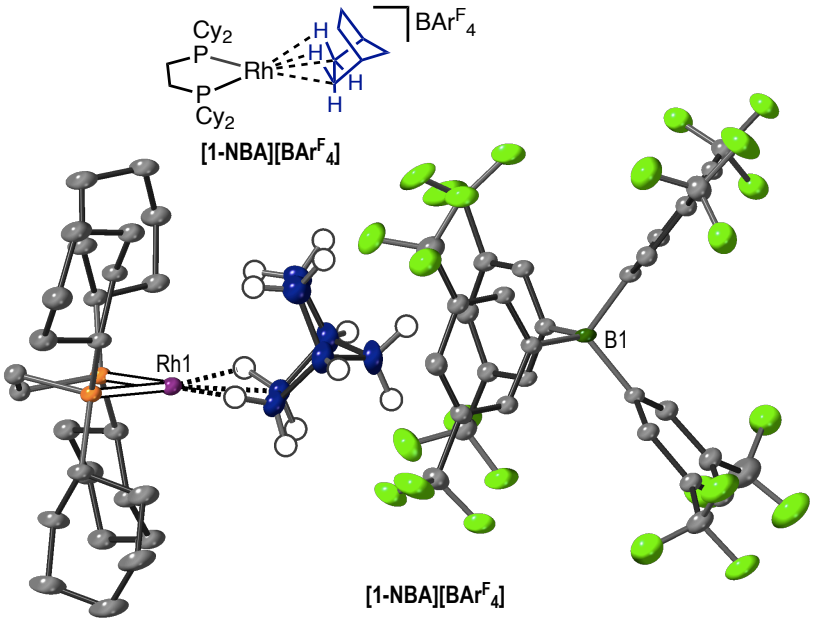

Figure 1.5: Solid-state structure of **[1-NBA][BAr$^F_4$]**. Hydrogen atoms on phosphine ligand and $[BAr^F_4]^-$ anion excluded for clarity and displacement ellipsoids set at 30 %.

This transformation was unequivocally confirmed as a σ-alkane complex by single-crystal x-ray diffraction, $^{31}P\{^1H\}$, $^{13}C\{^1H\}$, and further 2D solid-state NMR spectroscopy experiments. The appearance of the crystals also changes upon hydrogenation, where a colour change of orange to blood red (Scheme 1.16,) as well as physical cracking upon the surface of the crystals can be visually seen.

Selected bond metrics from the structure obtained from single-crystal x-ray diffraction studies are shown in Table 1.1. These data show an elongation of the carbon-carbon distances of the C=C bonds in the starting NBD ligand, consistent with the formation of alkane C–C bonds in the NBA ligand. Contraction of the Rh–P bonds upon addition of H_2 is observed, signalling the reduced *trans*-influences from the alkane ligand, and increased Rh•••C distances reflecting the weak 3c–2e$^-$ bonds of the NBA ligand. A space group change reflects the increase in symmetry from hydrogenation of the twisted coordination of the NBD ligand. Changes in the unit cell angles and distances also occur resulting in the increased volume of the unit cell (~ 2%), comparable to previous SC-SC reactions.[88]

Table 1.1: Selected crystallographic information of **[1-NBD][BAr$^F_4$]** and **[1-NBA][BAr$^F_4$]**.

	Rh–P1 / Rh–P2 (Å)	Rh–C1 / Rh–C2 (Å)	C1–C2 / C4–C5 (Å)	Unit Cell Volume (Å^3) / Space Group
[1-NBD][BAr$^F_4$]	2.2940(13) / 2.2845(13)	2.241(6) / 2.217(5)	1.385(10) / 1.374(10)	3287.01(13) / P–1
[1-NBA][BAr$^F_4$]	2.1932(7) / 2.1950(7)	2.389(3) / 2.400(3)	1.552(4) / 1.546(7)	6691.6(9) / P2$_1$/n

The anion framework, which is established during the crystallisation of the precursor diene complexes, is key for not only supporting the SC-SC reaction, but also for the stability of **[1-NBA][BAr$^F_4$]** in the solid-state. **[1-NBA][BAr$^F_4$]** exhibited remarkable stability of greater than 4 months under an inert atmosphere at room temperature, easily proving to be the new benchmark system in σ-alkane complex synthesis and stability. The pseudo-O_h arrangement of [BAr$^F_4$]$^-$ anions, shown in Figure 1.6a, encloses the cationic fragment and creates a microenvironment which supports the coordinated σ-alkane ligand. The orientation of the cation in **[1-NBA][BAr$^F_4$]** is pointing towards a [BAr$^F_4$]$^-$ anion vertex. This allows for the -Ar^F arms to encompass the alkane ligand, further stabilising alkane coordination, Figure 1.6b.

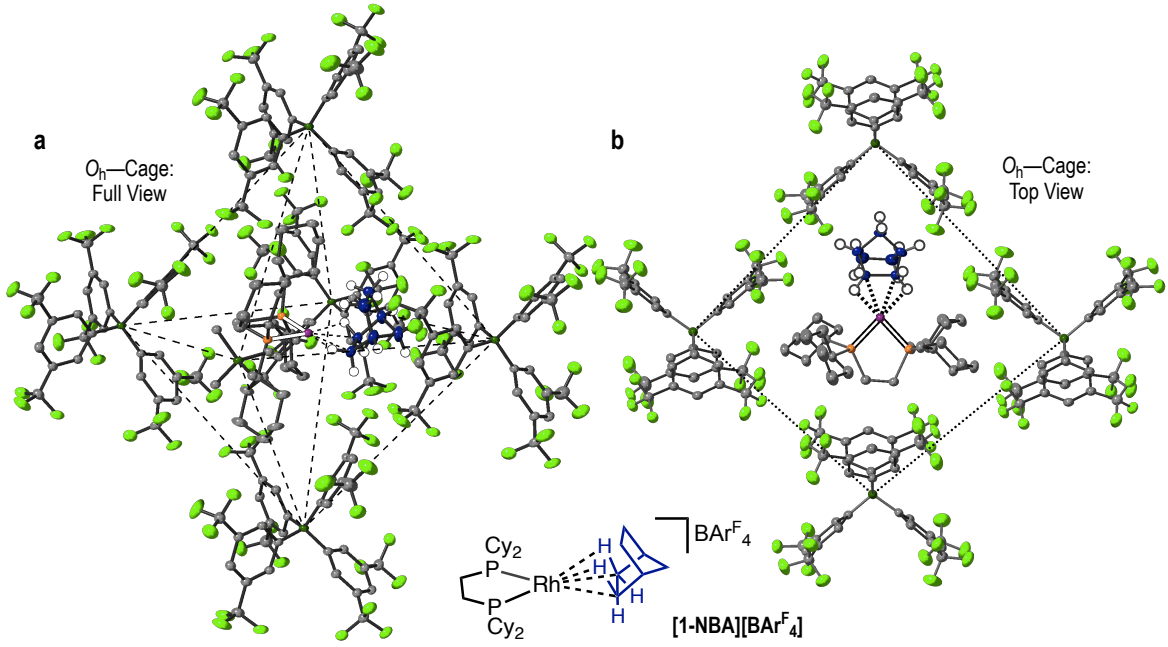

Figure 1.6: **a**) Pseudo-octahedral framework of [BAr$^F_4$]$^-$ encapsulating the cation. **b**) Top view of the pseudo-octahedral framework, showing cation orientation. Hydrogen atoms on phosphine ligand and [BAr$^F_4$]$^-$ anions excluded for clarity and displacement ellipsoids set at 30 % in both parts.

Due to the tall and ridged nature of cyclohexyl -PCy_2 substituents and bulky NBA ligand of **[1-NBA][BAr^F_4]**, the cationic fragment also benefits from numerous C–H•••F–C hydrogen bonding interactions with the [BAr^F_4]$^-$ anion support in the solid-state.[57] The relatively large size of the -cyclohexyl substituents and NBA ligand also reduces the void space within the O_h cavity, potentially aiding these hydrogen bonding interactions, which are shown in Figure 1.7.[57]

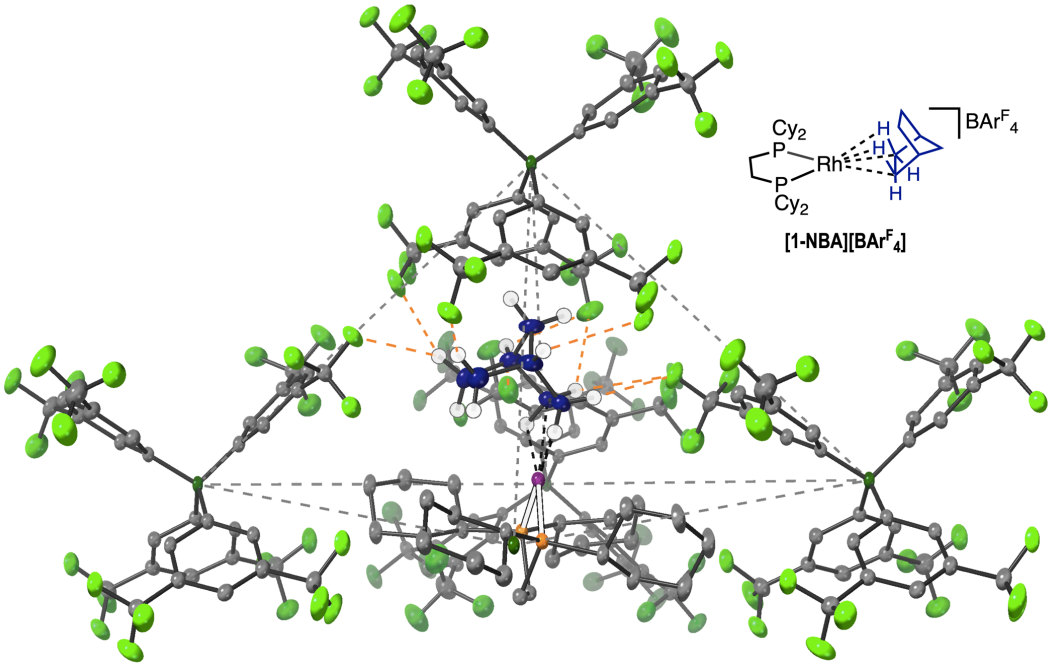

Figure 1.7: Solid-state structure of **[1-NBA][BAr^F_4]**, showing part of the pseudo-O_h framework of [BAr^F_4]$^-$ anions encapsulating the cation. C–H•••F–C hydrogen bonding interactions in the range of 2.30-2.99 Å, highlighted by orange dashes. Hydrogen atoms on phosphine ligand and [BAr^F_4]$^-$ anions, as well as -Ar^F_4 groups on selected B-atoms, excluded for clarity. Displacement ellipsoids set at 30 %.

The ^{31}P environments in the bisphosphine ligand are useful spectroscopic reporters. Upon hydrogenation, the resonances in the $^{31}P\{^1H\}$ SSNMR spectrum for **[1-NBA][BAr^F_4]** shift downfield (δ 79 to 110) from that of **[1-NBD][BAr^F_4]**. The $^{13}C\{^1H\}$ SSNMR spectrum show the disappearance of signals in the alkene region (δ 40 – 110), suggestive of the hydrogenation of alkene environments in the NBD ligand. Unfortunately, the alkane signals of NBA are concealed behind those of the broad ^{13}C environments of cyclohexyl R-groups, so could not be fully resolved. Indirect observation of the ^{1}H environments of the Rh•••H–C interactions could be detected by a $^{13}C/^1H$ frequency switched Lee Goldberg Heteronuclear Correlation (FSLG-HETCOR) experiment. This showed cross peaks

between ^{13}C signals at δ 70 and ^{1}H signals at δ 0.4, assigned to the coordinating environment of the NBA ligand.

Attempts to analyse **[1-NBA][BAr$^{F}_{4}$]** by solution routes, even at low temperatures (183 K) in Freon solvent, resulted in the formation of **[1-BAr$^{F}_{4}$]** (Scheme 1.17). Thus, the SMOM-methodology results in σ-alkane complexes unique to the solid-state. By working in a solventless, solid-state environment, any competitive solvent coordination pathway is removed, and anion coordination is minimised. Solvent coordination was shown as a major decomposition route in previous solution σ-alkane complexes.[46]

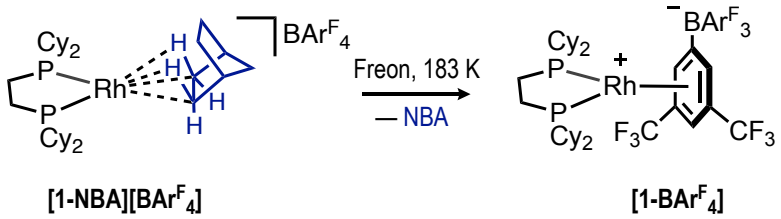

[1-NBA][BAr$^{F}_{4}$] **[1-BAr$^{F}_{4}$]**

Scheme 1.17: Solution decompositon of **[1-NBA][BAr$^{F}_{4}$]** to **[1-BAr$^{F}_{4}$]**.

Notably, this coordination does not occur in the solid-state. DFT calculations show that the proposed decomposition pathway of **[1-NBA][BAr$^{F}_{4}$]** to **[1-BAr$^{F}_{4}$]** in the solid-state is highly exergonic of –79.6 kcal mol^{-1} however.[57] This suggests a large kinetic barrier towards this solid-state decomposition must be present.

1.5.2.2. Computational Analysis of [1-NBA][BAr$^F_4$]

Computational studies gave further evidence towards the formation of **[1-NBA][BAr$^F_4$]**. Periodic DFT studies conducted, such as Quantum Theory of Atom in Molecules (QTAIM),[25,26] analysis calculated the topology of total electron density of the complex, showing the nature of the Rh•••C–H bond paths (Figure 1.8a) and the associated Bond Critical Points (BCP). Figure 1.8b shows the descriptors of this analysis.

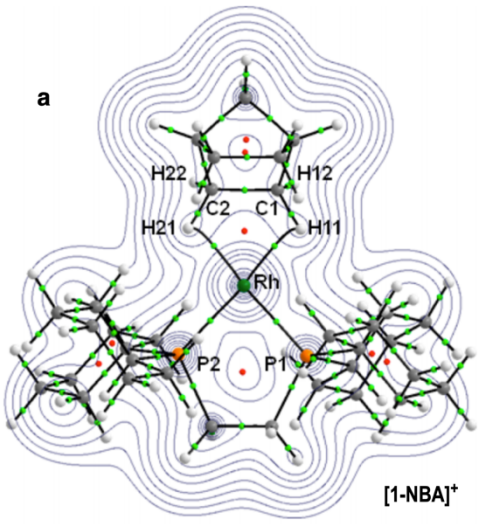

BCP	ρ (r)	$\nabla^2\rho$ (r)	H (r)
Rh•••H11	0.060	0.208	—0.013
C1—H11	0.231	—0.610	—0.198
C1—H12	0.274	—0.929	—0.274

Figure 1.8: **a**) Contour plot of the electron density in **[1-NBA]$^+$** cation, plotted in the Rh1-H11-H21 plane. BCP and RCP shown by green and red points respectively. **b**) Highlighted BCP metrics (au).

The curved bond paths and significant electron density between Rh•••H and reduced density of the C–H bond suggest an alkane σ-interaction. The presence of Ring Critical Points (RCP), shown by red dots, are areas of low electron density and are typically destabilising environments. The value of the descriptors, such as the electron density (ρ, is small and positive), Laplacian ($\nabla^2\rho$, is small and positive) and the total energy density (H, small and negative) are all consistent with that of that of two, η^2 σ-interactions.[27]

Furthering the QTAIM analysis, NCI (Non-Covalent Interaction)[91,92] plots can be produced, which highlight weak stabilising or destabilising interactions within the solid-state cavity. Shown in Figure 1.9a, the blue area of electron density suggests a relatively strong stabilising interaction as well as destabilising (red/orange) interactions. These are consistent with the RCP seen in Figure 1.8a. The large areas of green are assigned to weak, intermolecular dispersive interactions that are stabilising in nature, and are calculated between the NBA ligand and close aryl groups from neighbouring [BAr$^F_4$]$^-$ anions. Areas between the [BAr$^F_4$]$^-$ anion and -cyclohexyl R-group also display these

dispersive interactions. These forces are considered key in stabilising the alkane ligand within the solid-state cavity.

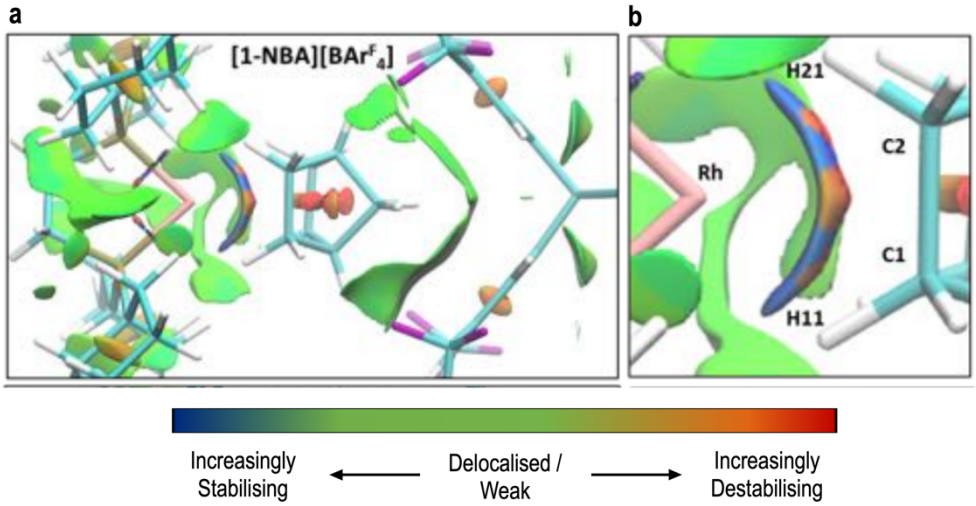

Figure 1.9: **a**) NCI plot of **[1-NBA][BAr$^F_4$] b**) detailed view of the Rh–NBA coordination. Isosurfaces generated for s = 0.3 au and -0.07 < ρ < 0.07 au.

Quantifying this interaction, in terms of orbital interactions and their binding energies, was achieved through Natural Bond Orders (NBO) calculations.[93] Important donor-acceptor pairs of the σ-interactions can be examined, which showed NBA coordination occurs through a $\sigma_{CH} \rightarrow$ *trans*-σ^*_{RhP} interaction, with an associated interaction energy of 20 kcal/mol. Back-donation from a rhodium lone pair, associated on a d_{xy} orbital, and the *cis*- and *trans*-σ_{RhP} orbitals into the σ^*_{CH} orbital are also significant, totalling 8.7 kcal/mol. The overall dominating component of the NBA coordination is therefore the $\sigma_{CH} \rightarrow$ *trans*-σ^*_{RhP} interaction. This bonding is extremely weak when compared to the bonding interaction involved in the precursor NBD complex of **[1-NBD][BAr$^F_4$]**, where $\pi_{CC} \rightarrow$ *trans*-σ^*_{RhP} = 56.3 kcal/mol and backbonding contributions = 36.1 kcal/mol.

1.5.2.3. A σ-cyclohexane Complex, [1-cyclohexane][BAr$^{F}_{4}$]

The second system to be discussed here is that of a σ-cyclohexane complex. By using the same RhP_2^+ fragment and $[BAr^F_4]^-$ anion as **[1-NBD][BAr$^{F}_{4}$]**, and changing the diene ligand, $[Rh(Cy_2PCH_2CH_2PCy_2)(C_6H_{12})][BAr^F_4]$, **[1-cyclohexane][BAr$^{F}_{4}$]** was reported. This was synthesised from the hydrogenation of the cyclohexadiene precursor complex $[Rh(Cy_2PCH_2CH_2PCy_2)(C_6H_8)][BAr^F_4]$, **[1-cyclohexadiene][BAr$^{F}_{4}$]** in a SC-SC reaction.[94] This was characterised by single-crystal x-ray diffraction and SSNMR spectroscopy, and the solid-state structure is shown in Figure 1.10a. Importantly, **[1-cyclohexadiene][BAr$^{F}_{4}$]** crystallised in a pseudo-O_h arrangement of $[BAr^F_4]^-$ anions, which is maintained upon hydrogenation and shown in Figure 1.10b.

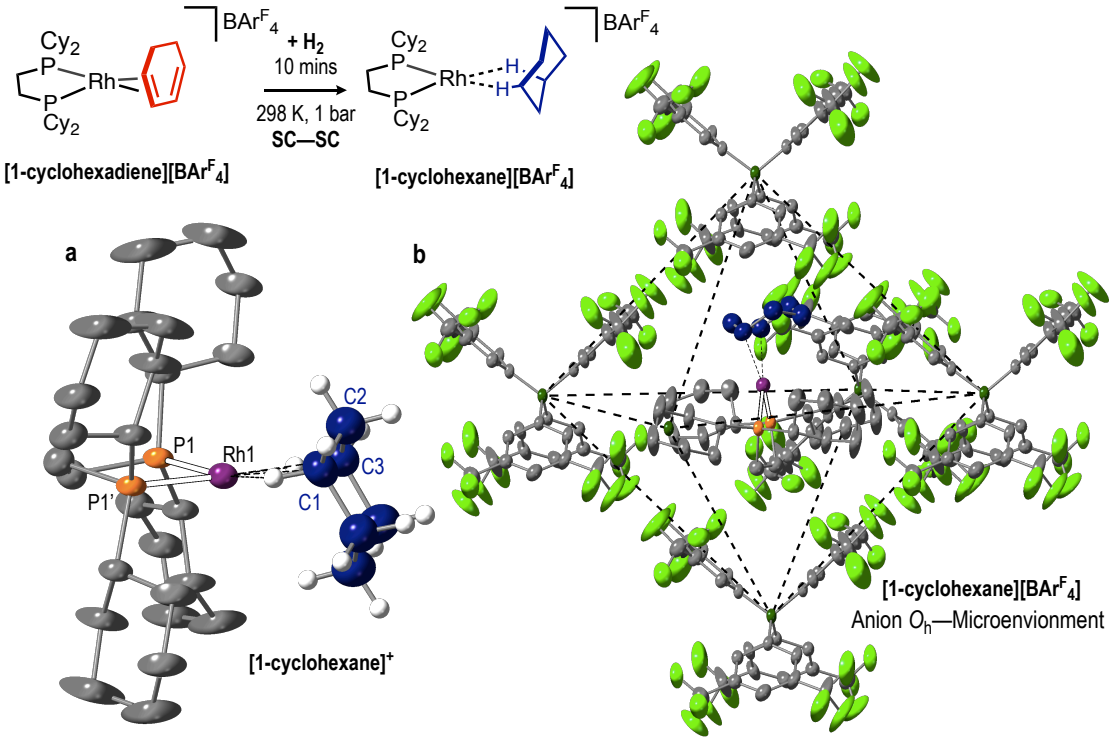

Figure 1.10: **a**) Solid-state structure of the cationic portion of **[1-cyclohexane][BAr$^{F}_{4}$]**. **b**) Pseudo-octahedral framework of $[BAr^F_4]^-$ encapsulating the cationic fragment. Hydrogen atoms on phosphine ligand and $[BAr^F_4]^-$ excluded for clarity and displacement ellipsoids set at 30 % in both parts.

The same changes that signalled the formation of an σ-alkane complex in **[1-NBA][BAr$^{F}_{4}$]** are also shown here. These include elongation of the C=C and Rh–C distances, and contraction of the Rh–P distances, shown in Table 1.2, as well as the structural change from a 1,3-cyclohexadiene ligand to the 1,3-coordinated σ-cyclohexane in **[1-cyclohexane][BAr$^{F}_{4}$]**.

Table 1.2: Selected crystallographic information of **[1-cyclohexadiene][BAr$^{F}_{4}$]** and **[1-cyclohexane][BAr$^{F}_{4}$]**.

	Rh–P1 (Å)	Rh–C1 / Rh–C3 (Å)	C1–C2 / C4–C5 (Å)	Unit Cell Volume (Å^3) / Space Group
[1-cyclohexadiene] [BAr$^{F}_{4}$]	2.2715(8)	2.20(2) / 2.284(9)	1.37(3) / 1.50(3)	6753.5(9) / C2/c
[1-cyclohexane] [BAr$^{F}_{4}$]	2.191(2)	2.62(2) / 2.53(2)	1.529(15) / 1.531(15)	6686.3(6) / C2/c

The higher symmetry space groups (C2/c) compared to **[1-NBA][BAr$^{F}_{4}$]** is reflected in the symmetry and disorder of the respective cyclohexadiene and cyclohexane ligands (Figure 1.11a). Numerous C–H•••F–C hydrogen bonding interactions between cyclohexane ligand and [BAr$^{F}_{4}$]$^{-}$ anion support in the solid-state can also be observed (Figure 1.11b).[57] The relatively large size of the cyclohexane ligand may reduce the void space within the O_h cavity, potentially aiding these hydrogen bonding interactions.[57]

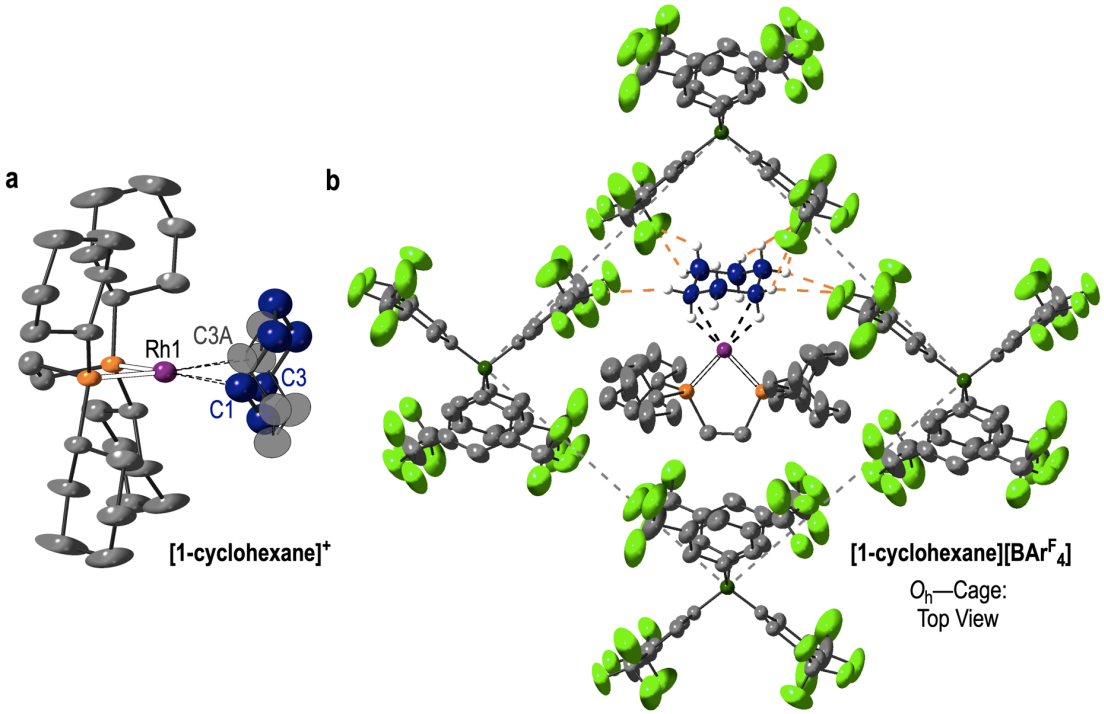

Figure 1.11: Solid-state structure of **[1-cyclohexane][BAr$^{F}_{4}$]** showing **a**) the 50:50 disorder components of the cyclohexane ligand and **b**) a section view of the pseudo-O_h framework of [BAr$^{F}_{4}$]$^{-}$ encapsulating the cation. C–H•••F–C hydrogen bonding interactions in the range of 2.30-2.99 Å, highlighted by orange dashes. Hydrogen atoms on phosphine ligand and [BAr$^{F}_{4}$]$^{-}$ anion as well as -Ar$^{F}_{4}$ groups on selected B-atoms excluded for clarity. Displacement ellipsoids set at 30 %.

Additionally, the high quality of the SSNMR spectra of **[1-cyclohexane][BAr$^F_4$]** shows how clean this transformation is. A single, down-fielded shift of the resonances in the $^{31}P\{^1H\}$ SSNMR spectra (δ 108 from δ 78) and absence of alkene signals in the $^{13}C\{^1H\}$ SSNMR spectra spectroscopically signal the formation of **[1-cyclohexane][BAr$^F_4$]**. Further SSNMR spectroscopy experiments such as $^{13}C\{^1H\}$, ^{13}C-NQS (Non-Quaternary Suppression) and $^{13}C/^1H$ FSLG-HECTOR probe the rapid mobility of the σ-cyclohexane ligand in the solid-state, discussed further in the introduction of Chapter 4.

Notably however, the stability of **[1-cyclohexane][BAr$^F_4$]** could not be definitively calculated. When placed under an inert atmosphere (or dynamic vacuum), rapid dehydrogenation to reform **[1-cyclohexadiene][BAr$^F_4$]** was seen, and this is further discussed in the introduction of Chapter 3.

1.5.2.4. A σ-pentane Complex, [1-pentane][BAr$^F_4$]

In this third example, by further changing just the diene ligand, the synthesis of a σ-pentane complex was reported.[95] The hydrogenation of a pentadiene precursor complex, [Rh($Cy_2PCH_2CH_2PCy_2$)(*n*-C_5H_8)][BAr$^F_4$] **[1-pentadiene][BAr$^F_4$]**, in the solid-state resulted in the formation of [Rh($Cy_2PCH_2CH_2PCy_2$)(*n*-C_5H_{12})][BAr$^F_4$], **[1-pentane)][BAr$^F_4$]**, (Figure 1.12). Confirmation of this complex was achieved by single-crystal x-ray diffraction. This not only shows a geometry change of the pentadiene to pentane ligand, the analogous changes in bond distances compared to the formation of **[1-NBA][BAr$^F_4$]** and **[1-cyclohexane][BAr$^F_4$]** are also observed (Table 1.3). SSNMR spectra were also indicative of the formation of a σ-pentane complex.

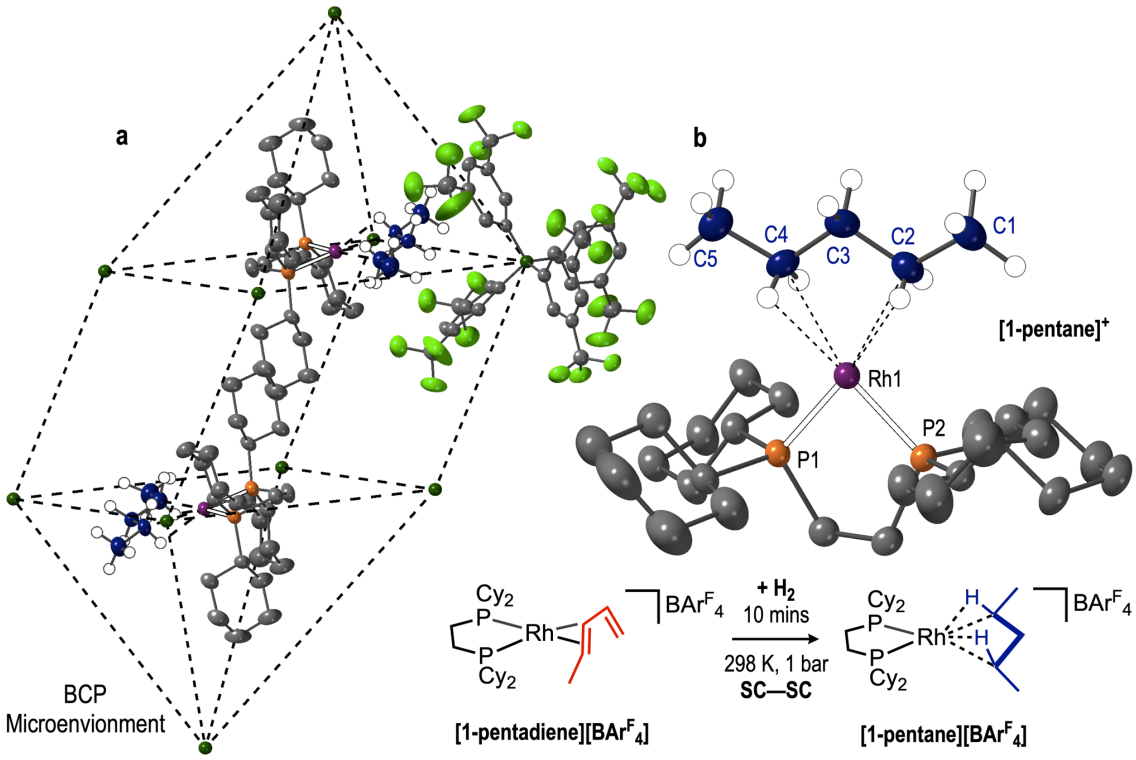

Figure 1.12: Solid-state structure showing **a**) the bicapped-square prism cage of $[BAr^{F}{}_{4}]^{-}$ anions and **b**) cationic portion of **[1-pentane][BAr$^{F}_{4}$]**. Hydrogen atoms on phosphine ligand and $[BAr^{F}{}_{4}]^{-}$ as well as -$Ar^{F}{}_{4}$ groups on selected B-atoms excluded for clarity. Displacement ellipsoids set at 30 % in both parts.

Table 1.3: Selected crystallographic information of **[1-pentadiene][BAr$^{F}_{4}$]** and **[1-pentane][BAr$^{F}_{4}$]**.

	Rh–P1 / Rh–P2 (Å)	Rh–C2 / Rh–C4 (Å)	C1–C2 / C3–C4 (Å)	Unit Cell Volume (Å^3) / Space Group
[1-pentadiene] [BAr$^{F}_{4}$]	2.272(1) / 2.264(1)	2.25(2) / 2.33(1)	1.272(9) / 1.386(9)	3244(1) / P–1
[1-pentane] [BAr$^{F}_{4}$]	2.197(1) / 2.196(1)	2.514 (4) / 2.522(5)	1.519(7) / 1.533(7)	3259(1) / P–1

Conversely, **[1-pentane][BAr$^{F}_{4}$]** was short lived compared to that of **[1-NBA][BAr$^{F}_{4}$]**. After 24 hours at 298 K under inert atmosphere, the resonances assigned to **[1-pentane][BAr$^{F}_{4}$]** in the $^{31}P\{^{1}H\}$ SSNMR spectra were reduced to less than 5 %, as the main product was that of **[1-BAr$^{F}_{4}$]**, from alkane loss and anion coordination. The poor stability was assigned to the solid-state $[BAr^{F}{}_{4}]^{-}$ anion packing structure. This is of a distorted bicapped-square prism (BCP) arrangement of $[BAr^{F}{}_{4}]^{-}$ anions, where two cations sit in within the well-defined cavity created by the anion network, shown in Figure 1.12a.

This is contrasting to the pseudo-O_h arrangement of $[BAr^F{}_4]^-$ anions in the structures of **[1-NBA][BAr$^F{}_4$]** and **[1-cyclohexane][BAr$^F{}_4$]**. Both cations of **[1-pentane][BAr$^F{}_4$]** sit facing a $[BAr^F{}_4]^-$ anion so that two -$Ar^F{}_4$ arms sandwich the pentadiene (pentane) fragment, the same orientation present in **[1-NBA][BAr$^F{}_4$]**.

This BCP arrangement of anions may form due to the linearity of the pentadiene ligand, which forms steric repulsions so cannot find a stable orientation within a potential O_h microenvironment. Importantly, this shows that the cationic fragment of the precursor alkene complex dictates the $[BAr^F{}_4]^-$ anion packing structure.

Overall, by analysing the components of **[1-NBA][BAr$^F{}_4$]**, **[1-cyclohexane][BAr$^F{}_4$]** and **[1-pentane][BAr$^F{}_4$]** that contribute to the formation and stability of these complexes, this could aid in the ongoing synthesis of σ-alkane complexes. The consistent use of the $[BAr^F{}_4]^-$ anion, along with the same chelating bisphosphine ligand, with -cyclohexyl R-groups, are present in all three complexes reported so far. This information can be contrasted against the range of less successful σ-alkane complexes, where these components have differed.

1.5.3. Importance of the Chelating Phosphine: Phosphine R-Groups

The -cyclohexyl R-groups present on the bisphosphine backbone are key towards the synthesis of stable, solid-state σ-alkane complexes, such as **[1-NBA][BAr$^F{}_4$]**.[57] This can be highlighted by examining previous, SMOM based, σ-alkane complexes that have varied this group.

Reported by the Weller group, the NBD complexes of $[Rh(Cyp_2PCH_2CH_2Cyp_2)(C_7H_8)][BAr^F{}_4]$, **[2-NBD][BAr$^F{}_4$]** (Cyp = cyclopentyl),[96] $[Rh(^tBu_2PCH_2CH_2{}^tBu_2)(C_7H_8)][BAr^F{}_4]$ **[3-NBD][BAr$^F{}_4$]**,[97] $[Rh(^iBu_2PCH_2CH_2{}^iBu_2)(C_7H_8)][BAr^F{}_4]$ **[4-NBD][BAr$^F{}_4$]**[83] and $[Rh(^iPr_2PCH_2CH_2{}^iPr_2)(C_7H_8)][BAr^F{}_4]$, **[5-NBD][BAr$^F{}_4$]**,[57] can be compared to **[1-NBA][BAr$^F{}_4$]** in terms of synthesis and stability by only having their R-group changed (Scheme 1.18). Notably, all but **[5-NBD][BAr$^F{}_4$]** of these diene complexes exhibit the same pseudo-octahedral arrangement of $[BAr^F{}_4]^-$ anions as **[1-NBD][BAr$^F{}_4$]**, as shown by single crystal x-ray diffraction studies. **[5-NBD][BAr$^F{}_4$]** shows an arrangement of eight $[BAr^F{}_4]^-$ units, formed of two face sharing trigonal pyramids adopting a gyrobifastigium structure.

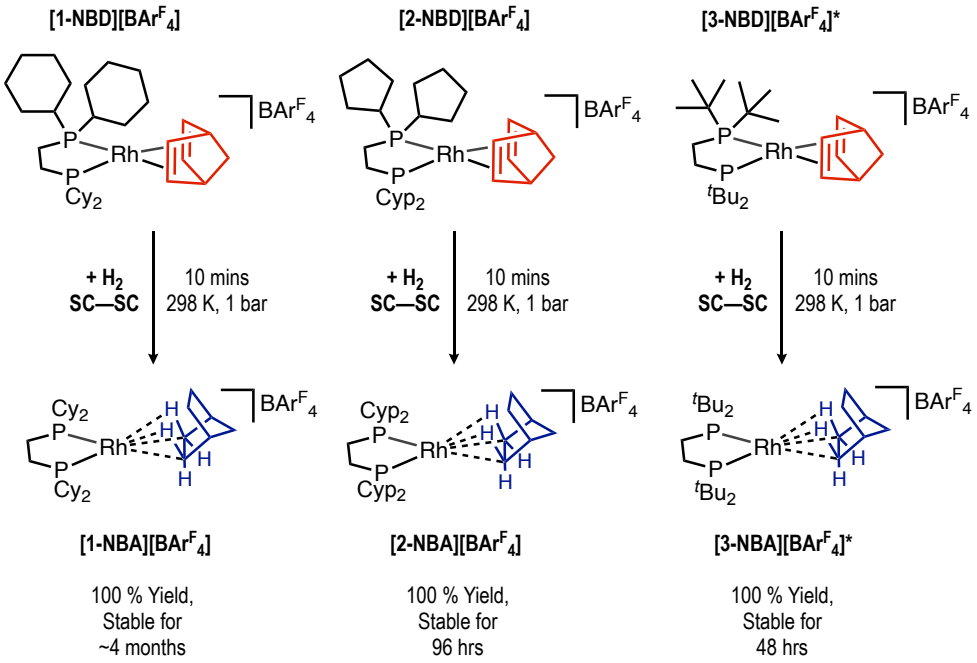

Scheme 1.18: The complexes of **[1-NBD][BAr$^F_4$]**, **[2-NBD][BAr$^F_4$]** to **[3-NBD][BAr$^F_4$]** and the formation of the respective σ-NBA complexes. * = assumed coordination structure based on SSNMR spectroscopy data.

Upon the solid/gas hydrogenation of **[2-NBD][BAr$^F_4$]** and **[3-NBD][BAr$^F_4$]**, single-crystal x-ray diffraction was used to confirm the corresponding σ-NBA complex of **[2-NBA][BAr$^F_4$]** (Figure 1.13a). This showed the structure of a coordinated σ-NBA ligand, analogous to that of **[1-NBA][BAr$^F_4$]**. Following the same experimental procedure upon **[3-NBD][BAr$^F_4$]**, no data on the solid-state structure could be determined by single-crystal x-ray diffraction, due to the complete loss of Bragg peaks upon hydrogenation. SSNMR spectroscopy was used to confirm both these σ-NBA complexes of **[2-NBA][BAr$^F_4$]** and **[3-NBA][BAr$^F_4$]**, shown by the downfield shift in signals in the $^{31}P\{^1H\}$ SSNMR spectra and loss of alkene resonances in the $^{13}C\{^1H\}$ SSNMR spectrum.

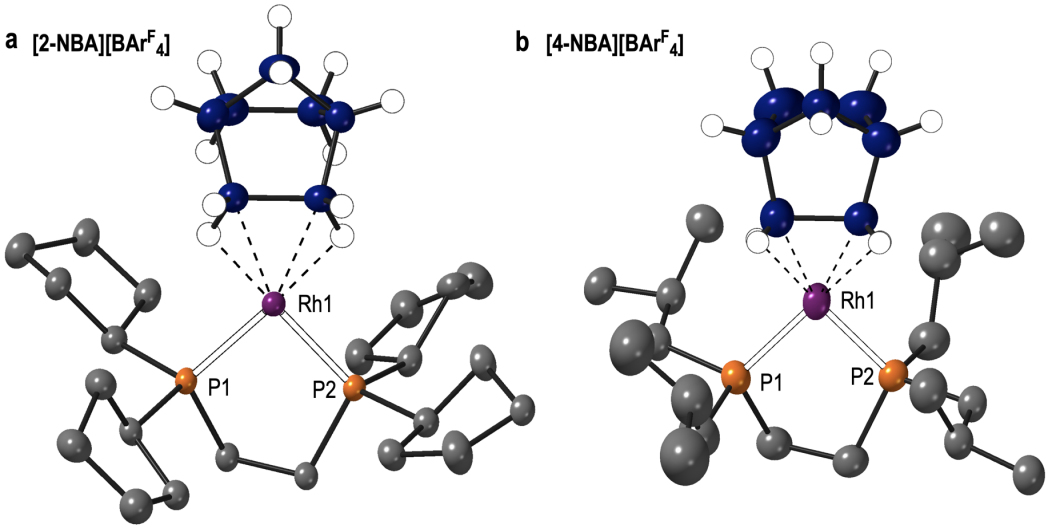

Figure 1.13: Cationic portion of **a**) **[2-NBA][BAr$^F_4$]** and **b**) **[4-NBA][BAr$^F_4$]**. Hydrogen atoms on phosphine ligand and $[BAr^F_4]^-$ anion excluded for clarity. Displacement ellipsoids set at 30 % in both parts.

The stability of **[2-NBA][BAr$^F_4$]** at 298 K (under inert atmosphere) was reported at 96 hours. After this time point, only signals for the zwitterionic, $[BAr^F_4]^-$ anion coordinated decomposition product were present in the $^{31}P\{^1H\}$ SSNMR spectra. **[3-NBA][BAr$^F_4$]** is stable for > 48 hours, as shown by $^{31}P\{^1H\}$ SSNMR spectroscopy. This was the longest measured time point recorded for this complex.

Upon hydrogenation of **[4-NBD][BAr$^F_4$]**, the solid-state structure of **[4-NBA][BAr$^F_4$]** could be collected by single-crystal x-ray diffraction, showing a well-defined cation of **[4-NBA]$^+$,** (Figure 1.13b), but includes minor disorder components relating to **[4-NBD]$^+$** of less than 10 %. This is suggestive of under hydrogenation of this sample, a result of the fine balance between synthesis and decomposition. No structural data could be collected upon the hydrogenation of **[5-NBD][BAr$^F_4$]** to **[5-NBA][BAr$^F_4$]** and like **[3-NBA][BAr$^F_4$]** it was confirmed by SSNMR spectroscopy only.

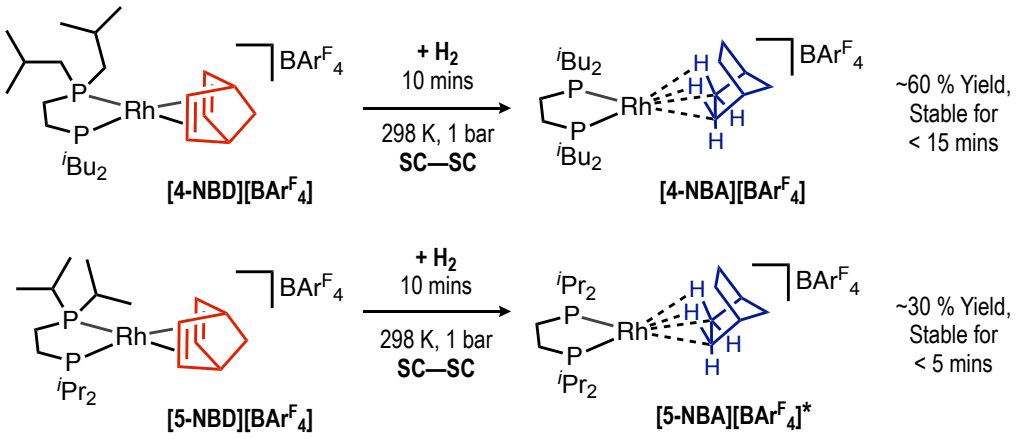

Scheme 1.19: The complexes of **[4-NBD][BAr$^F_4$]** and **[5-NBD][BAr$^F_4$]** and the formation to their respective σ-NBA complexes. * = assumed structure based on SSNMR spectroscopy data.

The $^{31}P\{^1H\}$ SSNMR spectra of **[4-NBA][BAr$^F_4$]** and **[5-NBA][BAr$^F_4$]** could only be collected as a mixture of species. Within the shortest time of measuring, the $^{31}P\{^1H\}$ SSNMR spectra at 223 K showed signals assigned to alkane complexes with spectroscopic yields of ~ 60 % and ~ 30 % respectively, Scheme 1.19. The remaining products were assigned to that of the respective, $[BAr^F_4]^-$ coordinated zwitterionic decomposition products. Upon warming to 298 K, a complete loss of signals assigned to **[4-NBA][BAr$^F_4$]** and **[5-NBA][BAr$^F_4$]** was observed after only 15 and 5 minutes respectively.

As the complexes **[1-NBD][BAr$^F_4$]**, **[2-NBD][BAr$^F_4$]**, **[3-NBD][BAr$^F_4$]** and **[4-NBD][BAr$^F_4$]** all show an pseudo-octahedral arrangement of $[BAr^F_4]^-$ anions, these data suggest decreasing the steric bulk of the R-group results in corresponding σ-NBA complexes of lower stability. This may be due to the analogous reasons of stability behind **[1-NBA][BAr$^F_4$]**,[57] of numerous C–H•••F–C hydrogen bonding interactions between cation fragment and the $[BAr^F_4]^-$ anion network in the solid-state. Notably, DFT calculations upon **[4-NBA][BAr$^F_4$]** and **[5-NBA][BAr$^F_4$]** revealed the formation of the respective $[BAr^F_4]^-$ coordinated complexes were calculated as also highly exergonic, –80.9 and –80.7 kcal mol^{-1} respectively,[57] again suggestive of the stabilising hydrogen bonding interactions as a form of kinetic stabilisation.

For **[5-NBA][BAr$^F_4$]**, the poor stability may be due to the gyrobifastigium anion packing structure. This change shows how the PR_2-group is a factor in the formation of the extended anionic framework upon crystallisation of the diene precursor, and therefore, the corresponding stabilising microenvironment provided for the alkane complex.

1.5.4. Importance of the Chelating Phosphine: Carbon Backbone

The importance of the bite angle within the bisphosphine ligand can also be shown to be important towards the synthesis of stable, solid-state σ-alkane complexes. This again can be highlighted by examining previous, SMOM based, σ-alkane complexes that have varied this group.

Changing the L–M–L bite angle is well documented in ML_2-type complexes.[98,99] This can lead to electronic changes, such as favouring different metal oxidation states, bond activation pathways[100] and control of steric influences, such as the bite and solid-cone angle.[101,102] Changing the bite angle can thus lead to control over reactivity and selectivity in catalysis. In SMOM systems, this can also lead to different structure and bonding modes of the corresponding σ-alkane complexes.

The complexes of $[Rh(Cy_2P(CH_2)_3PCy_2)(C_7H_8)][BAr^F{}_4]$, **[6-NBD][BAr^F$_4$]**, $[Rh(Cy_2P(CH_2)_4PCy_2)(C_7H_8)][BAr^F{}_4]$, **[7-NBD][BAr^F$_4$]** and $[Rh(Cy_2P(CH_2)_5PCy_2)(C_7H_8)][BAr^F{}_4]$, **[8-NBD][BAr^F$_4$]** were synthesised as precursors to σ-alkane complexes (Scheme 1.20). Each complex increases the number of -CH_2- units in the chelating phosphine backbone,[103] which increases the internal P–Rh–P bite angle (β). Single-crystal x-ray diffraction was used to show that the O_h arrangement of $[BAr^F{}_4]^-$ anions in the solid-state structure was retained, and further showed the cation orientation within the microenvironment was directed towards a boron vertex.

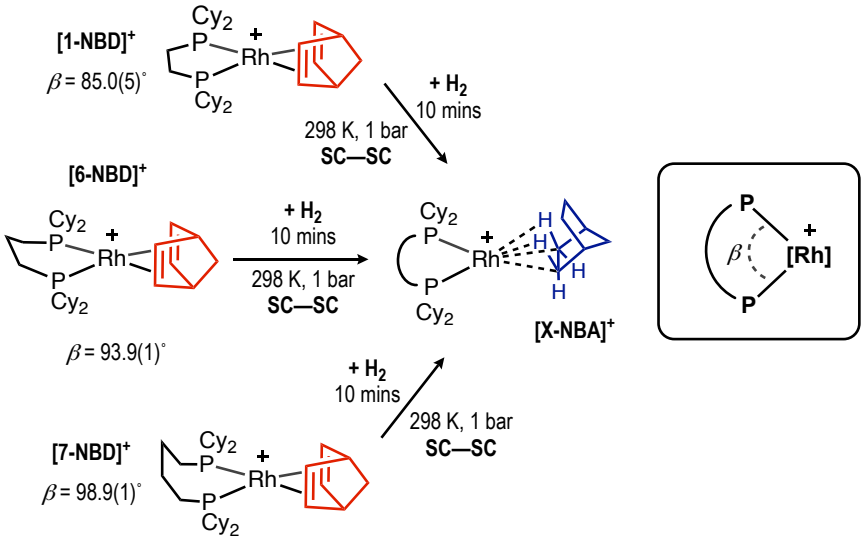

Scheme 1.20: The complexes of **[1-NBD][BAr^F$_4$]**, **[6-NBD][BAr^F$_4$]** and **[7-NBD][BAr^F$_4$]** and the formation to their respective σ-NBA complexes.

Both **[6-NBD][BAr$^F_4$]** and **[7-NBD][BAr$^F_4$]** reacted rapidly with H_2 (< 5 mins) to form the corresponding σ-NBA complexes of **[6-NBA][BAr$^F_4$]** and **[7-NBA][BAr$^F_4$]**, as shown by single-crystal x-ray diffraction and SSNMR spectroscopy studies. These are analogous in solid-state structural motif and bonding metrics to **[1-NBA][BAr$^F_4$]**. $^{31}P\{^1H\}$, $^{13}C\{^1H\}$ and FSLG-HETCOR SSNMR spectra comparable to **[1-NBA][BAr$^F_4$]** could be easily be afforded and in the absence of any decomposition species. The NBA ligand fits comfortably within the octahedral void with a number of stabilising C–H•••F–C interactions.

This change in bite angle was reported to have an effect on the stability of **[7-NBA][BAr$^F_4$]** however. When placed under a dynamic vacuum for 3 days, **[7-NBA][BAr$^F_4$]** decomposed into multiple, unidentifiable products.[103] In contrast, no such reactivity was observed for **[1-NBA][BAr$^F_4$]** or **[6-NBA][BAr$^F_4$]** when left for 7 days under the same conditions. It was noted that either increased steric pressure within the solid-state cavity, or increased stability of the corresponding decomposition product, may be the driving force for NBA liberation in **[7-NBA][BAr$^F_4$]**.

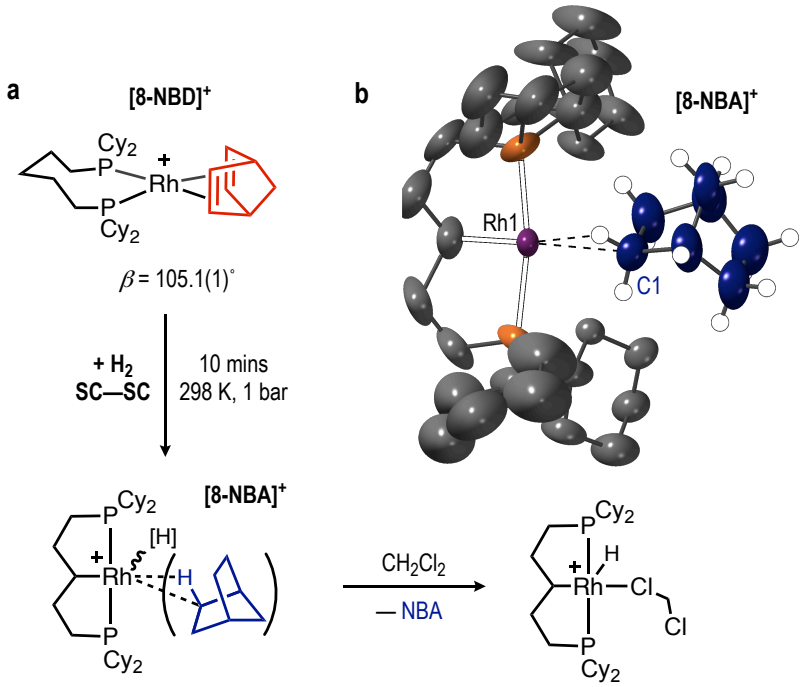

Figure 1.14: **a**) The hydrogenation of **[8-NBD][BAr$^F_4$]** and subsequent backbone C–H activation and solution trapping reaction **b**) Solid-state structure of **[8-NBA]$^+$**, where only one disorder componant of the NBA ligand is shown. Hydrogen atoms on the phosphine ligand for clarity and displacement ellipsoids set at 30 %.

Changing the backbone to a 5-carbon chain had a greater effect in the attempted synthesis of a σ-NBA complex from the diene precursor of **[8-NBD][BAr$^{F}_{4}$]**. Hydrogenation in the solid-state resulted in the C–H oxidative addition of the central CH_2 group in the backbone carbon, forming a wide bite-angle, Rh^{III}, PCP pincer complex, with a suggested η^1-σ-NBA ligand, shown in Figure 1.14a. **[8-NBA][BAr$^{F}_{4}$]** was confirmed by single-crystal x-ray diffraction (Figure 1.14b), SSNMR spectroscopy and solution trapping experiments. Although this type of activation has been reported in solution,[104,105] this is a rare example in a SC-SC solid-state reaction.[106,107] It was also noted as the first example of a Rh^{III} alkane complex.

Although this is a SC-SC hydrogenation reaction, the resulting crystalline data was poor, shown by poor mosaic spread and sharpness of Bragg peaks during the single-crystal x-ray diffraction study.[108] This is probably due to the large structural change occurring during the SC-SC transformation, which are typically not well supported.[88] As well, the NBA ligand is disordered over 4 positions, where the measurable Rh•••C distances to all the disordered components of the NBA ligand are relatively long (2.75–3.10 Å), suggestive of a weak σ-interactions. Therefore, the precise nature of the alkane coordination with the Rh centre could not be determined.

This unusual reactivity, bought about by the change in phosphine backbone, goes to show how a seemingly minor change in methylene units results in large structural changes, and may further suggest an upper limit to the number of methylene carbons in the backbone.

1.5.5. Importance of the Weakly Coordinating Anion

In **[1-NBD][BAr$^{F}_{4}$]**, the arrangement of $[BAr^{F}_{4}]^{-}$ anions in the solid-state is central in the formation and stability of **[1-NBA][BAr$^{F}_{4}$]**. The packing structure, notably of the pseudo-O_h arrangement, results in a robust microenvironment which can stabilise the cationic rearrangements in the SC-SC hydrogenations. Attempts to synthesise stable σ-NBA complexes of a range of anions has been reported;[109] where a range of complexes of the same cationic fragment of $[1\text{-NBD}]^{+}$ was substituted with the pseudo-structural anions of $[BAr^{Cl}_{4}]^{-}$, $[BAr^{F8}_{4}]^{-}$ (Ar^{F} = 3,5-$(F)_2C_6H_3$), and $[BAr^{H}_{4}]^{-}$ (Ar^{H} = -C_6H_5). This again highlights the importance of this individual factor in the synthesis of stable, solid-state σ-alkane complexes.

Single-crystal x-ray diffraction of these revealed a range of solid-state anion packing environments. **[1-NBD][BAr$^{H}_{4}$]** showed a pseudo-O_h nature, much like **[1-NBD][BAr$^{F}_{4}$]**. For **[1-NBD][BAr$^{F8}_{4}$]** and **[1-NBD][BAr$^{Cl}_{4}$]**, the extended solid-state structures are less straightforward. The structure of **[1-NBD][BAr$^{F8}_{4}$]** shows eight [BAr$^{F8}_{4}$]$^{-}$ anions formed in gyrobifastigium structure of two, face sharing, trigonal pyramids (Figure 1.15a). The framework in **[1-NBD][BAr$^{Cl}_{4}$]** is of two face sharing parallelepipeds arrangement of anions (Figure 1.15b).

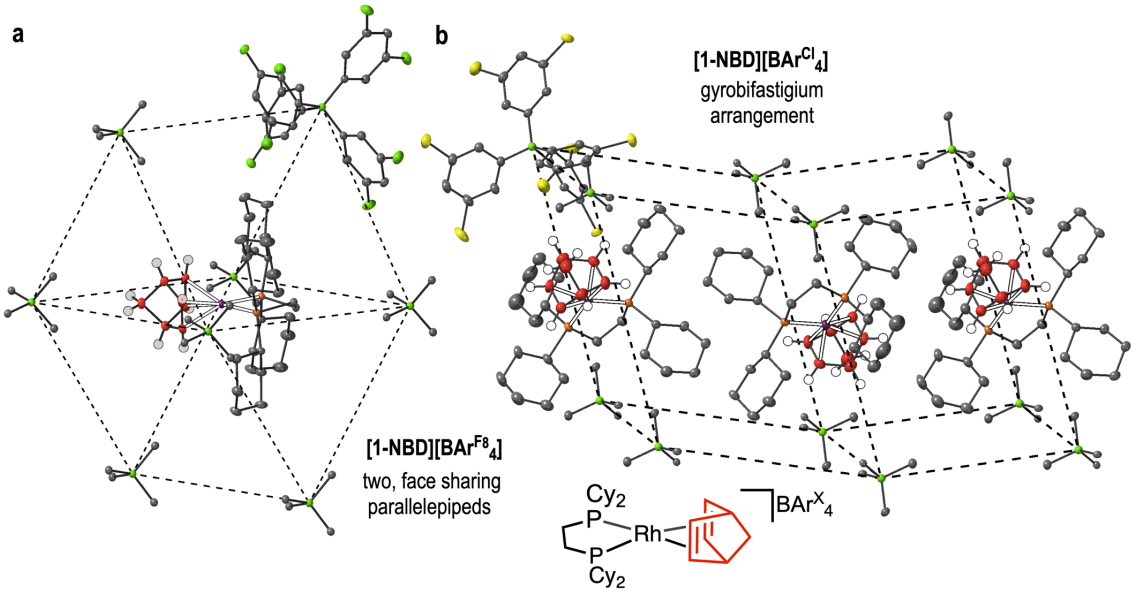

Figure 1.15: Solid-state packing environments of [BAr$^{X}_{4}$]$^{-}$ anions in **a**) **[NBD][BAr$^{F8}_{4}$]** and **b**) **[NBD][BAr$^{Cl}_{4}$].** Hydrogen atoms on phosphine ligand and [BAr$^{F}_{4}$]$^{-}$ anion as well as -Ar$^{F}_{4}$ groups on selected B-atoms excluded for clarity. Displacement ellipsoids set at 30 % in both parts.

Upon H_2 addition to single-crystals of each NBD complex, only the [BAr$^{Cl}_{4}$]$^{-}$ anion network was supportive in the formation of the σ-NBA complex of **[1-NBA][BAr$^{Cl}_{4}$]**. This was characterised by single-crystal x-ray diffraction (Figure 1.16a), where notably, the alkane coordination in **[1-NBA][BAr$^{Cl}_{4}$]** is through the *exo*-hydrogens NBA methylene group. This is different from the *endo*-mode seen in **[1-NBA][BAr$^{F}_{4}$]** (Figure 1.16b). This goes to shows how the local microenvironment, established by the anion, can have a direct effect on metal-ligand coordination.

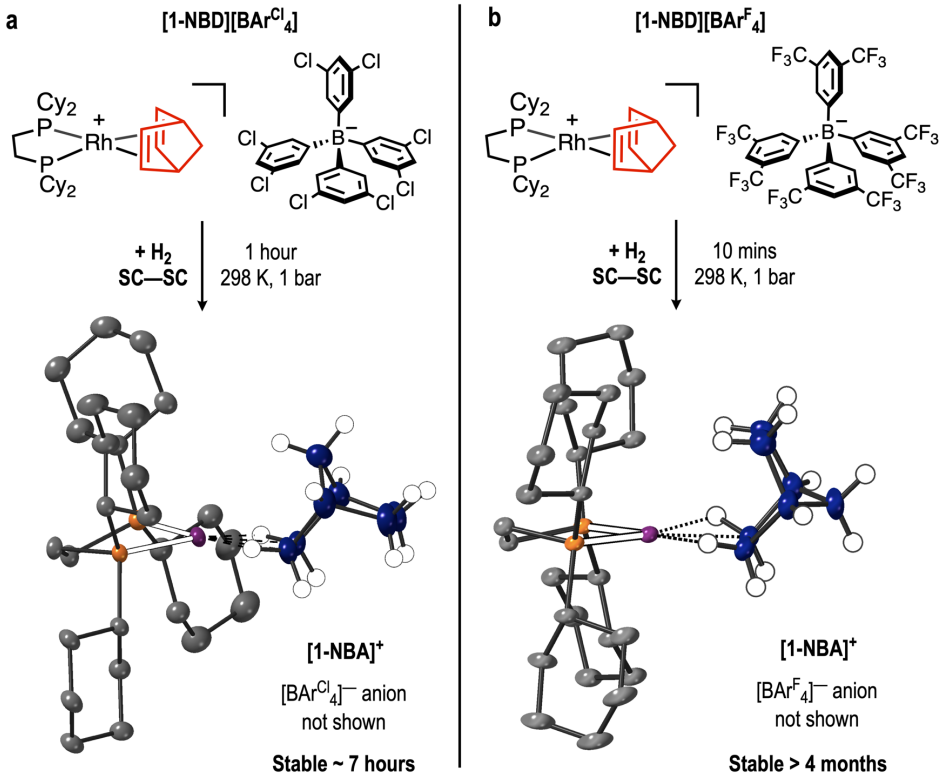

Figure 1.16: Synthetic routes to **a**) **[1-NBA][BAr$^{Cl}_4$]** and **b**) **[1-NBA][BAr$^{F}_4$]**. Hydrogen atoms on the phosphine ligand for clarity and displacement ellipsoids set at 30 % in both parts.

$^{31}P\{^{1}H\}$ SSNMR spectroscopy was also used to confirm this. Upon hydrogenation, a new resonance at δ 103 appeared in the spectrum, assigned to that of **[1-NBA][BAr$^{Cl}_4$]** (~ 80 % spectroscopic yield). This complex was stable for greater than 48 hours at 158 K however, complete decomposition at 298 K to **[1-BAr$^{Cl}_4$]** occurred within 7 hours. Upon the hydrogenation of **[1-NBD][BAr$^{H}_4$]** and **[1-NBD][BAr$^{F8}_4$]**, any σ-NBA complexes could not be isolated (Scheme 1.21), and rapid decomposition to the respective anion coordinated complex was observed, shown by SSNMR spectroscopy.

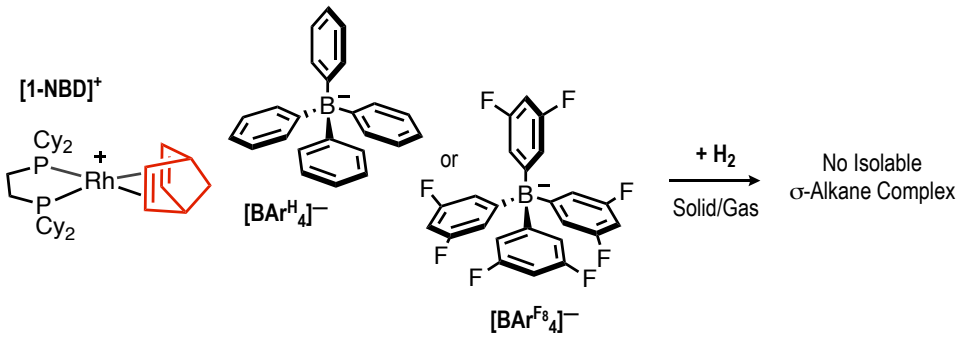

Scheme 1.21: The solid/gas hydrogenation of **[1-NBD][BAr$^{H}_4$]** and **[1-NBD][BAr$^{F8}_4$]** .

These data indicate that the $[BAr^F_4]^-$ anion is optimal for the formation and subsequent stability of σ-alkane complexes in the solid-state. The $[BAr^F_4]^-$ anion was least susceptible to undergo decomposition to the respective zwitterionic, anion coordinated complex. This may be due to the large kinetic barrier discussed in Section 1.4.1.[57]

The -CF_3 groups are also flexible enough to facilitate the movement of H_2 through the non-porous crystal lattices, yet retain enough rigidity needed for the SC-SC nature of the reactions. This is highlighted by the range of hydrogenation rates in the different systems. For example, the rate of NBD hydrogenation, established by solution trapping methods, varied between anion systems, from 15 minutes for **[1-NBD][BAr^F_4]** to 1 hour for **[1-NBD][BAr^{Cl}_4]**. Although the precise mechanism of gaseous movement throughout the crystal lattice has yet to be resolved, it has been studied (Scheme 1.22).[110]

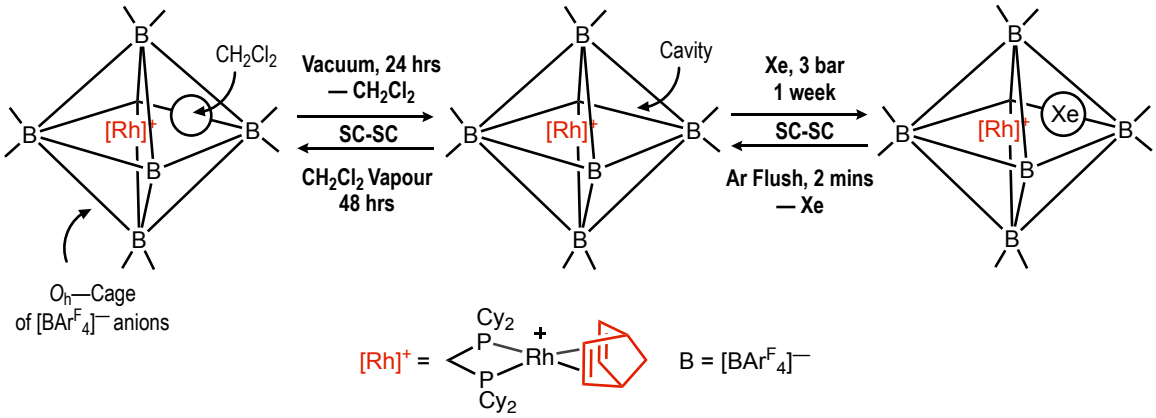

Scheme 1.22: Synthetic routes to the CH_2Cl_2 and Xe encapsulation complexes. All reactions are reversible SC-SC reactions.

By the use of either a xenon / dichloromethane probe, or a void space, host/guest type exchange can be explored within a well-defined metal localised cavity within a SMOM material. This example of a non-hydrogenative, SC-SC reaction in SMOM material was followed by $^{31}P\{^1H\}$, $^{13}C\{^1H\}$ and ^{129}Xe SSNMR spectroscopy and single-crystal x-ray diffraction. This suggested that the fluorous channels created by the -CF_3 groups of the $[BAr^F_4]^-$ anion facilitate this transfer. The $[BAr^F_4]^-$ anions also provide non-covalent interactions, stabilising the host/guest interactions; giving further evidence for the effectiveness of the $[BAr^F_4]^-$ anion system in SMOM studies.

1.5.6. Displacement Reactions within SMOM Materials

Although many solid-state σ-alkane complexes have been introduced within Section 1.5, none have matched **[1-NBA][BAr$^F_4$]** in terms of their quantitative spectroscopic yield during formation and onward stability in the solid-state. This stability even allowed for further SC-SC reactivity from this complex, shown in Scheme 1.23.

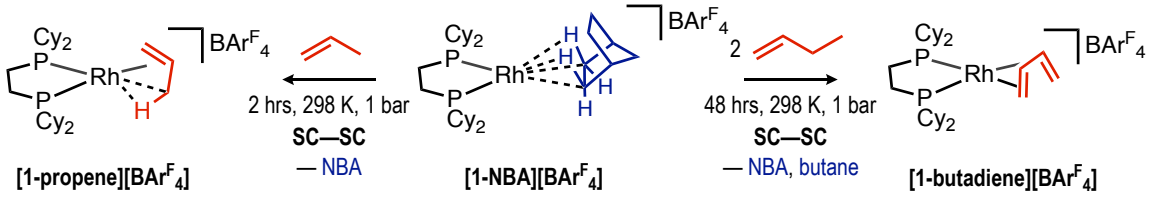

Scheme 1.23: Synthetic routes to **[1-propene][BAr$^F_4$]** and **[1-butadiene][BAr$^F_4$]**.[111]

When crystals of **[1-NBA][BAr$^F_4$]** were placed under an atmosphere of propene (2 hours, 1 bar, 298 K) or 1-butene (48 hours, 1 bar, 298 K), displacement of the weakly bound NBA ligand occurs to yield the respective alkene complexes of [Rh($Cy_2PCH_2CH_2PCy_2$)(C_3H_6)][BAr$^F_4$], **[1-propene][BAr$^F_4$]** and [Rh($Cy_2PCH_2CH_2PCy_2$)(C_4H_6)][BAr$^F_4$], **[1-butadiene][BAr$^F_4$]**, the latter also *via* a transfer hydrogenation reaction. Both of these new products were confirmed by solution and SSNMR spectroscopy. Only the solid-state structure of **[1-propene][BAr$^F_4$]** was reported however, as single crystals of **[1-butadiene][BAr$^F_4$]** of suitable quality for standard single-crystal x-ray diffraction techniques could not be formed (see Chapter 2, Section 2.2.1.)

[1-propene][BAr$^F_4$] is an example of system that can withstand two consecutive SC-SC reactions,[84,88,112] but suffers from severely reduced crystallographic quality. The loss in mosaic spread and a reduction in high angle data resulted in relatively large R value (10.7 % for **[1-propene][BAr$^F_4$]**), consistent with that of multiple SC-SC reaction products.[88] The propene ligand in **[1-propene][BAr$^F_4$]** coordinates *via* a π-bound alkene and γ-agostic Rh•••C–H interaction (Figure 1.17a), which was also shown to undergo fluxional process in solution and solid-state at 298 K, proposed *via* an allyl-hydride intermediate.[111]

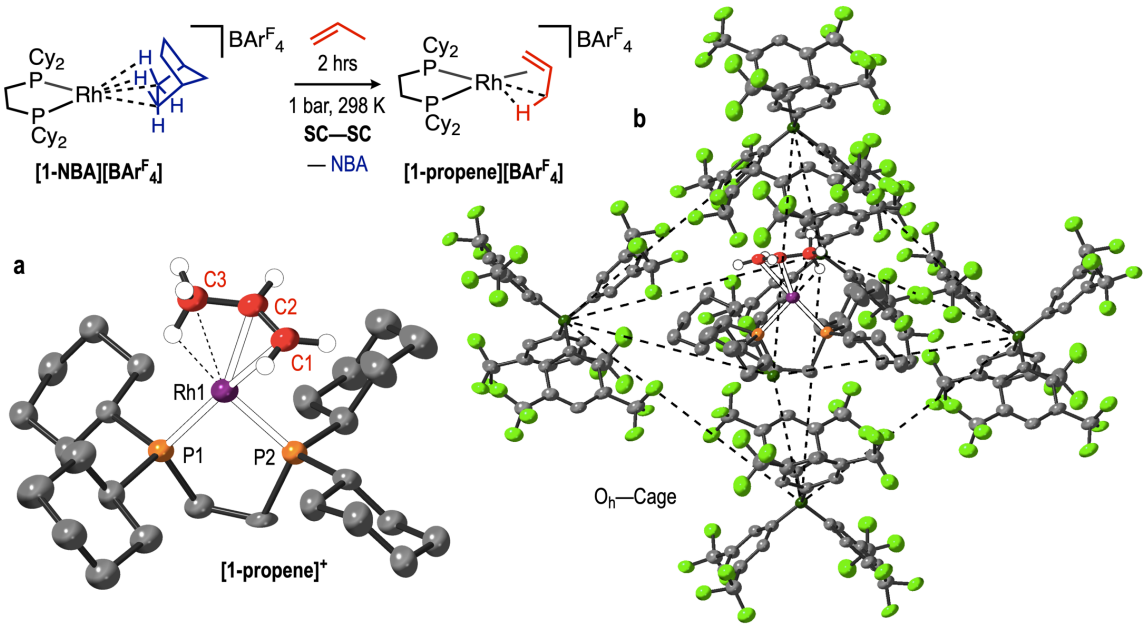

Figure 1.17: a) Solid-state structure of the cationic portion of **[1-propene][BAr$^F_4$]**. **b**) Pseudo-octahedral framework of [BAr$^F_4$]$^-$ encapsulating the cationic fragment of **[1-propene][BAr$^F_4$]**. Hydrogen atoms on phosphine ligand and [BAr$^F_4$]$^-$ excluded for clarity and displacement ellipsoids set at 30 % in both parts.

As **[1-propene][BAr$^F_4$]** is derived from **[1-NBA][BAr$^F_4$]**, it retains the psudeo-O_h arrangement of [BAr$^F_4$]$^-$ anions (Figure 1.17b). The [BAr$^F_4$]$^-$ anions and plasticity of the -CF_3 arms were also noted to facilitate the movement of alkene gas throughout the lattice, and consequent displacement of the NBA ligand in this non-porous crystal system. The exclusion of the NBA ligand in both reactions was observed by a thin coating of oil upon the crystalline surface, previously noted as liquid NBA.[111]

Recrystallisation was attempted to increase the quality structure collected of **[1-propene][BAr$^F_4$]**, however dissolution of **[1-propene][BAr$^F_4$]** in a range of solvents lead to decomposition over the period of time required for crystallisation. When crystallised under propene-saturated solution this resulted in the formation of a bispropene complex of [Rh($Cy_2PCH_2CH_2PCy_2$)(C_3H_6)$_2$][BAr$^F_4$] **[1-(propene)$_2$][BAr$^F_4$]**, Scheme 1.24.

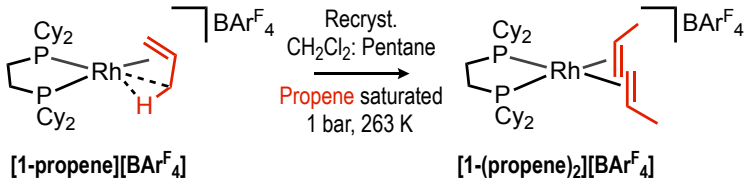

Scheme 1.24: Synthetic route to **[1-(propene)$_2$][BAr$^F_4$]**.[111]

Both **[1-propene][BAr$^F_4$]** and **[1-butadiene][BAr$^F_4$]** have shown it is possible to create new alkene complexes from σ-alkane complexes. This follows a simple displacement reaction of the weakly coordinating alkane with far stronger coordinating alkene, yet no further hydrogenation reactivity upon them however was reported. This again, is returned to in Chapter 2.

1.6. Chapter Summary and Thesis Aims

This Chapter has shown that the SMOM-methodology has been most successful towards the synthesis of σ-alkane complexes, in terms of the ease of synthetic procedures and complex stability. This route has produced σ-alkane complexes in the solid-state which are stable for long periods of time at room temperatures, and on the gram scale.[57,94] This stability allows for their isolation, full characterisation and studies on their further reactivity. In comparison, previous solution routes have been limited by adverse solvent reactions, leading to σ-alkane complexes only stable at low temperatures and on NMR spectroscopy scales, rendering the full exploration of their coordination and reactivity near impossible.

All the σ-alkane complexes within this SMOM-framework can be compared (Table 1.4).[94–96,103] **[1-NBA][BAr$^F_4$]** can be seen as most prominent σ-alkane complex; from its high spectroscopic yield and indefinite stability in the solid-state. This stability even allows for **[1-NBA][BAr$^F_4$]** to undergo a range of further, SC-SC reactions, such as displacement by propene and 1-butene. A hypothesis for the reason for this stability lies with the holistic consideration of each individual component of this system, such as the anion and chelating phosphine, that needs to be taken into account when designing new systems.

Table 1.4: Summary of solid-state σ-alkane complexes presented in Section 1.4.

Cation	R-Group	Carbon Backbone	Anion	Solid-State Structure[a]	Measured Yield[b] / %	SS Stability at 298 K[c]
[1-NBA]$^+$	Cyclohexyl	-CH_2CH_2-	[BAr$^F_4$]$^-$	O_h	100	**> 4 months**
[2-NBA]$^+$	Cyclopentyl	-CH_2CH_2-	[BAr$^F_4$]$^-$	O_h	100	**96 hours**
[1-cyclohexane]$^+$	Cyclohexyl	-CH_2CH_2-	[BAr$^F_4$]$^-$	O_h	> 95	**> 48 hours**
[3-NBA]$^+$	*tert*butyl	-CH_2CH_2-	[BAr$^F_4$]$^-$	O_h	100	**48 hours[d]**
[6-NBA]$^+$	Cyclohexyl	-$(CH_2)_3$-	[BAr$^F_4$]$^-$	O_h	100	**48 hours[d]**
[7-NBA]$^+$	Cyclohexyl	-$(CH_2)_4$-	[BAr$^F_4$]$^-$	O_h	100	**48 hours[d]**
[1-pentane]$^+$	Cyclohexyl	-CH_2CH_2-	[BAr$^F_4$]$^-$	BCP	~ 85	**12 hours**
[1-NBA]$^+$	Cyclohexyl	-CH_2CH_2-	[BAr$^{Cl}_4$]$^-$	Parallelepiped	~ 80	**7 hours**
[4-NBA]$^+$	*iso*butyl	-CH_2CH_2-	[BAr$^F_4$]$^-$	O_h	~ 60	**< 15 mins**
[5-NBA]$^+$	*iso*propyl	-CH_2CH_2-	[BAr$^F_4$]$^-$	Gyrobifastigium	~ 30	**< 5 mins**

[a] [BAr$^F_4$]$^-$ anion packing structure of the precursor NBD complex as measured by single-crystal x-ray diffraction. [b] Spectroscopic yield measured by approximate ratio of products in the $^{31}P\{^1H\}$ SSNMR spectra. [c] as measured by time taken for disappearance of signals in the $^{31}P\{^1H\}$ SSNMR spectra. [d] Longest measured time point recorded.

Expanding upon the successes of **[1-NBA][BAr$^{F}_{4}$]**, these thesis aims to explore the synthesis of a homologous series of linear and branched solid-state σ-alkane complexes. These will be comprised from the same chelating phosphine and anion, and will focus on lower molecular weight, and industrially important alkanes such as propane, *iso*butane and hexane.[113] Building upon initial results towards this (e.g., **[1-pentane][BAr$^{F}_{4}$]** and **[1-cyclohexane][BAr$^{F}_{4}$]**), this will not only expand the range of σ-alkane complexes characterised in the solid-state, but will aim to discover the limits and trends towards the synthesis of solid-state σ-alkane complexes (Scheme 1.25).

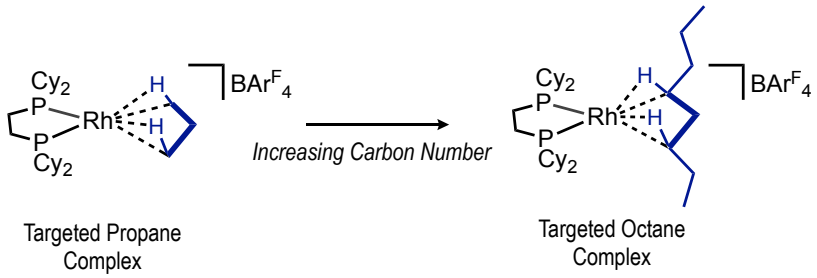

Scheme 1.25: A selection of targeted σ-alkane complexes within this thesis.

Not only will the synthesis of such complexes be targeted, considerations into any further reactivity of each new σ-alkane complex will be explored. This will not only look at previously reported SMOM reactivity, such as H/D exchange within the complex,[114,115] but also explore the dehydrogenation of such σ-alkane complexes.

1.7. References

1 P. C. A. Bruijnincx and B. M. Weckhuysen, *Angew. Chem. Int. Ed.*, 2013, **52**, 11980–11987.
2 G. B. Shul'pin and A. E. Shilov, *Activation and Catalytic Reactions of Saturated Hydrocarbons in the Presence of Metal Complexes*, Kluwer Academic Publishers, 2000.
3 S. Wang and Z. H. Zhu, *Energy and Fuels*, 2004, **18**, 1126–1139.
4 P. J. Perez, *Alkane C-H Activation by Single-Site Metal Catalysis*, Springer US, 2012.
5 A. H. Janowicz and R. G. Bergman, *J. Am. Chem. Soc.*, 1982, **104**, 352–354.
6 A. S. Goldman, A. H. Roy, Z. Huang, R. Ahuja, W. Schinski and M. Brookhart, *Science*, 2006, **312**, 257–261.
7 A. S. Goldman and K. I. Goldberg, *ACS Symp. Ser.*, 2004, **885**, 1–43.
8 R. G. Bergman, *Nature*, 2007, **446**, 391–393.
9 M. G. Crestani, A. K. Hickey, X. Gao, B. Pinter, V. N. Cavaliere, J. I. Ito, C. H. Chen and D. J. Mindiola, *J. Am. Chem. Soc.*, 2013, **135**, 14754–14767.
10 A. A. Bengali, R. H. Schultz, B. C. Moore and R. G. Bergman, *J. Am. Chem. Soc.*, 1994, **116**, 9585–9589.
11 A. B. Chaplin, A. I. Poblador-Bahamonde, H. A. Sparkes, J. A. K. Howard, S. A. Macgregor and A. S. Weller, *Chem. Commun.*, 2009, **91**, 244–246.
12 R. H. Crabtree, *Angew. Chem. Int. Ed.*, 1993, **32**, 789–805.
13 J. C. Green, M. L. H. Green and G. Parkin, *Chem. Commun.*, 2012, **48**, 11481–11503.
14 R. H. Crabtree, *Chem. Rev.*, 2016, **116**, 8750–8769.
15 C. Hall and R. N. Perutz, *Chem. Rev.*, 1996, **96**, 3125–3146.
16 R. H. Crabtree, *J. Organomet. Chem.*, 2004, **689**, 4083–4091.
17 K. K. Pandey, *Coord. Chem. Rev.*, 2009, **253**, 37–55.
18 G. Sean McGrady, P. Sirsch, N. P. Chatterton, A. Ostermann, C. Gatti, S. Altmannshofer, V. Herz, G. Eickerling and W. Scherer, *Inorg. Chem.*, 2009, **48**, 1588–1598.
19 A. L. Allred, *J. Inorg. Nucl. Chem.*, 1961, **17**, 215–221.
20 E. A. Cobar, R. Z. Khaliullin, R. G. Bergman and M. Head-Gordon, *Proc. Natl. Acad. Sci.*, 2007, **104**, 6963–6968.
21 J. Yves Saillard and R. Hoffmann, *J. Am. Chem. Soc.*, 1984, **106**, 2006–2026.
22 G. J. Kubas, *Metal Dihydrogen and sigma-Bond Complexes - Structure, Theory and Reactivity*, Plenum Publishers, 2001.
23 G. J. Kubas, C. J. Unkefer, B. I. Swanson and E. Fukushima, *J. Am. Chem. Soc.*, 1986, **108**, 7000–7009.
24 M. Brookhart, M. L. H. Green and G. Parkin, *Proc. Natl. Acad. Sci.*, 2007, **104**, 6908–6914.
25 P. L. A. Popelier and G. Logothetis, *J. Organomet. Chem.*, 1998, **555**, 101–111.
26 M. Lein, *Coord. Chem. Rev.*, 2009, **253**, 625–634.
27 A. S. Weller, F. M. Chadwick and A. I. McKay, in *Advances in Organometallic Chemistry*, Academic Press, 2016, pp. 223–276.
28 R. D. Young, *Chem. - A Eur. J.*, 2014, **20**, 12704–12718.
29 S. D. Pike, DPhil Thesis, University of Oxford, UK., 2014.
30 R. N. Perutz and J. J. Turner, *J. Am. Chem. Soc.*, 1975, **97**, 4791–4800.
31 H. Hermann, F. W. Grevels, A. Henne and K. Schaffner, *J. Phys. Chem.*, 1982, **86**, 5151–5154.
32 A. J. Cowan and M. W. George, *Coord. Chem. Rev.*, 2008, **252**, 2504–2511.
33 J. M. Morse, G. H. Parker and T. J. Burkey, *Organometallics*, 1989, **8**, 2471–2474.
34 C. E. Brown, Y. Ishikawa, P. A. Hackett and D. M. Rayner, *J. Am. Chem. Soc.*, 1990, **112**, 2530–2536.
35 M. W. George, M. B. Hall, O. S. Jina, P. Portius, X. Z. Sun, M. Towrie, H. Wu, X. Yang and S. D. Zaric, *Proc. Natl. Acad. Sci. U. S. A.*, 2010, **107**, 20178–20183.
36 X. Z. Sun, D. C. Grills, S. M. Nikiforov, M. Poliakoff and M. W. George, *J. Am. Chem. Soc.*, 1997, **119**, 7521–7525.
37 S. Geftakis and G. E. Ball, *J. Am. Chem. Soc.*, 1998, **120**, 9953–9954.
38 R. D. Young, A. F. Hill, W. Hillier and G. E. Ball, *J. Am. Chem. Soc.*, 2011, **133**, 13806–13809.
39 J. A. Calladine, S. B. Duckett, M. W. George, S. L. Matthews, R. N. Perutz, O. Torres and K. Q. Vuong, *J. Am. Chem. Soc.*, 2011, **133**, 2303–2310.
40 S. B. Duckett, M. W. George, O. S. Jina, S. L. Matthews, R. N. Perutz, X.-Z. Sun and K. Q. Vuong, *Chem. Commun.*, 2009, 1401–1403.
41 D. J. Lawes, S. Geftakis and G. E. Ball, *J. Am. Chem. Soc.*, 2005, **127**, 4134–4135.
42 A. J. Cowan, P. Portius, H. K. Kawanami, O. S. Jina, D. C. Grills, X. Z. Sun, J. McMaster and M. W. George, *Proc. Natl. Acad. Sci. U. S. A.*, 2007, **104**, 6933–6938.
43 B. Chan and G. E. Ball, *J. Chem. Theory Comput.*, 2013, **9**, 2199–2208.
44 J. A. Calladine, S. B. Duckett, M. W. George, S. L. Matthews, R. N. Perutz, O. Torres and K. Q. Vuong, *J. Am. Chem. Soc.*, 2011, **133**, 2303–2310.
45 O. Torres, J. A. Calladine, S. B. Duckett, M. W. George and R. N. Perutz, *Chem. Sci.*, 2015, **6**, 418–424.
46 W. H. Bernskoetter, C. K. Schaur, K. I. Goldberg and M. Brookhart, *Science*, 2009, **326**, 553–557.

47 J. F. Hartwig, *Organotransition Metal Chemistry. From Bonding to Catalysis.*, University Science Books, 2010.
48 M. Saunders, L. Telkowski and M. R. Kates, *J. Am. Chem. Soc.*, 1977, **99**, 8070–8071.
49 W. H. Bernskoetter, S. K. Hanson, S. K. Buzak, Z. Davis, P. S. White, R. Swartz, K. I. Goldberg and M. Brookhart, *J. Am. Chem. Soc.*, 2009, **131**, 8603–8613.
50 H. M. Yau, A. I. McKay, H. Hesse, R. Xu, M. He, C. E. Holt and G. E. Ball, *J. Am. Chem. Soc.*, 2016, **138**, 281–288.
51 E. You-Xian Chen and T. J. Marks, *Chem. Rev.*, 2000, **100**, 1391–1434.
52 I. M. Riddlestone, A. Kraft, J. Schaefer and I. Krossing, *Angew. Chem. Int. Ed.*, 2018, **57**, 13982–14024.
53 I. Krossing and I. Raabe, *Angew. Chem. Int. Ed.*, 2004, **43**, 2066–2090.
54 S. H. Strauss, *Chem. Rev.*, 2002, **93**, 927–942.
55 A. B. Chaplin and A. S. Weller, *Eur. J. Inorg. Chem.*, 2010, 5124–5128.
56 D. Langford, I. Göttker-Schnetmann, F. P. Wimmer, L. A. Casper, P. Kenyon, R. F. Winter and S. Mecking, *Organometallics*, 2019, **38**, 2710–2713.
57 S. D. Pike, F. M. Chadwick, N. H. Rees, M. P. Scott, A. S. Weller, T. Krämer and S. A. Macgregor, *J. Am. Chem. Soc.*, 2015, **137**, 820–833.
58 T. M. Douglas, E. Molinos, S. K. Brayshaw and A. S. Weller, *Organometallics*, 2007, **26**, 463–465.
59 S. D. Pike and A. S. Weller, *Dalton Trans.*, 2013, **42**, 12832–12835.
60 I. Krossing, *Chem. - A Eur. J.*, 2001, **7**, 490–502.
61 D. R. Evans, T. Drovetskaya, R. Bau, C. A. Reed and P. D. W. Boyd, *J. Am. Chem. Soc.*, 1997, **119**, 3633–3634.
62 B. Cordero, V. Gómez, A. E. Platero-Prats, M. Revés, J. Echeverría, E. Cremades, F. Barragán and S. Alvarez, *Dalton Trans.*, 2008, 2832–2838.
63 I. Castro-Rodriguez, H. Nakai, P. Gantzel, L. N. Zakharov, A. L. Rheingold and K. Meyer, *J. Am. Chem. Soc.*, 2003, **125**, 15734–15735.
64 J. Jung, S. T. Löffler, J. Langmann, F. W. Heinemann, E. Bill, G. Bistoni, W. Scherer, M. Atanasov, K. Meyer and F. Neese, *J. Am. Chem. Soc.*, 2020, **142**, 1864–1870.
65 N. R. Andreychuk and D. J. H. Emslie, *Angew. Chem. Int. Ed.*, 2013, **52**, 1696–1699.
66 E. D. Bloch, W. L. Queen, R. Krishna, J. M. Zadrozny, C. M. Brown and J. R. Long, *Science*, 2012, **335**, 1606–1610.
67 J. D. A. Pelletier and J. M. Basset, *Acc. Chem. Res.*, 2016, **49**, 664–677.
68 S. J. M. Thomas, *Design and Applications of Single-Site Heterogeneous Catalysts*, Imperial College Press, 2012.
69 C. Copéret, F. Allouche, K. W. Chan, M. P. Conley, M. F. Delley, A. Fedorov, I. B. Moroz, V. Mougel, M. Pucino, K. Searles, K. Yamamoto and P. A. Zhizhko, *Angew. Chem. Int. Ed.*, 2018, **57**, 6398–6440.
70 S. Lwin and I. E. Wachs, *ACS Catal.*, 2014, 4, 2505–2520.
71 J. J. H. B. Sattler, J. Ruiz-Martinez, E. Santillan-Jimenez and B. M. Weckhuysen, *Chem. Rev.*, 2014, **114**, 10613–10653.
72 M. I. Gonzalez, J. A. Mason, E. D. Bloch, S. J. Teat, K. J. Gagnon, G. Y. Morrison, W. L. Queen and J. R. Long, *Chem. Sci.*, 2017, **8**, 4387–4398.
73 Z. Li, A. W. Peters, V. Bernales, M. A. Ortuño, N. M. Schweitzer, M. R. Destefano, L. C. Gallington, A. E. Platero-Prats, K. W. Chapman, C. J. Cramer, L. Gagliardi, J. T. Hupp and O. K. Farha, *ACS Cent. Sci.*, 2017, **3**, 31–38.
74 J. M. Falkowski, T. Sawano, T. Zhang, G. Tsun, Y. Chen, J. V. Lockard and W. Lin, *J. Am. Chem. Soc.*, 2014, **136**, 5213–5216.
75 A. Burgun, C. J. Coghlan, D. M. Huang, W. Chen, S. Horike, S. Kitagawa, J. F. Alvino, G. F. Metha, C. J. Sumby and C. J. Doonan, *Angew. Chem. Int. Ed.*, 2017, **56**, 8412–8416.
76 C. Copéret, A. Comas-Vives, M. P. Conley, D. P. Estes, A. Fedorov, V. Mougel, H. Nagae, F. Núnez-Zarur and P. A. Zhizhko, *Chem. Rev.*, 2016, 116, 323–421.
77 J. J. Vittal and H. S. Quah, *Coord. Chem. Rev.*, 2017, **342**, 1–18.
78 A. Chaudhary, A. Mohammad and S. M. Mobin, *Cryst. Growth Des.*, 2017, 17, 2893–2910.
79 M. Kawano and M. Fujita, *Coord. Chem. Rev.*, 2007, **251**, 2592–2605.
80 J. J. Vittal, *Coord. Chem. Rev.*, 2007, **251**, 1781–1795.
81 G. K. Kole and J. J. Vittal, *Chem. Soc. Rev.*, 2013, **42**, 1755–1775.
82 Z. Huang, P. S. White and M. Brookhart, *Nature*, 2010, **465**, 598–601.
83 S. D. Pike, A. L. Thompson, A. G. Algarra, D. C. Apperley, S. A. Macgregor and A. S. Weller, *Science*, 2012, **337**, 1648.
84 O. V. Zenkina, E. C. Keske, R. Wang and C. M. Crudden, *Angew. Chem. Int. Ed.*, 2011, **50**, 8100–8104.
85 L. Vaska, *J. Am. Chem. Soc.*, 1966, **88**, 5325–5327.
86 M. Albrecht, M. Lutz, A. L. Spek and G. van Koten, *Nature*, 2000, **406**, 970–974.
87 I. G. Georgiev and L. R. MacGillivray, *Chem. Soc. Rev.*, 2007, **36**, 1239–1248.
88 S. D. Pike and A. S. Weller, *Philos. Trans. R. Soc. A*, 2015, **373**, 20140187.
89 A. Das, Y. S. Chen, J. H. Reibenspies and D. C. Powers, *J. Am. Chem. Soc.*, 2019, **141**, 16232–16236.

90 R. R. Schrock and J. A. Osborn, *J. Am. Chem. Soc.*, 1976, **98**, 2134–2143.
91 J. Contreras-García, E. R. Johnson, S. Keinan, R. Chaudret, J. P. Piquemal, D. N. Beratan and W. Yang, *J. Chem. Theory Comput.*, 2011, **7**, 625–632.
92 R. Chauvin, C. Lepetit, B. Silvi and A. Esmail, Springer International Publishing, 2016.
93 W. Scherer, V. Herz, A. Brück, C. Hauf, F. Reiner, S. Altmannshofer, D. Leusser and D. Stalke, *Angew. Chem. Int. Ed.*, 2011, **50**, 2845–2849.
94 A. I. McKay, A. J. Bukvic, B. E. Tegner, A. L. Burnage, A. J. Martínez-Martínez, N. H. Rees, S. A. Macgregor and A. S. Weller, *J. Am. Chem. Soc.*, 2019, **141**, 11700–11712.
95 F. M. Chadwick, N. H. Rees, A. S. Weller, T. Krämer, M. Iannuzzi and S. A. Macgregor, *Angew. Chem. Int. Ed.*, 2016, **55**, 3677–3681.
96 A. I. McKay, T. Krämer, N. H. Rees, A. L. Thompson, K. E. Christensen, S. A. Macgregor and A. S. Weller, *Organometallics*, 2017, **36**, 22–25.
97 A. J. Martínez-Martínez, C. G. Royle, S. K. Furfari, K. Suriye and A. S. Weller, *ACS Catal.*, 2020, **10**, 1984–1992.
98 P. C. J. Kamer, P. W. N. M. Van Leeuwen and J. N. H. Reek, *Acc. Chem. Res.*, 2001, **34**, 895–904.
99 P. W. N. M. Van Leeuwen, P. C. J. Kamer, J. N. H. Reek and P. Dierkes, *Chem. Rev.*, 2000, **100**, 2741–2769.
100 M.-N. Birkholz (née Gensow), Z. Freixa and P. W. N. M. van Leeuwen, *Chem. Soc. Rev.*, 2009, **38**, 1099–1118.
101 C. A. Tolman, *J. Am. Chem. Soc.*, 1970, **92**, 2956–2965.
102 C. A. Tolman, *Chem. Rev.*, 1977, **77**, 313–348.
103 A. J. Martínez-Martínez, B. E. Tegner, A. I. McKay, A. J. Bukvic, N. H. Rees, G. J. Tizzard, S. J. Coles, M. R. Warren, S. A. Macgregor and A. S. Weller, *J. Am. Chem. Soc.*, 2018, **140**, 14958–14970.
104 M. A. McLoughlin, R. J. Flesher, W. C. Kaska and H. A. Mayer, *Organometallics*, 1994, **13**, 3816–3822.
105 C. Crocker, R. J. Errington, W. S. McDonald, K. J. Odell, B. L. Shaw and R. J. Goodfellow, *J. Chem. Soc.,Chem. Commun.*, 1979, 498–499.
106 W. Weng, C. Guo, C. Moura, L. Yang, B. M. Foxman and O. V. Ozerov, *Organometallics*, 2005, **24**, 3487–3499.
107 O. V. Ozerov, C. Guo, V. A. Papkov and B. M. Foxman, *J. Am. Chem. Soc.*, 2004, **126**, 4792–4793.
108 A. L. Thompson, *Crystallogr. Rev.*, 2019, **25**, 3–53.
109 A. I. McKay, A. J. Martínez-Martínez, H. J. Griffiths, N. H. Rees, J. B. Waters, A. S. Weller, T. Krämer and S. A. MacGregor, *Organometallics*, 2018, **37**, 3524–3532.
110 A. J. Martínez-Martínez, N. H. Rees and A. S. Weller, *Angew. Chem. Int. Ed.*, 2019, **58**, 16873–16877.
111 F. M. Chadwick, A. I. McKay, A. J. Martinez-Martinez, N. H. Rees, T. Krämer, S. A. Macgregor and A. S. Weller, *Chem. Sci.*, 2017, **8**, 6014–6029.
112 M. E. van der Boom, *Angew. Chem. Int. Ed.*, 2011, **50**, 11846–11848.
113 K. I. Goldberg and A. S. Goldman, *Acc. Chem. Res.*, 2017, **50**, 620–626.
114 S. D. Pike, T. Krämer, N. H. Rees, S. A. Macgregor and A. S. Weller, *Organometallics*, 2015, **34**, 1487–1497.
115 F. M. Chadwick, T. Krämer, T. Gutmann, N. H. Rees, A. L. Thompson, A. J. Edwards, G. Buntkowsky, S. A. Macgregor and A. S. Weller, *J. Am. Chem. Soc.*, 2016, **138**, 13369–13378.

Chapter 2:
The Synthesis of C_3 to C_6 σ-Alkane Complexes in the Solid-State

2.1. Chapter Introduction

Chapter 2 explores a range of σ-alkane complexes that can be synthesised in the solid-state, following the SMOM methdology presented in Chapter 1. This also aims to establish the trends and limits to such synthetic methodologies. The main focus of Chapter 2 expands upon the previously reported σ-alkane complexes of **[1-NBA][BAr$^{F}_{4}$]**,[1] **[1-cyclohexane][BAr$^{F}_{4}$]**[2] and **[1-pentane][BAr$^{F}_{4}$]**,[3] all of which use the cyclohexyl bisphosphine ligand and [BAr$^{F}_{4}$]$^{-}$ anion (Scheme 2.1). These components were shown to be key in supporting a range of σ-alkane complexes in the solid-state.

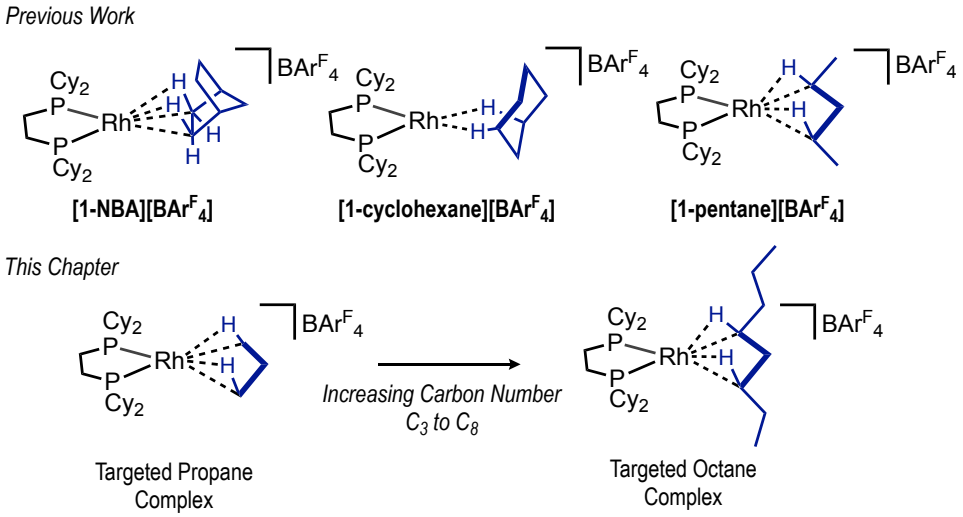

Scheme 2.1: Previous and targeted solid-state σ-alkane complexes.

A range of σ-alkane complexes will be targetted from low molecular weight, linear alkanes, such as propane and butane, to the higher molecular weight alkane of octane. The synthesis of branched analogues of these alkanes, such as *iso*butane, *iso*pentane and 3-methylpentane, are also reported. As these branched analogues are bulkier in nature compared to their linear counterparts, this may result in a greater number of non-covalent interactions between the σ-alkane ligand and [BAr$^{F}_{4}$]$^{-}$ anion, which has been shown to be pivotal in the long standing stability of **[1-NBA][BAr$^{F}_{4}$]**[1] and **[1-cyclohexane][BAr$^{F}_{4}$]**.[2]

2.2. The Synthesis of Linear, C_3 and C_4 σ-Alkane Complexes

2.2.1. The Hydrogenation of [1-propene][BAr^F_4] in the Solid-State

To start, the solid/gas hydrogenation of the propene-bound complex **[1-propene][BAr^F_4]** was conducted in an attempt to form a σ-propane complex. **[1-propene][BAr^F_4]** was introduced in Chapter 1 (Section 1.5.6.) and was synthesised from the SC-SC reaction of **[1-NBA][BAr^F_4]** with propene gas. When crystalline material of **[1-propene][BAr^F_4]** was placed under H_2 (1 bar, 298 K), complete solid/gas hydrogenation occurred within 30 seconds. This was confirmed by solution $^{31}P\{^1H\}$ NMR spectroscopy of the dissolved material after this time, where the spectrum recorded showed no signals relating to **[1-propene][BAr^F_4]**.

Although this short hydrogenation time is not necessarily a concern, the further rapid decomposition of the σ-alkane complex is. When left under an H_2 atmosphere for just 1 minute, a complete loss in crystallinity is observed, shown by the loss of diffraction Bragg peaks during a single-crystal x-ray diffraction experiment. This is consistent with the formation of the decomposition product, **[1-BAr^F_4]**,[1] and loss of coordinating alkane.

This short hydrogenation time, coupled with the poor crystalline quality of **[1-propene][BAr^F_4]**,[4] meant the standard single-crystal x-ray diffraction techniques and equipment could not be used. To overcome these factors, the structural characterisation of the targeted propane-complex was conducted on the beamline I19 at the Diamond Light Source synchrotron facility. An *in situ* hydrogenation, using an adapted gas line set-up (Figure 2.1), meant the hydrogenation time could be highly controlled.

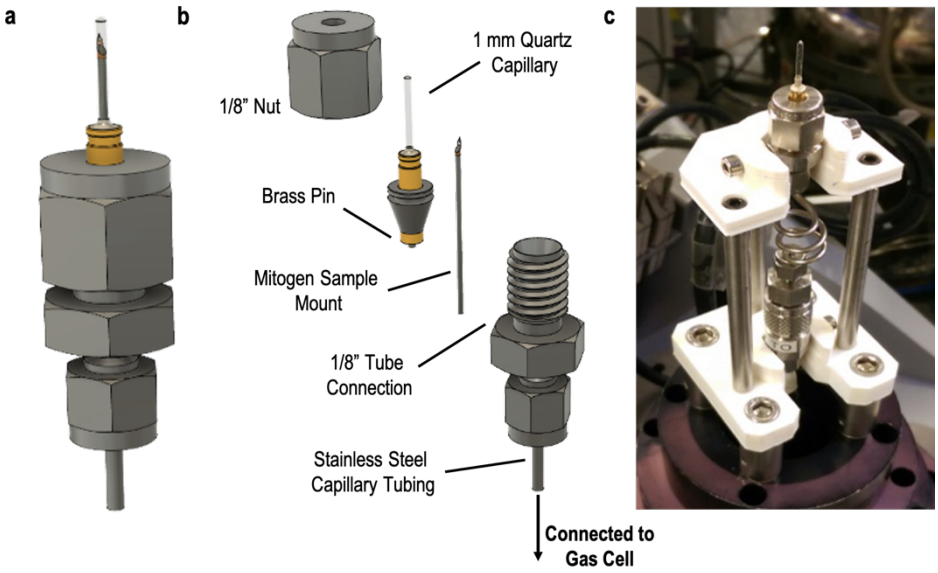

Figure 2.1: I19 Beamline 1mm quartz capillary gas cell equipment. **a**) Technical drawing of the head of the cell with **b**) showing the exploded view. **c**) Image of the diffractometer mounted cell. Image adapted with kind permission from Dr Mark Warren, Diamond Light Source.[5]

In this experimental set-up, a single crystal of **[1-propene][BAr$^{F}_{4}$]** was mounted on a pin and inserted within a capillary, both inside an argon filled glove box. The crystal was attached to the pin with a dab of epoxy resin, rather than coated in oil, to allow gas access to the crystal. The gas cell was then sealed by a locking nut (not shown), removed from the glove box and connected to the gas rig upon the diffractometer. Quick release connectors were used to retain the inert atmosphere within the cell during these transfer steps. Upon connection, the atmosphere within the cell could be controlled. The cell was placed under vacuum (10^{-4} mbar), then filled with a hydrogen atmosphere, to form the corresponding σ-alkane complex. The temperature of the cell capillary was controlled directly from the diffractometer cryostream.

This set-up meant that a mounted crystal of **[1-propene][BAr$^{F}_{4}$]** could be hydrogenated for only 30 seconds, after which the capillary could be flash-cooled to 150 K. As no onward reactivity was observed at this temperature, the complex (or complexes) formed were indefinitely stable. The synchrotron facility also provided an intense source of x-rays, which aided in overcoming the poor crystalline quality of the complexes. This gas cell set-up and synchrotron was necessary for the structural elucidation of the σ-propane complex of [Rh($Cy_2PCH_2CH_2PCy_2$)(C_3H_8)][BAr$^{F}_{4}$], **[1-propane][BAr$^{F}_{4}$]** by single-crystal x-ray diffraction, shown in Figure 2.2.

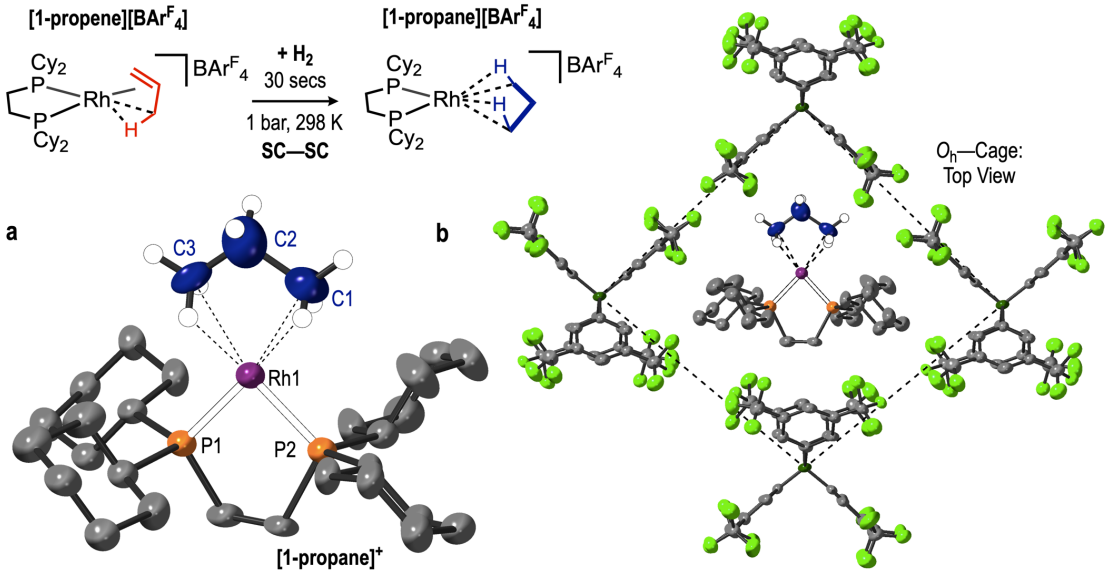

Figure 2.2: The formation of **[1-propane][BAr$^{F}_{4}$]**. **a**) The solid-state structure of the cationic portion of **[1-propane][BAr$^{F}_{4}$]**. **b**) Section view of the O_h cage of $[BAr^{F}_{4}]^-$ anions in **[1-propane][BAr$^{F}_{4}$]**. Hydrogen atoms on phosphine ligand and $[BAr^{F}_{4}]^-$ anions excluded for clarity. Displacement ellipsoids set at 30 % in both parts.

The solid-state structure of **[1-propane][BAr$^{F}_{4}$]** shows propane coordinated to the rhodium centre in an 1,3-mode similar to that of **[1-pentane][BAr$^{F}_{4}$]**.[3] Selected bond metrics are given in Table 2.1, which show the elongation of the C1–C2 distance, (1.239(9) and 1.511(5) Å in **[1-propene][BAr$^{F}_{4}$]** and **[1-propane][BAr$^{F}_{4}$]** respectively), confirming the hydrogenation reaction of propene to propane. The elongation of Rh•••C distances and contraction of Rh–P distances are both synonymous with the poorly donating 3c–2e$^-$ interaction of the propane ligand towards the rhodium centre, and reduced *trans* influence of the alkane to alkene ligand respectively.

Table 2.1: Selected crystallographic information of **[1-propene][BAr$^{F}_{4}$]** and **[1-propane][BAr$^{F}_{4}$]**.

	Rh–P1 / Rh–P2 (Å)	Rh–C1 / Rh–C3 (Å)	C1–C2 / C2–C3 (Å)	Unit Cell Volume (Å^3) / Space Group
[1-propene][BAr$^{F}_{4}$][4]	2.235(6) / 2.240(5)	2.15(2) / 2.29(3)	1.361(9) / 1.239(9)	3252.73(9) / P–1
[1-propane][BAr$^{F}_{4}$]	2.2002(6) / 2.1910(6)	2.527(3) / 2.546(4)	1.511(5) / 1.528(6)	3322.42(10) / P–1

The relatively short Rh•••C distances combined with relatively acute Rh•••H–C angles (104.4° and 105.4°) are suggestive of a $\eta^2\eta^2$-coordination. As the hydrogen atoms within this structure are not freely refined however, and are placed in their geometric positions, this can only be suggested as an $\eta^2\eta^2$-coordination,[6] where definitive proof through calculations are ongoing. Similar Rh•••C distances were observed in the solid-state structure of **[1-pentane][BAr$^F_4$]** (Rh•••C, 2.514(4) and 2.522(5) Å),[3] for which the $\eta^2\eta^2$-coordination of the pentane ligand was confirmed by calculations. These values are well matched to those in **[1-propane][BAr$^F_4$]** and are notably different from the distances and angles observed in previously structurally characterised η^1-alkane coordinated complexes (Rh•••C, 2.90(3) Å and Rh•••H–C, 140.7°).[7]

The pseudo-O_h arrangement of $[BAr^F_4]^-$ anions is retained, along with the cation orientation towards the octahedral vertex (Figure 1.2b). No disorder was present in the propane ligand, or residual electron density from the precursor **[1-propene][BAr$^F_4$]** complex. **[1-propane][BAr$^F_4$]** represents the only structurally characterised propane σ-complex to our knowledge. σ-Propane complexes of manganese, analysed by *in situ* low temperature, solution NMR spectroscopy have been previously reported.[8]

To analyse **[1-propane][BAr$^F_4$]** as a bulk material, and not just by single-crystal x-ray diffraction, characterisation by $^{31}P\{^1H\}$ and $^{13}C\{^1H\}$ SSNMR spectroscopy was conducted. Notably, the experimental conditions using SSNMR spectroscopy and single-crystal x-ray diffraction experiments are very different. The hydrogenation of **[1-propene][BAr$^F_4$]**, experimentally described in the next section, resulted in the SSNMR spectra at 158 K showing a mixture of products, Figure 2.3.

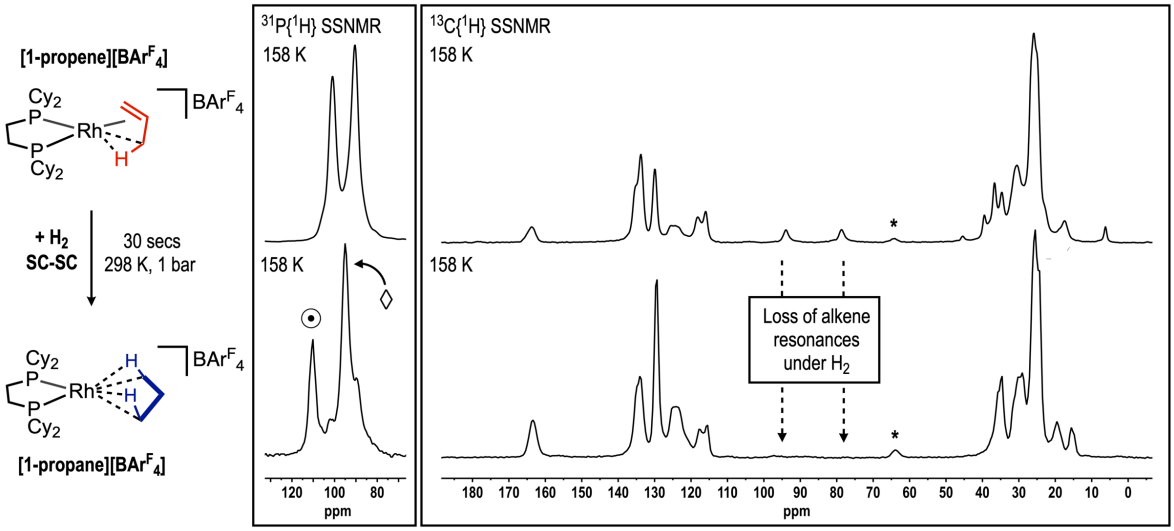

Figure 2.3: The $^{31}P\{^{1}H\}$ and $^{13}C\{^{1}H\}$ SSNMR (162 / 101 MHz, 10 kHz spin rate, 158 K) spectra of **[1-propene][BAr$^{F}_{4}$]** and **[1-propane][BAr$^{F}_{4}$]**. Peaks assigned to ⦿ = **[1-propane][BAr$^{F}_{4}$]**, ◊ = **[1-BAr$^{F}_{4}$]**. * = spinning sidebands.

The $^{31}P\{^{1}H\}$ SSNMR spectrum of **[1-propane][BAr$^{F}_{4}$]** shows a sharp resonance at δ 106, which is assigned to that of **[1-propane][BAr$^{F}_{4}$]**. This downfield shift comparative to the **[1-propene][BAr$^{F}_{4}$]** precursor and is in line with previously reported σ-alkane complexes.[1] A broad peak at δ 91 from **[1-BAr$^{F}_{4}$]** is also observed, from the over hydrogenation and consequent decomposition of **[1-propane][BAr$^{F}_{4}$]**. These two signals are observed in ~30: 65 ratio respectively, with remaining ~5 % of signal intensity relating to the precursor **[1-propene][BAr$^{F}_{4}$]** [δ 99, 83] from the under-hydrogenation of the sample. The $^{13}C\{^{1}H\}$ SSNMR spectrum also shows changes consistent with the formation of **[1-propane][BAr$^{F}_{4}$]**, through the reduction in relative intensity of the propene-assigned resonances at δ 95, 79 and 6. This is consistent with the complete hydrogenation of propene.

2.2.2. Single-Crystal X-Ray Diffraction *versus* SSNMR Techniques

The spectroscopic yield of **[1-propane][BAr$^{F}_{4}$]** from the $^{31}P\{^{1}H\}$ SSNMR spectrum is ~30 %. The solid-state structure as determined by single-crystal x-ray diffraction (Figure 2.2) was solved with no evidence for any **[1-propene][BAr$^{F}_{4}$]** present, and the quality of the diffraction frames observed are not consistent with a crystal containing ~70 % amorphous material of **[1-BAr$^{F}_{4}$]**.[9] This observed difference in the mixture of complexes arises from the synthetic routes to **[1-propane][BAr$^{F}_{4}$]** used in single-crystal x-ray diffraction and SSNMR spectroscopy.

As the procedure for running SSNMR spectroscopy and single-crystal x-ray diffraction experiments varied notably, this resulted in the time-to-measurement (and thus, the time the sample was exposed to a H_2 atmosphere at 298 K) being very different between the two techniques.

Contrasted to the experimental procedure for running *in situ* single-crystal x-ray diffraction experiments at Diamond Light Source (Section 2.2.1.), the procedure for running *in situ* SSNMR experiments is as follows: By taking a prepacked SSNMR rotor of the respective alkene complex, this can be left un-capped and placed under an H_2 atmosphere. This is then left for a predetermined hydrogenation time, capped under a flush of argon and transferred to the bore of a SSNMR spectrometer. Cooling of the sample to 158 K is then started, where upon these σ-alkane complexes exhibit no further reactivity and are indefinitely stable. This time from initial hydrogenation, transfer and cooling to 158 K is approximately 10 minutes and is the shortest experimental time possible for SSNMR analysis.

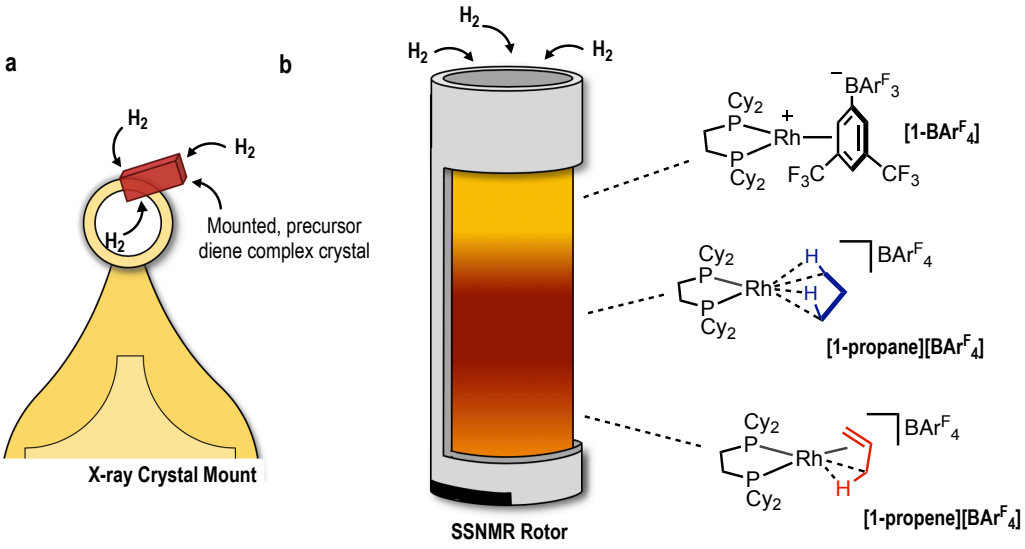

Figure 2.4: Hydrogen gas accessibility in **a**) single-crystal x-ray diffraction and **b**) SSNMR spectroscopy experiments.

The solid material within SSNMR rotor has to be densely packed as to form a uniform distribution throughout the rotor. This is important for achieving sharp signals in the SSNMR spectra.[10] This dense packing inhibits H_2 movement through the sample (Figure 2.4b), similar to that of plug flow fluid dynamics within flow reactors.[11] The dense packing and limited accessibility means hydrogenation times must therefore be increased for SSNMR experiments to allow for this gas/solid movement. This is opposed to

hydrogenation of a free-flowing powder, where this consideration is not required. This limitation has been previously noted for the hydrogenation times of SMOM materials packed within SSNMR rotors *versus* free-flowing crystals.[12]

In the case of **[1-propane][BAr$^{F}_{4}$]**, both these factors resulted in multiple products in the $^{31}P\{^{1}H\}$ SSNMR spectrum, Figure 2.3. **[1-BAr$^{F}_{4}$]** is suggested to be present from the over-hydrogenation of **[1-propane][BAr$^{F}_{4}$]** in the elongated hydrogenation time. Signals relating to **[1-propene][BAr$^{F}_{4}$]** are also observed, from the under-hydrogenation of the sample, which are presumably located at the base of the rotor.

These packing considerations are not present in single-crystal x-ray diffraction studies. As shown in Figure 2.4a for the gas cell set-up used for **[1-propane][BAr$^{F}_{4}$]**, hydrogen gas can access the crystal from multiple points. In **[1-propane][BAr$^{F}_{4}$]**, this results in only a single product collected by single-crystal x-ray diffraction. This unhindered access for H_2 also occurs for batch experiments, when free-flowing crystals within a J. Youngs NMR tube are placed under a hydrogen atmosphere. This juxtaposition between techniques is returned to throughout this Chapter.

2.2.3. The Attempted Synthesis of a σ-Butane Complex

As discussed in Chapter 1, Section 1.5.6, **[1-butadiene][BAr$^F_4$]** could be synthesised from the SC-SC reaction of **[1-NBA][BAr$^F_4$]** with 1-butene gas. Although this was confirmed by spectroscopic techniques, the poor crystallographic quality from this route meant a structure was not reported.[9] Analysed at Diamond Light Source, utilising the increased intensity of x-ray beams, a satisfactory structure could be solved, shown in Figure 2.5. This revealed the coordinated butadiene, in the expected η^4-fashion, analogous to that of **[1-pentadiene][BAr$^F_4$]**.

With crystals of **[1-butadiene][BAr$^F_4$]** in hand, the SC-SC hydrogenation was explored. Following the same experimental procedure on the gas rig at Diamond Light Source as for **[1-propane][BAr$^F_4$]**, after 30 seconds hydrogenation and rapid cooling to 158 K, the structure of [Rh($Cy_2PCH_2CH_2PCy_2$)(*n*-C_4H_{10})][BAr$^F_4$], **[1-butane][BAr$^F_4$]** was solved, also shown in Figure 2.5. 30 seconds was used again, as this was the minimal time needed for complete **[1-butadiene][BAr$^F_4$]** hydrogenation.

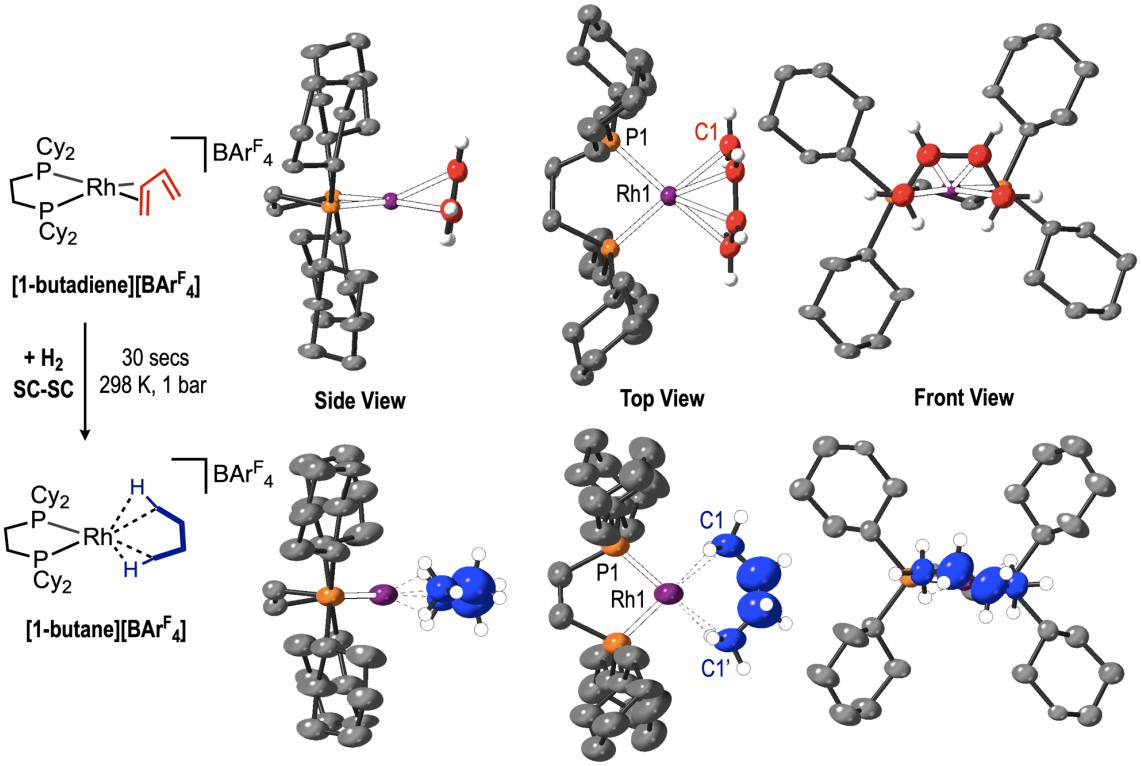

Figure 2.5: The formation of **[1-butane][BAr$^F_4$]**. The cationic portions and **[1-butane][BAr$^F_4$]** in three orientations showing the structural rearrangements upon hydrogenation reaction. Hydrogen atoms on phosphine ligand and $[BAr^F_4]^-$ anions excluded for clarity. Displacement ellipsoids set at 30 %.

Upon hydrogenation, a re-orientation of the butadiene to butane ligand within their respective structures was observed. This movement involves the butadiene ligand moving from being perpendicular to the RhP_2 plane, to being in the RhP_2 plane for butane. This new orientation, along with increased Rh–C1 distance (2.194(12) Å in **[1-butadiene][BAr$^F_4$]** to 2.345(10) Å in **[1-butane][BAr$^F_4$]**) is overall suggestive of a σ-1,4-coordinated butane ligand. The Rh–P distances are seen to decrease upon hydrogenation, due the weaker *trans* influence of the butane 3c–2e$^-$ interactions *versus* π-coordination in butadiene and are shown in Table 2.2.

Table 2.2: Selected crystallographic information of **[1-butadiene][BAr$^F_4$]** and **[1-butane][BAr$^F_4$]**.

	Rh–P1 (Å)	Rh–C1 / Rh–C2 (Å)	Unit Cell Volume (Å^3) / Space Group
[1-butadiene] [BAr$^F_4$]	2.608(11)	2.194(12) / 2.29(3)	6687.4(4) / C/2c
[1-butane] [BAr$^F_4$]	2.197(2)	2.345(10) / ~ 2.83(2)	6944.9(9) / C/2c

Due to the large displacement ellipsoids present however, and the hydrogen atoms of the butane ligand not being reliably located due to the poor crystal quality, this makes any bond metrics within the butane ligand and hapticity discussions inappropriate. Larger atoms, such as rhodium and phosphorus are solved in definitive places however, so bond distances discussions are appropriate. The large displacement ellipsoids of the butane ligand in the structure of **[1-butane][BAr$^F_4$]** may also mask any disorder components in the solid-state, such as the coordination of any butene species. This means that, unlike for **[1-propane][BAr$^F_4$]**, only the connectivity of **[1-butane][BAr$^F_4$]** can be definitively discussed.

The poor crystallographic quality of the crystals of **[1-butane][BAr$^F_4$]** may be explained in the formation of **[1-butadiene][BAr$^F_4$]**. Both **[1-propane][BAr$^F_4$]** and **[1-butane][BAr$^F_4$]** have now undergone three, consecutive SC-SC reactions. The data for **[1-propane][BAr$^F_4$]** however is considerably better (R = 10.5 and 12.4 % respectively). This may be due to the added transfer hydrogenation step of **[1-NBA][BAr$^F_4$]** with 1-butene to form **[1-butadiene][BAr$^F_4$]**, as discussed in Chapter 1, Section 1.5.6.

The recrystallisation of **[1-butadiene][BAr$^F_4$]**, with the aim to improve the crystallographic quality, was ultimately unsuccessful. Although **[1-butadiene][BAr$^F_4$]** exhibited solution stability (CH_2Cl_2) for weeks, the recrystallised product was found to be in a *tetragonal*-I

space group, which in this case, suffers from merohedral twinning. Although these crystals were shown to be of **[1-butadiene][BAr$^F_4$]** by solution and solid-state NMR spectroscopic techniques, no definitive solid-state structure could be solved from this crystal morphology.

Attempts to characterise **[1-butane][BAr$^F_4$]** by SSNMR spectroscopy, which also explores the bulk reactivity of this transformation, resulted in the spectrum presented in Figure 2.6. This reveals a mixture of complexes, assigned **[1-butane][BAr$^F_4$]** [δ 109], **[1-BAr$^F_4$]** [δ 91], **[1-(2-butene)][BAr$^F_4$]** [δ 96] and **[1-butadiene][BAr$^F_4$]** [δ 82]. This mixture of species meant the isolation of **[1-butane][BAr$^F_4$]** was not achieved.

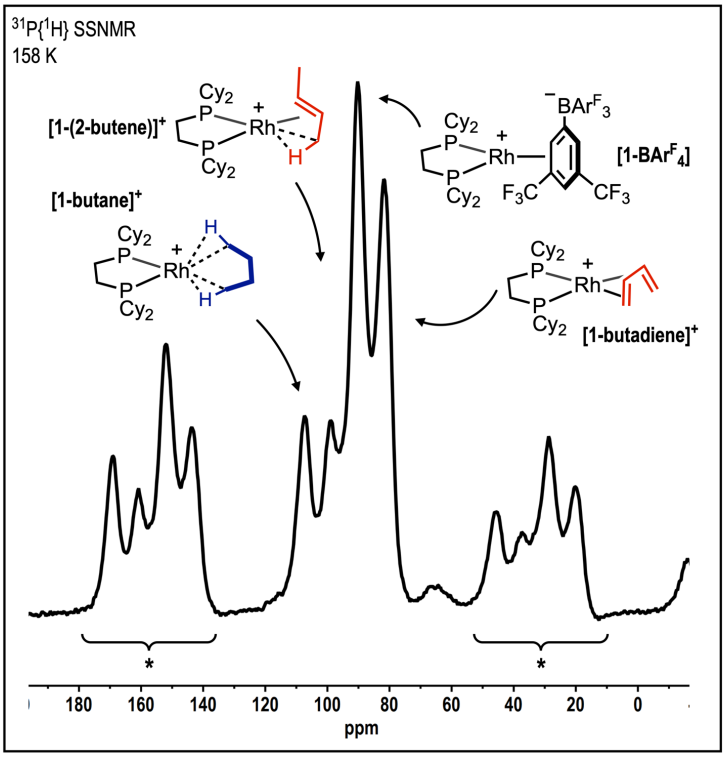

Figure 2.6: The $^{31}P\{^1H\}$ SSNMR (162 MHz, 10 kHz spin rate, 158 K) spectrum of the mixture of products observed upon **[1-butadiene][BAr$^F_4$]** hydrogenation. * = spinning sidebands.

By modelling and deconvoluting this $^{31}P\{^1H\}$ SSNMR spectra, as shown in Figure 2.7, the separate components could be visualised. It also suggests **[1-butane][BAr$^F_4$]** is only formed as a minor product in ~14 % spectroscopic yield.

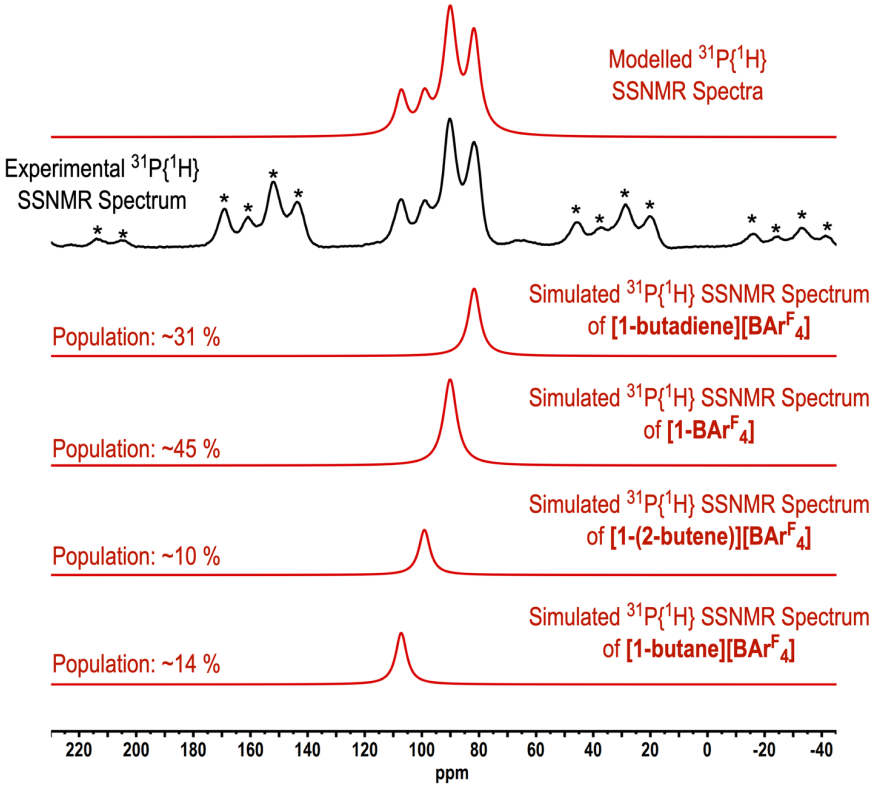

Figure 2.7: Simulated and experimental $^{31}P\{^{1}H\}$ SSNMR spectra of the mixture of species observed in the hydrogenation of **[1-butadiene][BAr$^{F}_{4}$]**. Peaks marked * are assigned to spinning sidebands.

This mixture of species observed here is a result of the limiting factors present in the SSNMR experimental produces, previously described for **[1-propane][BAr$^{F}_{4}$]** (Section 2.2.2.). The time of measurement for SSNMR experiments was not optimal at ~10 minutes, especially as it was found complete hydrogenation of **[1-butadiene][BAr$^{F}_{4}$]** occurred in 30 seconds. It is proposed that the densely packed nature of the SSNMR sample leads to both under- and over-hydrogenated products being observed and limits the full spectroscopic characterisation of **[1-butane][BAr$^{F}_{4}$]**.

2.2.4. The Solid-State Stabilities of [1-propane][BAr$^F_4$] and [1-butane][BAr$^F_4$]

The σ-alkane complexes of **[1-propane][BAr$^F_4$]** and **[1-butane][BAr$^F_4$]** both exhibited stabilities of less than an hour at 298 K in the solid-state. This was determined by *in situ* SSNMR spectroscopy studies, shown in Figure 2.8. During this time, the SSNMR rotors were left in the bore of the SSNMR spectrometer, capped under a flushing N_2 atmosphere. The collection of solid-state $^{31}P\{^1H\}$ spectra over a range of time points showed decreasing intensities of the assigned alkane complexes and increasing **[1-BAr$^F_4$]** concentration for both **[1-propane][BAr$^F_4$]** and **[1-butane][BAr$^F_4$]**.

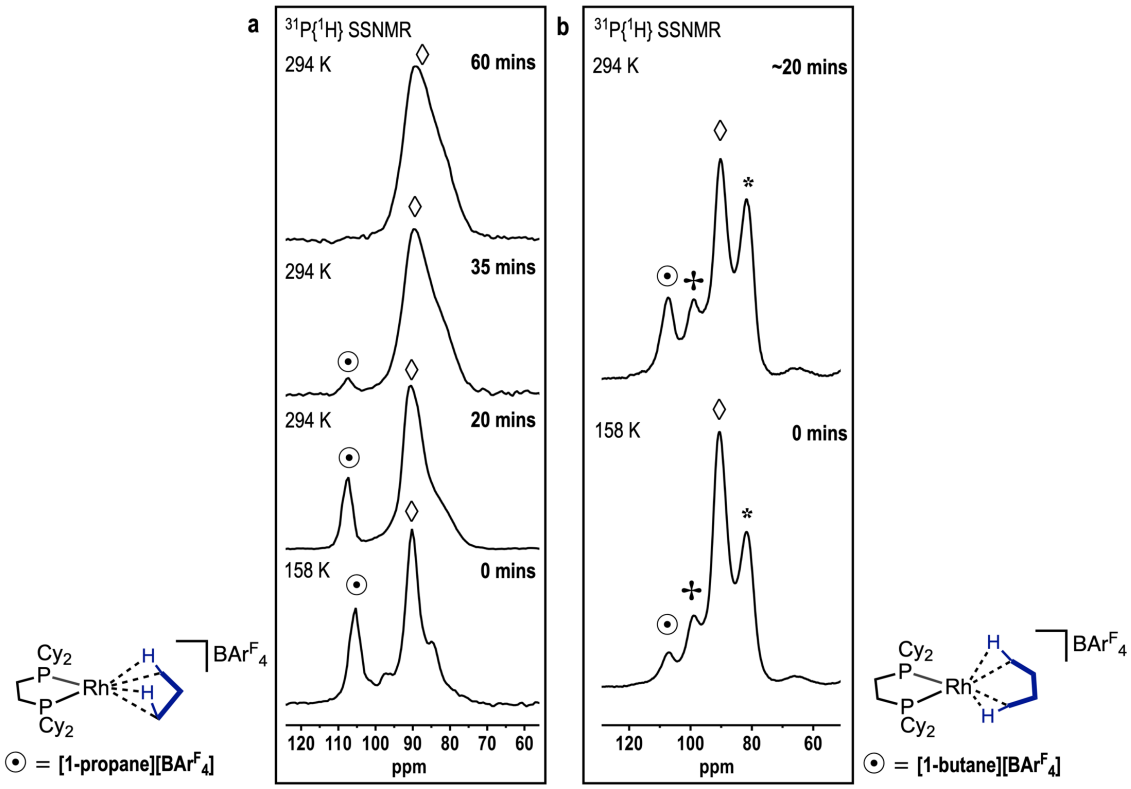

Figure 2.8: $^{31}P\{^1H\}$ SSNMR (162 MHz, 10 kHz spin rate) spectra of **a**) **[1-propane][BAr$^F_4$]** decomposition over 60 minutes and **b**) **[1-butane][BAr$^F_4$]** decomposition over ~20 minutes (~20 minutes includes instrument warming, stabilisation and experimental collection). Signals assigned ⦿ = σ-alkane complex. ◊ = **[1-BAr$^F_4$]**. ⊹ = **[1-(2-butene)][BAr$^F_4$]** and * = **[1-butadiene][BAr$^F_4$]**.

No signals assigned to **[1-propane][BAr$^F_4$]** were observed after 60 mins, and ~50 % reduction in intensity for **[1-butane][BAr$^F_4$]** were observed after just 20 minutes. This decomposition is a result of alkane loss and subsequent anion coordination (Scheme 2.2), shown spectroscopically by the broad signal of **[1-BAr$^F_4$]** [δ 91]. No evidence for any significant alkane dehydrogenation is observed for either complex, as the intensity of **[1-BAr$^F_4$]** is shown to increase, rather than the relative intensities of **[1-propene][BAr$^F_4$]** or **[1-(2-butene)][BAr$^F_4$]** / **[1-butadiene][BAr$^F_4$]** respectively.

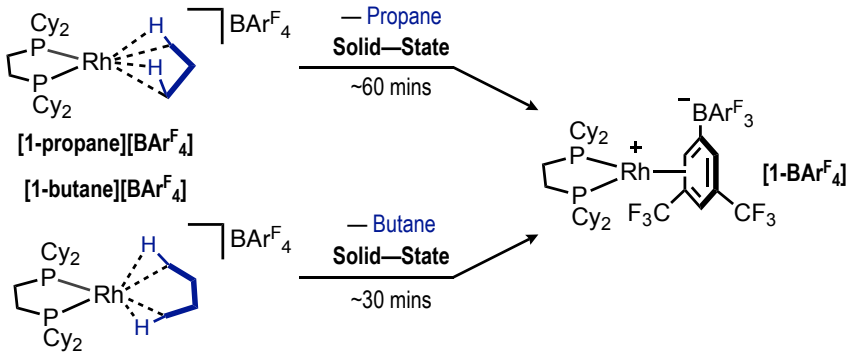

Scheme 2.2: Solid-state decomposition routes of **[1-propane][BAr$^F_4$]** and **[1-butane][BAr$^F_4$]**.

2.3. The Synthesis of a σ-*Iso*butane Complex

2.3.1. A Precursor *Iso*butene Complex

It was postulated that addition of bulk to the alkane ligand would lead to an increase in stabilising solid-state dispersion forces in the anion microenvironment, enhancing the overall stability of alkane complex. To prove this, an *iso*butane complex was targeted which could be compared to **[1-propane][BAr$^F_4$]**, as upon hydrogenation, the resultant *iso*butane ligand would have added bulk than propane from the additional methyl group. *Iso*butane is also an industrially relevant alkane, used as the monomer in *tert*-butyl rubber synthesis.[13,14]

To achieve a σ-*iso*butane complex, a precursor *iso*butene compex had to be synthesised. The optimised synthetic route to this was through a similar methodology presented for the synthesis of **[1-propene][BAr$^F_4$]**. By placing crystals of **[1-NBA][BAr$^F_4$]** under an atmosphere of *iso*butene gas for 18 hours, complete displacement of the NBA ligand occurs to yield [Rh($Cy_2PCH_2CH_2PCy_2$)(*iso*-C_4H_8)][BAr$^F_4$], **[1-*iso*butene][BAr$^F_4$]**. Although this SC-SC route formed **[1-*iso*butene][BAr$^F_4$]**, the quality of the resulting crystal structure was poor. Recrystallisation of the product in an *iso*butene-saturated layering of dichloromethane: pentane at 278 K resulted in crystalline material of increased quality and is used henceforth.

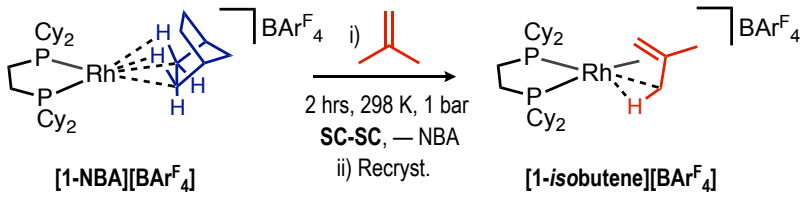

Scheme 2.3: Synthetic route to **[1-*iso*butene][BAr$^F_4$]**.

Unlike **[1-propene][BAr$^F_4$]**, recrystallisation under saturated conditions did not lead to the formation of a bis*iso*butene complex, analogous to that of **[1-(propene)$_2$][BAr$^F_4$]**. This difference is proposed to arise from the added methyl group on *iso*butene creating unfavourable steric interactions between two coordinated *iso*butenes.

The solid-state structure of recrystalised **[1-*iso*butene][BAr$^{F}_{4}$]** shows a single *iso*butene fragment bound to the rhodium centre in a η^2_{π}: $\eta^2_{C\text{-}H}$ binding mode (Figure 2.9a), exhibiting an agostic interaction similar to that of **[1-propene][BAr$^{F}_{4}$]**.[4] The η^2_{π}: $\eta^2_{C\text{-}H}$ is shown by the C1=C2 and C2–C3 distances of 1.320(12) and 1.474(13) Å respectively, as well as the Rh–C1 and Rh–C3 distances of 2.262(6) and 2.368(9) Å respectively.[6]

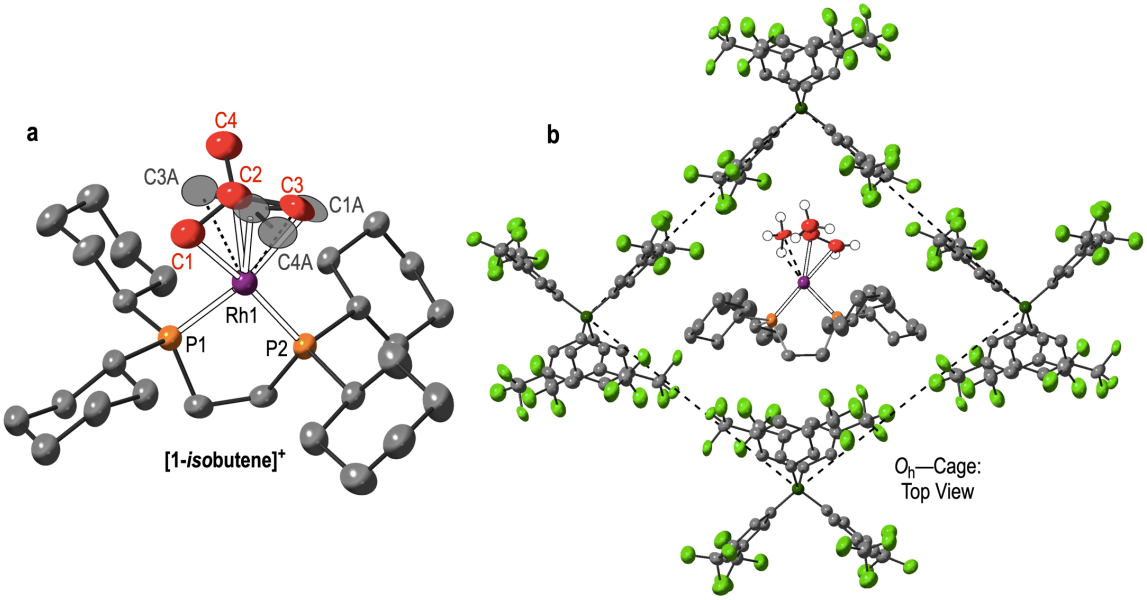

Figure 2.9: a) **[1-*iso*butene]$^{+}$** cation displaying major (red) and minor (grey) disorder components of the *iso*butene ligand. **b**) Section view of the O_h cage of [BAr$^{F}_{4}$]$^{-}$ anions in **[1-*iso*butene][BAr$^{F}_{4}$]**. Hydrogen atoms on phosphine ligand and selected [BAr$^{F}_{4}$]$^{-}$ anions excluded for clarity. Displacement ellipsoids set at 30 % in both parts.

Disorder of the *iso*butene ligand was present in the crystal structure, solved as two, non-crystallographic superimposable positions across a pseudo-C_2 axis, in 70: 30 population (Figure 2.9a). The packing structure of anions around this cationic fragment is shown to be a pseudo-O_h arrangement of [BAr$^{F}_{4}$]$^{-}$ anions (Figure 2.9b) with the cation orientated towards the vertex of an adjacent [BAr$^{F}_{4}$]$^{-}$ anion. This has been noted as imperative for the long-standing stability of **[1-NBA][BAr$^{F}_{4}$]**.[1] Importantly, this has been reformed in this recrystallised product.

At 273 K and above in solution, the $^{31}P\{^{1}H\}$ NMR spectra of **[1-*iso*butene][BAr$^{F}_{4}$]** exhibits a single doublet [δ 95, J_{RhP} = 179 Hz] and, upon cooling to 183 K, two mutually-coupled environments are observed [δ 97, J_{RhP} = 201 Hz, J_{PP} = 26 Hz and δ 93, J_{RhP} = 158 Hz, J_{PP} = 26 Hz] (Figure 2.10). This suggests a fluxional process occurs in the *iso*butene ligand at 298 K, which becomes static at 183 K in solution.

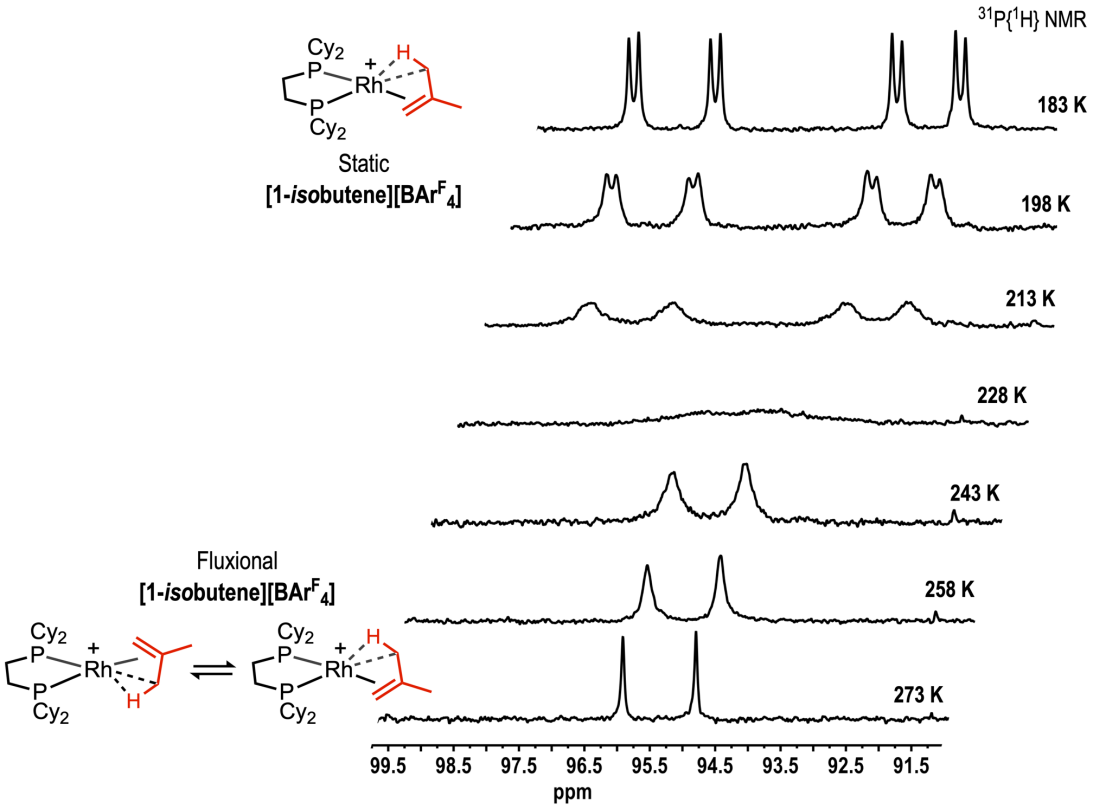

Figure 2.10: Solution VT $^{31}P\{^{1}H\}$ NMR spectra (162 MHz, CD_2Cl_2) of **[1-*iso*butene][BAr$^F_4$]**.

At 273 K and above, the doublet in the $^{31}P\{^{1}H\}$ NMR spectrum is formed from the averaging of both ^{31}P nuclei into a single environment that are coupled to the ^{103}Rh metal centre (^{103}Rh I = ½). At 183 K, the now static *iso*butene ligand shows an alkene and agostic interaction. This is shown by the difference in coupling constants [J_{RhP} = 201, 158 Hz] that reflect the ^{31}P environment *trans* to the agostic and alkene environments respectively. Line-shape analysis, and resulting Eyring plot, of these variable temperature spectra was modelled using calculated rate-contents. This gave a value of $\Delta G^{\ddagger}$ = 8.2(8) kcal mol^{-1} and $\Delta S^{\ddagger}$ = + 15.9(12) cal^{-1} K^{-1}, suggestive of a more disordered transition-state for this process.

The solution ^{1}H NMR spectra are consistent with this fluxional process occurring. The 183 K ^{1}H NMR spectra exhibited a signal [δ –0.15, integral of 3H] which is assigned to an -CH_3 group agostic interaction.[6] A broad alkene resonance [δ 3.75, integral of 2H] is also observed, assigned to that of the two coincident alkene ^{1}H environments present in the static structure. At 298 K, only a broad resonance is observed [δ 1.75, integral of 8H] and is assigned to the averaging of the all ^{1}H environments within the coordinated *iso*butene.

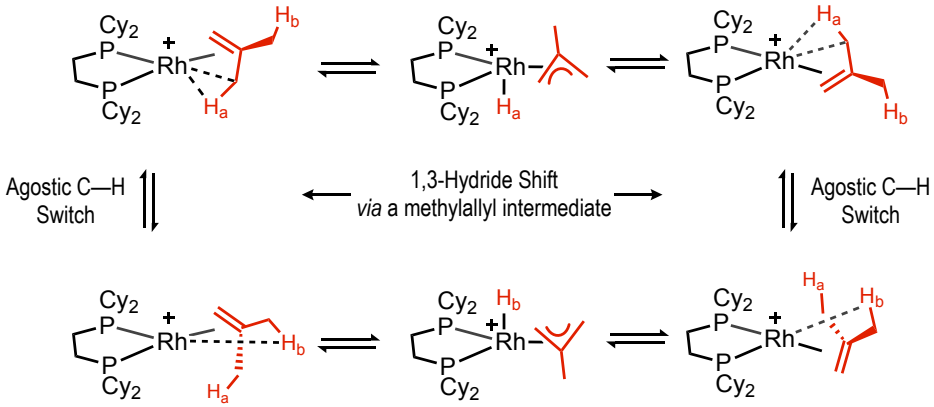

Scheme 2.4: A proposed mechanism for the rapid fluxional process of *iso*butene in **[1-*iso*butene][BAr$^F_4$],** *via* a methylallyl intermediate.

A proposed mechanism for this fluxional process is shown in Scheme 2.4. This involves the rapid exchange of the protons in the *iso*butene ligand and goes *via* a methylallyl hydride mechanism.[4,15,16] Although a 1,3-hydride shift averages the two ^{31}P environments, it does not average all ^{1}H environments. These unaveraged nuclei are shown by following either H_a or H_b in the 1,3-hydride shift steps; as they remain in non-coordinating, methyl environments. An agostic C–H switch step therefore must be occurring to exchange all ^{1}H nuclei and become consistent with the ^{1}H NMR spectroscopy data.

Also shown in Scheme 2.4, the proposed fluxional process shows the internal C=C environment is present in all coordinated *iso*butene intermediates within the process. This can be observed in the 298 K solution ^{13}C{^{1}H} NMR spectrum, which shows only one alkene-assigned signal at δ 111. At 183 K however, two resonances assigned to alkene environments [δ 112, 72] are observed. The signal at δ 72 is assigned to the now static terminal C=C environment within *iso*butene.

The same fluxional process is also observed in the solid-state, as shown by the variable temperature ^{13}C{^{1}H} SSNMR spectra of **[1-*iso*butene][BAr$^F_4$]** (Figure 2.11). As in solution, at 294 K, only one signal in an alkene environment is observed [δ 112] and upon cooling to 158 K, two resonances [δ 111, 73] appear. Unfortunately, a signal relating to the ^{13}C involved in the agostic interaction could not be identified. This would likely appear at δ ~5, consistent with that of **[1-propene][BAr$^F_4$]**.[4] Nevertheless, the solid-state ^{13}C{^{1}H} SSNMR spectra are consistent with this solution fluxional process, and so the fluxional behaviour of *iso*butene occurs in both the solution phase and solid-state.

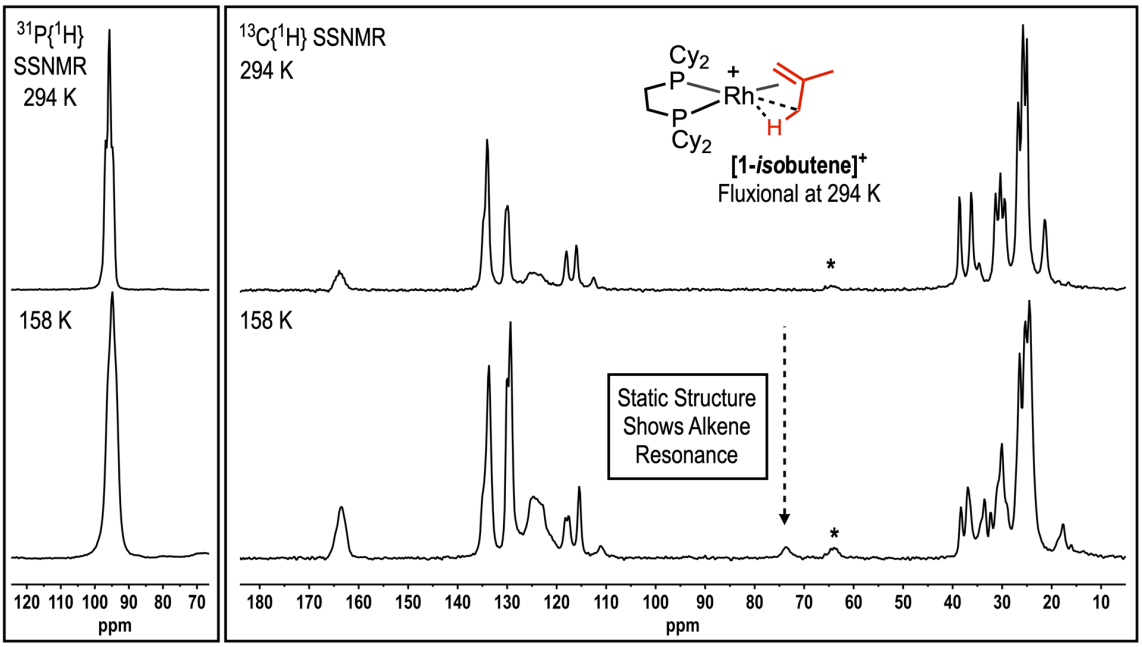

Figure 2.11: The $^{31}P\{^{1}H\}$ and $^{13}C\{^{1}H\}$ SSNMR (162 / 101 MHz, 10 kHz spin rate) spectra of **[1-*iso*butene][BAr$^{F}_{4}$]** at 294 K and 158 K. * = spinning sidebands.

Unlike in solution however, the $^{31}P\{^{1}H\}$ SSNMR spectra did not vary significantly upon cooling (Figure 2.11). The 294 K spectrum shows an apparent triplet at δ 95, assigned to two, almost, coincident ^{31}P environments in the solid-state. At 158 K, these signals only appear to broaden, which meant an Eyring plot could not be constructed from this data.

2.3.2. The Hydrogenation of [1-*iso*butene][BAr^F_4] in the Solid-State

2.3.2.1. Experimental Analysis

With **[1-*iso*butene][BAr^F_4]** in hand, attempts to isolate a σ-*iso*butane complex by single-crystal x-ray diffraction were conducted at the University of Oxford. As the crystals of recrystalised **[1-*iso*butene][BAr^F_4]** were of good quality, these SC-SC hydrogenation experiments did not require synchrotron radiation. The procedure for this is outlined below.

When orange crystals of **[1-*iso*butene][BAr^F_4]** were placed under an atmosphere of H_2 for 10 minutes (1 bar, 298 K), the crystals turned plum-red in colour (Figure 2.12b). The crystalline material was then coated with Fomblin® Y oil under an argon-flush and a suitable crystal was rapidly selected, mounted and transferred to the cryostream (set at 150 K) of a diffractometer and an x-ray diffraction study was undertaken. The resulting solid-state structure of [Rh($Cy_2PCH_2CH_2PCy_2$)(*iso*-C_4H_{10})][BAr^F_4], **[1-*iso*butane][BAr^F_4]** is shown in Figure 2.12c.

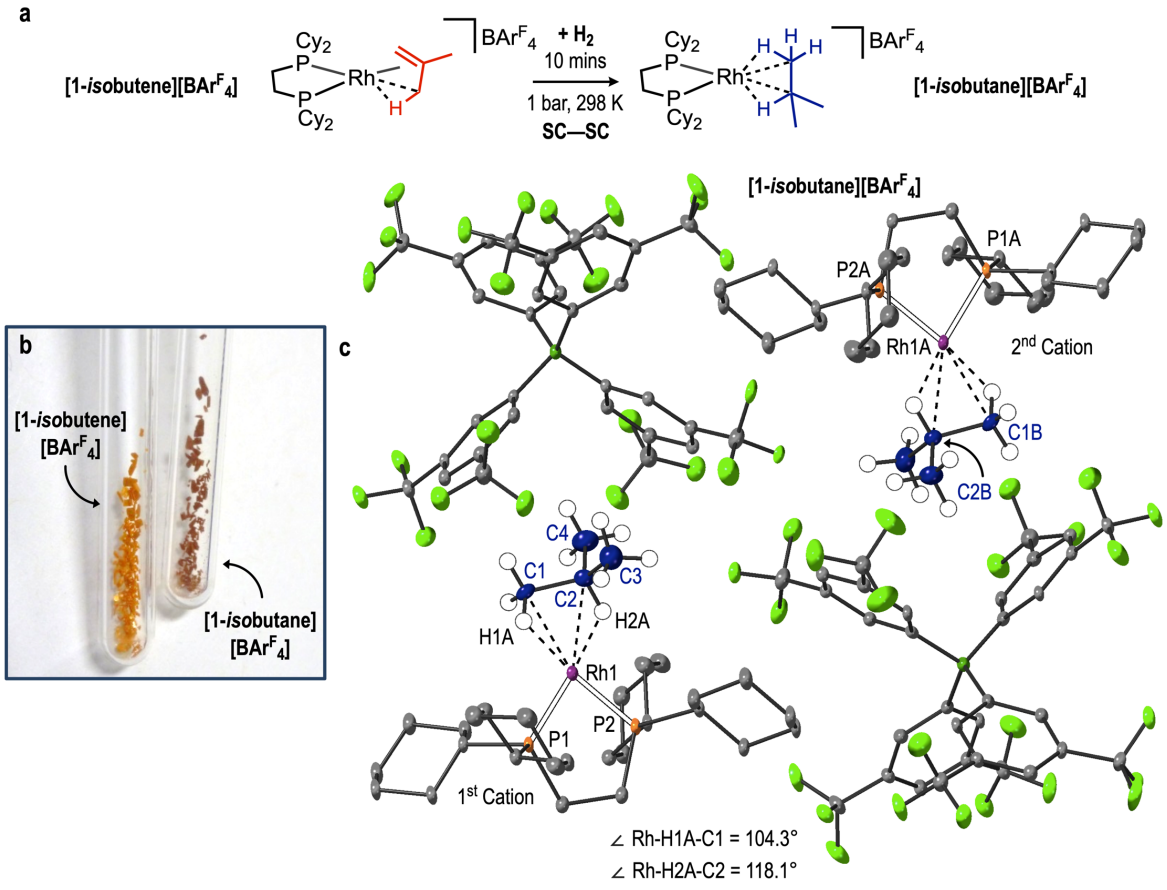

Figure 2.12: a) The synthetic procedure towards **[1-*iso*butane][BAr^F_4]**. **b**) Images of typical crystals of **[1-*iso*butene][BAr^F_4]** and **[1-*iso*butane][BAr^F_4]**. **c**) The solid-state structure of **[1-*iso*butane][BAr^F_4]**, showing all atoms in the asymmetric unit. Hydrogen atoms on phosphine ligand and $[BAr^F_4]^-$ anion excluded for clarity and displacement ellipsoids set at 30 %.

The *iso*butane ligand in **[1-*iso*butane][BAr$^{F}_{4}$]** exhibits a 1,2-coordination mode, interacting through adjacent -methyl and -methine C–H environments. Selected crystallographic metrics are given in Table 2.3, which follow the comparative trends previously outlined for the reaction of **[1-NBD][BAr$^{F}_{4}$]** to **[1-NBA][BAr$^{F}_{4}$]**.[1] Minimal disorder was found within the *iso*butane ligand in crystal structure, only slight rotations (~ 20°) around the -methine carbon producing chemical equivalent fragments. The structure collected shows that **[1-*iso*butane][BAr$^{F}_{4}$]** retained the pseudo-O_h framework of [BAr$^{F}_{4}$]$^{-}$ anions found in **[1-*iso*butane][BAr$^{F}_{4}$]**.

The 3c–2e^{-} coordinating nature of *iso*butane, compared to *iso*butene, is shown by the increased Rh•••C distances upon hydrogenation, consistent with a weaker bonding interaction. These distances are comparable to the sum of the covalent radii of Rh and C (2.18 Å),[17] suggesting a significant bonding interaction, unlike those in Complex **[x]** (Chapter 1, Section 1.3.5.).[18] Both coordinating *iso*butane interactions are labelled as η^2- from the relatively acute Rh•••H–C angles (104.3° and 118.1°) and relatively short Rh•••C distances (2.362(14) and 2.442(7) Å). This is returned to in Section 2.3.2.2.

The Rh–P distances have contracted, suggesting *iso*butane is a weaker *trans* influence ligand than that of *iso*butene. The elongation of the C1–C2 distance (1.320(12) to 1.551(13) Å respectively) shows the complete hydrogenation of *iso*butene to *iso*butane. The decrease in sum of C–C–C angles around this methine carbon of **[1-*iso*butane][BAr$^{F}_{4}$]** (C2 in both structures, 360° to 335.1°) shows the change from sp^2 to sp^3 hybridization upon alkene hydrogenation.

Table 2.3: Selected crystallographic information of **[1-*iso*butene][BAr$^{F}_{4}$]** and **[1-*iso*butane][BAr$^{F}_{4}$]**.

	Rh–P1 / Rh–P2 (Å)	Rh–C1 / Rh–C2 (Å)	C1–C2 / C2–C3 (Å)	Unit Cell Volume (Å^3) / Space Group
[1-*iso*butene] [BAr$^{F}_{4}$]	2.2238(9) / 2.2400(9)	2.262(6) / 2.136(8)	1.320(12) / 1.474(13)	3267.70(13) / P–1
[1-*iso*butane] [BAr$^{F}_{4}$] – 1st Cation	2.1830(14) / 2.1914(14)	2.362(14) / 2.442(7)	1.551(13) / 1.528(13)	12958.3(3) / P2$_1$/n
[1-*iso*butane] [BAr$^{F}_{4}$] – 2nd Cation (Rh1A, CXA, PXA)	2.1841(14) / 2.1887(15)	2.390(4) / 2.438(8)	1.544(16) / 1.500(19)	

A reduction in symmetry upon hydrogenation was accompanied by a space group change ($P2_1/n$ to P–1) such that two independent molecules in the unit cell were present. No significant difference in structural coordination or bond metrics (Table 2.3) is observed between these two crystallographically independent cations, which are arbitrarily assigned the 1st and 2nd Cation.

Bulk analysis of **[1-*iso*butane][BAr$^F_4$]** was performed by SSNMR spectroscopy, where the $^{13}C\{^1H\}$ spectrum collected exhibited no signals relating to alkene groups (δ 70 – 100), suggestive of complete *iso*butene hydrogenation (Figure 2.13). The Rh•••H–C interaction was revealed in the $^1H/^{13}C$ FSLG-HETCOR spectrum, which showed a cross-peak between the ^{13}C environment at δ 21 and ^1H environment at δ –3.4. These signals are consistent with ^1H nuclei in agostic-like environments and ^{13}C nuclei in aliphatic regions,[19] and are assigned to the coordinating C–H environments within the *iso*butane ligand.

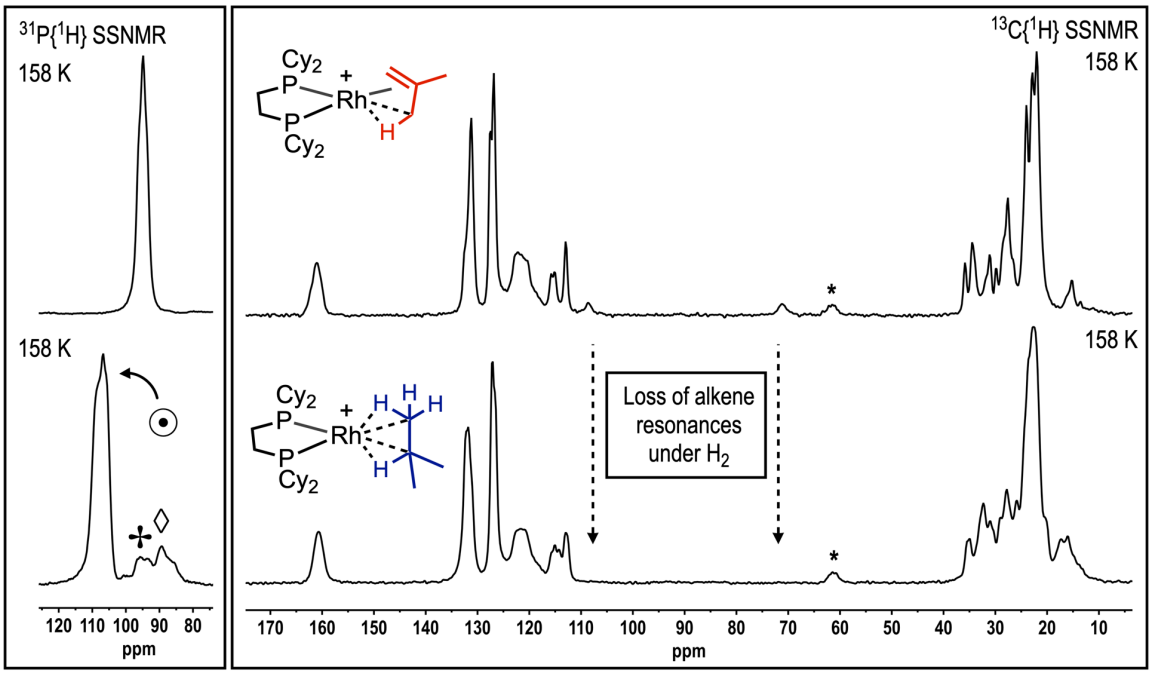

Figure 2.13: The $^{31}P\{^1H\}$ and $^{13}C\{^1H\}$ SSNMR (162 / 101 MHz, 10 kHz spin rate, 158 K) spectra of **[1-*iso*butene][BAr$^F_4$]** and **[1-*iso*butane][BAr$^F_4$]**. ⦿ = **[1-*iso*butane][BAr$^F_4$]**, ◊ = **[1-BAr$^F_4$]**, ⊹ = **[1-*iso*butene][BAr$^F_4$]** and * = spinning sidebands.

The $^{31}P\{^1H\}$ SSNMR spectrum of **[1-*iso*butane][BAr$^F_4$]** at 158 K showed an apparent triplet from two, coincident ^{31}P environments at δ 106. This however is shifted downfield by 12 ppm compared to that of **[1-*iso*butene][BAr$^F_4$]**. Other signals include that of **[1-BAr$^F_4$]** [δ 91], from a minor decomposition of **[1-*iso*butane][BAr$^F_4$]** under an H_2 atmosphere for 15 minutes. As discussed in Section 2.2.2., elongated hydrogenation

times were required during *in situ* SSNMR spectroscopy experiments, compared to free-flowing crystals using in single-crystal x-ray diffraction experiments. This was optimised at 10 minutes for **[1-*iso*butane][BAr$^{F}_{4}$]**. A signal observed at δ 95 is assigned to **[1-*iso*butene][BAr$^{F}_{4}$]**. This **[1-*iso*butene][BAr$^{F}_{4}$]** impurity may be from the under hydrogenation of the sample, or from rapid dehydrogenation of **[1-*iso*butane][BAr$^{F}_{4}$]**. This idea of potential dehydrogenation of the *iso*butane, along with the overall stability of **[1-*iso*butane][BAr$^{F}_{4}$]** at 298 K, is explored further in Chapter 3.

2.3.2.2. Computational Analysis

The calculations presented in Section 2.3.2.2. were performed by Arron L. Burnage and Bengt E. Tegner from the Stuart A. Macgregor group (Heriot-Watt University, Edinburgh).

The bonding in **[1-*iso*butane][BAr$^{F}_{4}$]** was also confirmed by calculations, using QTAIM, NBO and NCI analyses. As **[1-*iso*butane][BAr$^{F}_{4}$]** contains two, crystallographically independent, cations within the unit cell, analyses were conducted on both. There was no significant difference between the two, and so only one is used for analysis. Additionally, both fully optimised and heavy atom fixed bond length calculations based upon the structure were in good agreement with the experimentally derived values.

a

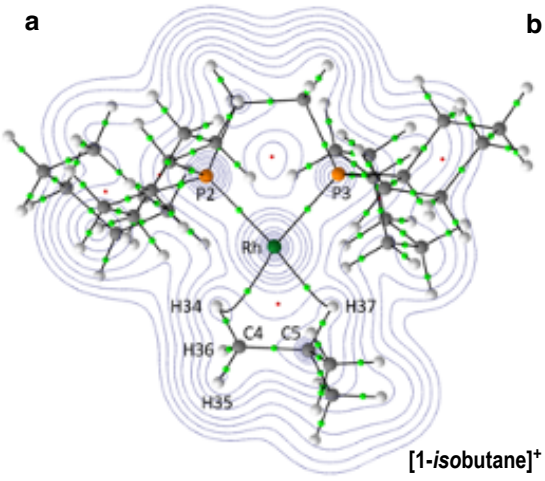

b

BCP	ρ (r)	$\nabla^2\rho$ (r)	H (r)
Rh•••H34	0.056	0.247	—0.004
Rh•••H37	0.060	0.241	—0.009
C4—H34	0.236	—0.643	—0.209
C4—H36	0.277	—0.953	—0.280
C5—H37	0.232	—0.601	—0.200

Figure 2.14: **a**) QTAIM contour plot of the electron density in **[1-*iso*butane]$^{+}$** cation, plotted in the Rh1-P2-P3 plane. Bond Critical Points (BCP) and Ring Critical Points (RCP) shown by green and red points respectively. **b**) Selected BCP metrics (au).

The QTAIM analysis of **[1-*iso*butane][BAr$^{F}_{4}$]** is shown in Figure 2.14a. The curved bond pathways and BCP are consistent with 3c–2e^{-} bonding and thus σ-alkane coordination through a η^2- Rh•••H–C interaction.[3] The NCI plot (Figure 2.15b) shows the significant stabilising interactions within the Rh•••H–C interaction, again consistent with the 3c–2e^{-} interaction.[20] This is shown by the area of blue electron density between Rh centre and C–H bonds. The large areas of green shown in the NCI plot of **[1-*iso*butane][BAr$^{F}_{4}$]** are assigned to weak, intermolecular dispersive interactions that are stabilising in nature.

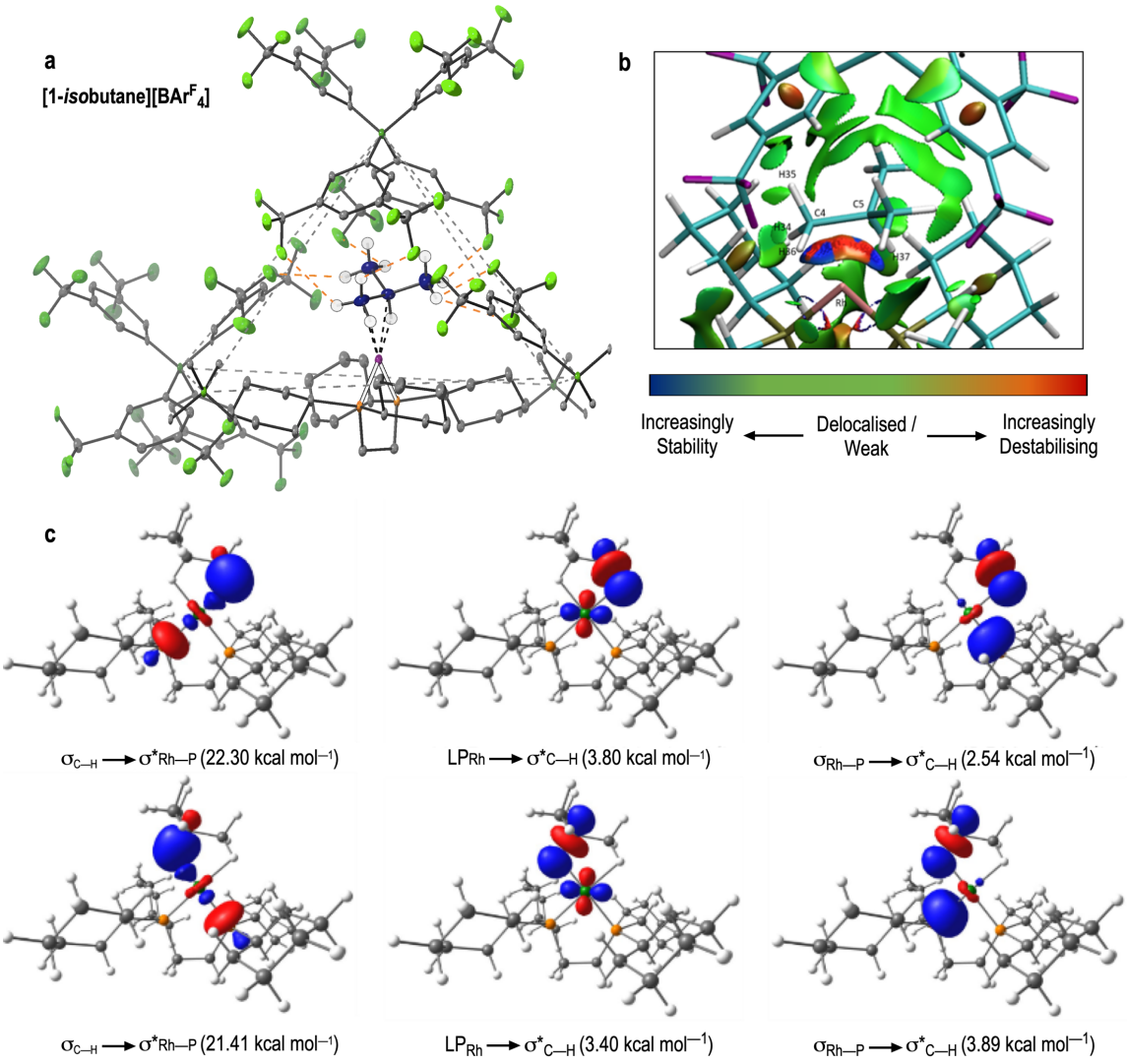

Figure 2.15: a) Solid-state structure of **[1-*iso*butane][BAr$^{F}_{4}$]**, showing part of the pseudo-O_h framework of [BAr$^{F}_{4}$]$^{-}$ anions encapsulating the cation. C–H•••F–C hydrogen bonding interactions in the range of 2.30-2.99 Å, highlighted by orange dashes. Hydrogen atoms on phosphine ligand and [BAr$^{F}_{4}$]$^{-}$ anion as well as -Ar$^{F}_{4}$ groups on selected B-atoms excluded for clarity. Displacement ellipsoids set at 30 %. **b**) NCI plot of detailed view of the Rh–*iso*butane coordination in the 1st cation of **[1-*iso*butane][BAr$^{F}_{4}$]**. Isosurfaces generated for s = 0.3 au and -0.07 < ρ < 0.07 au. **c**) NBO donor-acceptor pairs for the 1st cation of **[1-*iso*butane][BAr$^{F}_{4}$]** with NBO occupancies as indicated.

These forces are also noted as C–H•••F–C hydrogen bonding interactions (2.30-2.99 Å), between the *iso*butane ligand and the pseudo-O_h framework of $[BAr^F{}_4]^-$ anions, encapsulating the cation (Figure 2.15a). These forces are considered key in stabilising the alkane ligand within the solid-state cavity.

NBO calculations revealed that both methyl and methine *iso*butane coordination occurs *via* donation from $\sigma_{CH} \rightarrow$ *trans*-σ^*_{RhP} orbitals, with associated interaction energies of 22.30 and 21.41 kcal mol^{-1}, with total backbonding interactions calculated at 6.34 and 7.29 kcal mol^{-1} respectively, shown in Figure 2.15c. These are visualised by the electron density coloured blue between the Rh centre and C–H bonds in the NCI plot (Figure 2.15b) and are consistent with **[1-NBA][BAr$^F{}_4$]**, in which the dominant component of coordination was the σ_{CH} donation.

2.4. The Synthesis of a σ-*Iso*pentane Complex

2.4.1. A Precursor *Iso*pentadiene Complex

In a similar fashion to that of **[1-*iso*butane][BAr$^F_4$]** compared to **[1-propane][BAr$^F_4$]**, the synthesis of a branched analogue of **[1-butadiene][BAr$^F_4$]** was also targeted. This again was to increase dispersive interactions within the solid-state cavity of the corresponding σ-alkane complex, in the hope that the stability of the corresponding branched alkane complex might be improved compared to that of **[1-butane][BAr$^F_4$]**.

For this, the complex of 2-methylbutane (*iso*pentane) was proposed, where a suitable precursor diene complex came from the direct addition of 2-methyl-1,4-butadiene (*iso*pentadiene) to a solution of **[1-F$_2$C$_6$H$_4$][BAr$^F_4$]** in dichloromethane. The diene rapidly displaced the weakly coordinating difluorobenzene and forms [Rh(Cy$_2$PCH$_2$CH$_2$PCy$_2$)(*iso*-C$_5$H$_8$)][BAr$^F_4$], **[1-*iso*pentadiene][BAr$^F_4$]** (Figure 2.16a).

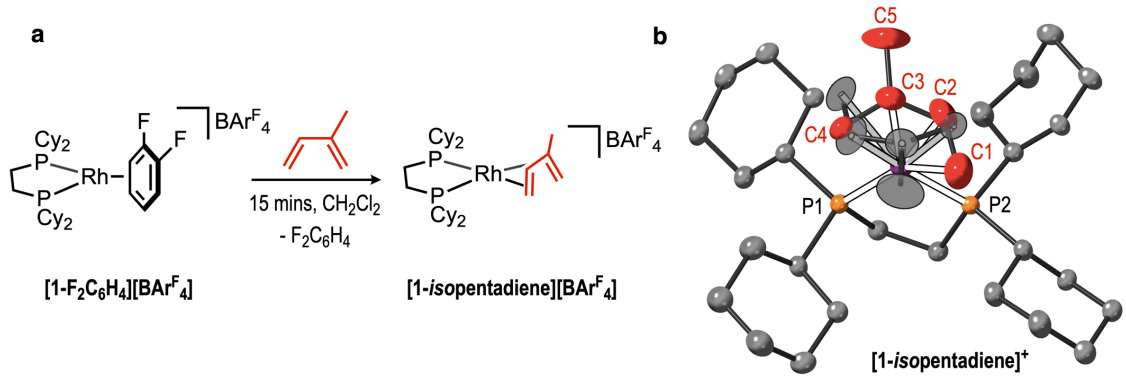

Figure 2.16: a) Synthetic route to **[1-*iso*pentadiene][BAr$^F_4$]** and **b**) **[1-*iso*pentadiene]$^+$** displaying major (red) and minor (grey) disorder components of *iso*pentadiene shown. Hydrogen atoms on phosphine ligand and [BAr$^F_4$]$^-$ excluded for clarity and displacement ellipsoids set at 30 %.

Dark red crystals of **[1-*iso*pentadiene][BAr$^F_4$]** of sufficient quality for single-crystal x-ray diffraction could be easily grown from a dichloromethane: pentane layering. The structure revealed two, non-crystallographically imposed disorder components of the *iso*pentadiene ligand within the solid-state structure, Figure 2.16b. Both of these are coordinated in an η^4-diene binding mode, related by a pseudo-C_2 axis, and are in 51: 49 population. The anion packing structure is that of a pseudo-O_h arrangement of [BAr$^F_4$]$^-$ anions, where the cation is directed towards a boron vertex.

These two crystallographically independent disorder components are also observed in the SSNMR spectra for **[1-*iso*pentadiene][BAr$^F_4$]**. In the ^{31}P{^{1}H} SSNMR spectra, four

resonances are observed, each coupled to ^{103}Rh [δ 86, J_{RhP} = 152 Hz; δ 75, J_{RhP} = 165 Hz and δ 81, J_{RhP} = 147 Hz; δ 74, J_{RhP} = 150 Hz] (Figure 2.17a). Each peak is assigned to one of the four chemically independent ^{31}P environments within the solid-state. These two sets however are crystallographically superimposed, so are indistinguishable within the solid-state structure.

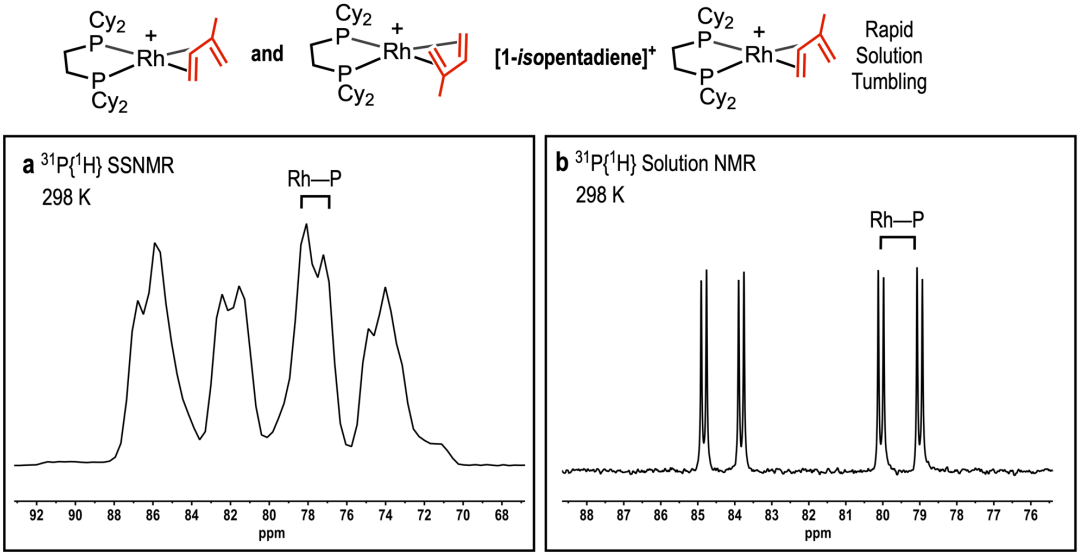

Figure 2.17: a) The ^{31}P{^{1}H} SSNMR (162 MHz, 10 kHz spin rate, 298 K) and **b**) solution ^{31}P{^{1}H} NMR (162 MHz, CD_2Cl_2, 298 K) spectra of **[1-*iso*pentadiene][BAr$^{F}_{4}$]**.

In solution however, this disorder is no longer present and only two ^{31}P environments are therefore observed, which reduces the number of signals by half. The 298 K solution ^{31}P{^{1}H} NMR spectrum shows these two resonances, which are doublets of doublets [δ 84, J_{RhP} = 163 Hz, J_{PP} = 23 Hz and δ 79, J_{RhP} = 169 Hz, J_{PP} = 23 Hz] (Figure 2.17b).

The ^{13}C{^{1}H} SSNMR spectrum shows eight signals within the alkene region [δ 120, 104, 103, 96, 94, 91, 88, 60], again consistent with two orientations of *iso*pentadiene in the solid-state, each with four ^{13}C alkene environments. Although the resonances at δ 100+ are perhaps a little high for alkene regions, they have been assigned given that they disappear upon hydrogenation of the sample (see Section 2.4.2.). Previous diene complexes of the same RhP_2^+ fragment also show alkene resonances in this region, for example **[1-pentadiene][BAr$^{F}_{4}$]**.[3] The solution ^{13}C{^{1}H} NMR spectra only reveals four alkene environments [δ 120, 101, 63, 32], consistent again with only a single isomer.

2.4.2. The Hydrogenation of [1-*iso*pentadiene][BAr$^{F}_{4}$] in the Solid-State

When cherry-red crystals of **[1-*iso*pentadiene][BAr$^{F}_{4}$]** were placed under an atmosphere of H_2 (25 minutes, 1 bar, 298 K), the crystals darkened to a plum-red colour. Following the same experimental procedure outlined in the structural determination of **[1-*iso*butane][BAr$^{F}_{4}$]**, the solid-state structure of [Rh($Cy_2PCH_2CH_2PCy_2$)(*iso*-C_5H_{12})][BAr$^{F}_{4}$], **[1-*iso*pentane][BAr$^{F}_{4}$]** was obtained by single-crystal x-ray diffraction (Figure 2.18b).

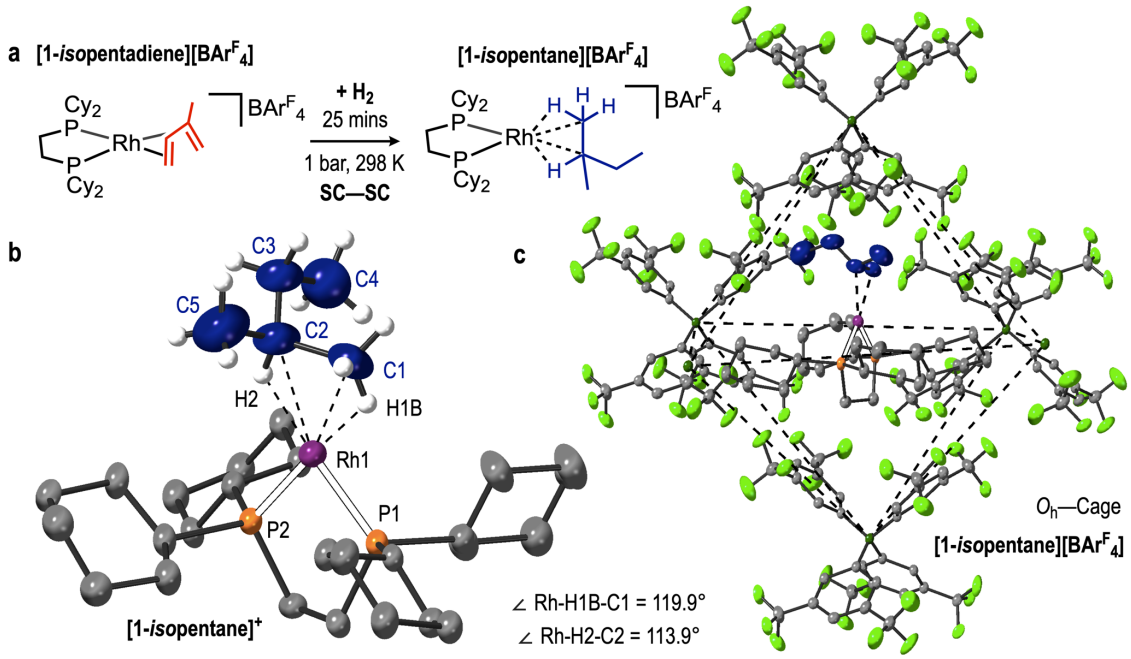

Figure 2.18: a) The formation of **[1-*iso*pentane][BAr$^{F}_{4}$]. b**) Cationic portion of **[1-*iso*pentane]$^{+}$** and **c**) O_h cage of [BAr$^{F}_{4}$]$^{-}$ anions in **[1-*iso*pentane][BAr$^{F}_{4}$]**. Hydrogen atoms on phosphine ligand and [BAr$^{F}_{4}$]$^{-}$ as well as -Ar$^{F}_{4}$ groups selected B atoms excluded for clarity. Displacement ellipsoids set at 30 % in both parts.

The solid-state structure of **[1-*iso*pentane][BAr$^{F}_{4}$]** exhibits many similarities to that of **[1-*iso*butane][BAr$^{F}_{4}$]** (Figure 2.12a). The *iso*pentane ligand is shown to coordinate in a 1,2-mode through adjacent -methyl and -methine C–H environments, like that of *iso*butane. Both these interactions are 3c–2e^{-} in nature, shown by the increased Rh••C distances compared to that of **[1-*iso*pentadiene][BAr$^{F}_{4}$]** (shown in Table 2.4). This is consistent with the weaker, 3c–2e^{-} nature of the alkane ligand. Both Rh•••H–C bonding interactions are suggested to be η^2- from the relatively acute Rh•••H–C angles (119.9° and 113.9°) and relatively short Rh•••C distances (1.335(12) / 1.422(14) Å). Like **[1-propane][BAr$^{F}_{4}$]**, as the hydrogen atoms involved are only geometrically placed, in the absences of computational studies these are only suggested as η^2-interactions.

Table 2.4: Selected crystallographic data of **[1-*iso*pentadiene][BAr$^{F}_{4}$]** and **[1-*iso*pentane][BAr$^{F}_{4}$]**.

	Rh–P1 / Rh–P2 (Å)	Rh–C1 / Rh–C2 (Å)	C1–C2 / C3–C4 (Å)	Unit Cell Volume (Å^3) / Space Group
[1-*iso*pentadiene][BAr$^{F}_{4}$]	2.2814(9) / 2.2709(9)	2.259(17) / 2.166(8)	1.350(19) / 1.290(2)	3282.54(13) / P–1
[1-*iso*pentane][BAr$^{F}_{4}$]	2.1885(19) / 2.186(2)	2.335(12 / 2.422(14)	1.50(3) / 1.520(3)	3307.52(5) / P–1

The lengthening of the C1–C2 and C3–C4 distances (1.350(19) / 1.290(2) Å to 1.50(3) / 1.520(3) Å respectively) is consistent with the hydrogenation of the double bonds. A decrease in sum of C–C–C angles around the methine carbons (C3 in **[1-*iso*pentadiene][BAr$^{F}_{4}$]** and C2 in **[1-*iso*pentane][BAr$^{F}_{4}$]**, 360° to 326.5°) is also suggestive of this sp^2 to sp^3 hybridization change. The contraction of the Rh–P distances in **[1-*iso*pentane][BAr$^{F}_{4}$] (**2.1885(19) / 2.186(2) Å) *versus* **[1-*iso*pentadiene][BAr$^{F}_{4}$] (**2.2814(9) / 2.2709(9) Å) show the weaker *trans* influence of the *iso*pentane *versus* *iso*pentadiene ligand.

Previously reported *iso*pentane coordinated complexes, from the UV irradiation of Mn-carbonyl complexes in *iso*pentane solvent, showed no evidence for coordination of the tertiary C–H group (Complex **[v]**, Chapter 1, Section 1.3.1.).[21] This was proposed to be due to steric hindrance around this C–H bond. As this coordination is observed in **[1-*iso*pentane][BAr$^{F}_{4}$]**, this may highlight the influence of the surrounding solid-state environment.

The structure of **[1-*iso*pentane][BAr$^{F}_{4}$]** has also retained the pseudo-O_h arrangement of [BAr$^{F}_{4}$]$^-$ anions (Figure 2.18b), where the alkane ligand is sandwiched between two -Ar$^{F}_{4}$ arms of a neighbouring [BAr$^{F}_{4}$]$^-$ anion. An enlargement of the unit cell volume can be seen (~3280 to ~3310 Å^3, ~1 % increase). This is consistent with that of previously reported SC-SC transformations,[22] including previous solid-state σ-alkane complexes. This is likely due to the expanded volume of *iso*pentane *versus* *iso*pentadiene ligands. Unlike **[1-*iso*butane][BAr$^{F}_{4}$]**, this transformation does not incur a change in symmetry, where both structures are in P–1 space group and no disorder around this fragment could be modelled.

Additionally, the solid-state structure of **[1-*iso*pentadiene][BAr$^{F}_{4}$]** exhibits two, crystallographically independent orientations of the *iso*pentadiene ligand. In **[1-*iso*pentane][BAr$^{F}_{4}$]** however, only one orientation of *iso*pentane is observed. This is suggestive of a low energy rotation of the *iso*pentane ligand upon hydrogenation, which results in the thermodynamically favoured orientation (Scheme 2.5). Alternatively, these two orientations in **[1-*iso*pentadiene][BAr$^{F}_{4}$]** may also become equivalent if hydrogenation occurs stepwise, *via* a possible *iso*pentene intermediate.

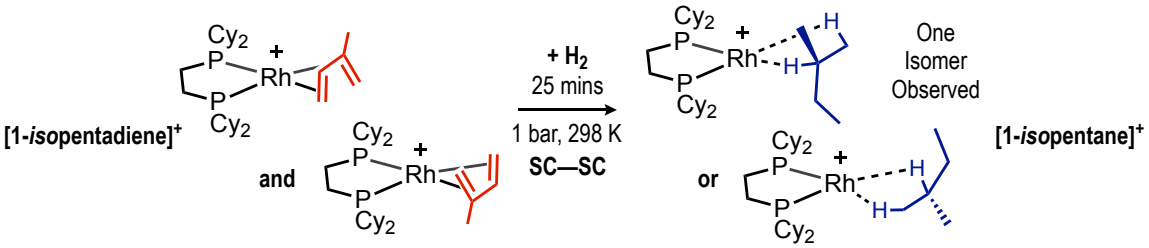

Scheme 2.5: Solid-state hydrogenation of the two *iso*pentadiene orientations present in **[1-*iso*pentadiene][BAr$^{F}_{4}$]**, and proposed rotation of the *iso*pentane ligand in **[1-*iso*pentane][BAr$^{F}_{4}$]**.

Bulk analysis of **[1-*iso*pentane][BAr$^{F}_{4}$]** was also undertaken. Following the SSNMR spectroscopy procedures outlined in Section 2.2.2., the $^{31}P\{^{1}H\}$ and $^{13}C\{^{1}H\}$ SSNMR spectra at 158 K of **[1-*iso*pentane][BAr$^{F}_{4}$]** are shown in Figure 2.19.

The $^{31}P\{^{1}H\}$ SSNMR spectrum shows two sets of doublets [δ 106, J_{RhP} = 204 Hz and δ 104, J_{RhP} = 220 Hz], shifted downfield by 15 ppm from that of **[1-*iso*pentadiene][BAr$^{F}_{4}$]**. These show Rh–P coupling constants which have increased compared to **[1-*iso*pentadiene][BAr$^{F}_{4}$]** (average of 153 and 212 Hz respectively), which is consistent with the weaker *trans*-influence of the *iso*pentane ligand. The $^{13}C\{^{1}H\}$ SSNMR spectrum at 158 K shows no signals within the alkene region (δ 70 – 100), suggestive of complete hydrogenation of the sample. Numerous signals that appear in the region of δ 5 – 25 are proposed to be from the new, aliphatic ^{13}C environments of the coordinated *iso*pentane ligand.

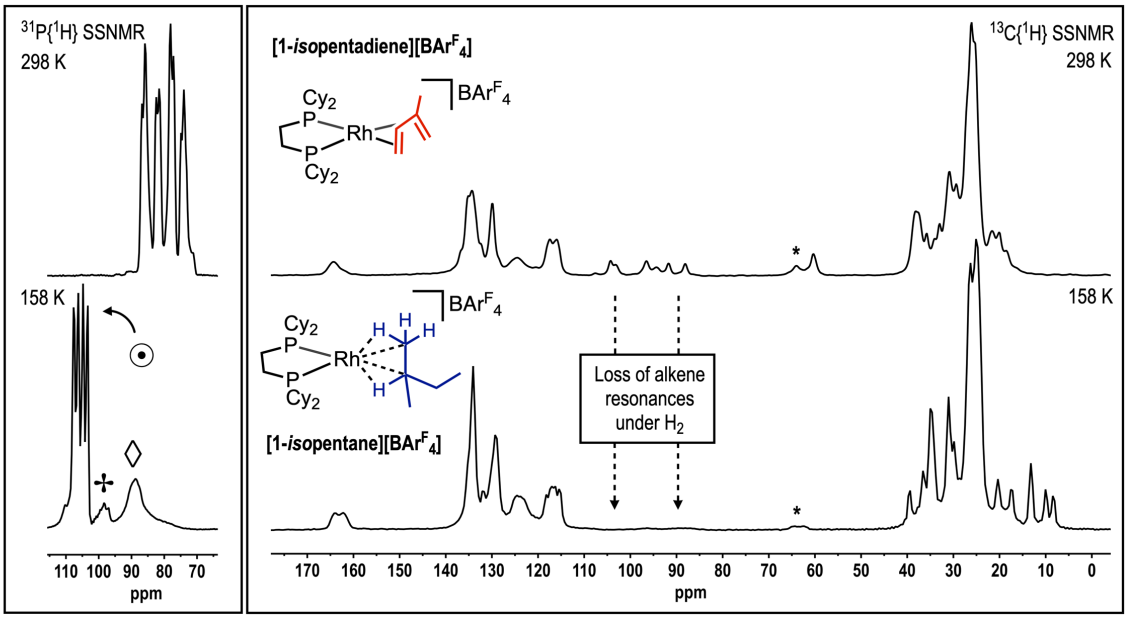

Figure 2.19: The $^{31}P\{^{1}H\}$ and $^{13}C\{^{1}H\}$ SSNMR (162 / 101 MHz, 10 kHz spin rate) spectra of **[1-*iso*pentadiene][BAr$^{F}_{4}$]** (298 K) and **[1-*iso*pentane][BAr$^{F}_{4}$]** (158 K). ⦿ = **[1-*iso*pentane][BAr$^{F}_{4}$]** ◊ = **[1-BAr$^{F}_{4}$]**. ✢ = **[1-*iso*pentene][BAr$^{F}_{4}$]**. * = spinning sidebands.

The signals assigned to **[1-*iso*pentane][BAr$^{F}_{4}$]** in the $^{31}P\{^{1}H\}$ SSNMR spectrum (labelled ⦿, Figure 2.19) are of relative intensity of ~75 %. Two other resonances can be clearly seen. The signal at δ 91 (labelled ◊, Figure 2.19) is assigned to **[1-BAr$^{F}_{4}$]**, proposed from the ~20 % decomposition of **[1-*iso*pentane][BAr$^{F}_{4}$]** during the relatively long hydrogenation time, optimised at 25 minutes for free-flowing crystals. This decomposition under a H_2 (or D_2) atmosphere is further explored in Chapter 4. The signals at δ 95 in ~5 % intensity (labelled ✢, Figure 2.19) is assigned to a dehydrogenation product from **[1-*iso*pentane][BAr$^{F}_{4}$]**. This product, along with the overall stability of **[1-*iso*pentane][BAr$^{F}_{4}$]** at 298 K, is discussed in Chapter 3.

2.5. The Synthesis of a Linear σ-Hexane Complex

2.5.1. A Precursor Linear Hexadiene Complex

To further increase the bulk of alkane ligand, a non-cyclic six-carbon alkane complex was targeted. To do this, a suitable alkene precursor had to be synthesised. In an analogous reaction to the formation of **[1-*iso*pentadiene][BAr$^F_4$]**, excess 1,5-hexadiene was added to a dichloromethane solution of **[1-F$_2$C$_6$H$_4$][BAr$^F_4$]** to form [Rh(Cy$_2$PCH$_2$CH$_2$PCy$_2$)(*n*-C$_6$H$_{10}$)][BAr$^F_4$], **[1-hexadiene][BAr$^F_4$]** (Scheme 2.6). This reaction occurred in quantitative yields, as shown by solution ^{31}P{^{1}H} NMR spectroscopy.

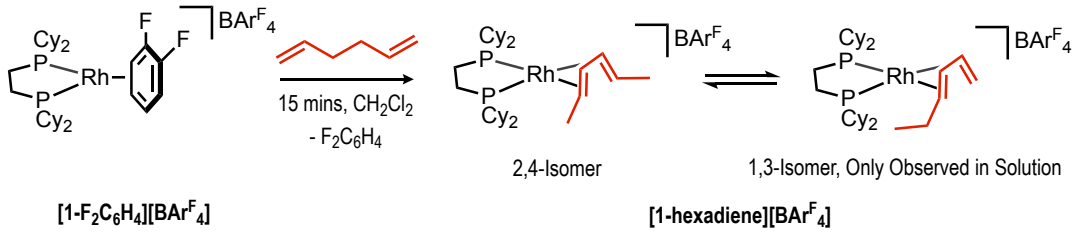

Scheme 2.6: The formation of **[1-hexadiene][BAr$^F_4$]**

The 1,5-hexadiene used in this synthesis is unconjugated which, after coordination, underwent rapid alkene isomerisation form the conjugated diene isomers. This type of diene isomerisation using late transition metals has been previously reported.[19-21]

For **[1-hexadiene][BAr$^F_4$]**, two sets of signals are observed in the solution ^{31}P{^{1}H} NMR spectrum, in ~50: 50 ratio. One of the isomers shows a single environment, and is assigned to the symmetrical 2,4-isomer, [δ 80, J_{RhP} = 179 Hz]. The second set of signals [δ 84, J_{RhP} = 174 Hz, J_{PP} = 22 Hz and δ 77, J_{RhP} = 171 Hz, J_{PP} = 22 Hz] is assigned to the 1,3-isomer as this shows two individual ^{31}P environments, coupled to ^{103}Rh and the each other. This produces the doublet of doublet pattern shown in Figure 2.20a. The two isomers of 2,4-hexadiene and 1,3-hexadiene are related by a simple isomerisation of, effectively, a diene chain walk. Multiple alkene environments are also present in the ^{1}H and ^{13}C{^{1}H} NMR spectra, consistent with this mixture.

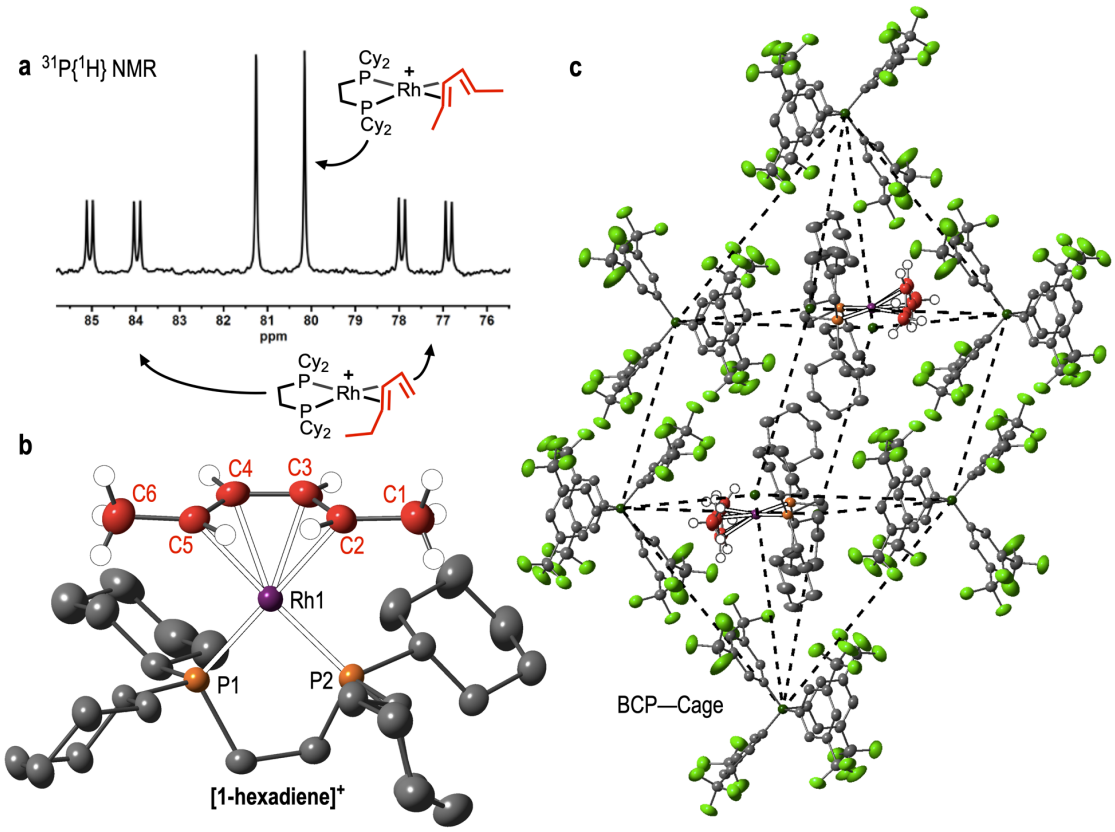

Figure 2.20: a) The $^{31}P\{^{1}H\}$ NMR (CD_2Cl_2, 298 K, 162 MHz) spectrum of **[1-hexadiene][BAr$^{F}_{4}$]**, showing chain walking isomers. **b**) Cationic portion of **[1-hexadiene][BAr$^{F}_{4}$]**. **c**) Bicapped-square pyramidal cage of $[BAr^{F}_{4}]^{-}$ anions. Hydrogen atoms on phosphine ligand and $[BAr^{F}_{4}]^{-}$ as well as -Ar^{F}_{4} groups on selected B-atoms excluded for clarity. Displacement ellipsoids set at 30 % in both parts.

Crystals of **[1-hexadiene][BAr$^{F}_{4}$]** of sufficient quality for single-crystal x-ray diffraction could be grown from a dichloromethane: pentane recrystallisation at 298 K. The only coordinated isomer of hexadiene observed in the solid-state is that of the 2,4-isomer (Figure 2.20b), showing this is favoured in the solid-state. This may be a direct result of the packing considerations dictated by the anion framework, which cannot support the 1,3-isomer. No evidence for any coordinated 1,3-isomer within the structure could be modelled, which suggests the hexadiene ligand is also static within the solid-state. Additionally, no pseudo-rotational disorder components of this 2,4-isomer was found. This is unlike the *iso*pentadiene ligand in **[1-*iso*pentadiene][BAr$^{F}_{4}$]** (Figure 2.16). The solid-state packing structure of **[1-hexadiene][BAr$^{F}_{4}$]** is of bicapped-square prism (BCP) arrangement of $[BAr^{F}_{4}]^{-}$ anions (Figure 2.20c) and is closely related to that of **[1-pentadiene][BAr$^{F}_{4}$]**.[3] These two cations within the anion cage are crystallographically

identical, yet the two ^{31}P environments of each cation are crystallographically independent.

The presence of a single isomer in a single orientation in the solid-state is also confirmed by $^{31}P\{^{1}H\}$ SSNMR spectroscopy. Only two sharp signals [δ 82, J_{RhP} = 189 Hz; δ 74, J_{RhP} = 182 Hz] were observed, from the two crystallographically independent ^{31}P environments. If two orientations or two isomers were present, four signals would be expected in the $^{31}P\{^{1}H\}$ SSNMR spectrum. The $^{13}C\{^{1}H\}$ SSNMR spectrum exhibits only three ^{13}C environments in the alkene region, consistent with the single isomer in a single orientation. Although four signals would be expected from the four alkene ^{13}C nuclei in **[1-hexadiene][BAr$^{F}_{4}$]**, the fourth alkene resonance is masked behind the $[BAr^{F}_{4}]^{-}$ environments at δ ~ 110. This resonance can be seen however in the solution $^{13}C\{^{1}H\}$ NMR spectrum [δ 108].

Upon the dissolution of crystalline **[1-hexadiene][BAr$^{F}_{4}$]** at 298 K in CD_2Cl_2, the initial solution $^{31}P\{^{1}H\}$ NMR spectra showed only signals related to that of the 2,4-isomer. After 2 hours equilibration however, the ~50: 50 ratio mixture of the two isomers had formed. This confirms the two species are in equilibrium with each other in the solution-phase. No change in $^{31}P\{^{1}H\}$ spectrum was observed upon cooling to 183 K or heating to 345 K within an hour, suggestive of a slow equilibrium process between the two, or that they are very similar in free energy without the imposition of the solid-state microenvironment.

2.5.2. The Hydrogenation of [1-hexadiene][BAr$^{F}_{4}$] in the Solid-State

Cherry-red, single crystals of **[1-hexadiene][BAr$^{F}_{4}$]** were placed under an atmosphere of H_2 (10 minutes, 1 bar, 298 K) to form plum-red coloured crystals of [Rh($Cy_2PCH_2CH_2PCy_2$)(*n*-C_6H_{14})][BAr$^{F}_{4}$], **[1-hexane][BAr$^{F}_{4}$]** in a SC-SC reaction (Figure 2.21). This was confirmed by a single-crystal x-ray diffraction experiment, which followed the same experimental procedure as for the structure determination of **[1-*iso*butane][BAr$^{F}_{4}$]** by single-crystal x-ray diffraction.

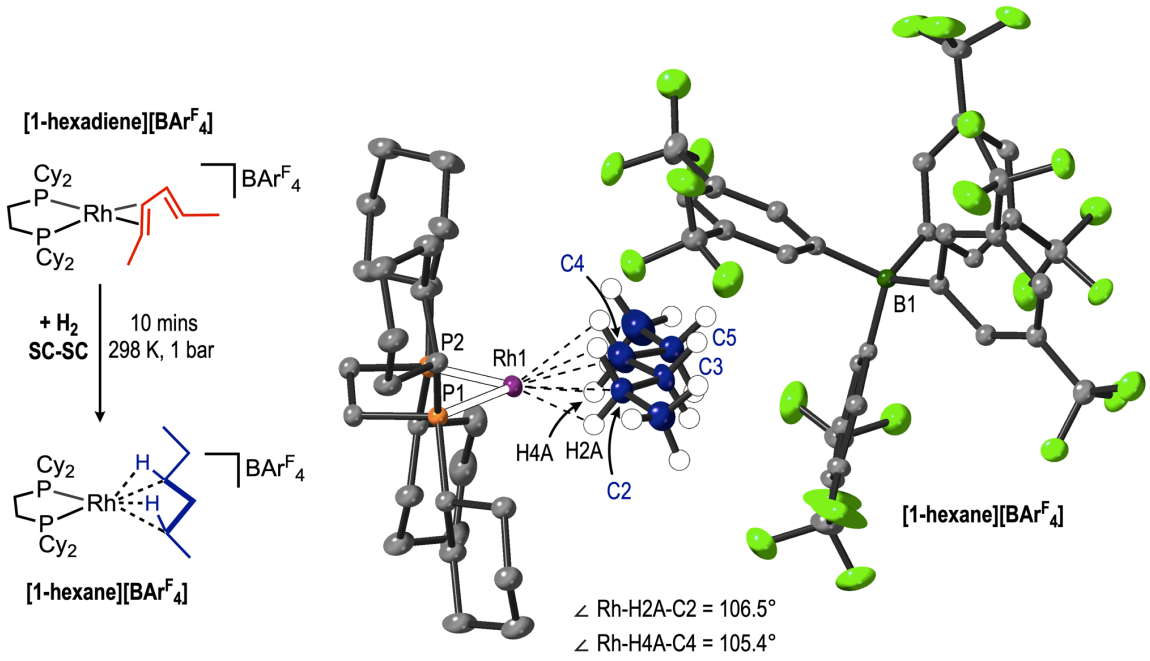

Figure 2.21: The solid-state structure of **[1-hexane][BAr$^{F}_{4}$]**. Hydrogen atoms on phosphine ligand and [BAr$^{F}_{4}$]$^{-}$ anion excluded for clarity. Displacement ellipsoids set at 30 % in both parts.

[1-hexane][BAr$^{F}_{4}$] remains in the BCP arrangement of [BAr$^{F}_{4}$]$^{-}$ anions and exhibits a 1,3-cordination of two methylene C–H environments on the hexane fragment. This is essentially isostructural to that of **[1-pentane][BAr$^{F}_{4}$]**.[3] The elongated Rh•••C distances, compared to that of **[1-hexadiene][BAr$^{F}_{4}$]**, are consistent with the weaker nature of the 3c–2e^{-} interactions of the hexane ligand. These bonding interactions are again suggested to be η^2- from the relatively acute Rh•••H–C angles (106.5° and 105.4°) and relatively short Rh•••C distances (2.527(3) / 2.546(4) Å). Like **[1-*iso*pentane][BAr$^{F}_{4}$]**, as the hydrogen atoms involved are only geometrically placed, in the absence of computational studies, these are only suggested as η^2-interactions.

Further selected bond metrics are shown in Table 2.5, which follow the same trends as previous σ-alkane complexes.[1,3] The Rh–P distances have contracted compared to **[1-hexadiene][BAr$^{F}_{4}$]** (2.2002(6) / 2.1910(6) Å from 2.2755(9) / 2.2689(6) Å respectively), showing hexane is a weaker *trans* influence ligand than that of hexadiene. The elongation of the C2–C3 and C4–C5 distances (1.356(4) / 1.352(5) Å to 1.511(5) / 1.528(6) Å respectively) reflects the complete hydrogenation of hexadiene to hexane. A minor disorder component of **[1-hexane][BAr$^{F}_{4}$]** is of an ethyl-group rotation of the C4 and C5 nuclei, disordered over two positions.

Table 2.5: Selected crystallographic information of **[1-hexadiene][BAr$^{F}_{4}$]** and **[1-hexane][BAr$^{F}_{4}$]**.

	Rh–P1 / Rh–P2 (Å)	Rh–C1 / Rh–C2 (Å)	C2–C3 / C4–C5 (Å)	Unit Cell Volume (Å^3) / Space Group
[1-hexadiene] [BAr$^{F}_{4}$]	2.2755(9) / 2.2689(6)	2.328(3) / 2.184(3)	1.356(4) / 1.352(5)	3273.92(16) / P–1
[1-hexane] [BAr$^{F}_{4}$]	2.2002(6) / 2.1910(6)	2.527(3) / 2.546(4)	1.511(5) / 1.528(6)	3322.42(10) / P–1

This solid-state transformation was also followed by SSNMR spectroscopy, following the same procedure outline for *in situ* SSNMR spectroscopy experiments detailed in Section 2.2.2. The resulting spectra are shown in Figure 2.22.

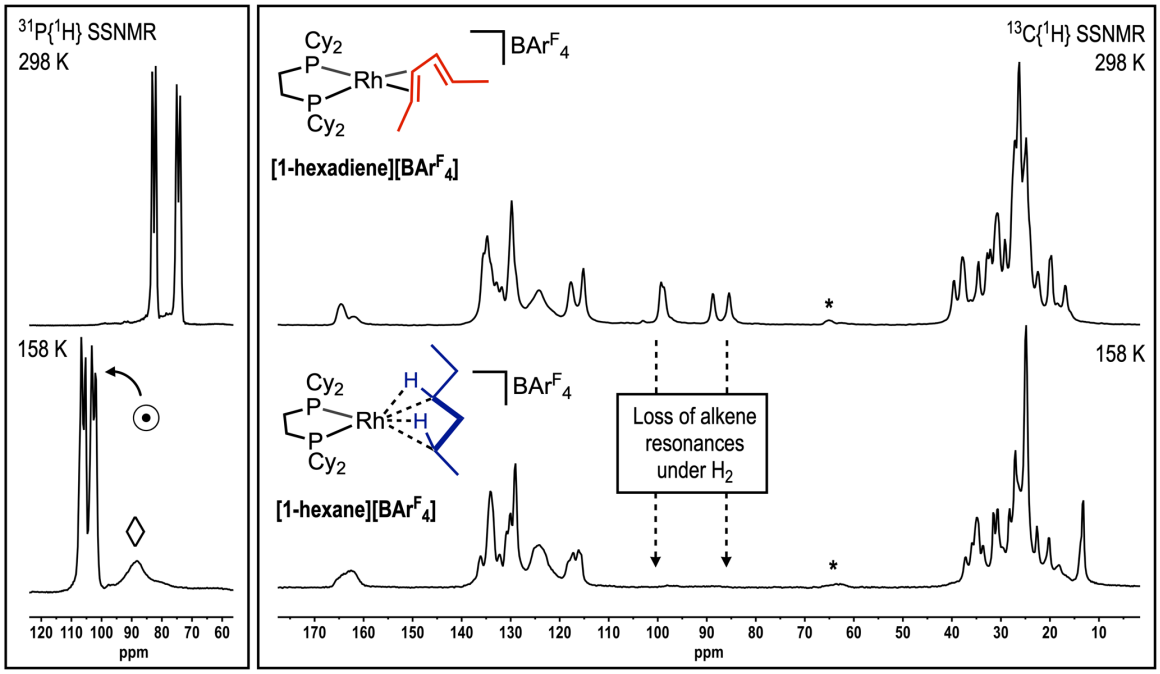

Figure 2.22: The $^{31}P\{^{1}H\}$ and $^{13}C\{^{1}H\}$ SSNMR (162 / 101 MHz, 10 kHz spin rate) spectra of **[1-hexadiene][BAr$^{F}_{4}$]** (298 K) and **[1-hexane][BAr$^{F}_{4}$]** (158 K). ◉ = **[1-hexane][BAr$^{F}_{4}$]** ◊ = **[1-BAr$^{F}_{4}$]**. * = spinning sidebands.

The $^{31}P\{^{1}H\}$ SSNMR spectrum of **[1-hexadiene][BAr$^{F}_{4}$]** exhibits two sets of doublets, which shift downfield in **[1-hexane][BAr$^{F}_{4}$]** [δ 106, J_{RhP} = 211 Hz and 102, J_{RhP} = 217 Hz], and is consistent with previous alkene to alkane complex transformations.[1,3] The increased value of the $^{103}Rh–^{31}P$ coupling constant is due to weaker *trans* influence of the Rh•••H–C interactions from the hexane ligand, compared to that of Rh–C=C interaction in **[1-hexadiene][BAr$^{F}_{4}$]**. **[1-hexane][BAr$^{F}_{4}$]** is observed in ~85% spectroscopic yield, where the remaining ~15 % of the signals are assigned to the decomposition product of **[1-BAr$^{F}_{4}$]**. The complete hydrogenation of the diene is confirmed by the removal of all resonances in the alkene region [δ ~ 70 – 110] of the $^{13}C\{^{1}H\}$ SSNMR spectrum, shown in Figure 2.22. A new signal [δ 10] is tentatively assigned to that of the new aliphatic ^{13}C environments of hexane.

2.5.3. Stability of [1-hexane][BAr$^F_4$] in the Solid-State

The solid-state stability of **[1-hexane][BAr$^F_4$]** was also explored, in an analogous experimental fashion to that of **[1-propane][BAr$^F_4$]** and **[1-butane][BAr$^F_4$]** described in Section 2.2.4. As determined by *in situ* SSNMR spectroscopy studies, **[1-hexane][BAr$^F_4$]** was found to be stable for less than 60 minutes at 298 K, before complete decomposition to **[1-BAr$^F_4$]** [δ 91]. No signals that could be assigned to any dehydrogenation products of **[1-hexane][BAr$^F_4$]** (for example, a hexene-coordinated complex) could be located.

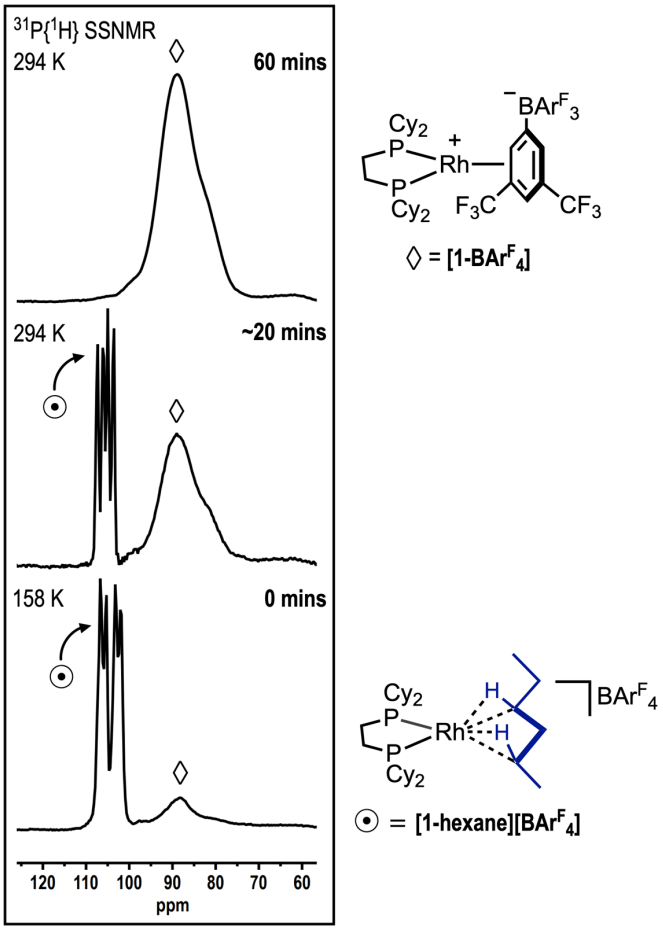

Figure 2.23: The $^{31}P\{^1H\}$ SSNMR (162 MHz, 10 kHz spin rate) spectrum of **[1-hexane][BAr$^F_4$]** decomposition over 60 minutes. ~20 minutes includes instrument warming, stabilisation and experimental collection. Signals assigned ⊙ = **[1-hexane][BAr$^F_4$]** and ◊ = **[1-BAr$^F_4$]**.

2.6. The Synthesis of a Branched, σ-Hexane Complex

2.6.1. A Precursor Branched Pentadiene Complex

The branched six-carbon alkane complex of 3-methylpentane was further targeted, again to see if the increased bulk altered the stability and reactivity of the corresponding σ-alkane complex. To synthesise a suitable precursor for this, excess 3-methyl-1,5-pentadiene was added to a pale-yellow dichloromethane solution of **[1-$F_2C_6H_4$][BAr^F_4]**, which immediately turned a deep red colour. This quantitatively yielded [Rh($Cy_2PCH_2CH_2PCy_2$)(C_6H_{10})][BAr^F_4], **[1-(C_6-dienes)][BAr^F_4]**, shown in Scheme 2.7. Unconjugated to conjugated diene isomerisation is again noted in this reaction.[23–25]

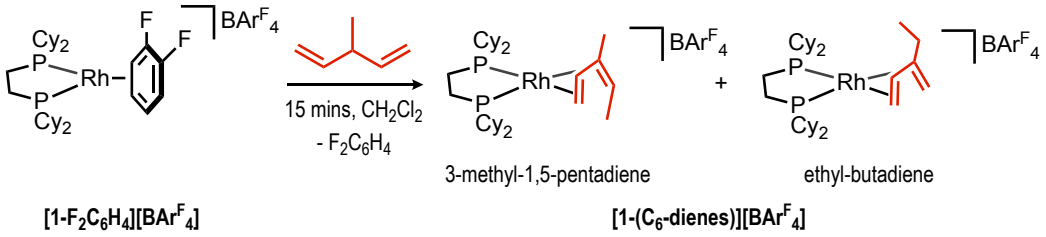

Scheme 2.7: The formation of **[1-(C_6-dienes)][BAr^F_4]**.

The solution $^{31}P\{^1H\}$ NMR spectrum of this reaction shows two sets of doublet of doublets [δ 85, J_{RhP} = 171 Hz, J_{PP} = 23 Hz; δ 79, J_{RhP} = 169 Hz, J_{PP} = 23 Hz and δ 84, J_{RhP} = 172 Hz, J_{PP} = 24 Hz; δ 75, J_{RhP} = 163 Hz, J_{PP} = 24 Hz], with ratio of ~ 50: 50 (Figure 2.24a). This suggests the presence of two coordinated isomers of C_6H_{10}. No change in $^{31}P\{^1H\}$ spectrum was observed upon cooling to 183 K or heating to 345 K within an hour. Because of this, it is unclear whether these isomers are in an equilibrium with each other or are static isomers.

Recrystallisation of **[1-(C_6-dienes)][BAr^F_4]** from a dichloromethane: pentane layering formed crystals of sufficient quality for single-crystal x-ray diffraction. The solid-state structure confirmed that two isomers of C_6H_{10} were coordinating to the rhodium centre and had co-crystalised together. These isomers were of (*Z*)-3-methyl-1,3-pentadiene and ethyl-butadiene. As these isomers could not be isolated from each other, the name **[1-(C_6-dienes)][BAr^F_4]** refers to the mixture of these complex isomers throughout this thesis.

The solid-state structure was modelled showing these isomers as two, non-crystallographically related disorder components of one another, in a ratio of 50: 50 (Figure 2.24b and c). The in-space orientation of both isomers is in the same direction, as

these disorder components sit on top of one another, and are not related by a pseudo-C_2 rotation. This is unlike the disorder of *iso*pentadiene in **[1-*iso*pentadiene][BAr$^F_4$]**, shown in Figure 2.16. Furthermore, **[1-(C$_6$-dienes)][BAr$^F_4$]** was found to have crystallised in a pseudo-O_h arrangement of [BAr$^F_4$]$^-$ anions, rather than the BCP arrangement seen in the isomeric **[1-hexadiene][BAr$^F_4$]**.

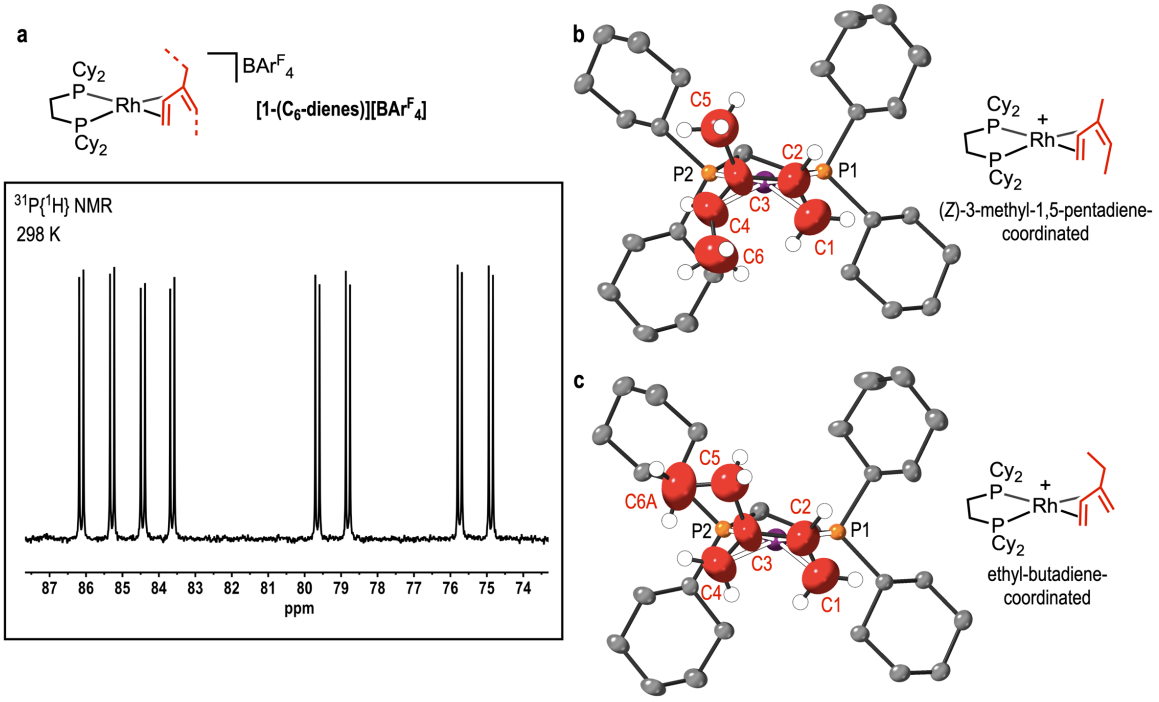

Figure 2.24: a) $^{31}P\{^1H\}$ NMR (CD_2Cl_2, 298 K, 162 MHz) spectrum of **[1-(C$_6$-dienes)][BAr$^F_4$]**. The solid-state structure showing the cationic portion of **b**) the (*Z*)-3-methyl-1,3-pentadiene and **c**) ethyl-butadiene coordinated isomers of **[1-(C$_6$-dienes)][BAr$^F_4$]**. Hydrogen atoms on phosphine ligand and [BAr$^F_4$]$^-$ anion excluded for clarity. Displacement ellipsoids set at 30 % in both parts.

The $^{31}P\{^1H\}$ SSNMR spectrum of **[1-(C$_6$-dienes)][BAr$^F_4$]** shows three, broad signals [δ 86, 79, 73] where the approximate integration is 2: 1: 1, see Figure 2.25b. This is from the two signals in solution [δ 85, 84] becoming coincident in the solid-state at δ 86, and hence the relative integration of ~2 of this signal in the $^{31}P\{^1H\}$ SSNMR spectrum. This also confirms the mixture of isomers spectroscopically. The broad nature of these signals, as well as the absence of any observable ^{103}Rh–^{31}P coupling, may suggest an array of very similar overlapping ^{31}P environments in the solid-state.

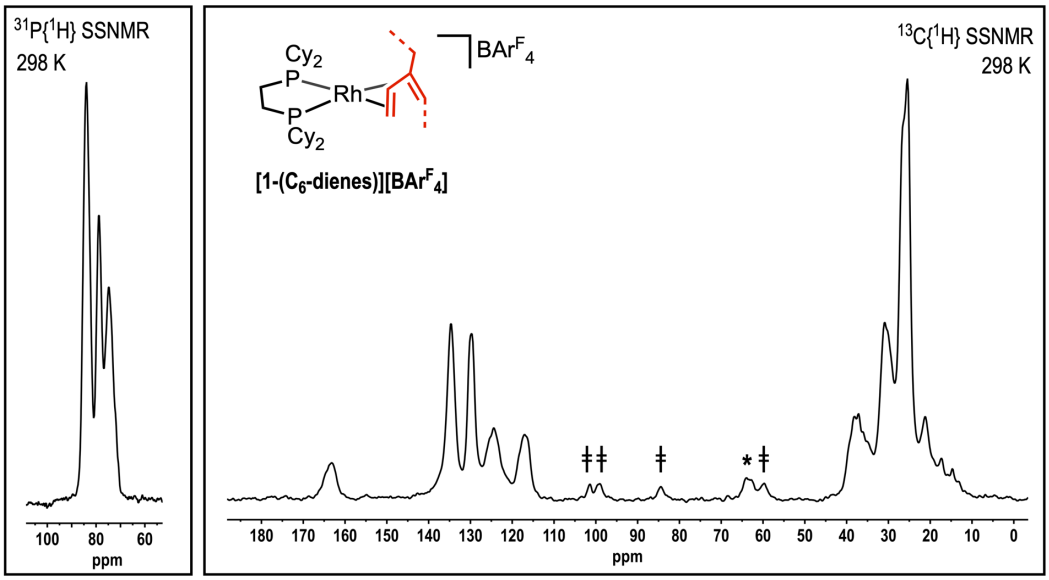

Figure 2.25: The $^{31}P\{^{1}H\}$ and $^{13}C\{^{1}H\}$ SSNMR (162 / 101 MHz, 298 K, 10 kHz spin rate) spectra of **[1-(C_6-dienes)][BAr^F_4]**. Signals marked ‡ are assigned to ^{13}C alkene environments and * = spinning sidebands

The $^{13}C\{^{1}H\}$ SSNMR spectrum shows four, broad alkene ^{13}C environments [δ 101, 99, 84, 63]. As two isomers are present in the solid-state however, the spectra would be expected to have eight signals. On the other hand, the two isomers of 3-methylpentadiene are simple, chain-walked disorder components of one another. This may result in the solid-state ^{13}C environments being very similar, and the broad nature of these resonances may mask these overlapping signals. The solution $^{13}C\{^{1}H\}$ NMR spectrum shows the expected eight signals assigned to alkene environments [δ 125, 119, 99, 98, 86, 63, 62, 59], and the signals at δ 125 and 119 are most likely masked by the $[BAr^F_4]^-$ ^{13}C environments [δ ~ 140 – 115] in the solid-state.

To definitively prove that these two coordinated isomers are as assigned correctly, the organic fragments could be liberated and isolated from the complexes. Upon the dissolution of **[1-(C_6-dienes)][BAr^F_4]** in MeCN-d_3; the solvent displaces the diene fragments and forms the deuterated analogue of [$Rh(Cy_2PCH_2CH_2PCy_2)(MeCN)_2$][$BAr^F_4$], **[1-$(MeCN)_2$][$BAr^F_4$]**.[4] Trap-to-trap distillation of the liberated volatile components, and subsequent analysis by ^{1}H, $^{13}C\{^{1}H\}$, COSY and HSQC NMR spectroscopy, confirms the isomers are of (*Z*)-3-methyl-1,3-pentadiene[22] and ethyl-butadiene.[23]

This data is best displayed by the $^{13}C\{^1H\}$ NMR spectrum (Figure 2.26), as overlapping alkene resonances in the ^1H NMR spectrum makes definitive analysis difficult. Although a small amount of (*E*)-3-methyl-1,3-pentadiene is observed, no evidence could be seen for a complex of this by single-crystal x-ray diffraction or SSNMR spectroscopy. This may suggest that is a result of an isomerisation process during liberation, or that signals for the (*E*)-3-methyl-1,3-pentadiene coordinated complex are masked by the broad nature of the SSNMR spectra.

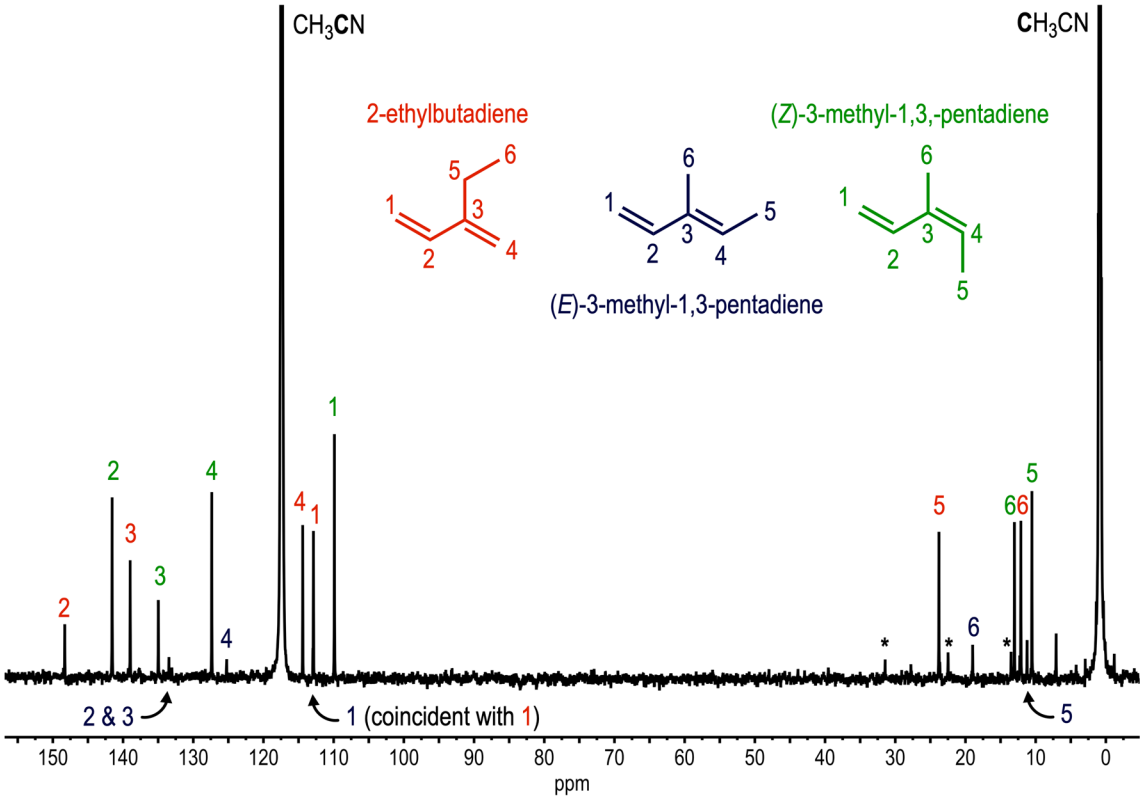

Figure 2.26: The solution $^{13}C\{^1H\}$ NMR (MeCN, 298 K, 126 MHz) spectrum of the isolated C_6-dienes. * = *n*-hexane impurity.

Importantly, the above procedure was repeated in a solid/gas reaction of **[1-(C_6-dienes)][BAr^F_4]** with CO. When placed under an atmosphere of CO (48 hours, 1 bar, 298 K), displacement of the coordinated organic diene occurs, resulting in the organometallic complex of [Rh($Cy_2PCH_2CH_2PCy_2$)$(CO)_2$][BAr^F_4], **[1-$(CO)_2$][BAr^F_4]**.[4] The liberated volatiles can then be isolated by trap-to-trap distillation into CD_2Cl_2 solvent and analysed by $^{13}C\{^1H\}$ NMR spectroscopy. No significant difference in spectra obtained spectra between the two methods was seen.

2.6.2. The Hydrogenation of [1-(C_6-dienes)][BAr^F_4] in the Solid-State

When cherry-red, single crystals of **[1-(C_6-dienes)][BAr^F_4]** were placed under an atmosphere of H_2 (15 minutes, 1 bar, 298 K), the crystals turned a plum-red in colour. A suitable crystal was selected, and rapidly transferred to the diffractometer, to which the solid-state structure of [Rh($Cy_2PCH_2CH_2PCy_2$)(C_6H_{14})][BAr^F_4], **[1-(3-methylpentane)][BAr^F_4]** was obtained by single-crystal x-ray diffraction (Figure 2.27).

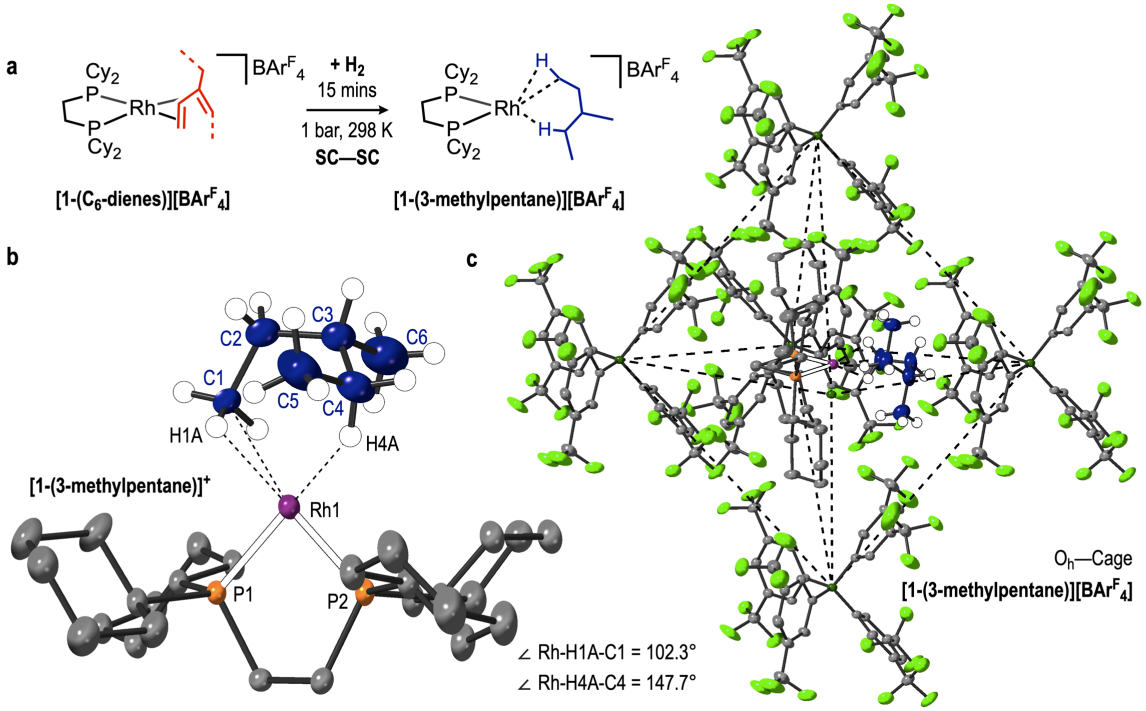

Figure 2.27: a) The formation of **[1-(3-methylpentane)][BAr^F_4]**. **b**) Cationic portion of **[1-(3-methylpentane)]$^+$** and **c**) O_h cage of [BAr^F_4]$^-$ anions in **[1-(3-methylpentane)][BAr^F_4]**. Hydrogen atoms on phosphine ligand and [BAr^F_4]$^-$ as well as -Ar^F_4 groups around front B-atoms excluded for clarity. Displacement ellipsoids set at 30 % in both parts.

The solid-state structure for **[1-(3-methylpentane)][BAr^F_4]** shows 3-methylpentane coordinated at the rhodium centre in a 1,4-mode, *via* a methyl and a methine C–H environment. Both these interactions are 3c–2e$^-$ in nature, shown by the increased Rh•••C distances compared to that of the Rh–C=C distances in **[1-(C_6-dienes)][BAr^F_4]** (Rh–C1 / Rh–C4, 2.430(4) / 2.788(6) Å to 2.237(10) / 2.287 (9) Å respectively).

The Rh–C4 distance however is significantly greater than the Rh–C1 distance (2.788(6) and 2.430(4) Å respectively). This combined with the obtuse angle of the Rh1•••H4A–C4 interaction of 147.7°, compared to 102.3° for Rh1•••H1A–C1, suggests 3-methylpentane coordinating to the rhodium centre in an $\eta^2\eta^1$-fashion. This is unlike the previous alkane

complexes in this Chapter which were all suggested, and computationally shown for **[1-*iso*butane][BAr$^{F}_{4}$]** as well as previously reported examples,[1–3] to coordinate in an $\eta^2\eta^2$-fashion. This suggested η^1-interaction will be confirmed by ongoing calculations, however it is analogous to the previously reported, structurally characterised η^1-alkane complex with a Rh•••C distance of 2.90(3) Å and Rh•••H–C angle of 140.7°, which gives evidence towards this assignement.[7]

Table 2.6: Selected crystallographic information of **[1-(C$_6$-dienes)][BAr$^{F}_{4}$]** and **[1-(3-methylpentane)][BAr$^{F}_{4}$]**.

	Rh–P1 / Rh–P2 (Å)	Rh–C1 / Rh–C4 (Å)	C1–C2 / C3–C4(Å)	Unit Cell Volume (Å^3) / Space Group
[1-(C$_6$-dienes)] [BAr$^{F}_{4}$]	2.2628(12) / 2.924(14)	2.237(10) / 2.287(9)	1.278(14) / 1.245(13)	3331.86(2) / P–1
[1-(3-methylpentane)] [BAr$^{F}_{4}$]	2.1965(7) / 2.1959(7)	2.430(4) / 2.788(6)	1.504(7) / 1.475(8)	3334.03(9) / P–1

Shown in Table 2.6, the lengthening of the C1–C2 and C3–C4 distances is consistent with the hydrogenation across the C=C environments. The contraction of the Rh–P distances in **[1-(3-methylpentane)][BAr$^{F}_{4}$]** *versus* **[1-(C$_6$-dienes)][BAr$^{F}_{4}$]** show the weaker *trans* influence of 3-methylpentane compared to that of either (*Z*)-3-methyl-1,3-pentadiene or ethyl-butadiene. Notably, the η^2- *versus* η^1-interaction has little effect on the Rh–P bond *trans* to these.

During the hydrogenation, the pseudo-O_h arrangement of [BAr$^{F}_{4}$]$^-$ anions is retained, shown in Figure 2.27c. A small disorder component of 3-methylpentane is present, of the -methyl group labelled C5 over two positions. Similar to the hydrogenation of **[1-*iso*pentadiene][BAr$^{F}_{4}$]**, the two C$_6$-diene isomers must hydrogenate and rearrange to give one isomer. This may result again from a low energy rotation present in the solid-state, or hydrogenation occurring *via* an intermediate that dictates selectivity. This alkane coordination mode is proposed to be from increased steric demand between the two non-coordinated methyl groups of 3-methylpentane and [BAr$^{F}_{4}$]$^-$ anion microenvironment, which forces this geometry. This shows how the solid-state environment dictates the bonding motif.

Bulk analysis of **[1-(3-methylpentane)][BAr$^F_4$]** was conducted following the *in situ* SSNMR spectroscopy procedures outlined in Section 2.2.2. The $^{31}P\{^1H\}$ and $^{13}C\{^1H\}$ SSNMR spectra at 285 K of **[1-(3-methylpentane)][BAr$^F_4$]** are shown in Figure 2.28. The $^{13}C\{^1H\}$ SSNMR spectrum shows no signals within the alkene region (δ 70 – 100), suggestive of complete hydrogenation of the sample. Numerous signals that appear in the region of δ 5 – 15 are suggestive of new aliphatic ^{13}C environments, likely from the coordinated 3-methylpentane ligand.

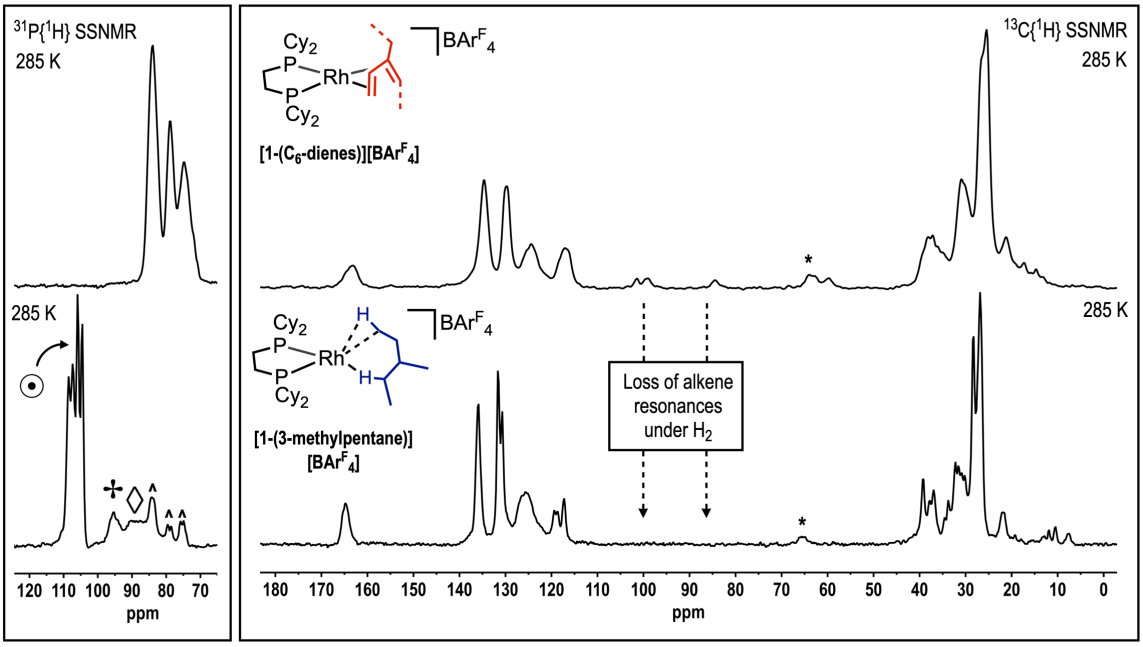

Figure 2.28: The $^{31}P\{^1H\}$ and $^{13}C\{^1H\}$ SSNMR (162 / 101 MHz, 298 K, 10 kHz spin rate) spectra of **[1-(C$_6$-dienes)][BAr$^F_4$]** and **[1-(3-methylpentane)][BAr$^F_4$]** (⦿). Signals marked ◊ = **[1-BAr$^F_4$]**, ✢ = a proposed dehydrogenation product from **[1-(3-methylpentane)][BAr$^F_4$]**, ^ = from the initial under-hydrogenation of **[1-(C$_6$-dienes)][BAr$^F_4$]** and * = spinning sidebands.

The $^{31}P\{^1H\}$ SSNMR spectrum of **[1-(3-methylpentane)][BAr$^F_4$]** is consistent with previous examples of σ-alkane complexes in this Chapter. A set of signals observed around δ 106 is constructed of two doublets, arising from two crystallographically unique ^{31}P environments, both coupled to ^{103}Rh. The value of these constants differs significantly between each ^{31}P environment [δ 108, J_{RhP} = 188 Hz; 105, J_{RhP} = 236 Hz]. The signal at δ 105, with the larger Rh–P coupling constant, is assigned to the ^{31}P environment *trans* to the suggested Rh1•••H4A–C4 η^1-interaction. This is consistent with the different *trans* influences exhibited by η^1 and η^2 interactions. The signals are also noted as being sharp, compared to the signals from the $^{31}P\{^1H\}$ SSNMR spectrum of **[1-(C$_6$-dienes)][BAr$^F_4$]**. This may be from the simplification of the coordinating species upon hydrogenation, as no isomers are present.

Also observed in this spectrum are multiple signals between δ 95 to 78. These can be assigned to **[1-BAr$^{F}_{4}$]** [δ 91], from the over-hydrogenation of the sample and consequent decomposition, and to **[1-(C$_6$-dienes)][BAr$^{F}_{4}$]** [δ 86, 79, 73] from the under-hydrogenation of the sample, or rapid dehydrogenation of the 3-methylpentane ligand. The latter however is discounted in Chapter 3. The presence of both **[1-BAr$^{F}_{4}$]** and **[1-(C$_6$-dienes)][BAr$^{F}_{4}$]** is explained by the hydrogenation procedure used when conducting reactions within SSNMR rotors, discussed in Section 2.2.2. The signal at δ 95 however is assigned to a proposed dehydrogenation product from **[1-(3-methylpentane)][BAr$^{F}_{4}$]**. This product, along with the overall stability of **[1-(3-methylpentane)][BAr$^{F}_{4}$]** at 298 K, is explored further in Chapter 3

2.7. The Attempted Synthesis of a σ-Octane Complex

2.7.1. A Precursor Octadiene Complex

To explore the limits of linear σ-alkane complexes using SMOM techniques with $[BAr^F{}_4]^-$ anions and this RhP_2 fragment, the synthesis of an octane-bound complex was targeted. Addition of excess 1,7-octadiene to a solution of **$[1\text{-}F_2C_6H_4][BAr^F{}_4]$** in dichloromethane yielded the octadiene complex of $[Rh(Cy_2PCH_2CH_2PCy_2)(n\text{-}C_8H_{14})][BAr^F{}_4]$, **$[1\text{-octadiene}][BAr^F{}_4]$** (Scheme 2.8).

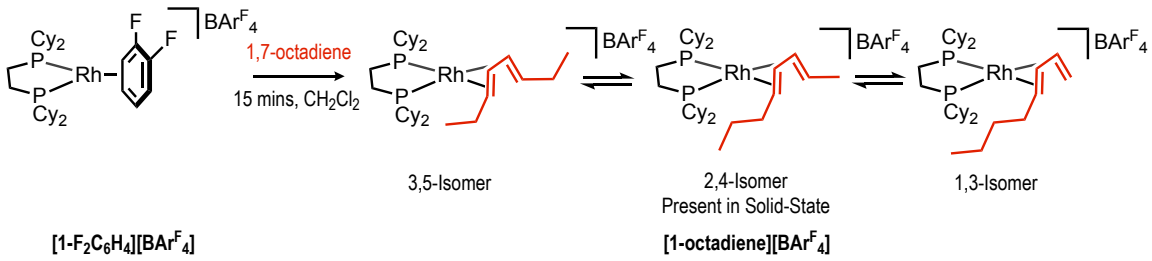

Scheme 2.8: The formation of **$[1\text{-octadiene}][BAr^F{}_4]$.**

The solution $^{31}P\{^1H\}$ NMR spectrum for **$[1\text{-octadiene}][BAr^F{}_4]$** reveals a similar set of resonances to that of **$[1\text{-hexadiene}][BAr^F{}_4]$**. Three octadiene isomers were observed, shown in Figure 2.29a. The doublet at δ 81 [J_{RhP} = 178 Hz], is assigned to the symmetrical, 3,5-octadiene isomer, from the identical ^{31}P environments also coupled to ^{103}Rh.

The set of signals at [δ 80, J_{RhP} = 178 Hz, J_{PP} = 24 Hz and δ 81, J_{RhP} = 178 Hz, J_{PP} = 24 Hz] and [δ 84, J_{RhP} = 175 Hz, J_{PP} = 22 Hz and δ 77, J_{RhP} = 173 Hz, J_{PP} = 23 Hz] are representative of two unsymmetrical coordinated dienes, such as the 2,4-isomer and 1,3-isomers of octadiene. These two could not be definitively distinguished, however. The large difference in chemical shifts of the ^{31}P environments in the second set of signals are indicative of two ^{31}P environments with largely different *trans* substituents. One explanation for this involves a coordinating terminal and internal C=C environment, as observed in the 1,3-isomer.

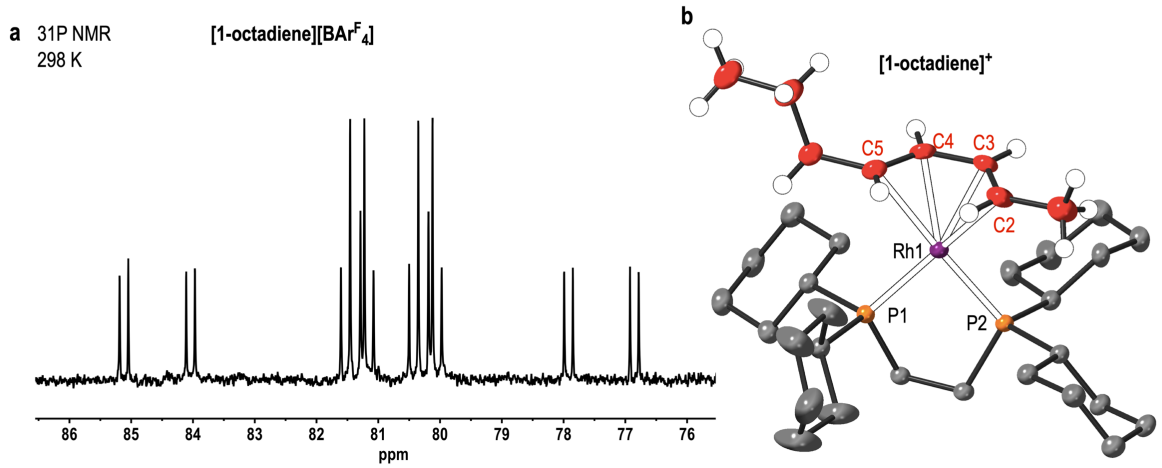

Figure 2.29: a) $^{31}P\{^{1}H\}$ NMR (CD_2Cl_2, 298 K, 162 MHz) spectrum of **[1-octadiene][BAr$^F_4$]**. **b**) Cationic portion of **[1-octadiene][BAr$^F_4$]**, showing coordination of the solid-state favoured 2,4-isomer of octadiene. Hydrogen atoms on phosphine ligand and $[BAr^F_4]^-$ anion excluded for clarity. Displacement ellipsoids set at 30 % in all parts.

Upon crystallisation from a dichloromethane: pentane layering, **[1-octadiene][BAr$^F_4$]** crystallises as the 2,4-isomer in the solid-state, shown by single-crystal x-ray diffraction (Figure 2.29b). No residual electron density or disorder components could be located when solving the structure, suggesting only the 2,4-isomer is present. **[1-octadiene][BAr$^F_4$]** also exhibits a pseudo-O_h arrangement of $[BAr^F_4]^-$ anions, however, the cation is twisted and does not point towards the vertex of the adjacent $[BAr^F_4]^-$ anions. This is in contrast to the previous alkene structures presented in this Chapter, where the cation does align facing the boron vertex, Figure 2.30, and maybe due to the increased steric demand of the octadiene ligand compared to that of hexadiene.

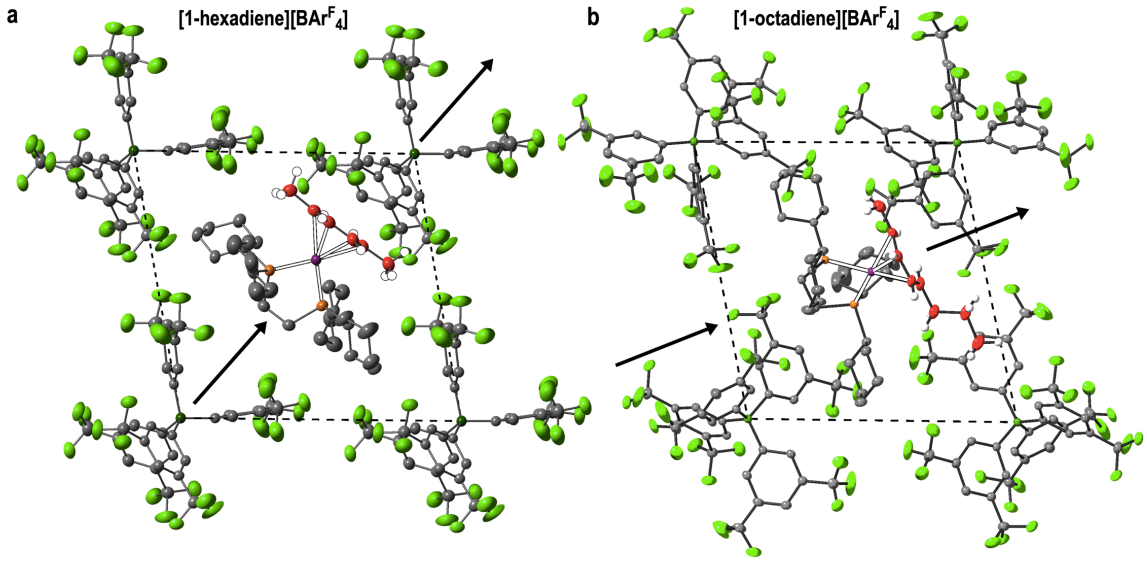

Figure 2.30: Section view of the $[BAr^{F}_{4}]^{-}$ anionic network in **a**) **[1-hexadiene][BAr$^{F}_{4}$]** and **b**) **[1-octadiene][BAr$^{F}_{4}$]**. Arrows added to help visualise the orientation of the cation fragments with respect to the neighbouring $[BAr^{F}_{4}]^{-}$ anion. Hydrogen atoms on phosphine ligand and $[BAr^{F}_{4}]^{-}$ anions as well as -Ar^{F}_{4} groups around selected B-atoms excluded for clarity. Displacement ellipsoids set at 30 % in both parts.

2.7.2. Solid-State Hydrogenation of [1-octadiene][BAr$^{F}_{4}$]

With the complex of **[1-octadiene][BAr$^{F}_{4}$]** in hand, the addition of H_2 (10 minutes, 1 bar, 298 K) to a sample of **[1-octadiene][BAr$^{F}_{4}$]** crystals (10 mgs) resulted in the crystals changing colour, from cherry-red to light yellow. An attempted single-crystal x-ray diffraction experiment showed this product exhibited no Bragg peaks, suggestive of an amorphous material. Dissolution of the product in dichloromethane showed signals only relating to **[1-BAr$^{F}_{4}$]** in the $^{31}P\{^{1}H\}$ NMR spectrum, and no signals relating to **[1-octadiene][BAr$^{F}_{4}$]** were found, showing that complete hydrogenation of the sample has occurred. Distillation of the volatiles from this solution showed only signals assigned to *n*-octane by ^{1}H NMR spectroscopy. Any reduction in the hydrogenation time (e.g., 5 minutes) resulted in a mixture of **[1-octadiene][BAr$^{F}_{4}$]** starting material and **[1-BAr$^{F}_{4}$]** products, shown by $^{31}P\{^{1}H\}$ NMR spectroscopy.

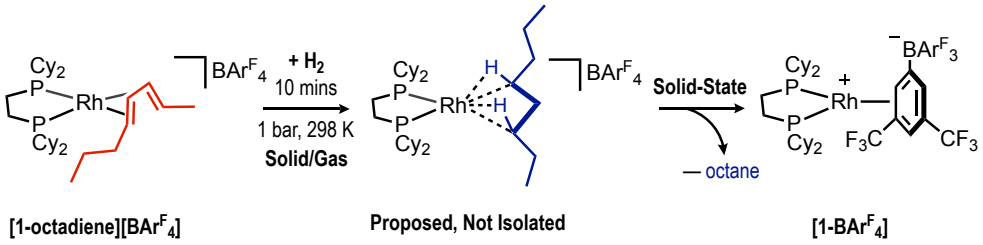

Scheme 2.9: The solid-state hydrogenation of **[1-octadiene][BAr$^F_4$]**.

These data suggest that although the hydrogenation of **[1-octadiene][BAr$^F_4$]** was possible in the solid-state, it did not produce a stable σ-octane complex on any appreciable timescales. Upon formation, rapid decomposition by alkane loss and anion coordination occurred to form **[1-BAr$^F_4$]** (Scheme 2.9). This may be due to the 'twisted' nature of the cation within the pseudo-O_h arrangement of [BAr$^F_4$]$^-$ anions, as shown in Figure 2.30b. This results in the corresponding alkane fragment not being sandwiched between two -Ar$^F_4$ arms, as shown in previous, stable σ-alkane complexes.[1,3] This structural suicide is established during the crystallisation of **[1-octadiene][BAr$^F_4$]**. If oriented towards the boron vertex, the linearity of the octadiene ligand may create steric repulsions with the neighbouring [BAr$^F_4$]$^-$ anions, and so adopts this twisted form. Overall, this complex may show the upper limit to linear σ-alkane complex synthesis in the solid-state lies with **[1-hexane][BAr$^F_4$]**.

2.8. Void Space Calculations

Throughout this Chapter, the relative bulkiness of each alkane ligand has been commented on but not quantified. Section 2.8. aims to quantify this term by looking at solvent void spaces present within the crystal structures of the σ-alkane complexes.

Analysis of the structures by calculating their solvent-accessible voids in Olex2 software[28] allows for the volume of each alkane to be calculated using a 1.41 Å probe radius. These solvent-excluded isosurfaces have been calculated for the complexes presented in this Chapter, as well as previously reported examples (e.g., **[1-NBA][BAr$^{F}_{4}$])** and a selection are shown in Figure 2.31 and Table 2.7.

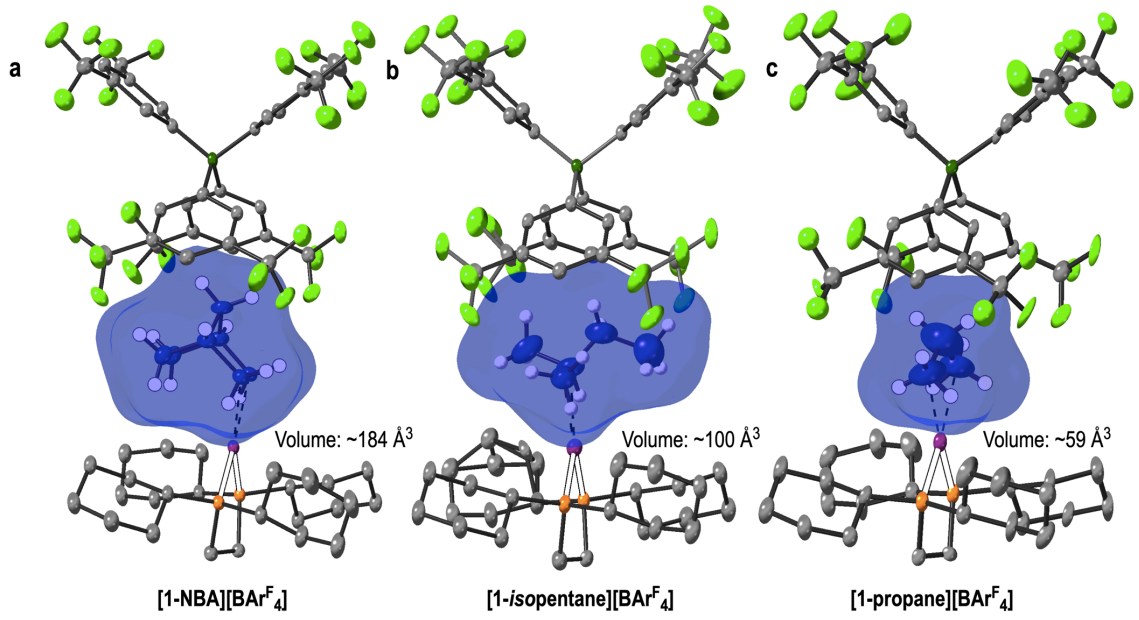

Figure 2.31: Solvent excluded isosurfaces and calculated alkane-cavity volumes of **a**) **[1-NBA][BAr$^{F}_{4}$]**, **b**) **[1-*iso*pentane][BAr$^{F}_{4}$]** and **c**) **[1-propane][BAr$^{F}_{4}$]**.

As well as these volume calculations, the total internal volume of each pseudo-octahedral framework of [BAr$^{F}_{4}$]$^{-}$ anions can be approximated (Figure 2.31). To calculate this volume, the octahedron was separated into two square based pyramids. By placing a centroid within the base of the pyramid, the base-vertex height of each pyramid can be calculated. These values, combined with the known B–B vertex distances, meant the volume could be approximated using the equation shown in Figure 2.32. This equation however is designed for a completely planar, square-based pyramid, which is not present in the pseudo-octahedral framework of [BAr$^{F}_{4}$]$^{-}$ anions. To overcome this, averages of these 4 B–B distances were taken. These are shown in Table 2.7 for all the complexes with a

pseudo-octahedral framework of $[BAr^F_4]^-$ anions, along with solvent exuded isosurfaces for each alkane ligand.

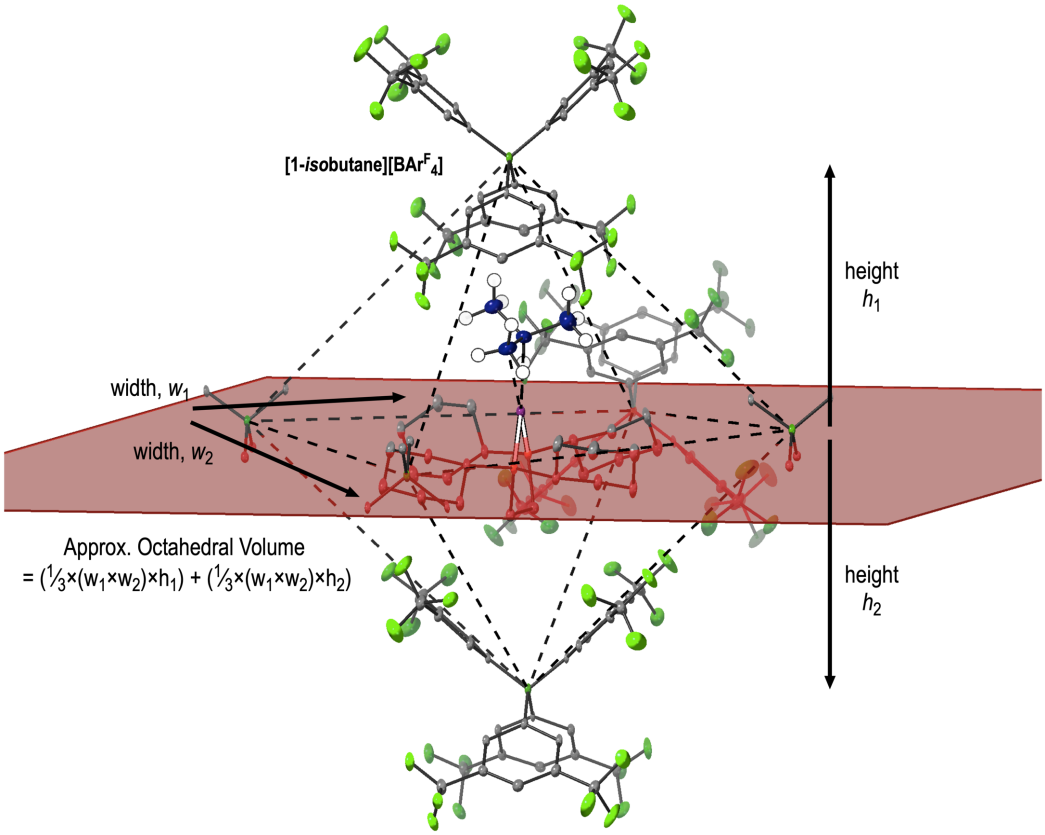

Figure 2.32: Pseudo-octahedral framework of $[BAr^F_4]^-$ anions within **[1-*iso*butane][BAr^F_4]**, showing height and widths calculated for approximate octahedral volumes. Plane added to aid the visualisation of plane of boron vertices.

Table 2.7: Summary of selected solid-state σ-alkane complexes.

Complex	Solid-State Structure	~ Alkane Volume / Å³	~ Octahedral Volume / Å³	Alkane-to-Octahedron Volume / %
[1-propane][BAr^F_4]	O_h	59	1248	4.6
[1-*iso*butane][BAr^F_4]	O_h	87	1094	7.9
[1-*iso*pentane][BAr^F_4]	O_h	100	1105	9.0
[1-(3-methylpentane)][BAr^F_4]	O_h	153	1187	12.8
[1-cyclohexane][BAr^F_4]	O_h	152	1112	13.6
[1-NBA][BAr^F_4]	O_h	184	1362	13.5
[1-pentane][BAr^F_4]	BCP	126	–	–
[1-hexane][BAr^F_4]	BCP	125	–	–

The table shows how increasing the carbon number of the alkane increases the solvent excluded isosurfaces, and overall alkane volume. The propane ligand in **[1-propane][BAr$^{F}_{4}$]**, composed of only three carbons, occupies ~59 Å^3, whilst the NBA ligand in **[1-NBA][BAr$^{F}_{4}$]** containing seven carbons occupies ~184 Å^3. This is visualised in Figure 2.31. The steady increase in volume with each carbon addition can also be seen throughout Table 2.7.

The octahedral volume calculated for each alkane however shows no large difference upon alkane size. This is expected, as all these complexes are of similar unit cell dimensions and all only contain one cationic fragment per octahedron. Notably, **[1-propane][BAr$^{F}_{4}$]** and **[1-NBA][BAr$^{F}_{4}$]** have similar volumes, explained by the fact **[1-propane][BAr$^{F}_{4}$]** is synthesised from two further SC-SC reactions from **[1-NBA][BAr$^{F}_{4}$]**.

By combining the solvent-excluded isosurface calculations and the approximate octahedral volumes, the alkane-to-octahedron volume ratios can be calculated. Notably, the complexes with smallest alkane to octahedron volumes are those with limited stability at 298 K, for example, **[1-propane][BAr$^{F}_{4}$]** (4.6 %). When compared to that of **[1-NBA][BAr$^{F}_{4}$]** (13.5 %), this may be reflected in their respective stability times under an H_2 atmosphere of > 72 hours and 1 minute respectively. Given a greater alkane volume, a better fit within the octahedron may be achieved, shown by an increased alkane-to-octahedron volume percentage. This may increase the number of C–F•••H–C interactions within the solid-state cavity, previously discussed as key stabilising motifs for σ-alkane complexes in the solid-state (see Section 2.3.2.2).

The alkane volumes of *n*-pentane and *n*-hexane are ~125 and ~126 Å^3 respectively, which is not expected given the increase in methylene unit. This is suggestive that these particular cavities present in **[1-pentane][BAr$^{F}_{4}$]**[3] and **[1-hexane][BAr$^{F}_{4}$]** maybe a result of the bi-capped square pyramidal arrangement of [BAr$^{F}_{4}$]$^-$ anions, rather than the alkanes themselves. If this space is not optimised, fewer stabilising C–F•••H–C interactions may be present, leading to an unsupported alkane ligand, potentially explaining the relatively poor stability of these complexes.

2.9. Notes on All Solid-State σ-Alkane Complexes

As with all the σ-alkane complexes presented in this Chapter, dissolution of the crystals in MeCN or 1,2-$F_2C_6H_4$ led to the instantaneous formation of the solvent complexes **[1-(MeCN)$_2$][BAr$^F_4$]**[4] or **[1-$F_2C_6H_4$][BAr$^F_4$]**[3] respectively. Dissolution in poorly coordinating solvents, such as dichloromethane, lead to the formation of the anion coordinated **[1-BAr$^F_4$]** (Scheme 2.10). As no evidence for these σ-alkane complexes could be gathered in solution, this suggests they are only stable in solvent-free conditions, such as the solid-state.

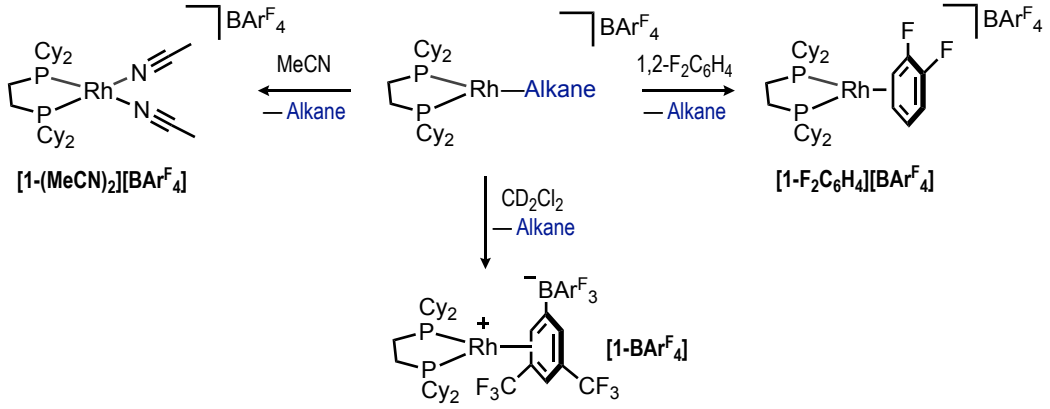

Scheme 2.10: A selection of solvent decomposition pathways for solid-state σ-alkane complexes.

Additionally, these liberated alkane fragments could be separated by trap-to-trap distillation and analysed by ^{1}H NMR spectroscopy. In all complexes, the resulting spectra matched that of the literature values reported for each respective alkane. Not only does this show the complete hydrogenation of each sample, it also shows that no C–C rearrangement of the alkane fragment has occurred.

2.10. Chapter Conclusions

Chapter 2 has reported the synthesis of the σ-alkane complexes of **[1-propane][BAr$^F_4$]**, **[1-butane][BAr$^F_4$]**, **[1-*iso*butane][BAr$^F_4$]**, **[1-*iso*pentane][BAr$^F_4$]**, **[1-hexane][BAr$^F_4$]** and **[1-(3-methylpentane)][BAr$^F_4$]**. These were all synthesised in SC-SC reactions, from the hydrogenation of their respective alkene or diene precursor complexes following the SMOM methodology. These are summarised in Scheme 2.11.

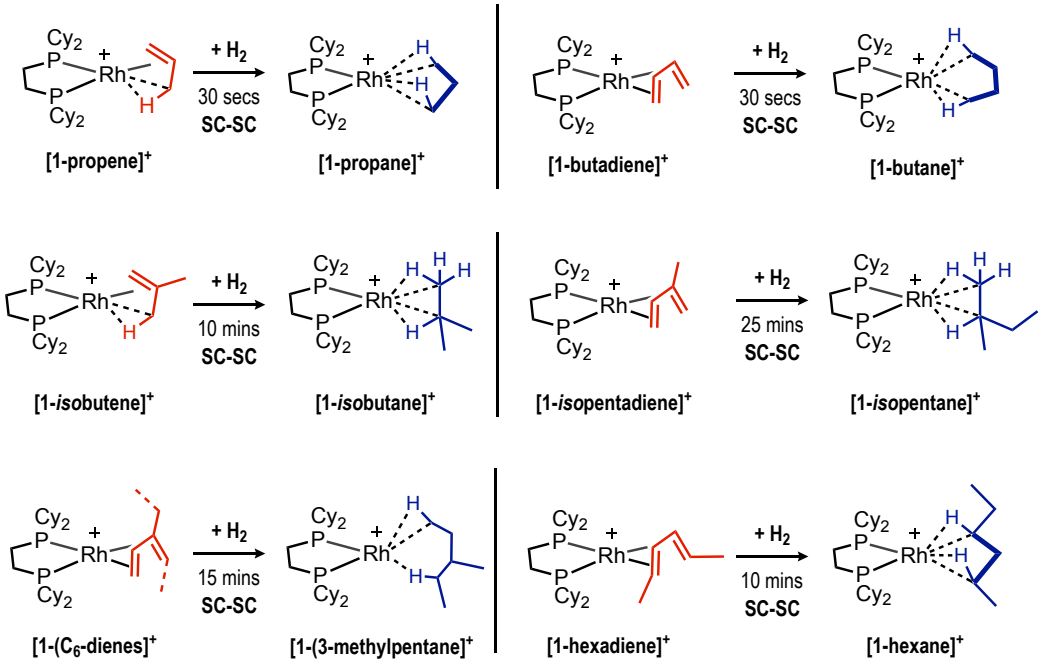

Scheme 2.11: Summary of the syntheses of all σ-alkane complexes presented in Chapter 2.

All the complexes present are unique to the solid-state, and rapidly decompose upon dissolution. The solid-state structures of these complexes were characterised by single-crystal x-ray diffraction, and bulk spectroscopic evidence, including yields, were provided by solid-state $^{31}P\{^1H\}$ and $^{13}C\{^1H\}$ NMR spectroscopy. The stability of these complexes in the solid-state was monitored by *in situ* SSNMR spectroscopy. These data can be presented in comparison to previously reported solid-state σ-alkane complexes of the same $[Rh(Cy_2PCH_2CH_2PCy_2)]^+$ fragment, shown in Table 2.8.

Table 2.8: Summary of selected solid-state σ-alkane complexes.

Cation	R-Group	Carbon Backbone	Anion	Solid-State Structure[a]	Spectroscopic Yield[b] / %	SS Stability at 298 K[c]
[1-NBA]$^+$	Cyclohexyl	-CH_2CH_2-	[BAr^F_4]$^-$	O_h	100	**> 4 months**
[1-cyclohexane]$^+$	Cyclohexyl	-CH_2CH_2-	[BAr^F_4]$^-$	O_h	> 95	**min. 48 hours**
[1-*iso*butane]$^+$	Cyclohexyl	-CH_2CH_2-	[BAr^F_4]$^-$	O_h	> 95	**min. 24 hours**
[1-*iso*pentane]$^+$	Cyclohexyl	-CH_2CH_2-	[BAr^F_4]$^-$	O_h	~ 80	**min. 24 hours**
[1-(3-methylpentane)]$^+$	Cyclohexyl	-CH_2CH_2-	[BAr^F_4]$^-$	O_h	~ 80	**< 18 hours**
[1-pentane]$^+$	Cyclohexyl	-CH_2CH_2-	[BAr^F_4]$^-$	BCP	~ 85	**12 hours**
[1-hexane]$^+$	Cyclohexyl	-CH_2CH_2-	[BAr^F_4]$^-$	BCP	~ 85	**1 hour**
[1-propane]$^+$	Cyclohexyl	-CH_2CH_2-	[BAr^F_4]$^-$	O_h	~ 30	**1 hour**
[1-butane]$^+$	Cyclohexyl	-CH_2CH_2-	[BAr^F_4]$^-$	O_h	~ 14	**~ 30 mins**

[a] [BAr^F_4]$^-$ anion packing structure of the precursor NBD complex as measured by single-crystal x-ray diffraction. [b] Spectroscopic yield measured by approximate ratio of products in the $^{31}P\{^1H\}$ SSNMR spectra. [c] As measured by time taken for disappearance of signals in the $^{31}P\{^1H\}$ SSNMR spectra. [d] Longest measured time point available. min. = minimum of.

These data suggest that the σ-alkane complexes with alkanes of larger, bulkier size tend to be of higher yielding and exhibit a greater stability than those of alkanes that occupy less volume. This is best shown by alkanes of which the branched and linear isomers can be synthesised. For example, branched alkanes, such as *iso*butane and *iso*pentane, have increased stabilities and yields than the linear analogues of butane and the previously reported pentane-complex. A similar trend is observed for 3-methylpentane in comparison to pentane and hexane, however the change from BCP to O_h arrangement of [BAr^F_4]$^-$ anions may add to the increased stability.

This increase in size/bulk is suggested to form a greater number of C–H•••F–C solid-state interactions between the cation and neighbouring [BAr^F_4]$^-$ anions. This is backed up by the calculated NCI plots, which highlight these weak stabilising interactions within the solid-state cavities, as well as relative alkane-to-octahedron volume ratios. These stabilising interactions have been shown to aid the kinetic stabilities of previous solid-state σ-alkane complexes.[1,3]

From the σ-alkane complexes presented in Chapter 2, the following Chapters aim to explore any onward solid/gas reactivity these complexes may have. Chapter 3 aims to make this hydrogenation reversible, so as to dehydrogenate the σ-alkane complexes presented. Likewise, Chapter 4 explores any isotopic exchange when these are placed under an atmosphere of D_2.

2.11. References

1 S. D. Pike, F. M. Chadwick, N. H. Rees, M. P. Scott, A. S. Weller, T. Krämer and S. A. Macgregor, *J. Am. Chem. Soc.*, 2015, **137**, 820–833.
2 A. I. McKay, A. J. Bukvic, B. E. Tegner, A. L. Burnage, A. J. Martínez-Martínez, N. H. Rees, S. A. Macgregor and A. S. Weller, *J. Am. Chem. Soc.*, 2019, **141**, 11700–11712.
3 F. M. Chadwick, N. H. Rees, A. S. Weller, T. Krämer, M. Iannuzzi and S. A. Macgregor, *Angew. Chem. Int. Ed.*, 2016, **55**, 3677–3681.
4 F. M. Chadwick, A. I. McKay, A. J. Martinez-Martinez, N. H. Rees, T. Krämer, S. A. Macgregor and A. S. Weller, *Chem. Sci.*, 2017, **8**, 6014–6029.
5 H. Nowell, S. A. Barnett, K. E. Christensen, S. J. Teat and D. R. Allan, *J. Synchrotron Radiat.*, 2012, **19**, 435–441.
6 M. Brookhart, M. L. H. Green and G. Parkin, *Proc. Natl. Acad. Sci.*, 2007, **104**, 6908–6914.
7 A. J. Martínez-Martínez, B. E. Tegner, A. I. McKay, A. J. Bukvic, N. H. Rees, G. J. Tizzard, S. J. Coles, M. R. Warren, S. A. Macgregor and A. S. Weller, *J. Am. Chem. Soc.*, 2018, **140**, 14958–14970.
8 J. A. Calladine, S. B. Duckett, M. W. George, S. L. Matthews, R. N. Perutz, O. Torres and K. Q. Vuong, *J. Am. Chem. Soc.*, 2011, **133**, 2303–2310.
9 A. L. Thompson, *Crystallogr. Rev.*, 2019, **25**, 3–53.
10 D. C. Apperley, R. K. Harris and P. Hodgkinson, *Solid-State NMR : Basic Principles & Practice*, Momentum Press, 2012.
11 B. Malengier, J. L. Tamalapakula and S. Pushpavanam, *Chem. Eng. Sci.*, 2012, **83**, 2–11.
12 A. J. Martínez-Martínez, C. G. Royle, S. K. Furfari, K. Suriye and A. S. Weller, *ACS Catal.*, 2020, **10**, 1984–1992.
13 K. I. Goldberg and A. S. Goldman, *Acc. Chem. Res.*, 2017, **50**, 620–626.
14 M. Bohnet, *Ullmanns' Encyclopedia of Industrial Chemistry*, Wiley-VCH, 2004.
15 S. Biswas, Z. Huang, Y. Choliy, D. Y. Wang, M. Brookhart, K. Krogh-Jespersen and A. S. Goldman, *J. Am. Chem. Soc.*, 2012, **134**, 13276–13295.
16 S. M. Chapp and N. D. Schley, *Organometallics*, 2017, **36**, 4355–4358.
17 B. Cordero, V. Gómez, A. E. Platero-Prats, M. Revés, J. Echeverría, E. Cremades, F. Barragán and S. Alvarez, *Dalton Trans.*, 2008, 2832–2838.
18 D. R. Evans, T. Drovetskaya, R. Bau, C. A. Reed and P. D. W. Boyd, *J. Am. Chem. Soc.*, 1997, **119**, 3633–3634.
19 J. C. Green, M. L. H. Green and G. Parkin, *Chem. Commun.*, 2012, **48**, 11481–11503.
20 J. Contreras-García, E. R. Johnson, S. Keinan, R. Chaudret, J. P. Piquemal, D. N. Beratan and W. Yang, *J. Chem. Theory Comput.*, 2011, **7**, 625–632.
21 O. Torres, J. A. Calladine, S. B. Duckett, M. W. George and R. N. Perutz, *Chem. Sci.*, 2015, **6**, 418–424.
22 S. D. Pike and A. S. Weller, *Philos. Trans. R. Soc. A*, 2015, **373**, 20140187.
23 V. H. Rawal, *Synthesis by Isomerization of Unconjugated Dienes, Allenes, Alkynes, and Methylenecyclopropanes*, Georg Thieme Verlag, 2009.
24 E. Larionov, H. Li and C. Mazet, *Chem. Commun.*, 2014, **50**, 9816–9826.
25 J. R. Clark, J. R. Griffiths and S. T. Diver, *J. Am. Chem. Soc.*, 2013, **135**, 3327–3330.
26 *(Z)-3-methyl-1,3-pentadiene -- AIST Spectr. Database Org. Compd. -- (SDBS No. 292) -- Date Acc. 25-06-2020*.
27 K. Hasegawa, R. Asami and K. Takahashi, *Bull. Chem. Soc. Jpn.*, 1978, **51**, 916–920.
28 O. V. Dolomanov, L. J. Bourhis, R. J. Gildea, J. A. K. Howard and H. Puschmann, *J. Appl. Crystallogr.*, 2009, **42**, 339–341.

Chapter 3:
Alkane Dehydrogenation from Solid State σ-Alkane Complexes

3.1. Chapter Introduction

3.1.1. Alkane Dehydrogenation

The catalytic, non-oxidative dehydrogenation of low value, light alkanes to produce alkenes of increased economic and chemical value is an industrially important process.[1] As introduced in Chapter 1, the applications of low molecular weight alkanes are limited and are generally only focussed on their calorific potential.[2] To increase the value of these potential feedstock materials,[3] alkane dehydrogenation pathways to form alkenes can be applied (Scheme 3.1).[4]

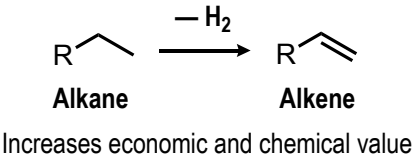

Scheme 3.1: Alkane dehydrogenation.

Alkane dehydrogenation is typically energy intensive, due to the large positive enthalpy related to these reactions (~120 kcal mol^{-1}).[5] The thermodynamic barriers of these systems are typically overcome by the use of high temperatures.[6–8] The heterogeneous dehydrogenation of *iso*butane to *iso*butene for example is conducted at 525–700 ºC over a Pt/Sn catalyst, in the Oleflex process (Scheme 3.2a).[9] As well as being energy intensive, issues such as product selectivity, coking and catalyst decomposition are often present at these temperatures.

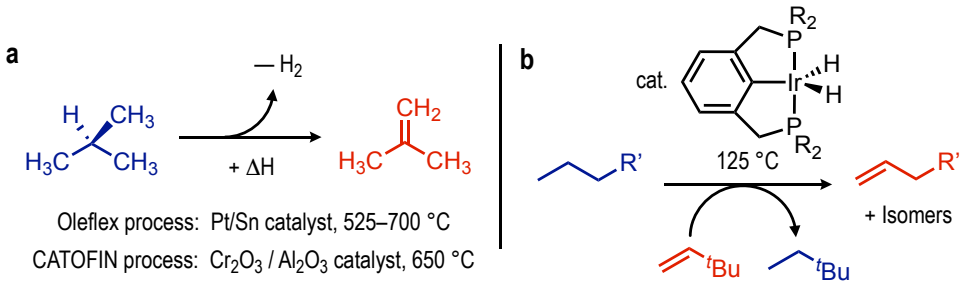

Scheme 3.2: Examples of **a**) heterogeneous[9] and **b**) homogeneous (transfer) alkane dehydrogenation pathways. R = ^{t}Bu, R = C_5H_{11}, R' includes alkyl and aryl examples.[10]

A range of lower temperature pathways (125–200 ºC) involving homogeneous catalysts are available,[10–12] yet typically require sacrificial hydrogen acceptors, which reduce the overall atom economy of the process (Scheme 3.2b). Other reported methods include the continuous removal of H_2, by constant bubbling of inert gas through the reaction.[13,14] This

biases the equilibrium involved in hydrogen removal, which provides the driving force for the reaction, however still requires elevated temperatures. Other processes include photolytic pathways, where the use of UV-irradiation has been used to drive this reaction.[15,16]

Further heterogeneous processes for solid/gas alkane dehydrogenation involves utilising Surface OrganoMetallic Catalysts (SOMCs). Reported by Celik *et al.*, a well-established iridium pincer ligand complex, originally developed by Brookhart and Goldman,[17] was supported upon a silica surface.[18] This SOMC allowed for the gas-phase, acceptorless dehydrogenation of butane to butene under flow conditions. Similarly to the heterogeneous Oleflex process (Scheme 3.2a), high temperatures (~340 ºC) had to be used however. Moreover, the structural coordination of the active species involved are ill-defined.

Goldman *et al.* have also shown that similar iridium complexes can be used in the solid-phase, in the solid/gas transfer dehydrogenation of pentane to pentenes.[19] The term solid-phase refers to the catalyst in a melt-phase, so techniques such as x-ray diffraction or solid-state NMR spectroscopy could not be used upon the organometallic species present during the reaction. Although this reaction is highly regioselective for the formation of 1-pentene, it still requires temperatures of 200–240 ºC, alongside propene or ethene hydrogen acceptors.

This required high energy, or use of sacrificial acceptors, means that these systems presented may not be economically viable as a whole, as the alkene products do not justify the costs of the alkane dehydrogenation process. This presents an opportunity to design a system that conducts catalytic, acceptorless alkane dehydrogenation at reduced temperatures, from a well-defined, discrete catalyst.

3.1.2. Mechanisms for Alkane Dehydrogenation

Shown in Scheme 3.3 is the mechanism of a typical catalytic homogeneous alkane dehydrogenation pathway.[20,21] As alkanes are poor ligands, solvents and other ligands can easily outcompete them in coordination to the metal centre.[22] This results in the pre-equilibrium towards σ-alkane complex formation, where this equilibrium typically lies far to the left that is, without the alkane coordinated. Therefore, σ-alkane complexes are only present as transient intermediates within this mechanism.

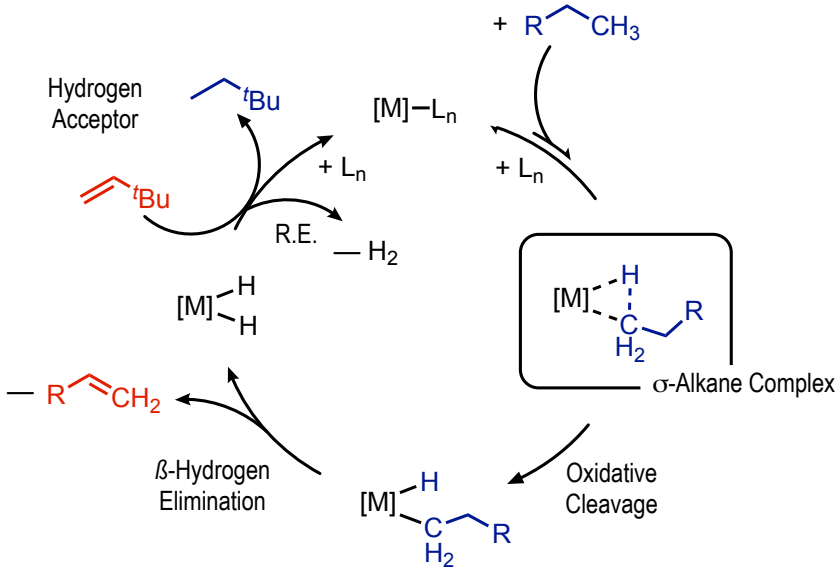

Scheme 3.3: Mechanism of catalytic homogeneous alkane dehydrogenation and intermediates involved. R.E. = Reductive Elimination.

Upon initial σ-alkane complex formation, oxidative cleavage of the C–H bond occurs, followed by *β*-hydrogen elimination which results in the alkene product.[22] The C–H activation steps within these two processes have been reported as facile processes,[23–25] suggesting the initial formation of a σ-alkane complex is challenging. Finally, a reductive elimination step to regenerate the active catalyst, and complete the catalytic cycle, is driven by the use of a hydrogen acceptor or by the constant removal of H_2.

As σ-alkane complexes are generally short lived and exist in low concentrations, their individual kinetic contributions to the overall dehydrogenation process is difficult to study. Previous studies have looked at all of these steps as an ensemble, rather than their individual contributions.[10]

3.1.3. SMOM Systems

Solid-state Molecular OrganoMetallic (SMOM) systems utilised for the dehydrogenation of molecular σ-alkane complexes have previously been reported.[26] Introduced in Chapter 1 is the σ-cyclohexane complex **[1-cyclohexane][BAr$^F_4$]**. When crystals of this complex were placed under a dynamic vacuum or flushing argon, a rapid solid/gas dehydrogenation occurs to form the intermediate complex [Rh($Cy_2PCH_2CH_2PCy_2$)(C_6H_{10})][BAr$^F_4$], **[1-cyclohexene][BAr$^F_4$]**. This was followed by a second solid/gas dehydrogenation step to form **[1-cyclohexadiene][BAr$^F_4$]**, as shown in Scheme 3.4.

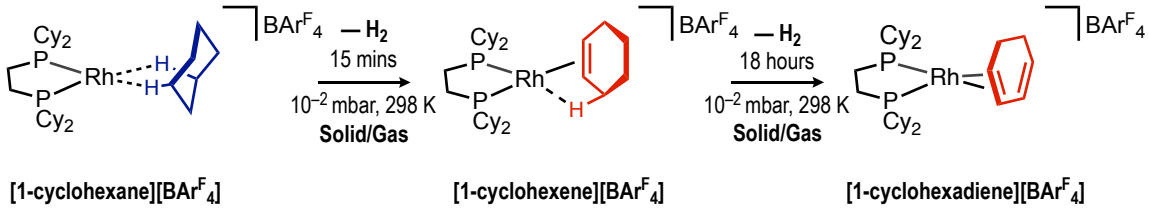

Scheme 3.4: Reaction scheme of the dehydrogenation of **[1-cyclohexane][BAr$^F_4$]**.

These dehydrogenation products were confirmed by a range of spectroscopic techniques, including solid-state and solution NMR spectroscopy, as well as solution NMR spectroscopy of the trapped volatiles from each step. The crystals however did not retain long-range order within this dehydrogenation reaction, so single-crystal x-ray diffraction could not be conducted. The kinetics of these individual dehydrogenation steps could even be followed. This, along with other significant results for this system, are discussed in comparison to the work presented throughout this Chapter.

This result shows how the SMOM methodology, which allows for the isolation of solid-state σ-alkane complexes on meaningful scales, enables the analysis of key intermediates within the alkane dehydrogenation pathway. Chapter 3 aims to explore the dehydrogenation reactions of all the solid-state σ-alkane complexes reported in Chapter 2 following the procedures established in **[1-cyclohexane][BAr$^F_4$]** dehydrogenation. This will not only explore if alkane dehydrogenation within these complexes is feasible, but also the kinetics and selectivity of such processes.

3.2. Alkane Dehydrogenation from σ-Alkane Complexes

3.2.1. σ-*Iso*butane Complex Dehydrogenation

In Chapter 2, the σ-*iso*butane complex **[1-*iso*butane][BAr$^{F}_{4}$]** was formed from the single crystal to single crystal (SC-SC) hydrogenation of the precursor *iso*butene complex, **[1-*iso*butene][BAr$^{F}_{4}$]**. Remarkably, when a simple Schlenk line vacuum (10^{-2} mbar) or a flushing argon stream was applied to the system, it was found that dehydrogenation of the *iso*butane ligand in **[1-*iso*butane][BAr$^{F}_{4}$]** occurs, to reform the precursor alkene complex **[1-*iso*butene][BAr$^{F}_{4}$]**, shown in Scheme 3.5.

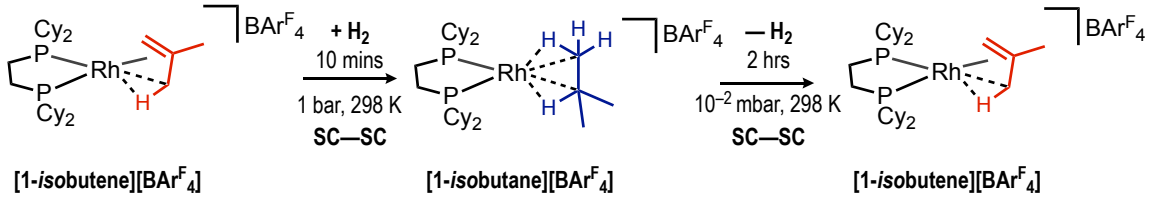

Scheme 3.5: Reaction scheme of the dehydrogenation of **[1-*iso*butane][BAr$^{F}_{4}$]**.

This acceptorless, room temperature dehydrogenation is complete within 2 hours and a 30 % yield of **[1-*iso*butene][BAr$^{F}_{4}$]** is even recovered within 5 minutes. This transformation is shown by both solution and solid-state NMR spectroscopy of the products. Notably, the dehydrogenation of *iso*butane is industrially important, as it is used as an additive in gasoline and is the key monomer in butyl rubber production.[27]

As this dehydrogenation event was even shown to have retained crystallinity, this means both the hydrogenation and dehydrogenation reactions follow consecutive SC-SC transformations. This allows for single-crystal x-ray diffraction to be used to confirm the structure, shown in Figure 3.1. This retention of crystallinity was unlike **[1-cyclohexane][BAr$^{F}_{4}$]**, which did not retain any long-range order during dehydrogenation.

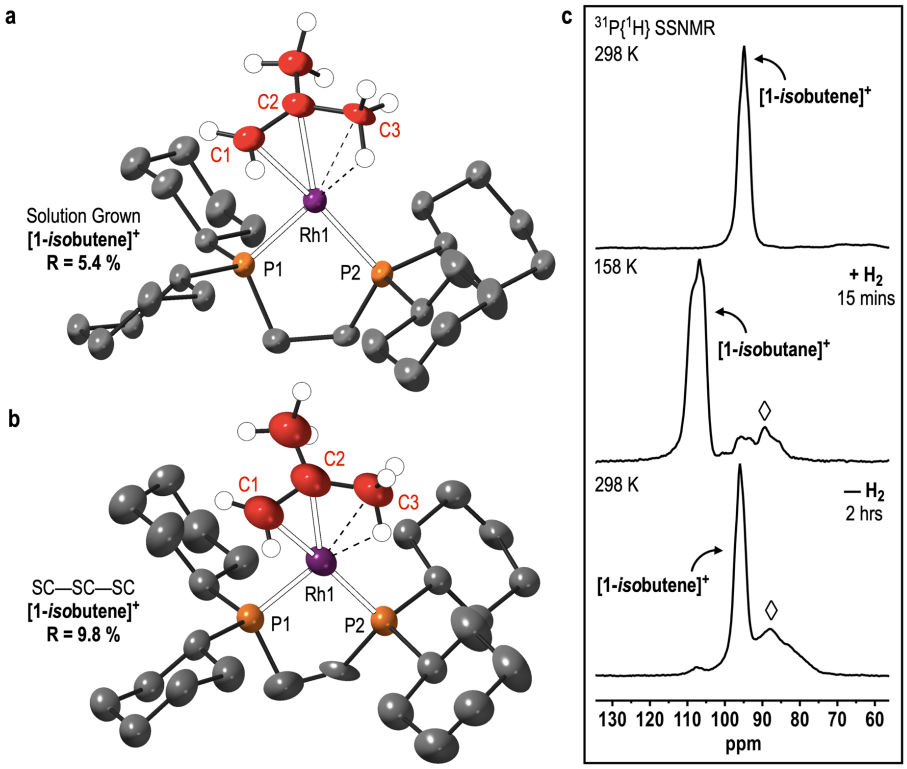

Figure 3.1: Solid-state structure of the cationic portion from **a**) solution grown crystals and **b**) SC-SC-SC reacted **[1-*iso*butene][BAr$^F_4$]**. Hydrogen atoms on bisphosphine ligand and [BAr$^F_4$]$^-$ anion excluded for clarity and displacement ellipsoids set at 30 % in both structures. **c**) The ^{31}P{^{1}H} SSNMR spectra (162 MHz, 10 kHz spin rate) of **[1-*iso*butane][BAr$^F_4$]** (158 K) and **[1-*iso*butene][BAr$^F_4$]** (298 K), ◊ = **[1-BAr$^F_4$]**.

The structural coordination for **[1-*iso*butene][BAr$^F_4$]** formed through the SC-SC-SC process *versus* solution grown crystals are almost indistinguishable, shown in Figure 3.1a and b. Both show the *iso*butene ligand coordinated through η^2_π: $\eta^2_{C\text{-}H}$ interaction, and both contain a disorder component of a second coordinated *iso*butene rotated around a pseudo-C_2 axis. This is not shown, but previously described in Figure 2.20.

The two consecutive SC-SC processes result in the reduced data quality of this sample. The increased R-value between solution grown crystals and crystalline products from the SC-SC-SC processes (5.4 % vs 9.8 % respectively), along with the reduced precision of the selected bond lengths shown in Table 3.1, are consistent with other reported multiple solid-state transformations.[28] This can also be visualised by the larger ellipsoids of the atoms seen between the two collected structures (Figure 3.1), despite both structures containing displacement ellipsoids set at 30 %.

Table 3.1: Selected crystallographic data for solution grown and SC-SC-SC crystals of **[1-*iso*butene][BAr$^F_4$]**.

	Rh–P1 / Rh–P2 (Å)	Rh–C1 / Rh–C3 (Å)	C1–C2 / C2–C3 (Å)	Unit Cell Volume (Å^3) / Space Group
[1-isobutene]$^+$ Solution Grown	2.2238(9) / 2.2400(9)	2.262(6) / 2.368(9)	1.320(12) / 1.474(13)	3267.70(13) / P–1
[1-isobutene]$^+$ SC–SC–SC	2.222(3) / 2.343(3)	2.27(3) / 2.31(2)	1.37(4) / 1.43(3)	3253.5(6) / P–1

Figure 3.1c also shows the $^{31}P\{^1H\}$ SSNMR spectra of each step of the SC-SC-SC process, prepared in consecutive hydrogenation and dehydrogenation reactions *in situ* within the SSNMR rotor. These shows the major signal shift from δ 95 to δ 109 and back again to δ 95, consistent with the **[1-*iso*butene][BAr$^F_4$]** to **[1-*iso*butane][BAr$^F_4$]** to **[1-*iso*butene][BAr$^F_4$]** transformation. A large amount of anion coordinated decomposition product of **[1-BAr$^F_4$]** (~20 %) can also be seen in the SSNMR spectrum of the dehydrogenated **[1-*iso*butene][BAr$^F_4$]**, most likely from decomposition during the reactions within the SSNMR rotor. This can be explained by the non-ideal conditions of running *in situ* SSNMR experiments, discussed in Chapter 2, Section 2.2.2.

When this reaction was carried out in a J. Youngs NMR tube however, on free-flowing powder rather than material packed within solid-state NMR rotor, the hydrogenation time could be optimised and reduced to only 8 minutes. This is opposed to 15 minutes seen in Figure 3.1c. When this material was placed under a dynamic vacuum for 2 hours, dissolution of this material in CD_2Cl_2 revealed only a single doublet [δ 95, J_{RhP} = 179 Hz] in the solution $^{31}P\{^1H\}$ NMR spectrum, of **[1-*iso*butene][BAr$^F_4$]**. No evidence for any **[1-BAr$^F_4$]** formation could be found. This suggests that **[1-*iso*butane][BAr$^F_4$]** is not stable under longer exposure times to H_2 (15 *versus* 8 minutes), decomposing to **[1-BAr$^F_4$]** in the solid-state. Additionally, this further shows that the dehydrogenation reaction occurs with quantitative yield. This stability under an H_2 atmosphere is returned to in Chapter 4.

To confirm the initial hydrogenation to form **[1-*iso*butane][BAr$^F_4$]** had occurred, and the recovered **[1-*iso*butene][BAr$^F_4$]** is not just a result of under-hydrogenation of the sample, a split-batch experiment was conducted (Scheme 3.6). In this experiment, a sample of **[1-*iso*butene][BAr$^F_4$]** was hydrogenated for 8 minutes, to which this batch was split. Half was exposed to a dynamic vacuum for 2 hours, and half was dissolved in CD_2Cl_2 solvent immediately. No signals relating to **[1-*iso*butene][BAr$^F_4$]** could be found from the latter sample in the solution $^{31}P\{^1H\}$ NMR spectrum, only signals of either **[1-BAr$^F_4$]** [δ 91] or

further C–Cl activated products of this [δ 88].[29] This confirms the complete hydrogenation occurs within 8 minutes and dehydrogenation reaction occurs with quantitative yield.

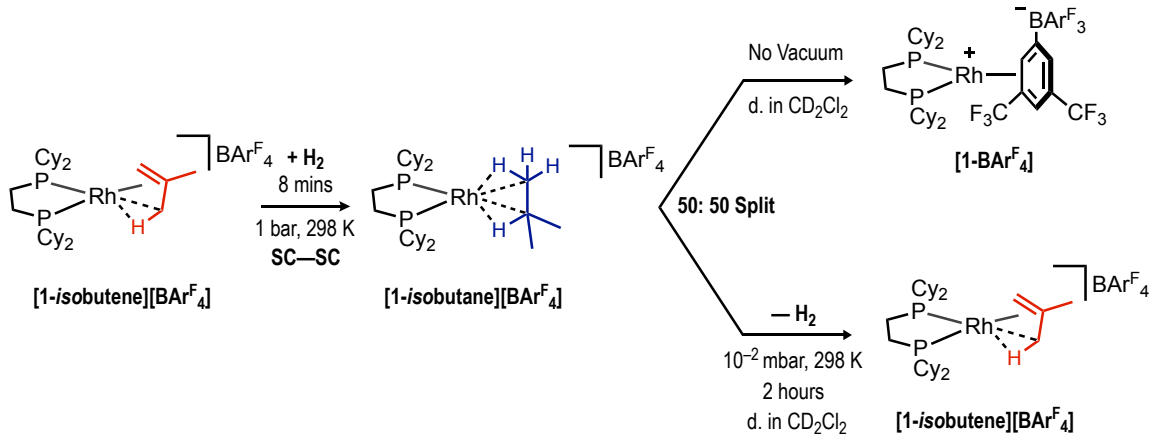

Scheme 3.6: Outline of a split-batch experiment upon **[1-*iso*butene][BAr$^F_4$]**.

3.2.2. σ-*Iso*pentane Complex Dehydrogenation

Analogous to **[1-*iso*butane][BAr$^F_4$]**, **[1-*iso*pentane][BAr$^F_4$]** was also found to undergo acceptorless, room temperature dehydrogenation. This was shown to undergo the loss of one equivalent of H_2, to form the new complex [Rh($Cy_2PCH_2CH_2PCy_2$)(*iso*-C_5H_{10})][BAr$^F_4$], **[1-*iso*pentenes][BAr$^F_4$]**, again in a SC-SC reaction (Scheme 3.7). Data for **[1-*iso*pentenes][BAr$^F_4$]** were collected by solution and solid-state NMR spectroscopy, alongside structural characterisation by single-crystal x-ray diffraction.

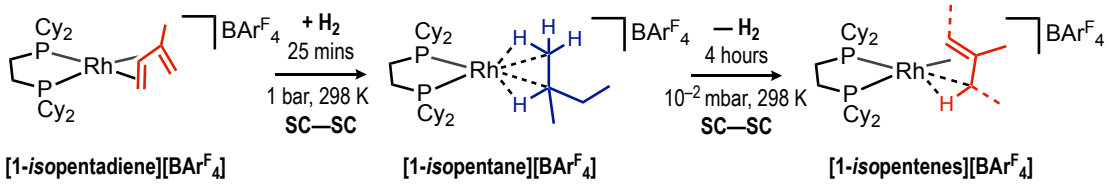

Scheme 3.7: Synthetic route to **[1-*iso*pentenes][BAr$^F_4$]**.

This selective dehydrogenation occurs within 4 hours when placed under dynamic, Schlenk line vacuum (10^{-2} mbar). Upon longer exposure time to vacuum (up to 7 days), no evidence for the second dehydrogenation step could be found, which would supposedly form **[1-*iso*pentadiene][BAr$^F_4$]**. This is unlike the dehydrogenation of **[1-cyclohexane][BAr$^F_4$]**, where the loss of two equivalents of H_2 can occur to form **[1-cyclohexadiene][BAr$^F_4$]** within 18 hours.[26]

The structure of **[1-*iso*pentenes][BAr$^F_4$]** collected by single-crystal x-ray diffraction revealed the coordinated *iso*pentene ligand to be a mixture of isomers. These are solved as two, non-crystallographically imposed disordered components of the terminal alkene isomer of 2-methyl-but-1-ene and internal isomer of 2-methyl-but-2-ene, in a 50:50 ratio (Figure 3.2). As these two isomers could not be individually separated as pure complexes and are always present as a mixture of the two isomers, the complex name of **[1-*iso*pentenes][BAr$^F_4$]** refers to this mixture of isomers throughout this thesis.

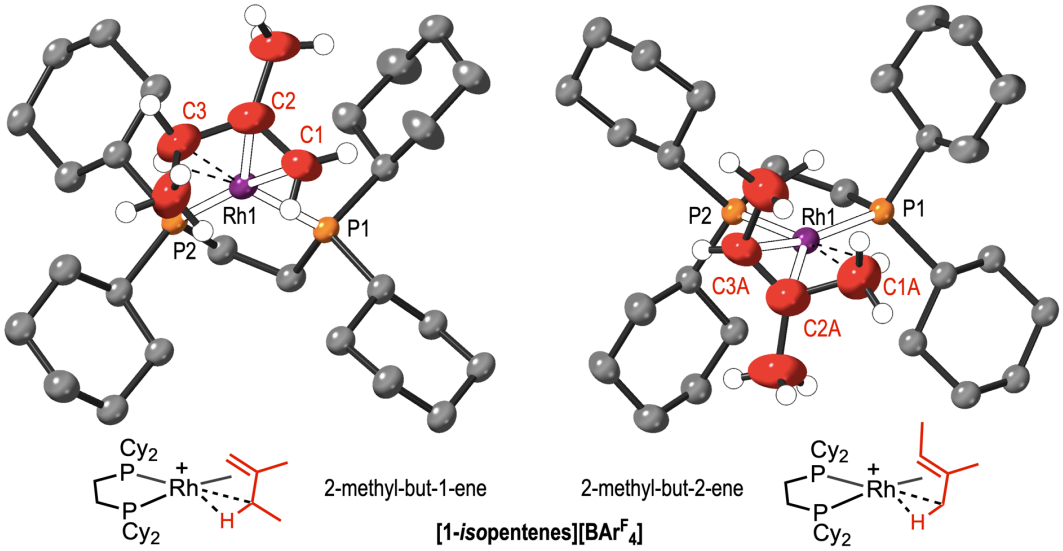

Figure 3.2: The structural connectivity of the cationic portions of **[1-*iso*pentenes][BAr$^F_4$]**, showing coordinated terminal and internal isomers of *iso*pentene. Hydrogen atoms on bisphosphine ligand and [BAr$^F_4$]$^-$ excluded for clarity and displacement ellipsoids set at 30 % in both structures.

Both isomers are shown to coordinate through η^2_π: $\eta^2_{C\text{-}H}$ interactions, which is analogous to **[1-propene][BAr$^F_4$]**[29] and **[1-*iso*butene][BAr$^F_4$]**. Notably, the agostic interaction in the terminal alkene isomer of 2-methyl-but-1-ene coordinates *via* a methylene C–H, unlike the 2-methyl-but-2-ene isomer, where the methyl C–H environment is coordinating. These two isomers are solved as two superimposed disorder components, related by a 1,3-alkene shift and psuedo-C_2 rotation in the solid-state.

The averaging of the Rh–P distances (shown in Table 3.2) is consistent with the crystallographically superimposed isomers. The values of 2.2370(15) and 2.2314(16) Å for Rh1–P1 and Rh1–P2 respectively arise from both ^{31}P atoms being *trans* to both agostic and alkene coordination modes. The lengthening of the Rh–P distances and contraction of [Rh]•••C and C–C distances compared to **[1-*iso*pentane][BAr$^F_4$]** are expected, as this

is the reverse of the changes in bond distances observed in hydrogenation reactions.[30–32] The decrease in unit cell volume is also opposite to that of alkene to alkane transformations.[28] The relatively low precision and large ESDs of C–C bond distances shown in Table 3.2 are a result of a SC-SC-SC reaction, whereby crystalline quality has been shown to suffer upon each transformation.[28]

Table 3.2: Selected bond metrics for **[1-*iso*pentane][BAr$^F_4$]** and **[1-*iso*pentenes][BAr$^F_4$]**

	Rh1–P1 / Rh1–P2 (Å)	Rh1–C1(A) / Rh1–C3(A) (Å)	C1(A)–C2(A) / C2(A)–C3(A) (Å)	Unit Cell Volume (Å^3) / Space Group
[1-*iso*pentane] [BAr$^F_4$]	2.1885(19) / 2.186(2)	2.335(12) / 2.422(14)	1.50(3) / 1.520(3)	3307.52(5) / P–1
[1-*iso*pentenes]$^+$ 2-methyl-but-1-ene	2.2370(15) / 2.2314(16)	2.23(2) / 2.360(18)	1.39(3) / 1.52(3)	3263.06(11) / P–1
[1-*iso*pentenes]$^+$ 2-methyl-but-2-ene		2.41(3) / 2.27(16)	1.54(3) / 1.37(3)	

Importantly, to confirm that these two isomers are the branched-butenes, addition of CO gas to crystalline **[1-*iso*pentenes][BAr$^F_4$]** was conducted. This results in the liberation of the coordinated alkenes and the formation of **[1-(CO)$_2$][BAr$^F_4$]**[33] in a solid/gas reaction. The volatiles were isolated by vacuum distillation and confirmed as the mixture of *iso*pentene isomers by solution ^{1}H NMR spectroscopy.

The ^{31}P{^{1}H} SSNMR spectrum of **[1-*iso*pentenes][BAr$^F_4$]** at 298 K shows a broad resonance at δ 95, upfield shifted from that of **[1-*iso*pentane][BAr$^F_4$]**. This is similar to the spectroscopic data for **[1-*iso*butene][BAr$^F_4$]**. The ^{13}C{^{1}H} SSNMR spectrum at 298 K exhibited no resonances in the typical alkene region (δ 40 – 100) however, upon cooling to 158 K, the ^{13}C{^{1}H} SSNMR spectrum exhibits three signals in the alkene region [δ 108, 88, 69], shown in Figure 3.3. As multiple alkene resonances are observed, this suggests that both *iso*pentene isomers are present in the low temperature static structure. This is consistent with the structure collected by single-crystal x-ray diffraction and suggests there is no preference in static isomer dictated by the solid-state environment. No significant change in the ^{31}P{^{1}H} SSNMR spectra at 158 K was observed.

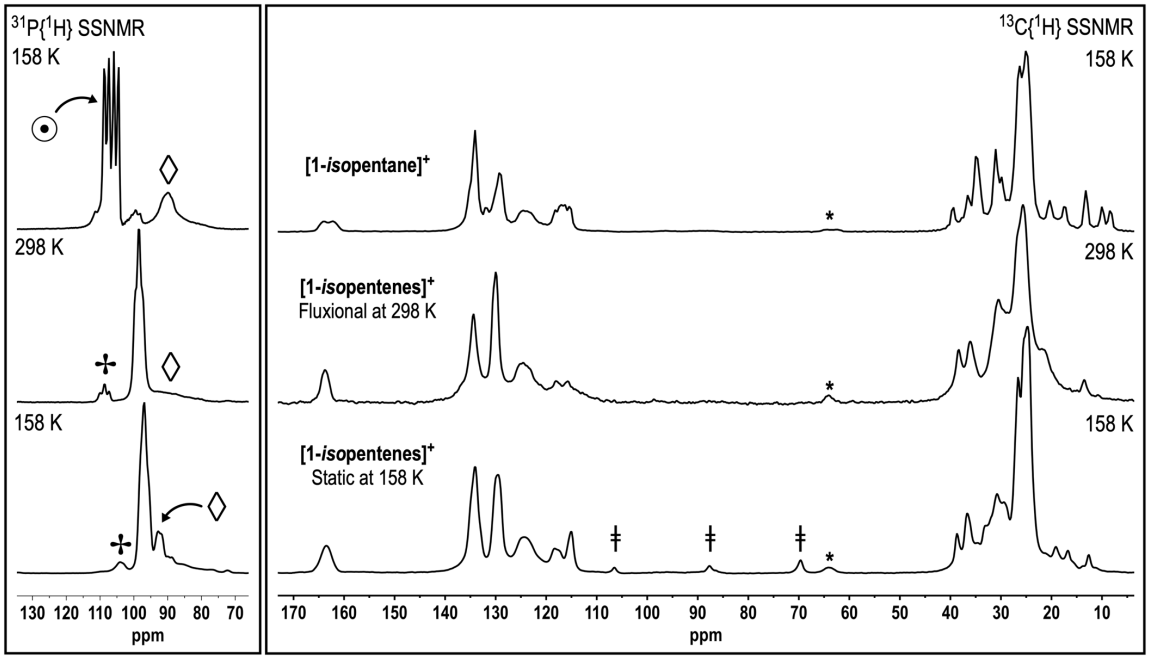

Figure 3.3: The $^{31}P\{^{1}H\}$ and $^{13}C\{^{1}H\}$ SSNMR (162 / 101 MHz, 10 kHz spin rate) spectra of **[1-*iso*pentane][BAr$^{F}_{4}$]** (158 K), **[1-*iso*pentenes][BAr$^{F}_{4}$]** (298 K) and **[1-*iso*pentenes][BAr$^{F}_{4}$]** (158 K). Signals marked ⦿ = **[1-*iso*pentane][BAr$^{F}_{4}$],** ◊ = **[1-BAr$^{F}_{4}$]**, ⊹ = unassigned decomposition product under an H_2 atmosphere, ǂ = ^{13}C-alkene environments and * = spinning sidebands.

These changes suggest that the coordinated *iso*pentenes are undergoing a fluxional process at room temperature, where a fully resolved spectrum is observed at 158 K. A proposed fluxional process is shown in Scheme 3.8, and is similar to that proposed in **[1-propene][BAr$^{F}_{4}$]** and **[1-*iso*butene][BAr$^{F}_{4}$]**,[29,34] (Chapter 2, Section 2.3.1.). This involves again exchange *via* a 1,3-alkene shift, which fluctuates between the two coordinated *iso*pentene ligands. A secondary 1,3-alkene shift, internal to each *iso*pentene isomer, also cannot be ruled out.

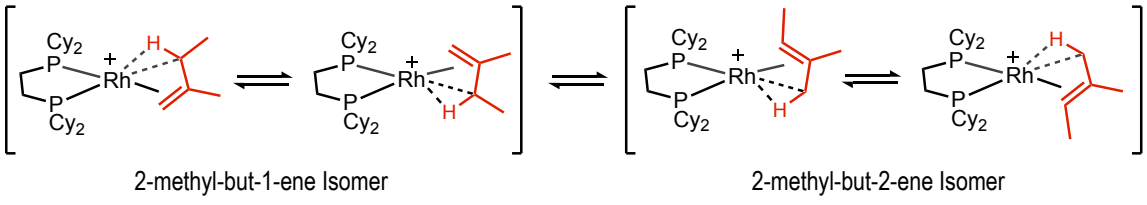

Scheme 3.8: Proposed fluxional processes of **[1-*iso*pentenes][BAr$^{F}_{4}$]**.

The solution $^{13}C\{^{1}H\}$ NMR spectroscopic data of **[1-*iso*pentenes][BAr$^{F}_{4}$]** in CD_2Cl_2 also suggests a fluxional process. The spectrum at 298 K shows no resonances assigned to alkene environments, and upon cooling to 183 K, four signals [δ 119, 104, 86, 71] are observed. Four alkene resonance are expected, from two alkene environments within each *iso*pentene isomer. Although the additional signal at δ 119 in solution is further downfield than expected for alkene environments, this is consistent with previously reported rhodium-alkene coordinated systems.[31] Additionally, this signal at δ 119 is obscured by $[BAr^{F}_{4}]^{-}$ anion assigned signals [between δ 140–110] in the 158 K $^{13}C\{^{1}H\}$ SSNMR spectrum, resulting in only three observable alkene signals in the solid-state spectrum.

The solution $^{31}P\{^{1}H\}$ NMR spectrum at 298 K exhibits a doublet (δ 95, J_{RhP} = 180 Hz) (Figure 3.4), which is assigned to that of **[1-*iso*pentenes][BAr$^{F}_{4}$]**. As **[1-*iso*pentenes][BAr$^{F}_{4}$]** is undergoing a rapid fluxional process at room temperature, this averages all ^{31}P environments, which are then coupled to the ^{103}Rh centre (^{103}Rh: I = ½). Upon cooling, this doublet transforms into two sets of two mutually coupled environments at 183 K. These are assigned to the complexes of the coordinated 2-methyl-but-1-ene isomer [δ 96.6, J_{RhP} = 199.6 Hz, J_{PP} = 25.8 Hz and 93.9, J_{RhP} = 155.9 Hz, J_{PP} = 25.8 Hz] and 2-methyl-but-2-ene isomer [δ 95.2, J_{RhP} = 152.6 Hz, J_{PP} = 26.5 Hz and 93.9, J_{RhP} = 212.0 Hz, J_{PP} = 26.5 Hz].

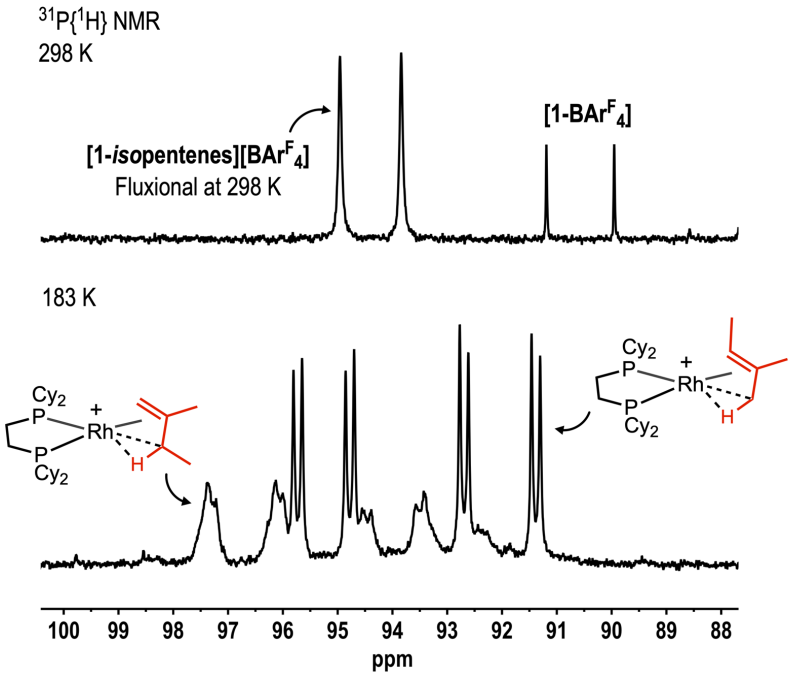

Figure 3.4: The solution $^{31}P\{^{1}H\}$ NMR spectra (162 MHz, CD_2Cl_2) of **[1-*iso*pentenes][BAr$^{F}_{4}$]** at 298 K and 183 K.

These signals were assigned compared to previously reported alkene complexes of the $[Rh(Cy_2PCH_2CH_2PCy_2)]^+$ fragment. The 2-methyl-but-1-ene isomer coordinates through a terminal CH_3 agostic interaction, previously observed in **[1-*iso*butene][BAr$^F_4$]**, **[1-propene][BAr$^F_4$]**[29] and **[1-(2-butene)][BAr$^F_4$]**,[29] for which the 183 K $^{31}P\{^1H\}$ NMR spectra of these are essentially identical. The second set of signals are assigned therefore to the 2-methyl-but-2-ene coordinated isomer. The broad nature of the signals is proposed to be due to a low energy exchange process between the two, diastereotopic proton agostic interactions which is poorly resolved at 183 K (Scheme 3.9).

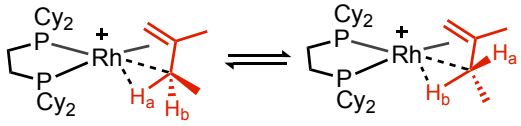

Scheme 3.9: Proposed exchange process between agostic interactions in the internal coordinated isomer of **[1-*iso*pentenes][BAr$^F_4$]**.

Furthermore, the ^1H NMR spectrum at 298 K is featureless in the alkene region. Upon cooling to 183 K, the ^1H NMR spectrum now shows resonances assigned to alkene environments as well as signals from agostic proton-environments (Figure 3.5).

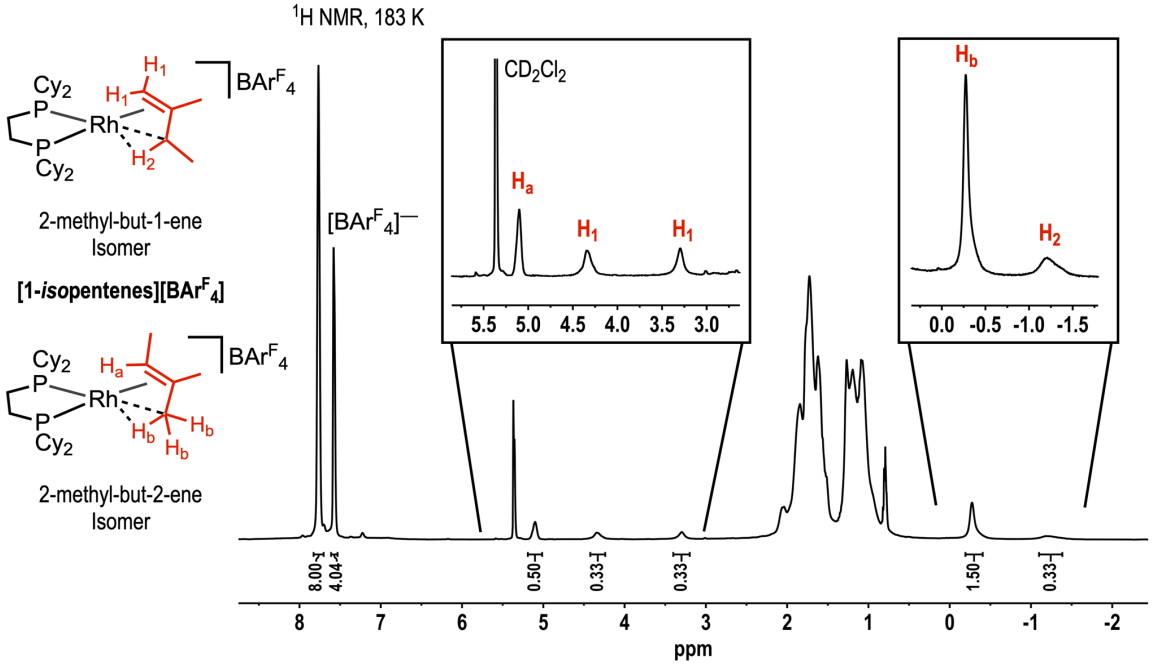

Figure 3.5: The solution ^1H NMR (CD_2Cl_2, 183 K, 400 MHz) spectrum of **[1-*iso*pentenes][BAr$^F_4$]**. The insert shows an enlargement of the signals at δ 5.5 – 3.0 and 0.0 – –1.5.

The signals at δ 4.3 and 3.3 are assigned to the two alkene environments of the 2-methyl-but-1-ene coordinated isomer. The relative integrals of these signals is 1: 1 and exhibit a cross-peak in the $^{1}H/^{1}H$ COSY NMR spectrum. These are assigned to each H_1 environment in Figure 3.5. The signal at δ –1.2 was assigned to that of the agostic interaction within the 2-methyl-but-1-ene coordinated isomer (H_2 in Figure 3.5) again, from the relative integrals of 1: 1: 1 compared to the two H_1 environments. The asymmetric shape of this signal may reflect the poorly resolved exchange process shown in Scheme 3.9.

The two remaining resonances at δ 5.1 and –0.3 have relative integrals of 1: 3 (H_a and H_b in Figure 3.5). These are in the correct ratio and chemical shifts to be assigned to the alkene and agostic environments respectively, within the 2-methyl-but-2-ene isomer of **[1-*iso*pentenes][BAr$^{F}_{4}$]**.

The population of these isomers is 1: 1.3, from ratio of the H_a: H_1 integrations. This shows the 2-methyl-but-2-ene isomer is the slightly favoured coordinated isomer at 183 K in solution. This is consistent with the relative integrals from the 183 K $^{31}P\{^{1}H\}$ NMR spectra (Figure 3.4), which shows a ~1: 1.2 ratio of internal: terminal isomers. The overlapping signals in the $^{31}P\{^{1}H\}$ NMR spectra, and therefore difficulties with integration, may explain the small difference in integration values.

Attempts to synthesise **[1-*iso*pentenes][BAr$^{F}_{4}$]** directly, without going *via* **[1-*iso*pentane][BAr$^{F}_{4}$]**, were unsuccessful. Addition of an excess of 2-methyl-but-1-ene to a dichloromethane solution of **[1-F$_2$C$_6$H$_4$][BAr$^{F}_{4}$]** led to the complete formation of **[1-*iso*pentadiene][BAr$^{F}_{4}$]**, Scheme 3.10.

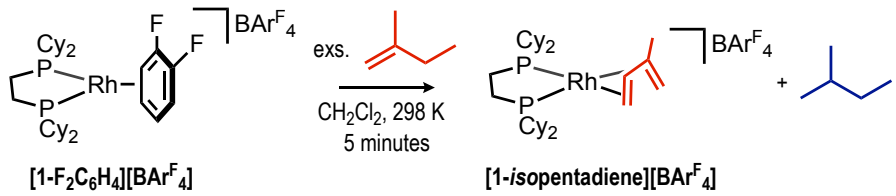

[1-F$_2$C$_6$H$_4$][BAr$^{F}_{4}$] **[1-*iso*pentadiene][BAr$^{F}_{4}$]**

Scheme 3.10: Solution reactivity of **[1-F$_2$C$_6$H$_4$][BAr$^{F}_{4}$]** with excess 2-methyl-but-1-ene.

This reaction follows a rapid transfer hydrogenation of two equivalents of 2-methyl-but-1-ene, to form an equivalent of coordinated *iso*pentadiene and free *iso*pentane. This is analogous to the reported synthesis of **[1-butadiene][BAr$^{F}_{4}$]**, where excess 1-butene is added to a solution of **[1-F$_2$C$_6$H$_4$][BAr$^{F}_{4}$]**.[29] This suggests that the

formation of **[1-*iso*pentadiene][BAr$^{F}_{4}$]** from **[1-*iso*pentenes][BAr$^{F}_{4}$]** is thermodynamically favourable, with the use of a sacrificial hydrogen acceptor. This second dehydrogenation step was shown not to be achievable in the solid-state. This may be because a hydrogen acceptor is needed for this, or due to a blocking of a specific transition state in the second dehydrogenation pathway by the [BAr$^{F}_{4}$]$^{-}$ anion microenvironment in the solid-state.

Dissolution of **[1-*iso*pentenes][BAr$^{F}_{4}$]** showed it to be unstable in CD_2Cl_2 solution for any long periods (> 2 hours) at 298 K. During this time, signals relating to **[1-*iso*pentadiene][BAr$^{F}_{4}$]** were observed in the solution $^{31}P\{^{1}H\}$ NMR spectrum. This may suggest *iso*pentene is liberated during this decomposition in CD_2Cl_2, and the liberated *iso*pentene is undergoing a transfer hydrogenation with any **[1-*iso*pentenes][BAr$^{F}_{4}$]** still present. After 16 hours, the $^{31}P\{^{1}H\}$ NMR spectrum showed only resonances for **[1-*iso*pentadiene][BAr$^{F}_{4}$]** and CD_2Cl_2 decomposition C–Cl activated products,[29] in ~50: 50 ratio, consistent with this observation.

Having initially explored the dehydrogenation of both **[1-*iso*butane][BAr$^{F}_{4}$]** and **[1-*iso*pentane][BAr$^{F}_{4}$]** alkane complexes, kinetics studies of these reactions were investigated. This is described in Section 3.3.

3.3. Reaction Progress Monitoring

3.3.1. σ-*Iso*butane Complex

To probe a mechanism into the dehydrogenation reactions presented in Section 3.2., kinetics studies were undertaken. The temporal profile of the dehydrogenation of **[1-*iso*butane][BAr$^F_4$]** to **[1-*iso*butene][BAr$^F_4$]** was followed by solution trapping experiments, where an outline of the procedure is shown in Scheme 3.11. Due to the precision needed when performing kinetic studies, solid-state spectroscopic techniques could not be used. This is due to experimental issues when performing solid/gas reactions in *in situ* SSNMR experiments, outlined in Chapter 2, Section 2.2.2.

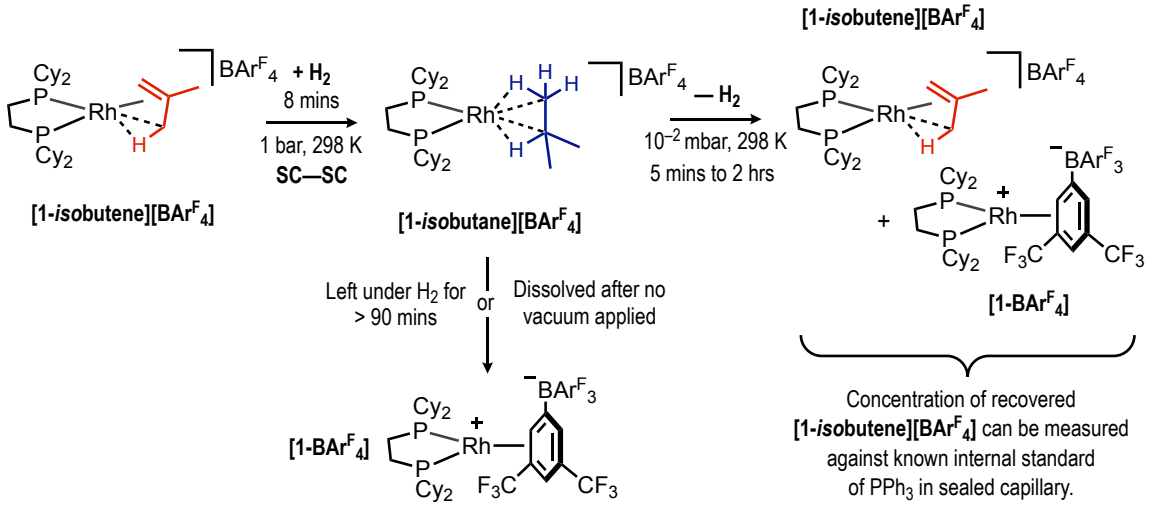

Scheme 3.11: Experimental procedure for kinetic analysis of alkane dehydrogenation experiments.

Experimentally, multiple, finely powdered samples of **[1-*iso*butene][BAr$^F_4$]** of the same mass (10 mgs) were loaded into individual J. Youngs NMR tubes. Each was placed under a hydrogen atmosphere (1 bar, 298 K) for 8 minutes and then exposed to a dynamic vacuum for varying times in a two-hour period. The samples were then dissolved in CD_2Cl_2 (0.35 mL) and measured by quantitative solution $^{31}P\{^1H\}$ NMR spectroscopy. The concentration of reformed **[1-*iso*butene][BAr$^F_4$]** present in each sample could be measured against an internal standard (PPh_3) within an isolated insert within each J. Youngs NMR tube. This provided a set of data suitable for quantitative analysis of the reaction progress.

The concentration of recovered **[1-*iso*butene][BAr$^{F}_{4}$]** was plotted against time and resulted in the temporal profiles shown in Figure 3.6. These data points, shown by blue circles, could be fitted against a calculated classical first order process, which follows **[1-*iso*butane][BAr$^{F}_{4}$]** → **[1-*iso*butene][BAr$^{F}_{4}$]**, with k = 1.5(2) × 10^{-3} s^{-1}. These data points could also be plotted against a second order process, following **2×[1-*iso*butane][BAr$^{F}_{4}$]** → **[1-*iso*butene][BAr$^{F}_{4}$] + [1-*iso*butane][BAr$^{F}_{4}$]**, with k = 1.6(2) × 10^{-4} M^{-1} s^{-1}. These were modelled using COPASI,[35] where the order was set with respect to rhodium (cation), and the fitted plots are shown in Figure 3.6a and b.

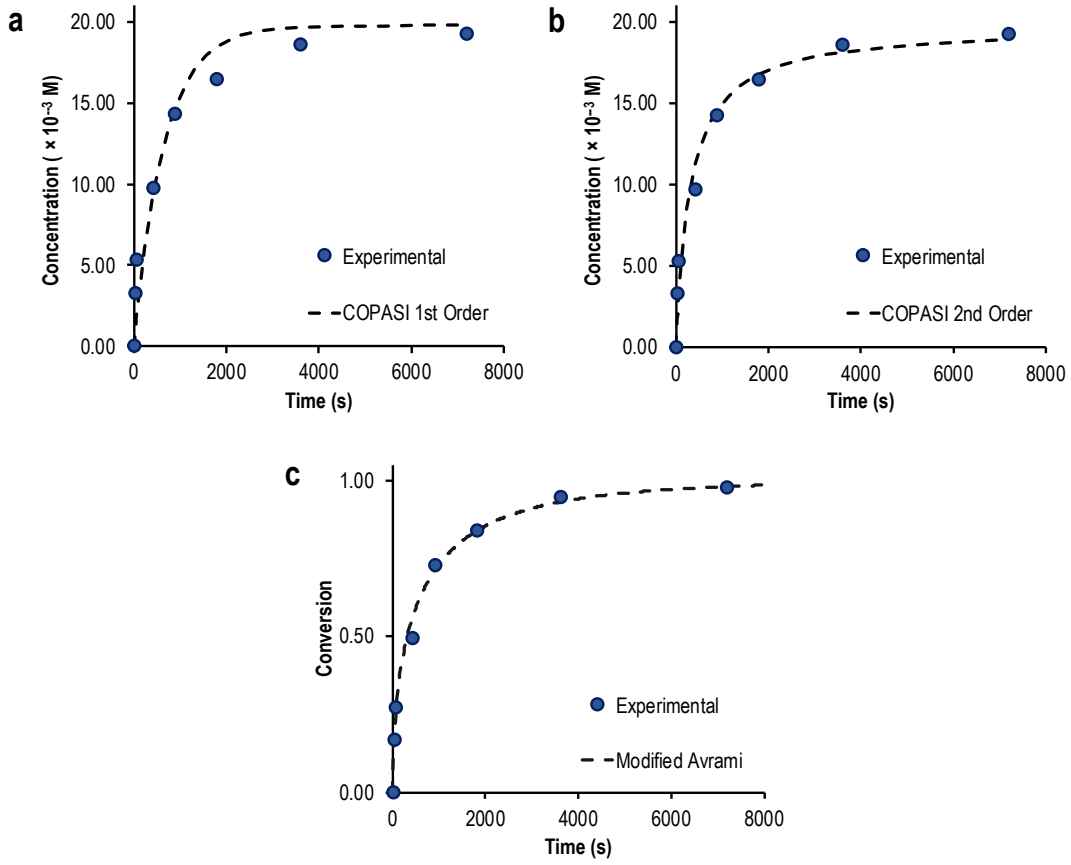

Figure 3.6: Temporal plots of **[1-*iso*butane][BAr$^{F}_{4}$]** dehydrogenation to form **[1-*iso*butene][BAr$^{F}_{4}$]**. Dashed lines show COPASI[35] simulated plots of **a**) First order process and **b**) Second order process and modified JMAK plot shown in **c**), where k = 1.6×10^{-3} (± 6×10^{-4}) s^{-1} and n = 0.55 ± 0.02. Each data point (blue circles) represents an individual dehydrogenation experiment.

Clearly, the first order curve does not result in an appropriate fit, especially when compared to the second order profile. This suggests that the reaction follows an overall second order process. One proposed mechanism for a cooperative process in the solid-state may involve the specific movement of a $[BAr^F{}_4]^-$ anion to allow for a certain transition step within the dehydrogenation mechanism. This idea is returned to in Section 3.4.

Figure 3.6c however shows a third way of modelling these data which, qualitatively, gave the best fit to the data presented. Johnson-Mehl-Avrami-Kologoromov (JMAK)[36–38] modelling allows for a solid-state reaction progress to be fitted to a simple expression. Originally formulated to follow crystallisation kinetics,[39] further examples include a range of areas, such as [2+2] solid-state photodimerisation reactions[40–42] and phase transformations within solids. The modified JMAK equation is shown in Equation 1, where k = rate constant and t = time, and the additional n parameter, of the Avrami Exponent.

$$conversion = 1 - e^{-k \cdot t^n} \qquad \text{(Equation 1)}$$

The Avrami Exponent, n, gives further details on the dimensionality of the solid-state reaction. n values nearing 2, 3 or 4, is suggestive of reactions occurring with 1 dimensional (1D), 2D and 3D growth respectively. When n = 1, the modified equation collapses to give a kinetics model similar to that of a classical, first order kinetics profile, where each reaction centre acts independently within the crystal lattice. It has been reported that appropriating classical, solution kinetics to solid-state reactions may not result in statistically valid fits.[43,44]

In the dehydrogenation of **[1-*iso*butane][$BAr^F{}_4$]**, the modified JMAK analysis resulted in a growth rate constant of 1.6×10^{-3} ($\pm 6 \times 10^{-4}$) s^{-1} and $n = 0.55 \pm 0.02$. This non-integer, less than one, value for n is suggestive of a diffusion-controlled reaction.[39] Proposed ideas to explain this diffusion control may be related to the loss of H_2 loss from the crystal lattice, or that specific **[1-*iso*butane]$^+$** cations have to dehydrogenate to allow for the further **[1-*iso*butane]$^+$** cations to dehydrogenate. Although this suggests the dehydrogenation reaction is diffusion controlled, an interplay between this and a classic, second order competitive mechanism cannot be ruled out.

In both cases, this would establish a reaction front moving through the crystalline solid. This type of reaction-front has been observed before in SMOM materials, in the previously reported reaction of a rhodium–butadiene complex with CO gas (Figure 3.7).[33]

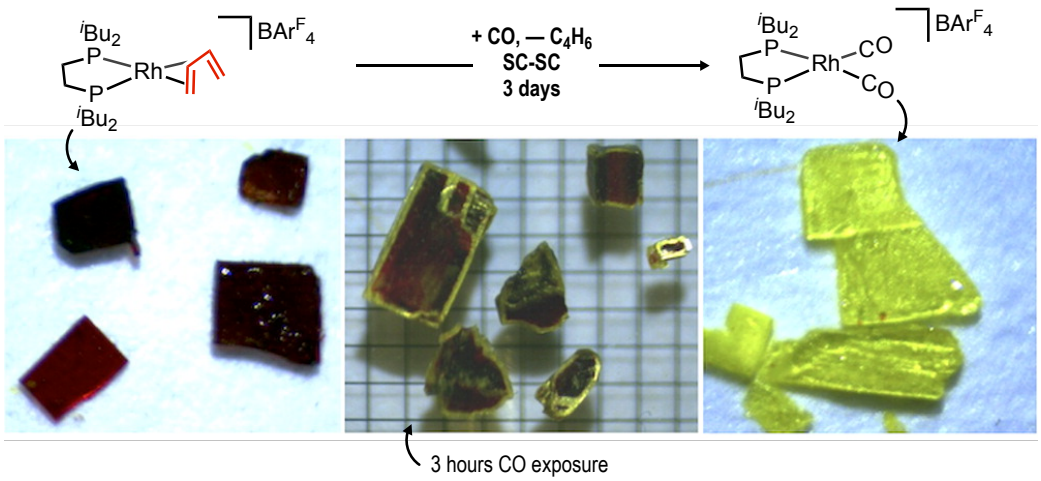

Figure 3.7: Passivation of molecular crystals of a rhodium–butadiene complex with CO gas, visualising a diffusion controlled solid-state reaction process. Image adapted from Weller *et al*., copyright 2015 American Chemical Society.[33]

In this example, when red coloured crystals of a rhodium-butadiene complex are exposed to a CO atmosphere they react to form the yellow coloured bis-CO complex, displacing the coordinated butadiene. Upon initial CO exposure, only the surface species were passivated (< 3 hours) and after longer exposure times (3 days), complete displacement throughout the bulk material is observed. This shows the clear visualisation of this diffusion-controlled reaction front by a colour change of the crystalline material. This also shows how a reaction front moves from outside-in, in a crystalline solid. A similar reaction mobility can be suggested to occur in **[1-*iso*butene][BAr^{F}_4]**, linking to the proposed diffusion-controlled reaction front during dehydrogenation.

3.3.2. σ-*Iso*pentane Complex

In analogous experimental conditions to that of the dehydrogenation of **[1-*iso*butane][BAr$^{F}_{4}$]**, the dehydrogenation of **[1-*iso*pentane][BAr$^{F}_{4}$]** could also be followed using reaction progress monitoring (Scheme 3.12).

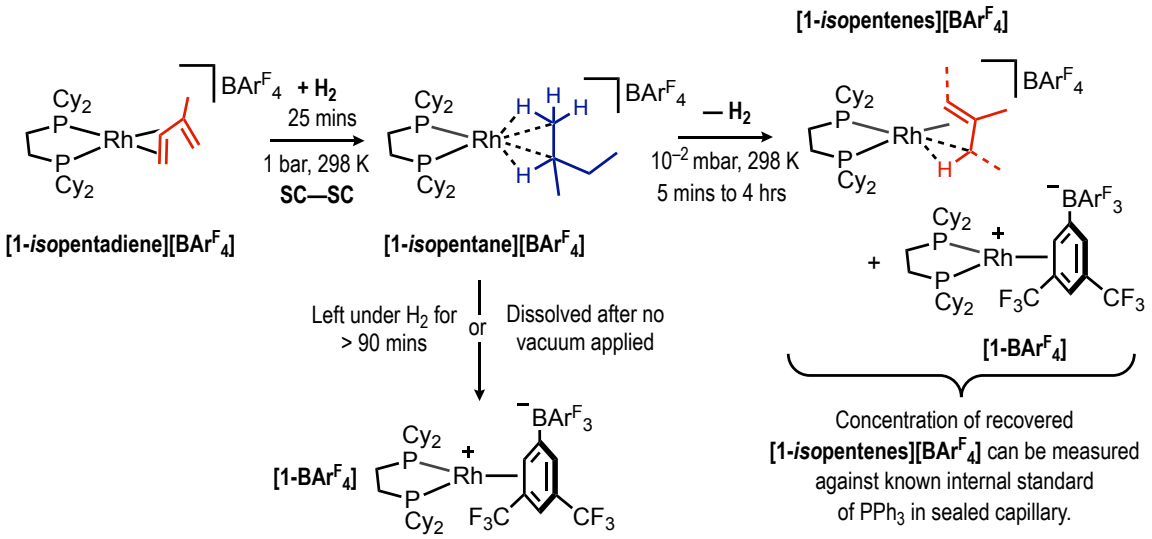

Scheme 3.12: Experimental procedures for kinetic analysis of alkane dehydrogenation experiments.

These data are shown in Figure 3.8 by blue circles, along with temporal profiles of COPASI modelled first and second order rate constants and JMAK analysis. As with the **[1-*iso*butane][BAr$^{F}_{4}$]** system, the modelled first order rate profile for **[1-*iso*pentane][BAr$^{F}_{4}$]** dehydrogenation did not give a good fit, and both the second order rate profile and modified JMAK profile gave a satisfactory visual fit.

The growth rate constant from the modified Avrami plot was found to be 9.5×10^{-4} ($\pm 6 \times 10^{-5}$) s^{-1} and $n = 0.50 \pm 0.02$. The smaller value of k reflects the longer time to completion compared to that of **[1-*iso*butane][BAr$^{F}_{4}$]**. The exponent value (n) is again suggestive of a diffusion-controlled reaction, as it is non-integer and less than one. This may suggest both the dehydrogenation of **[1-*iso*butane][BAr$^{F}_{4}$]** and **[1-*iso*pentane][BAr$^{F}_{4}$]** are following similar mechanisms, both occurring *via* an interplay between a diffusion controlled and second order process.

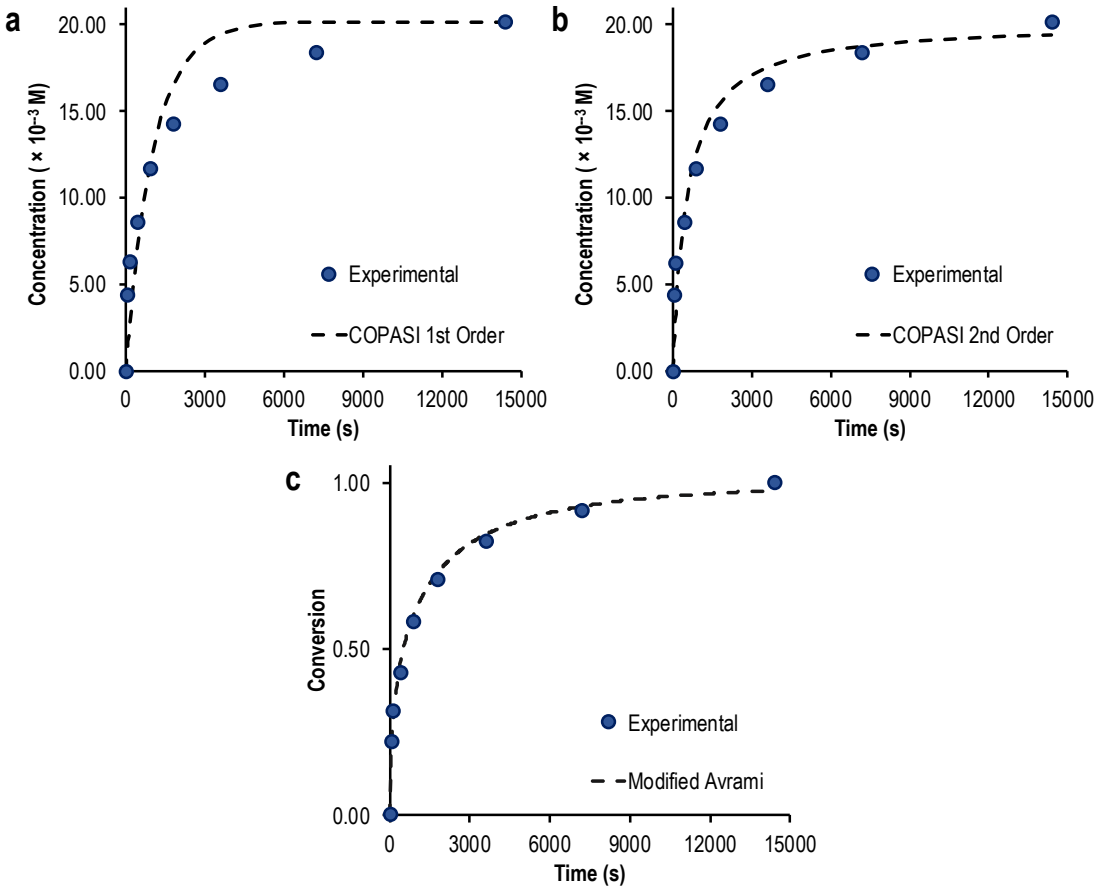

Figure 3.8: Temporal plots of **[1-*iso*pentane][BAr$^{F}_{4}$]** dehydrogenation to form **[1-*iso*pentenes][BAr$^{F}_{4}$]**. Dashed lines show COPASI[35] simulated plots of **a**) First order process and **b**) Second order process and modified JMAK plot shown in **c**), where 9.5×10^{-4} ($\pm 6 \times 10^{-5}$) s^{-1} and n = 0.50 ± 0.02. Each data point (blue circles) represents an individual dehydrogenation experiment.

The maximum yield of recoverable **[1-*iso*pentenes][BAr$^{F}_{4}$]** was found to be approximately 80 %, when compared to initial loading of **[1-*iso*pentadiene][BAr$^{F}_{4}$]**. As discussed in Chapter 2, the maximum spectroscopic yield of **[1-*iso*pentane][BAr$^{F}_{4}$]** was ~80 %. The ~20 % formation of **[1-BAr$^{F}_{4}$]** decomposition product was due to the instability of **[1-*iso*pentane][BAr$^{F}_{4}$]** under H_2 atmosphere during the relatively long hydrogenation time (25 minutes). This has been factored into the kinetic analysis.

3.4. Computational Studies

The computational calculations presented in Section 3.4. were performed by Arron L. Burnage or Bengt E. Tegner from Stuart A. Macgregor's research group at Heriot-Watt University, Edinburgh.

To further explore the mechanism of alkane dehydrogenation, computational studies were conducted. All calculations, unless otherwise stated, are inclusive of the surrounding $[BAr^F{}_4]^-$ anions using Periodic DFT techniques.

The dehydrogenation of free *iso*butane to *iso*butene is known to be endothermic (+28.2 kcal mol^{-1})[5] yet a far smaller energy penalty is present in **[1-*iso*butane][BAr$^F{}_4$]** dehydrogenation. Periodic DFT calculations investigating the thermodynamics of this system show that **[1-*iso*butane][BAr$^F{}_4$]** is slightly favoured over **[1-*iso*butene][BAr$^F{}_4$]**, thus making this dehydrogenation reaction of coordinated *iso*butane endogenic (+10.8 kcal mol^{-1}, Figure 3.13a). This value is consistent with the dehydrogenation of **[1-cyclohexane][BAr$^F{}_4$]** to **[1-cyclohexene][BAr$^F{}_4$]**, calculated at +6.6 kcal mol^{-1}.[26]

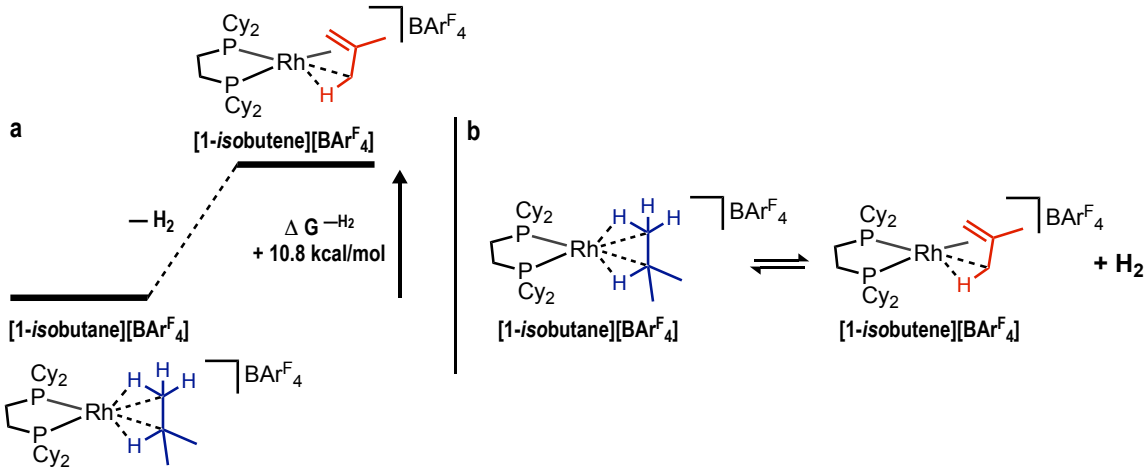

Scheme 3.13: **a**) Free energy profile of the hydrogenation of **[1-*iso*butene][BAr$^F{}_4$]** to **[1-*iso*butane][BAr$^F{}_4$]** and subsequent dehydrogenation to **[1-*iso*butene][BAr$^F{}_4$]**, with calculated energy penalty. **b**) Proposed equilibrium in **[1-*iso*butane][BAr$^F{}_4$]** (de)hydrogenation.

This relatively small energy penalty may suggest that an equilibrium between the two complexes is present in the solid-state. The dehydrogenation reaction therefore is likely driven by the constant removal of H_2 from the system, which biases this equilibrium (Scheme 3.13b).[14] The entropic contribution of hydrogen removal therefore overcomes the enthalpic penalty, and makes the overall free energy of the system favourable. Additionally, as **[1-*iso*butane][BAr$^F{}_4$]** is thermodynamically preferred over

[1-*iso*butene][BAr$^{F}_{4}$] in the solid-state, this may suggest that substitution of *iso*butene with *iso*butane may be achievable. Importantly however, no kinetic contributions are considered in this.

The mechanism of the dehydrogenation of **[1-*iso*butane][BAr$^{F}_{4}$]** was also calculated. Shown in Scheme 3.14, two possible pathways were postulated; which occur initially *via* either the initial primary or tertiary C–H activation on *iso*butane. Both pathways then follow β-hydride transfer step, to give a Rh^{III} dihydride *iso*butene complex, before undergoing reductive coupling to give a σ-H$_2$ complex. Dihydrogen loss then reforms **[1-*iso*butene][BAr$^{F}_{4}$]**. Although drawn as a cycle, substitution of the coordinated *iso*butene with *iso*butane in the final step has not been achieved and is indicated by a dashed arrow. This step is necessary however in order to make this process catalytic.

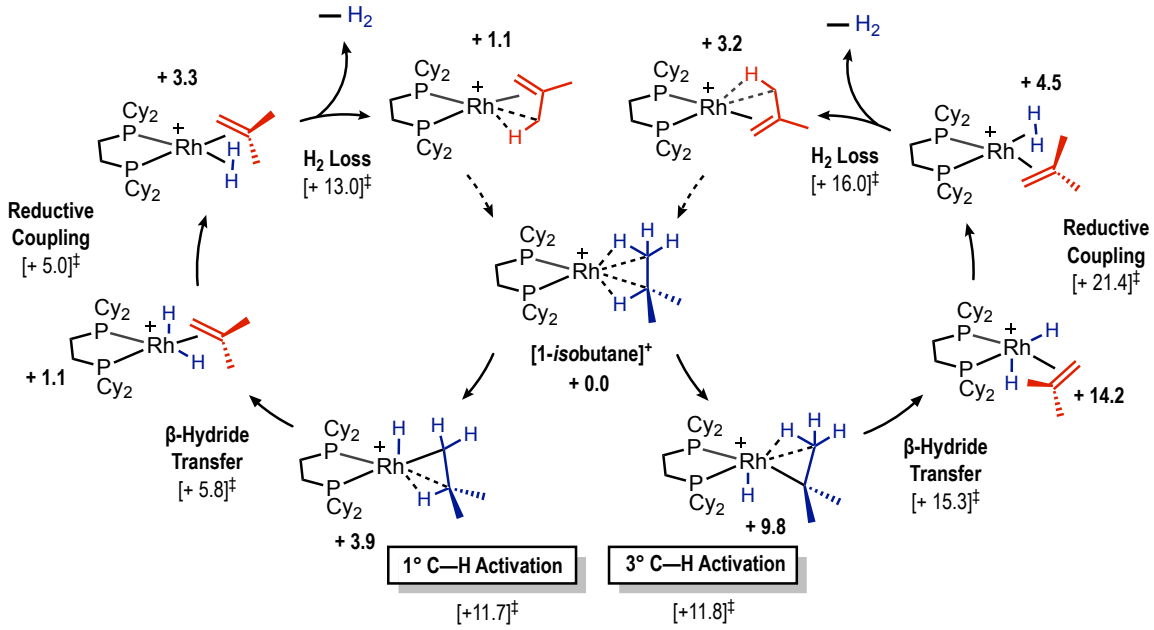

Scheme 3.14: Calculated dehydrogenation pathway in the solid-state for the dehydrogenation of **[1-*iso*butane][BAr$^{F}_{4}$]**, showing two potential pathways of initial primary C–H activation (left) *versus* tertiary C–H activation (right). [BAr$^{F}_{4}$]$^{-}$ anions not shown for clarity. Values given in bold refer to the free energy (ΔG / kcal mol^{-1}) compared to **[1-*iso*butane][BAr$^{F}_{4}$]**, and values in square brackets refer to transition state energies of each step.

Although the ΔG‡ of the initial oxidative cleavage of the respective C–H bonds is not favoured by either pathway (~11.7 kcal mol^{-1}), the products of primary C–H activation are calculated consistently as far more stable compared to their analogues in the tertiary C–H activated pathway. This is shown by the lower free energies with respect to **[1-*iso*butane]$^{+}$** throughout this cycle. A large difference in reductive coupling steps is observed between the two pathways however. The energy of the tertiary C–H activation

pathway is far greater (+21.4 kcal mol^{-1}) than the primary C–H activated pathway (+5.0 kcal mol^{-1}). This was due to the associated rotation of the coordinated *iso*butene ligand during the reductive coupling step.

In this rotation, it was found the methyl groups interact with the neighbouring $[BAr^F_4]^-$ anions within the solid-state cavity, obstructing this movement. This interplay between the *iso*butene rotation and neighbouring $[BAr^F_4]^-$ anions may be the cooperative mechanism linked to the second order rate kinetics discussed in Section 3.3. No such rotation is observed in the primary C–H activation pathway and so the activation Gibbs free energy is only +5.0 kcal mol^{-1}, and so the rate limiting step is now calculated as H_2 loss (+13.0 kcal mol^{-1}). This H_2 loss is consistent also with the JMAK kinetic analysis, suggesting the rate limiting step here could be diffusion controlled (Section 3.3).

Importantly, when the same pathway was calculated as an isolated cation, which removes any solid-state $[BAr^F_4]^-$ anion interactions, the rate determining step was found to be H_2 loss for both pathways (+14.5 kcal mol^{-1} and +15.1 kcal mol^{-1} for 1º and 3º activation respectively). This shows how large a factor the solid-state environment is when calculating SMOM reaction pathways.

3.5. Other σ-Alkane Complexes

As well as **[1-*iso*butane][BAr$^F_4$]** and **[1-*iso*pentane][BAr$^F_4$]**, all the σ-alkane complexes presented in Chapter 2 had their reactivity under a dynamic vacuum studied. These results are presented next. As **[1-butane][BAr$^F_4$]** itself is challenging to isolate, it is inappropriate to consider any dehydrogenation products.

3.5.1. σ-(3-methylpentane) Complex Dehydrogenation

To see if **[1-(3-methylpentane)][BAr$^F_4$]** undergoes acceptorless dehydrogenation in the solid-state, a sample of **[1-(3-methylpentane)][BAr$^F_4$]** was placed under a dynamic vacuum for 16 hours, outlined in Scheme 3.15.

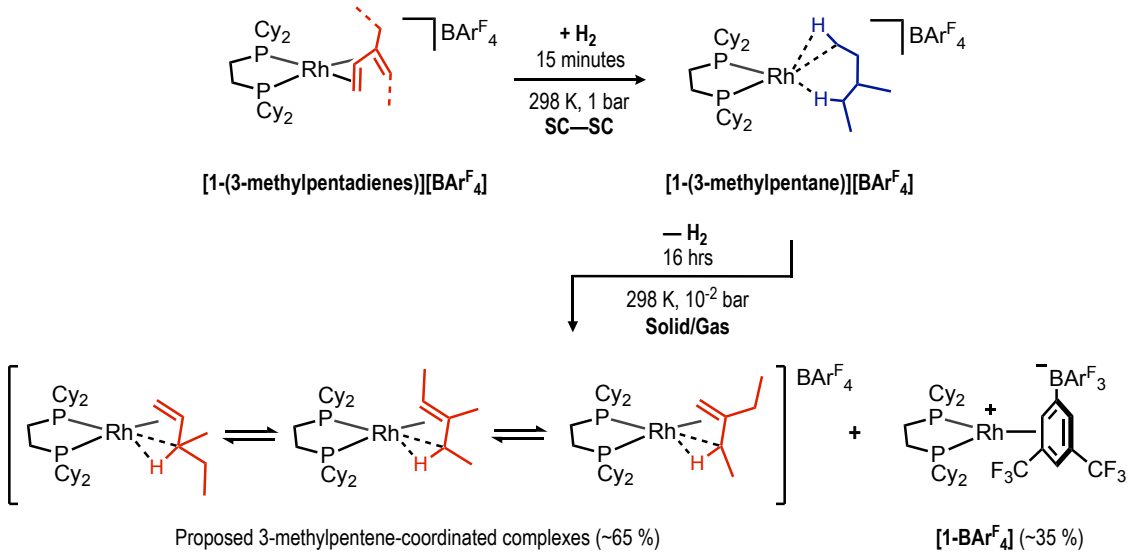

Scheme 3.15: Scheme outlining the (de)hydrogenation reactions and possible isomers of a bound 3-methylpentenes complex formed by the dehydrogenation of **[1-(3-methylpentane)][BAr$^F_4$]**.

The $^{31}P\{^1H\}$ SSNMR spectrum shows a major signal [δ 93] after 16 hours under a dynamic vacuum (Figure 3.9a). This is assigned to a proposed 3-methylpentenes-coordinated complex, as the spectrum is analogous to both $^{31}P\{^1H\}$ SSNMR spectra of **[1-*iso*butene][BAr$^F_4$]** and **[1-*iso*pentenes][BAr$^F_4$]**. This not only suggests that multiple 3-methylpentene isomers are formed, but they are also undergoing a rapid, fluxional process making the ^{31}P environments coincident.

A large amount of **[1-BAr$^F_4$]** is also observed [δ 91], proposed from the decomposition of **[1-(3-methylpentane)][BAr$^F_4$]** during the dehydrogenation reaction. Notably, the signals relating to **[1-(C$_6$-dienes)][BAr$^F_4$]** are a result of under-hydrogenation of the initial sample. As these signals have not changed relative intensities upon dehydrogenation, this

suggests these signals are not a product of a second dehydrogenation. To aid the visualisation of this mixture, the $^{31}P\{^{1}H\}$ SSNMR spectrum was modelled and deconvoluted, shown in Figure 3.9b.

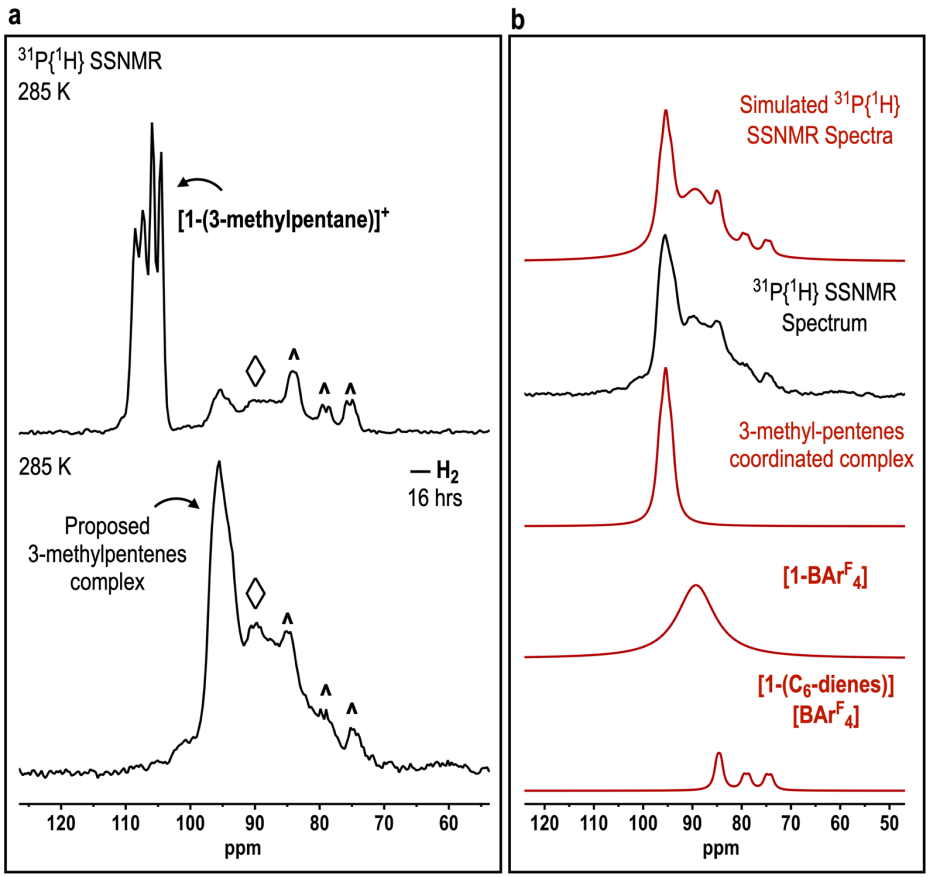

Figure 3.9: a) The $^{31}P\{^{1}H\}$ (162 MHz, 285 K, 10 kHz spin rate) SSNMR spectra of **[1-(3-methylpentane)][BAr$^{F}_{4}$]** and after the sample was placed under a dynamic vacuum for 16 hours. ◊ = **[1-BAr$^{F}_{4}$]** and **^** = **[1-(C$_6$-dienes)][BAr$^{F}_{4}$]**. **b**) Simulated and experimental $^{31}P\{^{1}H\}$ SSNMR spectra of a proposed 3-methylpentenes-complex compared with known signals from **[1-BAr$^{F}_{4}$]** and **[1-(C$_6$-dienes)][BAr$^{F}_{4}$]**.

The modelled spectrum suggests a spectroscopic yield of ~65 % of this proposed 3-methylpentenes complex. Single crystals of the dehydrogenated product were not of sufficient quality for a structure to be collected by single-crystal x-ray diffraction, so this not a SC-SC transformation. Unfortunately, this proposed 3-methylpentenes complex could not be isolated from the **[1-BAr$^{F}_{4}$]** decomposition product, inhibiting the full characterisation of the dehydrogenation product and making any kinetics studies inappropriate.

The presence of 3-methylpentenes however was confirmed by dissolution of the proposed 3-methylpentenes-bound complex in a C_6D_6/Acetone-d_6 mixture. This liberated the bound 3-methylpentenes, and formed the benzene-coordinated complex $[Rh(Cy_2PCH_2CH_2PCy_2)(C_6H_6)][BAr^F{}_4]$, **[1-$C_6H_6$][$BAr^F{}_4$]**.[32] The ^1H NMR spectrum of the isolated volatiles is shown in Figure 3.10, with assigned 3-methylpentene isomers highlighted. Although the exact ratios of the isomers of 3-methylpentenes in the solid-state was not found, this solution trapping method suggests (*E/Z*)-3-methyl-2-pentene is the favoured isomer in solution.

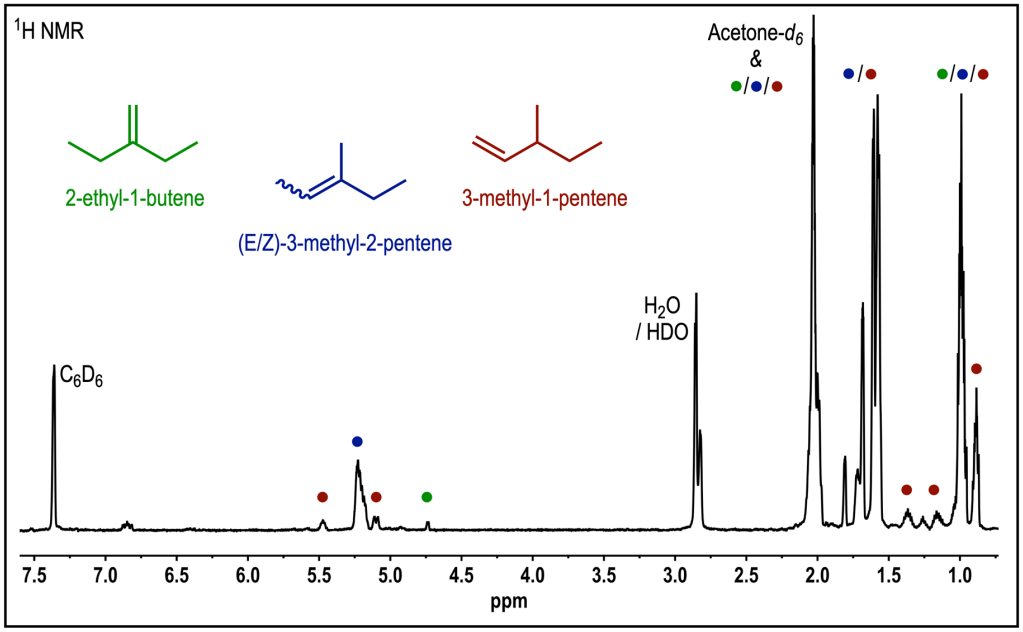

Figure 3.10: The solution ^1H NMR (C_6D_6 / $(CD_3)_2CO$, 298 K, 500 MHz) spectrum of isolated 3-methylpentenes volatiles. Signals from the mixture of 3-methylpentenes isomers of 2-ethyl-1-butene,[45] (*E/Z*)-3-methyl-2-pentene[46] and 3-methyl-1-pentene[47] are marked respectively.

Interestingly, when solid material of **[1-(3-methylpentane)][$BAr^F{}_4$]** was placed under dynamic vacuum for only 4 hours, signals for **[1-(3-methylpentane)][$BAr^F{}_4$]** were still present in $^{31}P\{^1H\}$ SSNMR spectrum (~30 % of the total signals). This suggests the dehydrogenation of **[1-(3-methylpentane)][$BAr^F{}_4$]** occurs at an attenuated rate compared to that of **[1-*iso*butane][$BAr^F{}_4$]** and **[1-*iso*pentane][$BAr^F{}_4$]**. These were shown to be quantitatively complete in 2 and 4 hours respectively.

This attenuated rate of dehydrogenation may result from the larger, bulkier size of 3-methylpentane compared to that of *iso*butane and *iso*pentane, making transition states within the dehydrogenation pathway in the solid-state more unfavourable in comparison.

During this dehydrogenation as well, decomposition by alkane loss and $[BAr^F_4]^-$ anion coordination to form **[1-BAr$^F_4$]** also occurs on a similar timescale. This was shown by the large amount of **[1-BAr$^F_4$]** formed from the solid-state NMR spectrum. The similar rates between dehydrogenation and decomposition is an idea discussed further in Section 3.6.

3.5.2. σ-Propane Complex Dehydrogenation

When a sample of **[1-propane][BAr$^F_4$]** was placed under a dynamic vacuum for 30 minutes, 30 % **[1-propene][BAr$^F_4$]** could be recovered (Scheme 3.16). This was shown by the solution $^{31}P\{^1H\}$ NMR spectrum of the dissolved material after this time, and this yield did not increase on longer timescales under vacuum.

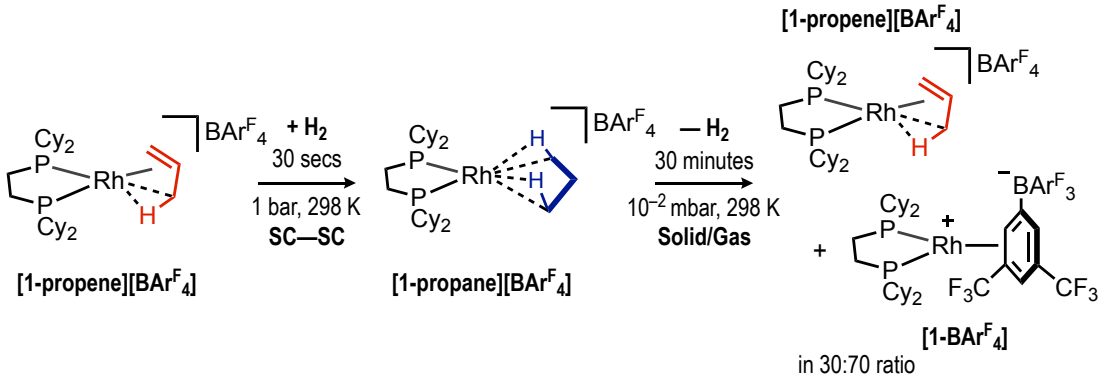

Scheme 3.16: Synthetic route to **[1-propene][BAr$^F_4$]** hydrogenation and dehydrogenation.

To confirm the **[1-propene][BAr$^F_4$]** recovered is a product of dehydrogenation, and not just under-hydrogenation of the sample, a split-batch experiment was conducted (see Scheme 3.6). After an initial 30 seconds of hydrogenation, no evidence for any **[1-propene][BAr$^F_4$]** could be found by solution $^{31}P\{^1H\}$ NMR spectroscopy within this half of the dissolved material.

The 30 % recovered **[1-propene][BAr$^F_4$]** means the dehydrogenation does occur for **[1-propane][BAr$^F_4$]**, however in poor yields. This may be limited by the fact **[1-propane][BAr$^F_4$]** has a lifetime of only 30 minutes, as described in Figure 2.10, suggesting, like **[1-(3-methylpentane)][BAr$^F_4$]**, a competitive rate between decomposition and dehydrogenation is present.

3.5.3. σ-Hexane Complex Dehydrogenation

For **[1-hexane][BAr$^F_4$]**, upon exposure to dynamic vacuum for 60 minutes, no evidence for any isolated *n*-hexenes could be found upon dissolution. Only signals relating to liberated *n*-hexane are observed in the ^{1}H NMR spectrum. As **[1-hexane][BAr$^F_4$]** was only shown to be stable for 60 minutes at 298 K before complete **[1-BAr$^F_4$]** formation (Figure 2.30), this suggests no dehydrogenation events occurred from **[1-hexane][BAr$^F_4$]** (Scheme 3.17).

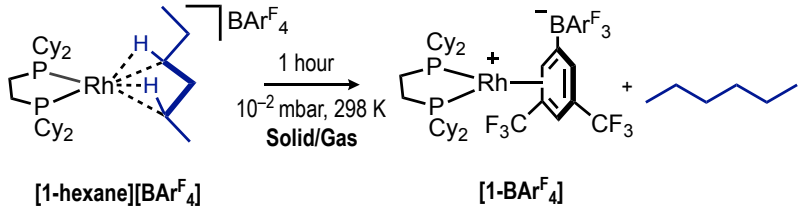

Scheme 3.17: Attempted dehydrogenation of **[1-hexane][BAr$^F_4$]**.

This may be due to an attenuated rate of dehydrogenation, possibly due to the bi-capped square prism arrangement of [BAr$^F_4$]$^-$ anions in the solid-state not supporting a specific transition state or intermediate complex within the dehydrogenation pathway. Additionally, if this packing structure is inherently unstable, this may also increase the relative rate of [BAr$^F_4$]$^-$ coordination and complex decomposition.

3.6. Rates of Dehydrogenation and Decomposition

Expanding upon these observations, the relative rates of alkane dehydrogenation in the solid-state can be compared with the rate of complex decomposition to **[1-BAr$^F_4$]**. These have been assigned the rates of k_1 and k_2 respectively and are depicted in Scheme 3.18.

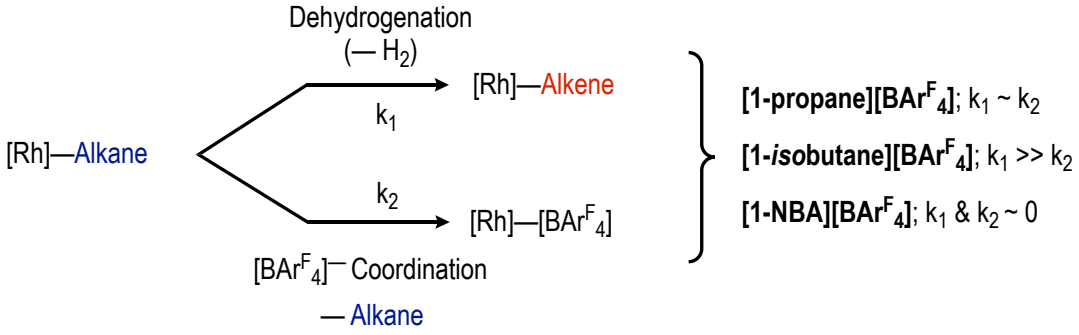

Scheme 3.18: Relative rates of dehydrogenation (K_1) or decomposition (K_2) for a selection of σ-alkane complexes.

For both **[1-propane][BAr$^F_4$]** and **[1-(3-methylpentane)][BAr$^F_4$]**, both k_1 and k_2 must be of a similar value, as a mixture of decomposition and dehydrogenated products is observed after vacuum is applied. These relative rates however must overwhelmingly favour the dehydrogenation pathway in the complexes of **[1-*iso*butane][BAr$^F_4$]** and **[1-*iso*pentane][BAr$^F_4$]**. As 100 % alkene complex is recovered, $k_1 >> k_2$. The inverse of this is observed for **[1-hexane][BAr$^F_4$]**, where $k_2 >> k_1$, as no dehydrogenation products are observed.

Interestingly, for **[1-NBA][BAr$^F_4$]** neither pathway is experimentally observed. After 4 months under an inert atmosphere, no significant decomposition is reported and when placed under a dynamic vacuum for 3 days, no evidence for any norbornene or norbornadiene was found, suggesting k_2 and $k_1 \sim 0$. Theoretically, an ideal system would therefore exhibit a fast k_1 and slow, or 0, k_2. This would result in a facile alkane dehydrogenation reaction, with no loss in yield of the desired product.

3.7. Chapter Conclusions

Chapter 3 has highlighted the ease in which alkane dehydrogenation can occur from a range of molecular σ-alkane complexes. Scheme 3.19 shows the products from dehydrogenation of the σ-alkane complexes presented in this thesis.

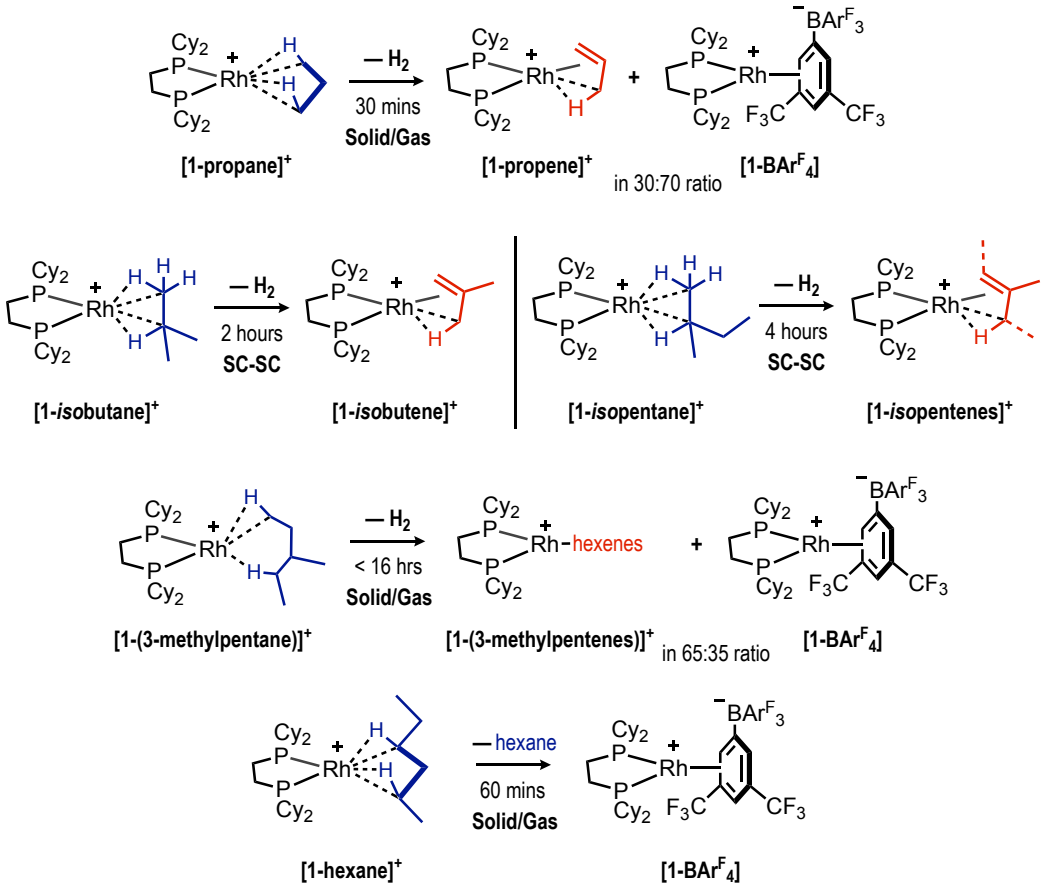

Scheme 3.19: Summary of a range of a σ-alkane complexes and their reactions under a dynamic vacuum.

Most notable are the complexes of **[1-*iso*butane][BAr$^F_4$]** and **[1-*iso*pentane][BAr$^F_4$]**, which underwent acceptorless alkane dehydrogenation at room temperature in the solid-state to yield **[1-*iso*butene][BAr$^F_4$]** and **[1-*iso*pentenes][BAr$^F_4$]** respectively. This is conducted by simple exposure to a dynamic vacuum or argon flow, showing the removal of H_2 from the system is the driving force behind these reactions. This suggests that once a σ-alkane complex is formed, the following C–H activation steps are facile and readily accessible. The instability of the σ-alkane complexes of **[1-propane][BAr$^F_4$]**, **[1-butane][BAr$^F_4$]**, **[1-hexane][BAr$^F_4$]** and **[1-(3-methylpentane)][BAr$^F_4$]** meant that fully deconvoluting the dehydrogenation reaction pathway for these complexes was not possible.

The SMOM methodology allows for the reliable production and isolation of solid-state σ-alkane complexes, which means the reaction progress of alkane dehydrogenation can be studied. This has been presented for both **[1-*iso*butane][BAr$^F_4$]** and **[1-*iso*pentane][BAr$^F_4$]**, and the temporal profiles modelled to that of modified JMAK kinetics; suggesting the rate limiting step in this process is a diffusion-controlled process, described as H_2 loss.

This is good agreement with computational calculations performed on these systems, again suggesting H_2 de-coordination is the rate limiting step from a reaction pathway involving the initial primary C–H activation. Calculations have also shown that a dehydrogenation pathway following initial tertiary C–H activation is less achievable, due to a rotation of the coordinated *iso*butene ligand, inhibited by the neighbouring [BAr$^F_4$]$^-$ anion.

Expanding upon this work would be to complete the dehydrogenation cycle and make this process catalytic, Scheme 3.20. The displacement of a coordinated alkene by an alkane in SMOM processes has yet to be achieved and represents probably the most difficult kinetic hurdle to overcome. Placing alkene complexes under high pressures of alkane gases, the use of continuous flow-conditions, or photophysical pathways, may be options for achieving a catalytic dehydrogenation process.

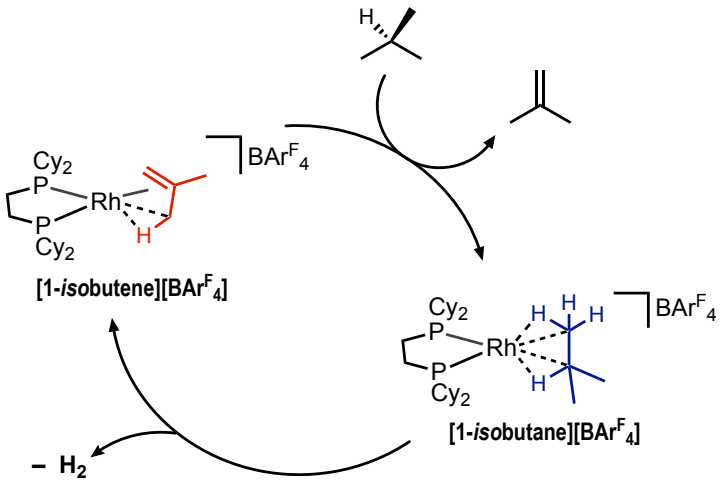

Scheme 3.20: Catalytic *iso*butane dehydrogenation.

3.8. References

1 K. I. Goldberg and A. S. Goldman, *Acc. Chem. Res.*, 2017, **50**, 620–626.
2 G. B. Shul'pin and A. E. Shilov, *Activation and Catalytic Reactions of Saturated Hydrocarbons in the Presence of Metal Complexes*, Kluwer Academic Publishers, 2000.
3 P. C. A. Bruijnincx and B. M. Weckhuysen, *Angew. Chem. Int. Ed.*, 2013, **52**, 11980–11987.
4 A. S. Goldman and K. I. Goldberg, in *ACS Symposium Series*, 2004, pp. 1–43.
5 P. J. Linstron and W. G. Mallard, *NIST Chemistry Webbook*, 2020.
6 J. J. H. B. Sattler, J. Ruiz-Martinez, E. Santillan-Jimenez and B. M. Weckhuysen, *Chem. Rev.*, 2014, **114**, 10613–10653.
7 K. Searles, K. W. Chan, J. A. Mendes Burak, D. Zemlyanov, O. Safonova and C. Copéret, *J. Am. Chem. Soc.*, 2018, **140**, 11674–11679.
8 U. Rodemerck, E. V. Kondratenko, T. Otroshchenko and D. Linke, *Chem. Commun.*, 2016, **52**, 12222–12225.
9 F. Obenaus, W. Droste and J. Neumeister, *Butenes: Ullmanns' Encyclopedia of Industrial Chemistry*, Wiley-VCH, 2012.
10 A. Kumar, T. M. Bhatti and A. S. Goldman, *Chem. Rev.*, 2017, 117, 12357–12384.
11 J. Choi, A. H. R. MacArthur, M. Brookhart and A. S. Goldman, *Chem. Rev.*, 2011, 111, 1761–1779.
12 X. Zhou, S. Malakar, T. Zhou, S. Murugesan, C. Huang, T. J. Emge, K. Krogh-Jespersen and A. S. Goldman, *ACS Catal.*, 2019, **9**, 4072–4083.
13 T. Aoki and R. H. Crabtree, *Organometallics*, 1993, **12**, 294–298.
14 W. Xu, G. P. Rosini, K. Krogh-Jespersen, A. S. Goldman, M. Gupta, C. M. Jensen and W. C. Kaska, *Chem. Commun.*, 1997, 2273–2274.
15 A. D. Chowdhury, N. Weding, J. Julis, R. Franke, R. Jackstell and M. Beller, *Angew. Chem. Int. Ed.*, 2014, **53**, 6477–6481.
16 J. A. Maguire, W. T. Boese, M. E. Goldman and A. S. Goldman, *Coord. Chem. Rev.*, 1990, **97**, 179–192.
17 Z. Huang, M. Brookhart, A. S. Goldman, S. Kundu, A. Ray, S. L. Scott and B. C. Vicente, *Adv. Synth. Catal.*, 2009, **351**, 188–206.
18 B. Sheludko, M. T. Cunningham, A. S. Goldman and F. E. Celik, *ACS Catal.*, 2018, **8**, 7828–7841.
19 A. Kumar, T. Zhou, T. J. Emge, O. Mironov, R. J. Saxton, K. Krogh-Jespersen and A. S. Goldman, *J. Am. Chem. Soc.*, 2015, **137**, 9894–9911.
20 C. Hall and R. N. Perutz, *Chem. Rev.*, 1996, **96**, 3125–3146.
21 P. J. Perez, *Alkane C-H Activation by Single-Site Metal Catalysis*, Springer US, 2012.
22 R. G. Bergman, *Nature*, 2007, **446**, 391–393.
23 M. G. Crestani, A. K. Hickey, X. Gao, B. Pinter, V. N. Cavaliere, J. I. Ito, C. H. Chen and D. J. Mindiola, *J. Am. Chem. Soc.*, 2013, **135**, 14754–14767.
24 A. A. Bengali, R. H. Schultz, B. C. Moore and R. G. Bergman, *J. Am. Chem. Soc.*, 1994, **116**, 9585–9589.
25 A. B. Chaplin, A. I. Poblador-Bahamonde, H. A. Sparkes, J. A. K. Howard, S. A. Macgregor and A. S. Weller, *Chem. Commun.*, 2009, **91**, 244–246.
26 A. I. McKay, A. J. Bukvic, B. E. Tegner, A. L. Burnage, A. J. Martĺnez-Martĺnez, N. H. Rees, S. A. Macgregor and A. S. Weller, *J. Am. Chem. Soc.*, 2019, **141**, 11700–11712.
27 M. Bohnet, *Ullmanns' Encyclopedia of Industrial Chemistry*, Wiley-VCH, 2004.
28 S. D. Pike and A. S. Weller, *Philos. Trans. R. Soc. A*, 2015, **373**, 20140187.
29 F. M. Chadwick, A. I. McKay, A. J. Martinez-Martinez, N. H. Rees, T. Krämer, S. A. Macgregor and A. S. Weller, *Chem. Sci.*, 2017, **8**, 6014–6029.
30 S. D. Pike, F. M. Chadwick, N. H. Rees, M. P. Scott, A. S. Weller, T. Krämer and S. A. Macgregor, *J. Am. Chem. Soc.*, 2015, **137**, 820–833.
31 F. M. Chadwick, N. H. Rees, A. S. Weller, T. Krämer, M. Iannuzzi and S. A. Macgregor, *Angew. Chem. Int. Ed.*, 2016, **55**, 3677–3681.
32 A. I. McKay, A. J. Bukvic, B. E. Tegner, A. L. Burnage, A. J. Martínez-Martínez, N. H. Rees, S. A. Macgregor and A. S. Weller, *J. Am. Chem. Soc.*, 2019, **141**, 11700–11712.
33 S. D. Pike, T. Krämer, N. H. Rees, S. A. Macgregor and A. S. Weller, *Organometallics*, 2015, **34**, 1487–1497.
34 S. M. Chapp and N. D. Schley, *Organometallics*, 2017, **36**, 4355–4358.
35 S. Hoops, S. Sahle, R. Gauges, C. Lee, J. Pahle, N. Simus, M. Singhal, L. Xu, P. Mendes and U. Kummer, *Bioinformatics*, 2006, **22**, 3067–3074.
36 M. Avrami, *J. Chem. Phys.*, 1939, **7**, 1103–1112.
37 M. Avrami, *J. Chem. Phys.*, 1940, **8**, 212–224.
38 M. Avrami, *J. Chem. Phys.*, 1941, **9**, 177–184.
39 M. J. Van Vleet, T. Weng, X. Li and J. R. Schmidt, *Chem. Rev.*, 2018, 118, 3681–3721.
40 J. B. Benedict and P. Coppens, *J. Phys. Chem. A*, 2009, **113**, 3116–3120.
41 A. G. Jarvis, H. A. Sparkes, S. E. Tallentire, L. E. Hatcher, M. R. Warren, P. R. Raithby, D. R. Allan, A. C. Whitwood, M. C. R. Cockett, S. B. Duckett, J. L. Clark and I. J. S. Fairlamb, *CrystEngComm*, 2012, **14**, 5564–5571.
42 M. Bertmer, R. C. Nieuwendaal, A. B. Barnes and S. E. Hayes, *J. Phys. Chem. B*, 2006, **110**, 6270–6273.
43 A. Khawam and D. R. Flanagan, *J. Phys. Chem. B*, 2006, **110**, 17315–17328.
44 E. E. Finney and R. G. Finke, *Chem. Mater.*, 2009, **21**, 4692–4705.
45 *2-Ethyl-1-butene -- AIST Spectr. Database Org. Compd. -- (SDBS No. 10346) -- Date Acc. 03-06-2020*.
46 *3-Methyl-2-pentene, Mix. cis trans -- Sigma-Aldrich -- (Cat. Number 111775) -- Date Acc. 03-07-2020*.
47 *3-Methyl-1-pentene -- Sigma-Aldrich -- (Cat. Number 111147) -- - Date Acc. 03-07-2020*.

Chapter 4:
H/D Exchange within Solid-State σ-Alkane Complexes

4.1. Chapter Introduction

The activation of C–H bonds at a metal centre enables a number of reaction pathways, a selection of which are shown in Scheme 4.1.[1–4] If these pathways are reversible, then H/D exchange can occur of the C–H bond. This reactivity upon the σ-alkane complexes reported in Chapter 2 forms the basis for Chapter 4.

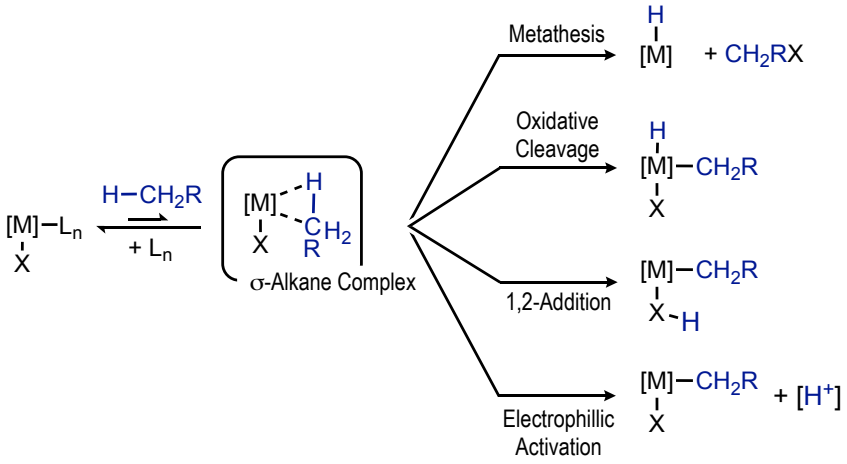

Scheme 4.1: C–H Activation pathways starting from an σ-alkane complex.

Isotope exchange reactions within M•••C–H interactions have been previously reported.[2,5–9] However, due to the non-quantitative formation, isolation and stability of σ-alkane complexes,[10,11] reports tend to study the overall H/D exchange process of free alkanes, rather than the on-metal exchange reaction steps. H/D exchange within E–H σ-complexes of B–H,[12] Si–H[13] and H–H[14,15] metal coordinated systems has been also reported, which start from the respective σ-complex. This is possible for E–H systems, due to the increased stabilities of the σ-complex compared to that of σ-alkane complexes.[16] H/D exchange is readily observed in agostic complexes, where C–H activation is readily achievable due to the forced close proximity of the C–H bond towards a metal centre.[17]

It has been shown that H/D exchange within σ-alkane complexes can be a facile process after initial C–H cleavage.[18,19] Evidence of H/D exchange has even been used to prove the formation of solution, transient, σ-alkane complexes.[20–22] Studies upon H/D exchange within alkanes may not follow trends predicted by bond dissociation energies, as rate limiting steps typically arise from either initial alkane coordination, or to β-elimination steps, rather than the preceding C–H activation steps.[23–25] This goes to show that however strong C–H bonds may be (~400 kJ mol^{-1}),[14] using an organometallic catalyst can make bond breaking processes facile.

Mechanistically, H/D exchange within coordinating σ-ligands in organometallic complexes can occur through several pathways.[26–28] Late transition metals, with a range of accessible oxidation states, typically undergo H/D exchange *via* oxidative addition / reductive elimination pathways (Scheme 4.2a). Oxidative cleavage of the σ-complex forms a metal hydride species, which can then reductively couple and release the new product.[28]

A second mechanism is that of σ-bond metathesis (Scheme 4.2b).[29] This is typically employed by transition metals that cannot undergo oxidation state changes, such as metals with a d^0 electronic configuration or late transition metals in high oxidation states. This involves a 4-centred transition state and a metal centre that remains in a constant oxidation state throughout.

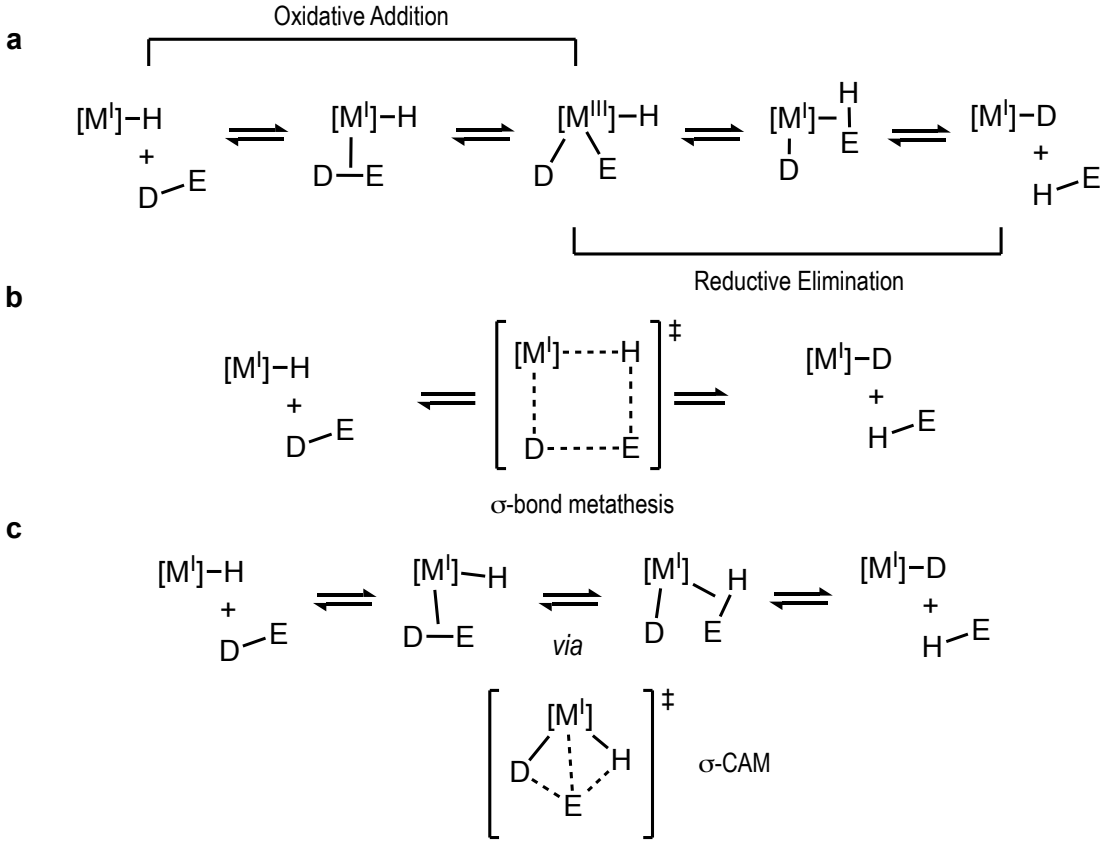

Scheme 4.2: Metathesis reaction following **a**) oxidative/reductive **b**) σ-bond metathesis and **c**) σ-CAM pathways, starting from a metal-hydride complex.

A third mechanism, σ-complex-assisted metathesis[30,31] (σ-CAM, Scheme 4.2c) has similarities with the first two mechanisms presented above. Similar to σ-bond metathesis, a constant oxidation state of the metal is observed throughout, however, σ-CAM proceeds *via* distinct σ-complex intermediates before and after the transition step. Additionally to these mechanisms, and specific to the ideas in this thesis, σ-alkane complexes can

undergo dehydrogenation, which is the microscopic reverse of alkene hydrogenation. β-elimination following C–H activation of the coordinated alkane leads to dehydrogenation, re-forming the alkene complex. Consequential deuteration of the alkene bond leads to deuterium enriched alkane products.

The SMOM methodology that is used in the isolation of σ-alkane complexes is perfectly poised to study C–H activation pathways. The removal of any competitive pre-equilibria and enhanced stability compared to the solution counterparts means reliable and robust experimental procedures can be followed. H/D Exchange within solid-state σ-alkane complexes has previously been reported for the complexes of **[1-NBA][BAr$^F_4$]**[32] and **[1-cyclohexane][BAr$^F_4$]**.[33]

When crystals of **[1-NBA][BAr$^F_4$]** were placed under a deuterium atmosphere over 18 hours, deuterium incorporation into the coordinated NBA ligand was observed, shown in Scheme 4.3a. Solution trapping of this organometallic complex and isolation of the reaction volatiles revealed the NBA isotopologue *exo*-NBA-d_4 to be formed, shown by solution ^{1}H and ^{2}H NMR spectroscopy as well as electron-ionisation mass spectroscopy (EI-MS). The H/D exchanged products of **[1-NBA][BAr$^F_4$]** as a complex, before any solution trapping, were also confirmed by ^{2}H SSNMR spectroscopy and neutron diffraction.

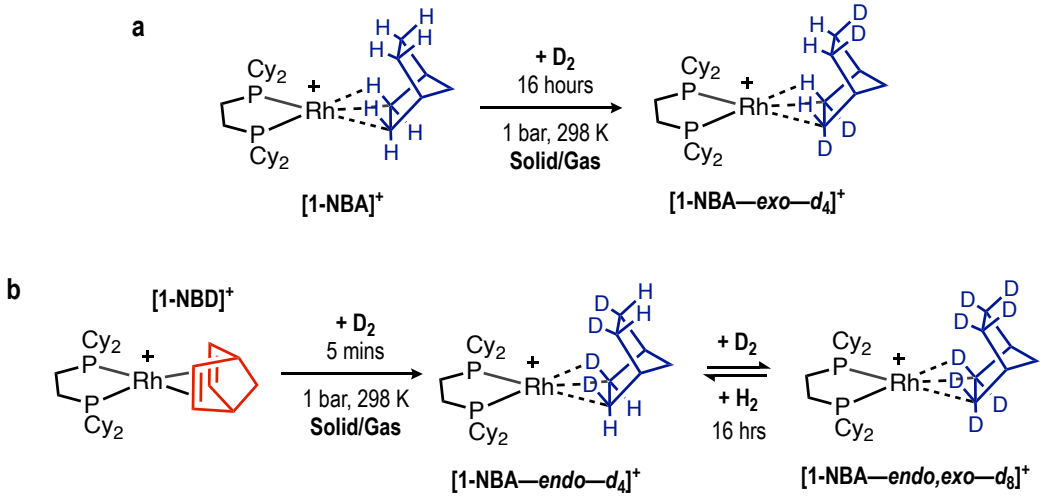

Scheme 4.3: Overview of the H/D exchange reaction for **[1-NBA][BAr$^F_4$]** when starting from **a**) **[1-NBA][BAr$^F_4$]** and **b**) **[1-NBD][BAr$^F_4$]**.[32]

Interestingly, if D_2 was added to crystalline **[1-NBD][BAr$^F_4$]**, *endo,exo*-NBA-d_8 was found following the same analytical methods, Scheme 4.3b. This suggests the initial hydrogenation/deuteration occurs only in the *endo*-proton positions, to form

[1-NBA-*endo*-d_4][BAr^F_4], and further H/D exchange occurring in the *exo*-positions, resulting in **[1-NBA-*endo,exo*-d_8][BAr^F_4]**. This substitution pattern shows that Rh•••C–H coordination of the NBA ligand can be *exo*- or *endo*-, and this translation was calculated by periodic DFT.

No evidence was observed for deuteration at the bridge or bridgehead positions on the NBA ligand, suggesting the NBA does not coordinate to the metal centre in these positions. It was calculated that this mode is not energetically feasible in the solid-state, again owing to the specific microenvironment provided by the $[BAr^F_4]^-$ anion framework. This selectivity, along with *exo*-/*endo*- deuterium incorporation, was noted as a further example of the importance of the micro-environment provided by the anions to which the cation resides.

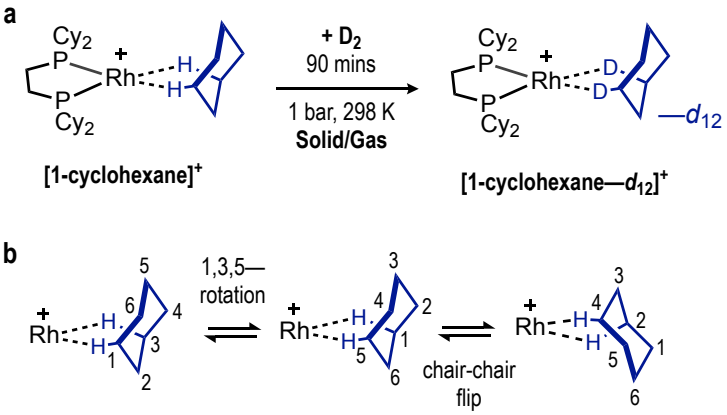

Scheme 4.4: a) Overview of the H/D exchange reaction in **[1-cyclohexane][BAr^F_4]**.[33] **b**) Fluxional processes of **[1-cyclohexane]$^+$** within in the solid-state.

When **[1-cyclohexane][BAr^F_4]** was reacted with exogenous D_2, H/D exchange occurs at all sites of the cyclohexane ligand within 90 minutes (Scheme 4.4a).[33] This suggests all 12 C–H bonds are in contact with the metal centre, made possible by both a *ring-walk* and *chair-chair flip* fluxional process occurring in the solid-state, shown in Scheme 4.4b. The exchange process and mobility was also probed by SSNMR spectroscopy in conjunction with periodic DFT calculations, as well as solution trapping analyses of the cyclohexane-d_{12}.

For both **[1-NBA][BAr^F_4]** and **[1-cyclohexane][BAr^F_4]**, the precise nature of the mechanism has yet to be elucidated, however stepwise C–H activation, σ-CAM and dehydrogenation pathways were considered. Notably, these complexes are prime examples of how C–H activation (H/D exchange) within σ-alkane complexes is a facile

process after initial σ-alkane complex formation. Chapter 4 will explore this reactivity, templated by the SMOM complexes of **[1-NBA][BAr$^F_4$]** and **[1-cyclohexane][BAr$^F_4$]**, towards the range of solid-state σ-alkane complexes presented in Chapter 2.

4.2. H/D Exchange in σ-Alkane Complexes

4.2.1. H/D Exchange within [1-*iso*butane][BAr$^F_4$]

To explore H/D exchange reactions in the σ-alkane complexes presented in Chapter 2, a methodology adapted from that reported of **[1-NBA][BAr$^F_4$]** and **[1-cyclohexane][BAr$^F_4$]** was followed. To start, when crystals of **[1-*iso*butene][BAr$^F_4$]** were placed under an atmosphere of D_2 and left for 90 mins (3 × 30 minutes), deuterium was shown to be incorporated into the *iso*butane ligand within **[1-*iso*butane][BAr$^F_4$]**. This resulted in the formation of the part-deuterated analogue of **[1-*iso*butane][BAr$^F_4$]**, **[1-*iso*butane-d_x][BAr$^F_4$]**, where x = 10–7 (Scheme 4.5).

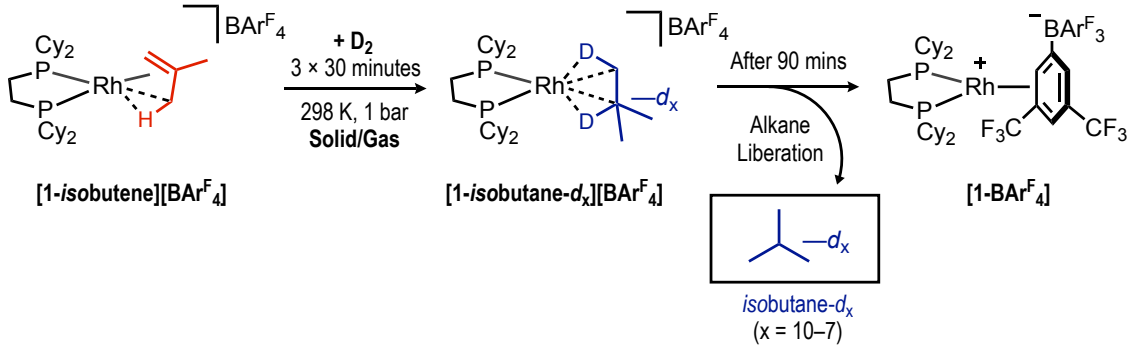

Scheme 4.5: Experimental procedures in the synthesis of *iso*butane-d_x (x = 10–7).

The use of 3 × 30 minutes of D_2 atmosphere, which involves degassing and recharging the reaction flask with fresh D_2 every 30 minutes, removes the build-up of any exchanged HD / H_2 within the reaction flask during the reaction. This build-up of HD / H_2 was found to limit the total deuterium incorporation.

After the total 90 minutes under a D_2 atmosphere, the partially deuterated *iso*butane was found to be liberated from the crystalline lattice, shown by signals corresponding to *iso*butane in the gas phase ^{1}H and ^{2}H NMR spectra of the headspace volume. These headspace gasses could be trapped into MeCN-d_3 for subsequent characterisation by solution ^{1}H, ^{2}H and ^{13}C{^{1}H} NMR spectroscopy, as well as Gas Chromatography Electron Ionisation Mass Spectrometry (GC EI-MS).

The GC EI-MS spectrum of liberated *iso*butane showed a molecular ion signal at *m/z* = 66.1265, suggestive of $C_4D_9^+$ (calc. 66.1269), and a base peak of *m/z* = 50.0980, assigned to $C_3D_7^+$ (calc. 50.0981, Figure 4.1a). Signals from the unfragmented $C_4D_{10}^+$ could not be located in significant quantities, explained due to the relative ease of fragmentation of C_4H_{10} which is regularly used as a chemical ionisation agent in certain mass spectrometry techniques.[34] Isotopologues of $C_4D_9^+$, notably $C_4D_8H^+$ and $C_4D_7H_2^+$ are further observed in the mass spectrum, however only as minor products. As these isotopologues are present, the isolated isobutane is best described as *iso*butane-d_x, where x = 10–7.

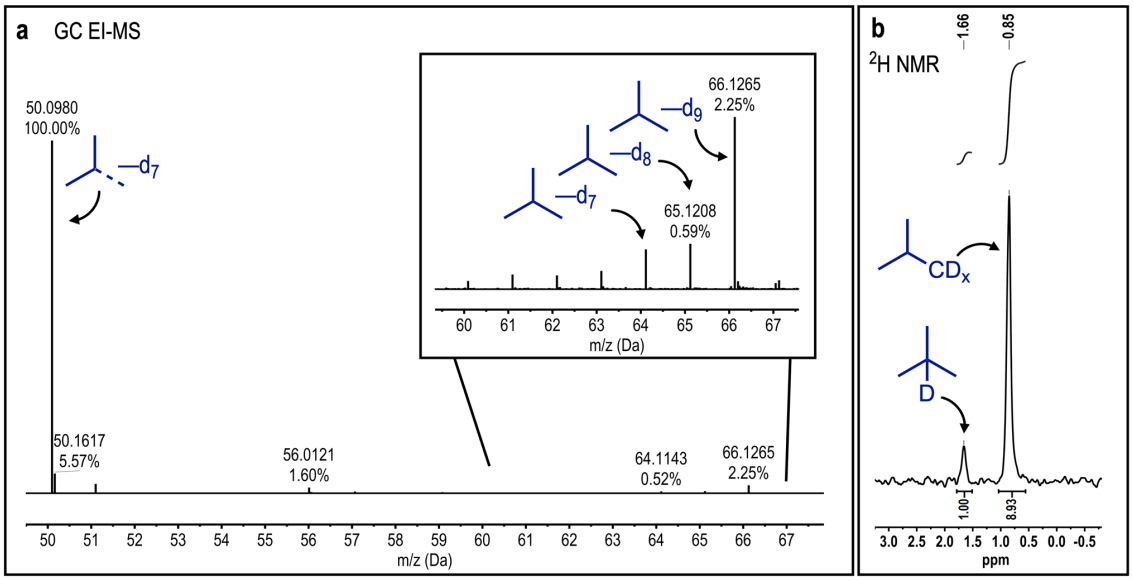

Figure 4.1: a) Mass spectrum of isolated *iso*butane-d_x, with enlargement of *m/z* = 60–67 region. Due to relative ease of fragmentation of isobutane,[34] the molecular ion peak is that of $C_4D_9^+$, *m/z* = **b**) The solution ^{2}H NMR spectrum (CD_2Cl_2, 298 K, 61 MHz) of *iso*butane-d_x isolated from the reaction presented in Scheme 4.5.

The solution ^{2}H NMR spectrum of this trapped *iso*butane shows two resonances [δ 1.65, 0.85] assigned to that of the tertiary and primary C–D groups of *iso*butane respectively (Figure 4.1b), suggesting H/D exchange occurs at all C–H sites of *iso*butane. The integrations of these signals are slightly below the predicted 1: 9 ratios [1: 8.9 of -CD to –$(CD_3)_3$ environments] again signalling *iso*butane-d_{10} is not the single product. The presence of isotopologues is confirmed in the ^{1}H NMR spectrum, which show low intensity signals assigned to residual protio-*iso*butane [δ 1.55, 0.82]. Both these data are consistent with the isotopologues observed in the GC EI-MS spectrum also.

The solution $^{13}C\{^1H\}$ NMR spectrum of the isolated *iso*butane-d_x (x = 10–7) reveals numerous signals in the range of δ 24 – 22, consistent with aliphatic carbon environments.

These signals were deconvoluted and simulated, shown in Figure 4.2, and were shown to be constructed of multiple, overlapping resonances from ^{13}C environments from a mixture of *iso*butane-d_x isotopologues.

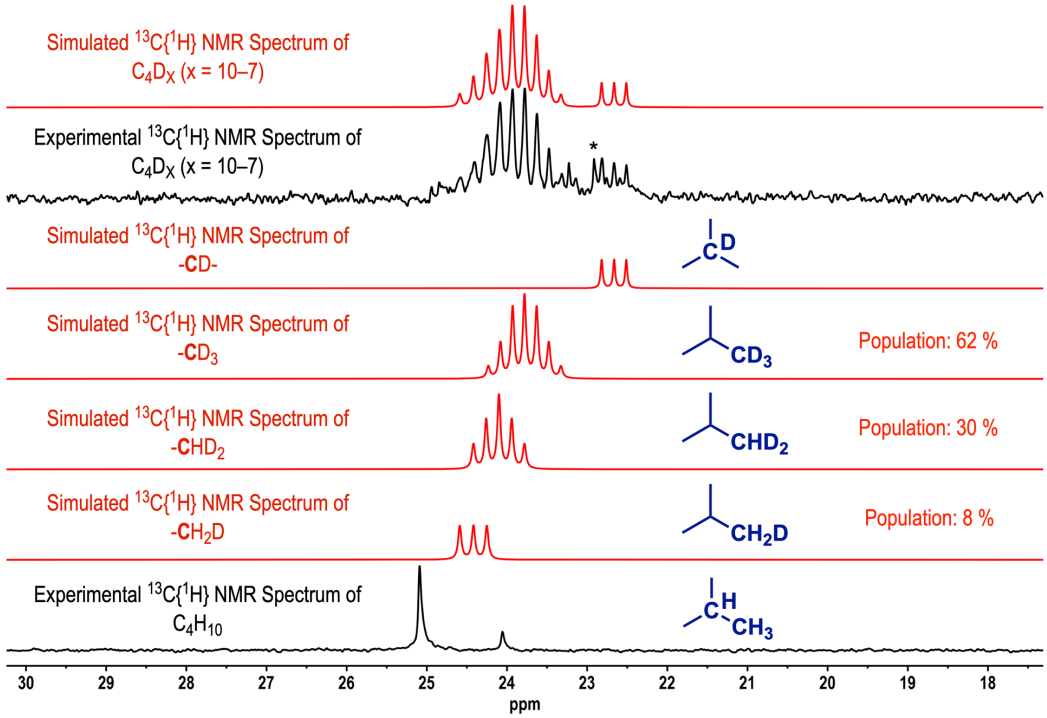

Figure 4.2: Simulated and experimental solution $^{13}C\{^1H\}$ NMR spectra (CD_2Cl_2, 298 K, 126 MHz) of *iso*butane-d_x (x = 10–7), showing approximated populations of varyingly levels of deuteration in the $–CD_x$ groups in *iso*butane. The signal marked by * is from a pentane impurity.

These simulations show that the multiple signals at δ ~24 are predominantly constructed (92 % in total) from an overlapping septet [δ 23.9, $^1J_{C\text{-}D}$ = 25 Hz] and quintet [δ 24.2, $^1J_{C\text{-}D}$ = 24 Hz] resonances. These splitting patterns are assigned to $–CD_3$ and $–CD_2H$ groups respectively (^2H: I = 1). The triplet at δ 22.6 is assigned to the methine carbon of *iso*butane-d_x, which is split by a single deuterium.

This is consistent with the data presented from the GC EI-MS and ^2H NMR spectroscopy. Although these show a high amount of deuterium incorporation into *iso*butane, complete H/D exchange in the alkane ligand was not achieved. This is unlike **[1-cyclohexane][BAr$^F_4$]** shown previously. For **[1-*iso*butane][BAr$^F_4$]**, this is due to the limited lifetime of **[1-*iso*butane][BAr$^F_4$]** under a D_2 (or H_2) atmosphere of ~90 minutes. This is explored further in Section 4.2.1.1.

Further to this, if crystals of **[1-*iso*butene][BAr$^F_4$]** are pre-hydrogenated (8 minutes, 298 K, 1 bar) to form **[1-*iso*butane][BAr$^F_4$]** and then placed under a D_2 atmosphere for 90 minutes, this yielded *iso*butane-d_x with considerably reduced x-values (x = 8–3). This could be shown by the increased presence of protio-isotopologues in the GC EI-MS spectrum, and increased ^{1}H signals and proton-bound carbon environments in the ^{1}H and ^{13}C{^{1}H} NMR spectra respectively. This again is a result of the limited lifetime of **[1-*iso*butane][BAr$^F_4$]** under a D_2 (or H_2) atmosphere.

H/D exchange was also attempted in solution (Scheme 4.6). The addition of D_2 to a sample of **[1-*iso*butene][BAr$^F_4$]** in 1,2-$C_6F_2H_4$ solvent resulted in the complete formation of **[1-$C_6F_2H_4$][BAr$^F_4$]** within 30 seconds, shown by ^{31}P{^{1}H} NMR spectroscopy.

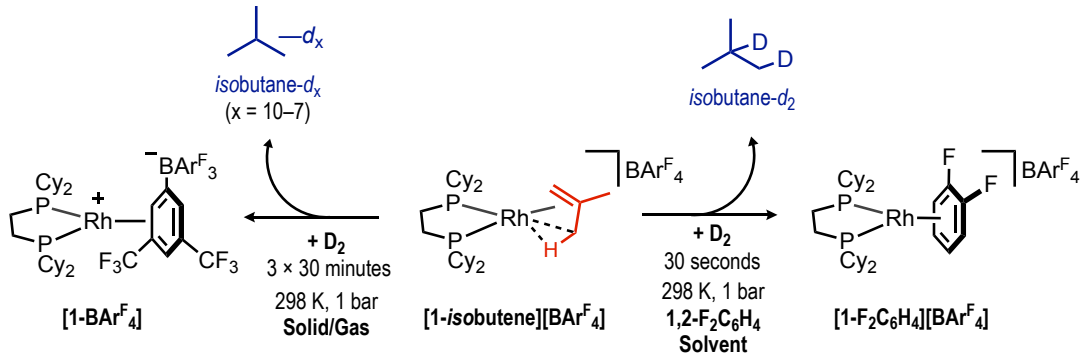

Scheme 4.6: Experimental procedures in the synthesis of *iso*butane-d_x in solution (left, x = 10 – 7) or solid/gas (right, x = 2) conditions.

The volatile *iso*butane product was isolated by distillation and spectroscopically identified as *iso*butane-d_2 by ^{2}H NMR spectroscopy [δ 1.66, singlet, 1D, -C**D**; δ 0.85, singlet, 1D, -C**D**H$_2$] and GC EI-MS. No evidence for any H/D exchange products could be found, as *iso*butane-d_2 is a result of D_2 addition across the C=C bond in *iso*butene. This makes H/D exchange upon this complex unique to the solid-state and SMOM methodology, where competing solvent coordination and pre-equilibria inhibits this process in solution.[16]

4.2.1.1. Decomposition of [1-*iso*butane][BAr$^F_4$] Under a H_2 Atmosphere

The organometallic complexes that result from the exposure of **[1-*iso*butene][BAr$^F_4$]** to H_2 for 90 minutes were also investigated. This is far increased from the 10 minutes needed to form **[1-*iso*butane][BAr$^F_4$]** from **[1-*iso*butene][BAr$^F_4$]**. The $^{31}P\{^1H\}$ SSNMR spectrum of this complex exhibited a new, sharp signal [δ 102, apparent triplet] of a relative integration of ~35 % (Figure 4.3b). The remaining ~65 % is assigned to that of **[1-BAr$^F_4$]**.

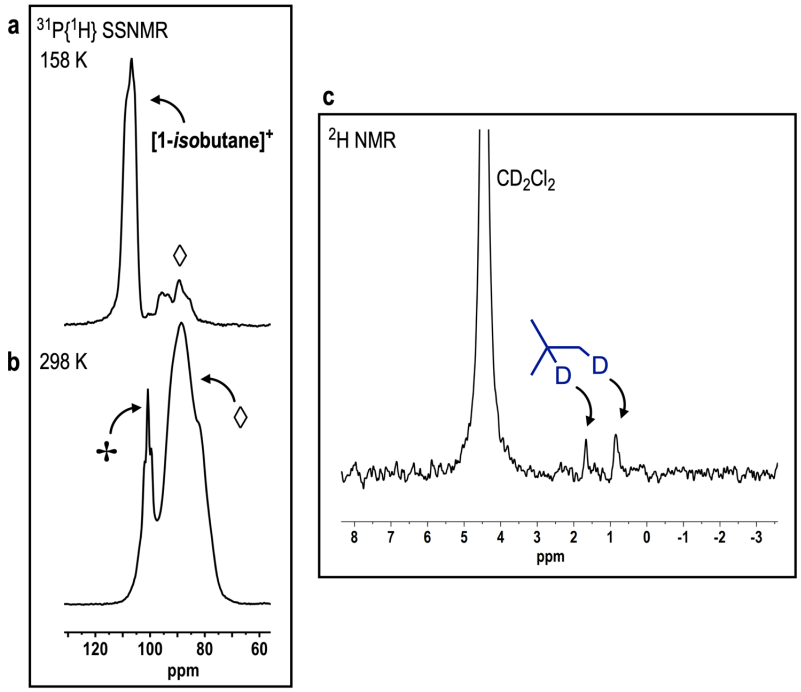

Figure 4.3: The $^{31}P\{^1H\}$ SSNMR (162 MHz, 10 kHz spin rate) spectrum of **a**) **[1-*iso*butane][BAr$^F_4$]** (158 K) as prepared and **b**) a sample of **[1-*iso*butene][BAr$^F_4$]** placed under a H_2 atmosphere (1 bar, 298 K) for 90 minutes, prepared separately to that of **a** (298 K). ◊ = **[1-BAr$^F_4$]**. ✢ = decomposition product under an H_2 atmosphere, proposed as a hydrogen-rich rhodium complex. **c**) The solution ^2H NMR (CD_2Cl_2 298 K, 61 MHz) spectrum of *iso*butane-d_2.

Interestingly, when this solid material was placed under an atmosphere of *iso*butene, the ^1H gas phase NMR spectrum of the reaction headspace revealed minor signals assigned to *iso*butane, consistent from the hydrogenation of *iso*butene. When repeated with D_2, *iso*butane-d_2 could be identified in the solution ^2H NMR spectrum upon condensing the headspace gases into CD_2Cl_2, shown in Figure 4.3c. This unusual observation suggests formation of a rhodium-hydride (deuteride) complex under a H_2 (D_2) atmosphere, assigned to that of the apparent triplet at δ 102 in the $^{31}P\{^1H\}$ SSNMR spectrum.

When excess *iso*butene is introduced, the reactive bound hydrides (deuterides) are consumed in a hydrogenation reaction resulting in the small amount of *iso*butane produced. This is then rapidly displaced by excess *iso*butene to yield **[1-*iso*butene][BAr$^F_4$]**. This lower intensity of this complex (~35 %) compared to that of **[1-BAr$^F_4$]** the in $^{31}P\{^1H\}$ SSNMR spectrum is consistent with only the small amount of *iso*butane produced.

This proposed rhodium-hydride complex could not be isolated pure, preventing further characterisation. Additionally, over the course of 2 hours under a N_2 atmosphere at 298 K in the solid-state, the signal at δ 102 disappears and only signals from **[1-BAr$^F_4$]** are seen. This may suggest this hydrogen-rich rhodium species is only an intermediate product along the way to **[1-BAr$^F_4$]** decomposition, shown in Scheme 4.7.

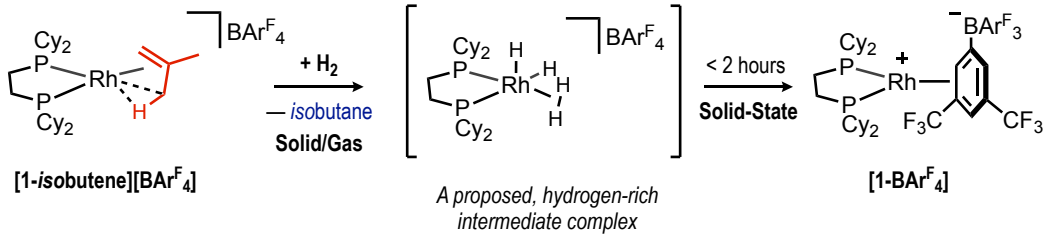

Scheme 4.7: The decomposition of **[1-*iso*butene][BAr$^F_4$]** under a H_2 atmosphere.

Additionally, when closely related SMOM materials are left for extended times under a H_2 atmosphere, products including hydride species have been noted. Examples reported by Weller *et. al.*,[35–37] reveal Rh(III) bisphosphine complexes with dihydrogen dihydride ligands, all from the initial hydrogenation of an alkene or diene ligands in the solid-state.

4.2.1.2. Mechansim of H/D Exchange

Although the exact mechanism of H/D exchange could not be defined; a range of possible mechanisms can be suggested. All these proposed pathways are consistent with previously reported H/D exchange within SMOM materials, which have included computational calculations.[32]

The first proposed pathway follows an oxidation and reductive pathway, coupled with a σ-CAM step (Scheme 4.8).[30,31] This initiates by oxidative addition of D_2 to the σ-alkane complex, to form a rhodium(III) di-deuteride complex. A σ-CAM step can occur, in a 4 membered transition state with the Rh•••C–H interaction, shown in the scheme with the primary Rh•••C–H interaction. This is followed by a rearrangement to allow the deuteride/alkyl to be in a *cis*-geometry, which itself is formally a second σ-CAM step. Reductive coupling of the deuteride and alkyl group reforms the deuterium incorporated alkane and HD, and the de-coordination of HD allows for this process to begin again.

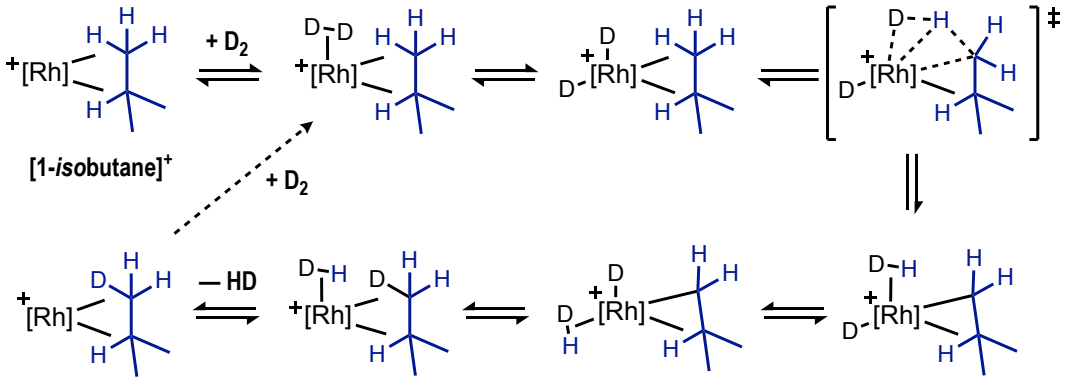

Scheme 4.8: H/D exchange within **[1-*iso*butane][BAr$^F_4$]** via a σ-CAM pathway.

A second proposed mechanism is shown in Scheme 4.9, which follows a dehydrogenation pathway. Chapter 3 shows the facile nature of **[1-*iso*butane][BAr$^F_4$]** dehydrogenation, so this pathway must be considered accessible. This is shown to proceed by the initial oxidative cleavage of the primary C–H position in *iso*butane, to form an *iso*butyl-hydride complex. β-hydride abstraction of this complex then forms a dihydride complex with coordinated *iso*butene. D_2 coordination and exchange with a hydride (shown *via* a σ-CAM step), results in an equivalent of coordinated HD. De-coordination of this and subsequent rehydrogenation of the coordinated *iso*butene then yields the part-deuterated σ-alkane complex.

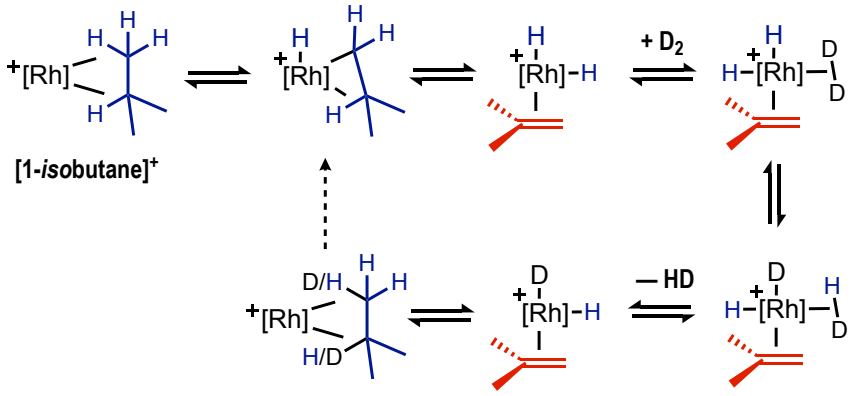

Scheme 4.9: H/D exchange within **[1-*iso*butane][BAr$^{F}_{4}$]** via a dehydrogenative pathway.

Both these pathways shown produce HD gas. This production of HD is observed in the H/D exchange reactions of both **[1-*iso*butane][BAr$^{F}_{4}$]** and **[1-*iso*pentane][BAr$^{F}_{4}$]** by the solution trapping of the H/D exchange reactions' headspace. The ^{1}H NMR spectrum revealed a signal at δ 4.57 [1:1:1 triplet, J_{HD} = 42 Hz] assigned to HD.[38] As well, the GC EI-MS spectrum of both isolated alkenes reveal monatomic increases of the alkane isotopologues. Both these observations are consistent with either proposed H/D exchange pathway.

4.2.2. H/D Exchange within [1-*iso*pentane][BAr^F_4]

H/D Exchange was also observed within the *iso*pentane ligand in **[1-*iso*pentane][BAr^F_4]**. Analogous to **[1-*iso*butene][BAr^F_4]**, when crystals of **[1-*iso*pentadiene][BAr^F_4]** are placed under an D_2 atmosphere for 90 minutes (3 × 30 minute cycles), initial deuteration of the C=C bonds and further H/D exchange occurs to yield part-deuterated *iso*pentane complex of **[1-*iso*pentane-d_x][BAr^F_4]**, where x = 12–7.

After this time under a D_2 atmosphere, *iso*pentane was also shown to have been displaced from the solid lattice. Due to the high volatility of *iso*pentane (b.p. 27 °C), this meant it was observed in the gas phase ^{1}H and ^{2}H NMR spectra of the reaction. Solution trapping of the reaction volatiles enabled analysis by solution ^{1}H, ^{2}H and ^{13}C{^{1}H} NMR spectroscopy and GC EI-MS. These conditions were optimised for maximum deuterium incorporation. When left under D_2 for greater than 90 minutes, no increased deuterium incorporation was found. This again suggests complete alkane-displacement and decomposition within 90 minutes under a H_2 (D_2) atmosphere.

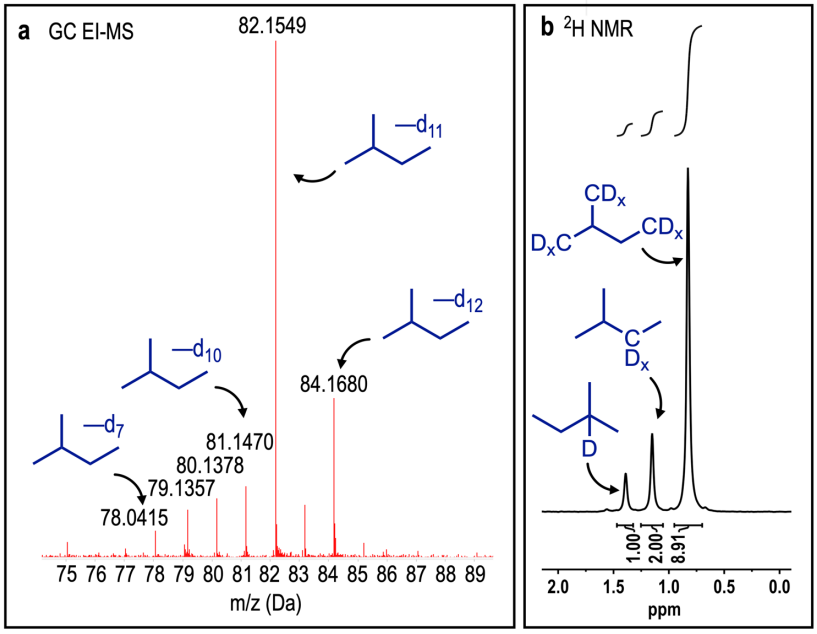

Figure 4.4: a) Mass spectrum of isolated *iso*pentane-d_x (x = 12–7). The molecular ion peak is that of $C_5D_{12}^+$, *m/z* = 84.1680 (calc. 84.1687). **b**) The solution ^{2}H NMR (CD_2Cl_2, 298 K, 61 MHz) spectrum of *iso*pentane-d_x.

The GC EI-MS spectrum (Figure 4.4a) again shows a range of isotopologues, yet the molecular ion signal at *m/z* = 84.1680 is suggestive of $C_5D_{12}^+$ (calc. 84.1687) and a base peak of *m/z* = 82.1549 assigned to $C_5D_{11}^+$ (calc. 84.1551). Analogous to *iso*butane-d_x, the

part-deuterated *iso*pentane is best described as *iso*pentane-d_x (x = 12–7). The ^{2}H NMR spectrum showed three resonances [δ 1.39, 1.15, 0.83] in ~1: 2: 9 ratio (Figure 4.4b). These are consistent with the analogous literature chemical shifts in the ^{1}H NMR spectrum for protio-*iso*pentane,[39] as well as being consistent to part-deuterated *iso*pentane.

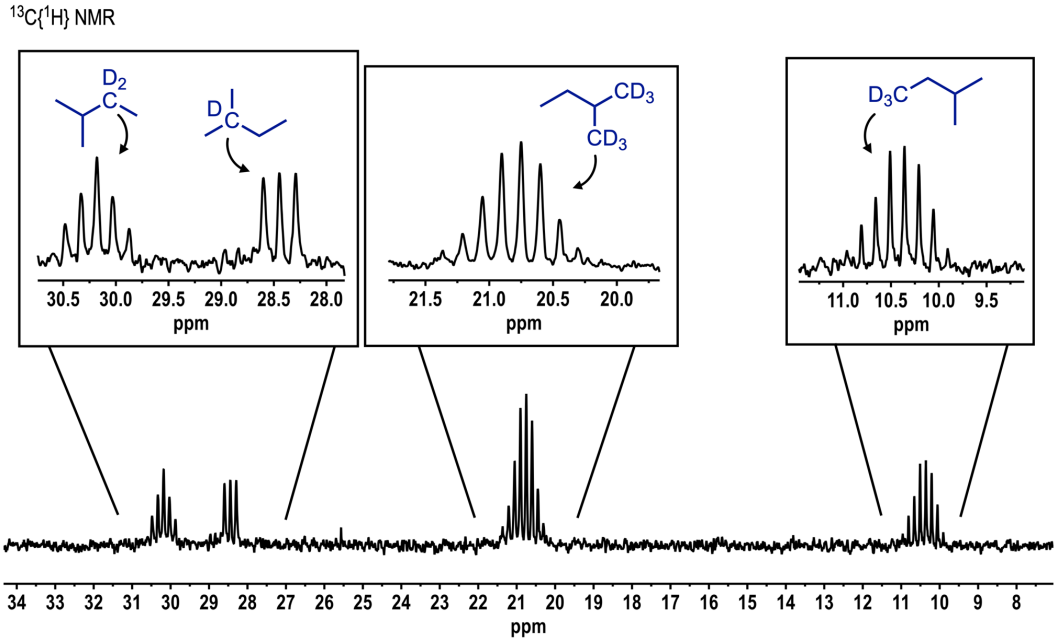

Figure 4.5: The solution $^{13}C\{^1H\}$ NMR (CD_2Cl_2, 298 K, 126 MHz) spectrum of *iso*pentane-d_x (x = 12–7).

The $^{13}C\{^1H\}$ NMR spectrum of the isolated *iso*pentane-d_x (x = 12–7) (Figure 4.5) shows four signals, again consistent with the analogous literature chemical shifts in the $^{13}C\{^1H\}$ NMR spectrum for protio-*iso*pentane.[39] The resonances are of a quintet [δ 30.2, $^1J_{C\text{-}D}$ = 25 Hz], triplet [δ 28.4, $^1J_{C\text{-}D}$ = 24 Hz], septet [δ 20.8, $^1J_{C\text{-}D}$ = 25 Hz] and septet [δ 10.4, $^1J_{C\text{-}D}$ = 24 Hz]. The splitting patterns observed of these signals are consistent with the corresponding number of bound ^{2}H nuclei to each ^{13}C, and are assigned to CD_2C, CDCC and –CD_3 groups respectively.

Unlike the $^{13}C\{^1H\}$ NMR spectrum of isolated *iso*butane-d_x (Figure 4.2), no residual protio-CH groups could be located and therefore could not be modelled. This, in combination with relative integrals in the ^{2}H NMR spectrum and decreased number of relative isotopologue signals in the GC EI-MS spectrum, suggests a greater deuterium incorporation within the same time frame compared to that of *iso*butane-d_x.

Additionally, if the diene complex **[1-*iso*pentadiene][BAr$^F_4$]** was hydrogenated first, to form **[1-*iso*pentane][BAr$^F_4$]**, then placed under a D_2 atmosphere, H/D exchange still occurs, but produces *iso*pentane-d_x with a far decreased x-value. This is shown best by the $^{13}C\{^1H\}$ NMR spectrum of the isolated *iso*pentane-d_x (Figure 4.6). The spectrum reveals a mixture of multiplets consistent with part-deuterated or fully protio ^{13}C environments. For example, the singlet at δ 31.3 and triplet at δ 30.9 are from the CH_2 and CDH groups of the methylene ^{13}C environment respectively. This mixture of neighbouring protio- and deuterio- groups is seen for each ^{13}C environment.

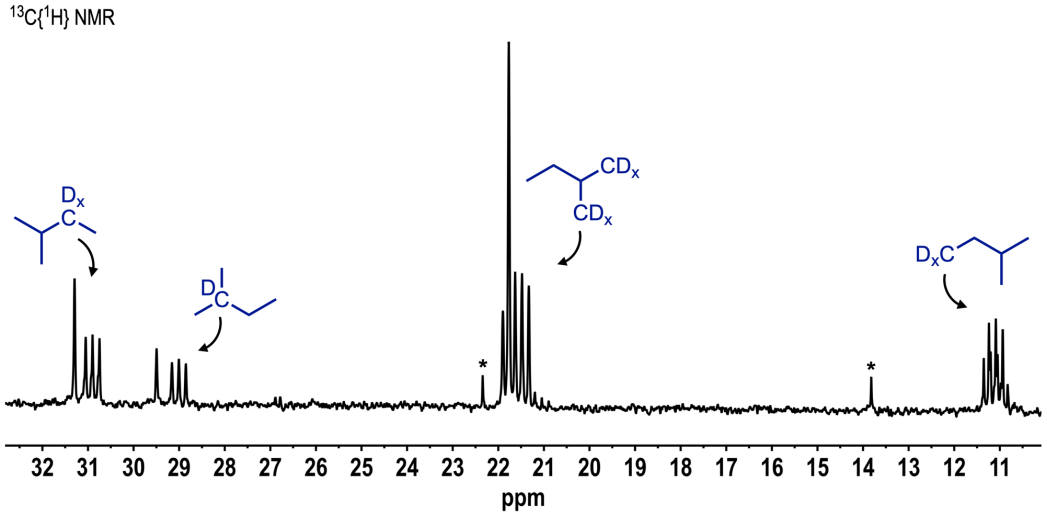

Figure 4.6: The solution $^{13}C\{^1H\}$ NMR (CD_2Cl_2, 298 K, 126 MHz) spectrum of *iso*pentane-d_x. Signals marked * are from a pentane impurity.

The $^{13}C\{^1H\}$ NMR spectroscopic data are consistent with the instability of **[1-*iso*pentane][BAr$^F_4$]** under a D_2 (H_2) atmosphere, where after the initial 25 minutes hydrogenation, **[1-*iso*pentane][BAr$^F_4$]** is only stable for another ~1 hour before decomposition to **[1-BAr$^F_4$]**. This shorter period of stability limits complete deuterium incorporation. The $^{13}C\{^1H\}$ NMR spectrum does show however that all C–H environments must come into contact with the rhodium centre during the H/D exchange pathway, as at least one deuterium has been incorporated into every ^{13}C environment.

Additionally, a control reaction of the solution-phase deuteration of **[1-*iso*pentadiene][BAr$^F_4$]** was conducted following the analogous procedure for **[1-*iso*butene][BAr$^F_4$]**. Dissolution of **[1-*iso*pentadiene][BAr$^F_4$]** in 1,2-$F_2C_6H_4$, followed by D_2 addition (90 minutes, 1 bar, 298 K) results in the production of *iso*pentane-d_4 and **[1-$F_2C_6H_4$][BAr$^F_4$]**. This reveals no evidence of H/D exchange in solution and thus, H/D exchange is unique to the solid-state. Competing solvent coordination and pre-equilibria again inhibits H/D exchange in solution.

4.2.3. H/D Exchange within Further σ-Alkane Complexes

As well as **[1-*iso*butane][BAr$^F_4$]** and **[1-*iso*pentane][BAr$^F_4$]**, H/D exchange experiments were performed on crystalline material of **[1-propene][BAr$^F_4$]**, **[1-hexadiene][BAr$^F_4$]** and **[1-(C_6-dienes)][BAr$^F_4$]**. The results of these are summarised in Scheme 4.10.

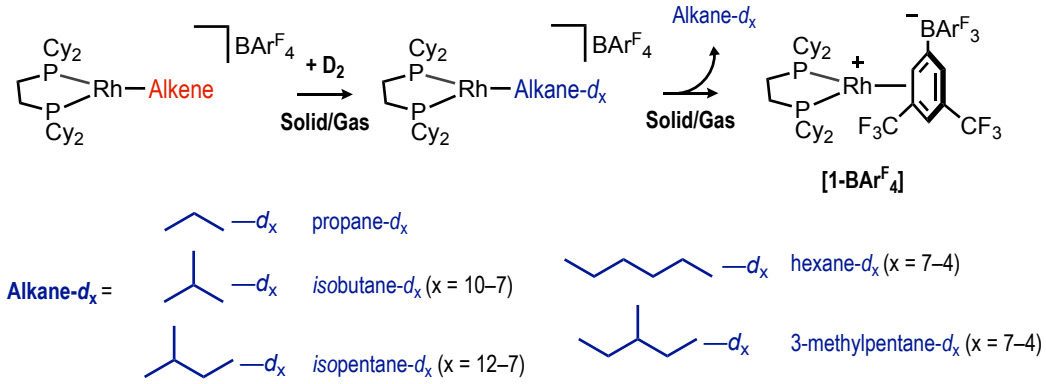

Scheme 4.10: Experimental procedures in the synthesis of part-deuterated alkanes from their respective alkene-complex precursors.

4.2.3.1. H/D Exchange within [1-propane][BAr$^F_4$]

Addition of D_2 to a sample of **[1-propene][BAr$^F_4$]** in a solid/gas reaction resulted in the liberation of propane-d_x within 5 minutes, confirmed by gas phase ^{1}H NMR spectroscopy of the reaction flasks' headspace. Unfortunately, the value for x was challenging to quantify, due to the experimental limitations in EI-MS on very low molecular weights (less than 50 g mol^{-1}). ^{31}P{^{1}H} SSNMR spectroscopy of the remaining solid also confirmed complete decomposition to **[1-BAr$^F_4$]** after 5 minutes under a D_2 atmosphere.

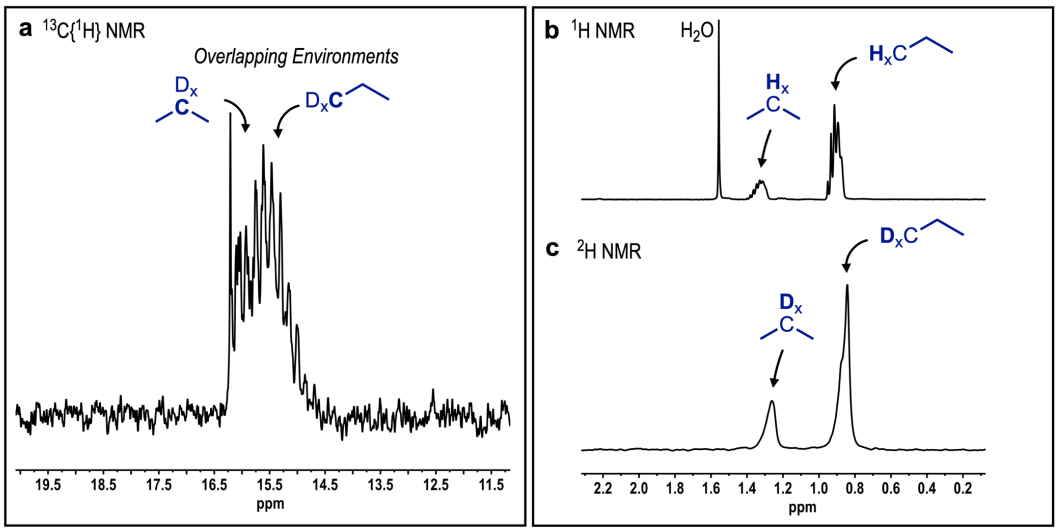

Figure 4.7: The solution **a**) $^{13}C\{^1H\}$ NMR (CD_2Cl_2, 298 K, 126 MHz) **b**) ^1H NMR (CD_2Cl_2, 298 K, 400 MHz) and **c**) ^2H NMR (CD_2Cl_2, 298 K, 62 MHz) spectra of propane-d_x.

Shown in Figure 4.7a is the solution $^{13}C\{^1H\}$ NMR spectrum of the liberated propane-d_x trapped into dichloromethane. The large number of overlapping multiplets at δ 15.0 – 16.5 are suggestive of both methyl and methylene ^{13}C environments of propane being split by multiple ^2H nuclei. In the absence of any H/D exchange, deuterium incorporation would be limited to propane-d_2 from the initial addition of D_2 across the C=C bond in propene. This would manifest as two, triplet signals in $^{13}C\{^1H\}$ NMR spectrum. Additionally, both the ^1H and ^2H NMR spectra of propane-d_x (Figure 4.7b and c) exhibit intense signals in both environments in propane-d_x. These data are suggestive that H/D exchange has occurred within propane, yet at a far reduced capacity. This results in a range of isotopologue products observed.

This incomplete deuterium incorporation is proposed due to the short-lived nature of **[1-propene][BAr$^F_4$]** under a D_2 atmosphere (5 minutes). This also means H/D exchange must be a relatively fast process in **[1-propane][BAr$^F_4$]**, as deuterium incorporation is observed before complex decomposition. This contrasts to **[1-NBA][BAr$^F_4$]**, where isotopologues of NBA were only initial observed after 4 hours under a D_2 atmosphere.[32]

4.2.3.2. H/D Exchange within C_6H_{14} Alkane Complexes

H/D exchange reactions were also performed on **[1-hexadiene][BAr$^F_4$]** and **[1-(3-methylpentane)][BAr$^F_4$]**, whereby crystalline material of the precursor complexes **[1-hexadiene][BAr$^F_4$]** and **[1-(C_6-dienes)][BAr$^F_4$]** respectively were placed under an atmosphere of D_2 (1 bar, 298 K).

The solution $^{13}C\{^1H\}$ NMR spectra of the isolated hexane-d_x and 3-methylpentane-d_x (the latter shown in Figure 4.8) reveal a mixture of sharp, singlet resonances as well as overlapping multiplets. This is suggestive of ^{13}C environments from multiple -CD_x environments, as well as ^{13}C environments with no ^2H coupling. The GC EI-MS spectra of both hexane-d_x and 3-methylpentane-d_x revealed a mix of isotopologues, with x-values of 7–4 in both cases.

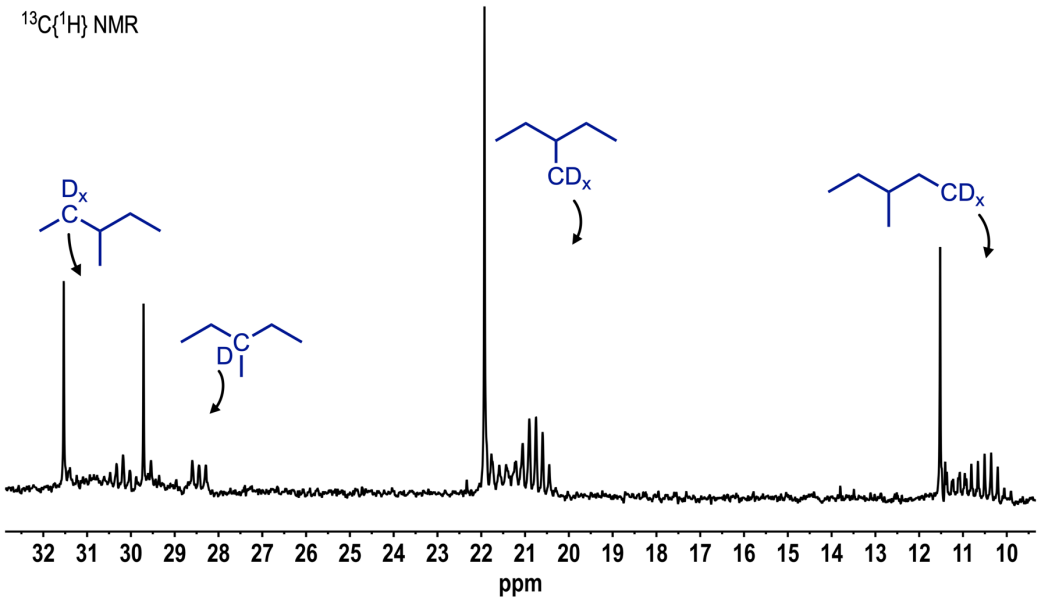

Figure 4.8: The solution $^{13}C\{^1H\}$ NMR (CD_2Cl_2, 298 K, 126 MHz) spectrum of 3-methylpentane-d_x (x = 7–4).

Complete decomposition of **[1-hexane][BAr$^F_4$]** and **[1-(3-methylpentane)][BAr$^F_4$]** under a D_2 (or H_2) atmosphere is thought to take place within 30 minutes. Multiple solution trapping experiments show no greater deuterium incorporation into the alkane fragment occurs after 30 minutes, suggesting a maximum level of deuterium incorporation has been achieved within this time. This is significantly longer than 5 minutes for **[1-propane][BAr$^F_4$]**, however far shorter than **[1-*iso*butane][BAr$^F_4$]** and **[1-*iso*pentane][BAr$^F_4$]** (90 minutes). The singlet signals observed in the $^{13}C\{^1H\}$ NMR spectrum may be some C–H sites that never directly coordinate to the rhodium-centre, and therefore cannot undergo complete H/D exchange. This is similar to the H/D exchange observed at only the *exo*-/*endo*-NBA positions in **[1-NBA][BAr$^F_4$]**.[32]

4.3. Combining H/D Exchange and Dehydrogenation

Section 4.1. described how **[1-cyclohexane][BAr$^F_4$]** undergoes H/D exchange to yield the fully deuterated cyclohexane-d_{12} analogue. When this complex is further placed under a dynamic vacuum, de-deuteration occurs to form the cyclohexadiene-d_8 analogue of **[1-cyclohexadiene][BAr$^F_4$]**.[33] Similar reactivity was proven with **[1-*iso*butane][BAr$^F_4$]**, as shown in Scheme 4.11.

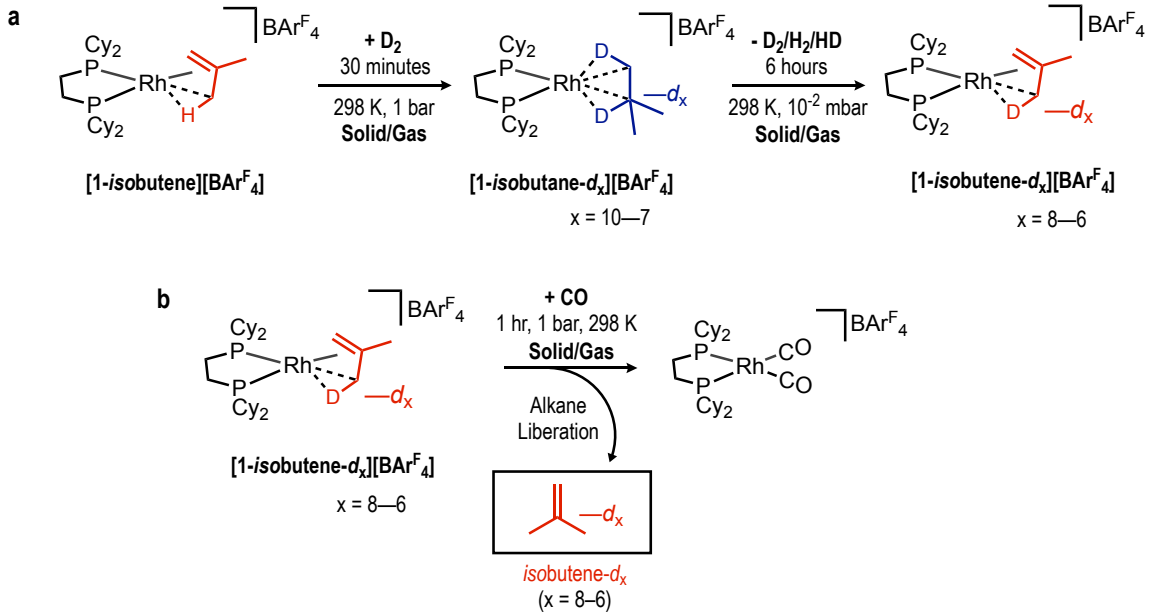

Scheme 4.11: a) Experimental procedures in the synthesis of **[1-*iso*butene-d_x][BAr$^F_4$]** and **b**) isolation of *iso*butene-d_x (x = 8–6).

Experimentally, crystals of **[1-*iso*butene][BAr$^F_4$]** were placed under a D_2 atmosphere (3 × 15 minutes, 45 minutes total). This reduced timeframe provides a high degree of deuterium enrichment, whilst limiting complex decomposition under a D_2 atmosphere to ~50 %. The deuterium-incorporated complex was then placed under a dynamic vacuum for 6 hours, to yield the deuterated analogue of **[1-*iso*butene][BAr$^F_4$]**, named **[1-*iso*butene-d_x][BAr$^F_4$]**, where x = 8–6 (Scheme 4.11a). This complex was characterised by solution $^{31}P\{^1H\}$, ^1H and ^2H NMR spectroscopy.

The solution $^{31}P\{^{1}H\}$ NMR spectrum of **[1-*iso*butene-d_x][BAr$^F_4$]** shows no significant difference in comparison to the protio-analogue of **[1-*iso*butene][BAr$^F_4$]**, as expected. A resonance at δ 1.8 in the ^{1}H NMR spectrum of **[1-*iso*butene][BAr$^F_4$]** however appears at a far reduced intensity in **[1-*iso*butene-d_x][BAr$^F_4$]**. As well as this, a signal in approximately the same position can be clearly seen in the 298 K ^{2}H NMR spectrum of **[1-*iso*butene-d_x][BAr$^F_4$]** [δ 1.6]. This is assigned to all the $^{1}H/^{2}H$ environments within the *iso*butene-d_x ligand becoming equivalent, from the fluxionality of the coordinated *iso*butene, shown in Chapter 2, Scheme 2.4.

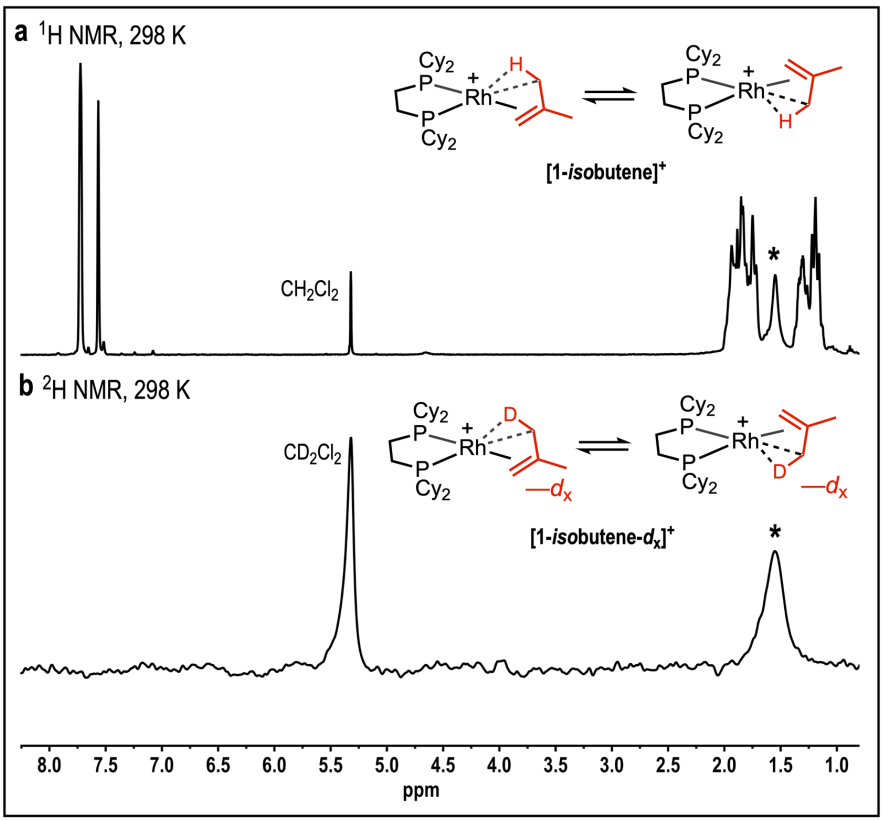

Figure 4.9: a) The solution ^{1}H NMR (CD_2Cl_2, 298 K, 400 MHz) spectrum of **[1-*iso*butene][BAr$^F_4$]** and **b**) the solution ^{2}H NMR (CD_2Cl_2, 298 K, 61 MHz) spectrum of **[1-*iso*butene-d_x][BAr$^F_4$]**. Signals marked * are assigned to the ^{1}H or ^{2}H environments within the fluxional coordinated *iso*butene.

To isolate the coordinated *iso*butene-d_x fragment and quantify the deuterium incorporation, addition of CO gas to crystals of **[1-*iso*butene-d_x][BAr$^F_4$]** in a solid-gas reaction was conducted (Scheme 4.11b). This liberates *iso*butene-d_x and forms the organometallic complex **[1-(CO)$_2$][BAr$^F_4$]**. This liberation allows for easy isolation by distillation and subsequent analysis of the isolated *iso*butene-d_x by ^{1}H, ^{2}H and $^{13}C\{^{1}H\}$ NMR spectroscopy and GC EI-MS (Figure 4.10).

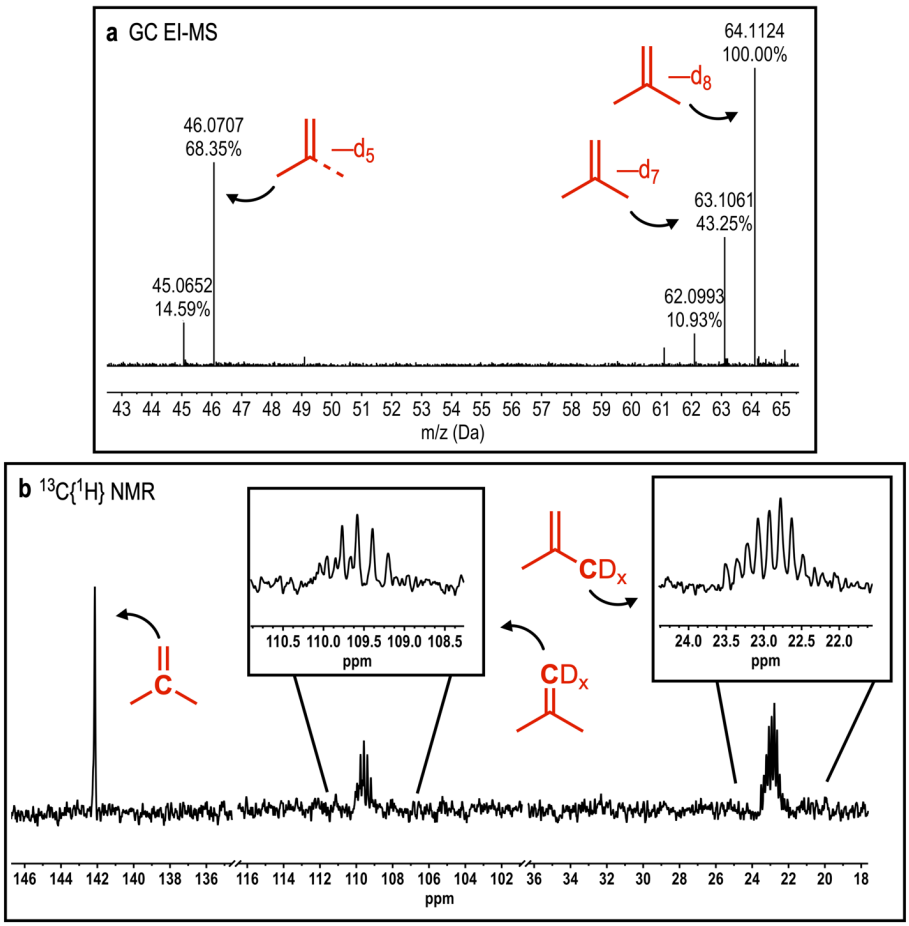

Figure 4.10: a) Mass spectrum of isolated *iso*butene-d_x. The molecular ion peak is that of $C_4D_8^+$, m/z = 64.1128 (calc. 64.1125). **b**) The solution $^{13}C\{^1H\}$ NMR (CD_2Cl_2, 298 K, 126 MHz) spectrum of *iso*butene-d_x (x = 8–6).

The GC EI-MS spectrum revealed a molecular ion signal at *m/z* = 64.1124, corresponding to $C_4D_8^+$ (calc. 64.1128). Multiple isotopologues from reduced deuterium incorporation are also observed, most significantly signals from C_4HD_7 and $C_6H_2D_6$. Therefore, *iso*butene-d_x is assigned as x = 8–6. The $^{13}C\{^1H\}$ NMR spectrum (Figure 4.10b) reveals multiple, overlapping ^{13}C environments; with splitting patterns from the neighbouring ^2H nuclei. These data reflect the reduced level of H/D exchange in the preceding *iso*butane-d_x has carried through to that of *iso*butene-d_x.

4.4. Stabilities and Reactivities of σ-Alkane Complexes Under a H_2 (D_2) Atmosphere

The relative rates of the two-process involved when placing solid-state σ-alkane complexes under a H_2 (D_2) atmosphere are visualised by the schematic in Scheme 4.12. This is expanded from the similar schematic presented for alkane dehydrogenation where the relative rates of alkane dehydrogenation (k_1) or solid-state anion coordination and alkane loss (decomposition) to form **[1-BAr$^F_4$]**, (k_2) was introduced in Chapter 3, Section 3.4.2.

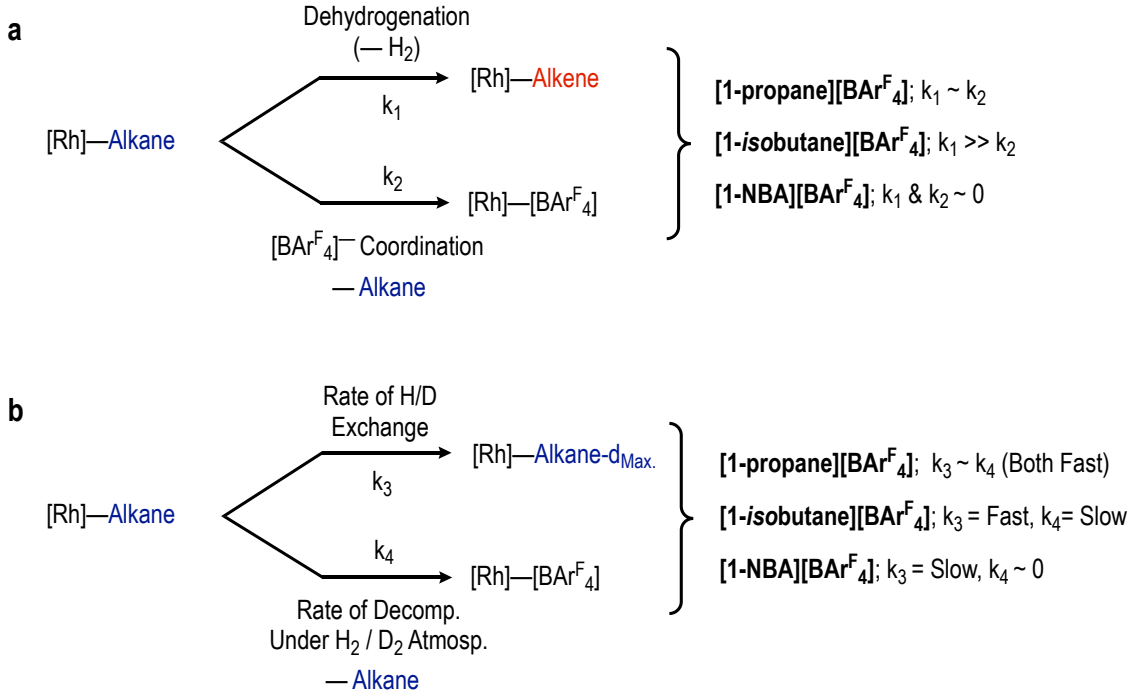

Figure 4.12: Relative rates of **a**) dehydrogenation (k_1) and decomposition (k_2) and **b**) of H/D exchange (k_3) and decomposition under H_2/D_2 atmosphere (k_4), with selected complexes.

When solid-state σ-alkane complexes are placed under a D_2 atmosphere, two predominant reaction events occur (Scheme 4.12b). The first is H/D exchange within the coordinated alkane fragment, which occurs at a rate, assigned k_3. A second reaction is the formation of the postulated deuterium-rich rhodium complex (see Section 4.2.1.1.), from this displacement and liberation of the alkane ligand. This was noted as an intermediate, before eventual decomposition to **[1-BAr$^F_4$]**. This complete decomposition route occurs at the assigned rate of k_4.

If complexes exhibit a rapid rate of H/D exchange (fast k_3) with minimal stability (fast k_4), this results in deuterium incorporation within the alkane ligand which is prevented from going to completion due to the instability of the σ-alkane complex. An example of this is

[1-propane][BAr$^F_4$], where relatively fast H/D exchange occurs to produce a range of deuterated propane isotopologues within 5 minutes. After 5 minutes under a D_2 atmosphere, the complete decomposition to **[1-BAr$^F_4$]** is observed, as no further H/D exchange occurs.

In contrast, **[1-NBA][BAr$^F_4$]** is an example of a complex that undergoes slow H/D exchange (slow k_3) yet does not decompose under a D_2 atmosphere ($k_4 \sim 0$). When exposed to a D_2 atmosphere, the NBA fragment in **[1-NBA][BAr$^F_4$]** is shown to maximise deuterium incorporation (NBA-d_4) in quantitative yields with no observable decomposition products. However, this H/D exchange process occurs slowly over the course of 18 hours. This is unlike **[1-propane][BAr$^F_4$]**, where rapid complex decomposition limits propane-d_8 formation.

Complexes including **[1-*iso*butane][BAr$^F_4$]** and **[1-*iso*pentane][BAr$^F_4$]** exhibit relatively rapid rates of complete H/D exchange (both ~ 90 minutes), yet completely decompose to form **[1-BAr$^F_4$]** within this time. They show a relative fast rate of H/D exchange (k_3) however suffer from the relatively slow, yet significant, rate of decomposition (k_4). Theoretically, an ideal system would therefore exhibit a fast k_3 and slow k_4. This would result in deuterium rich alkane products with no loss in yield of the overall complex.

4.5. Chapter Conclusions

All of the σ-alkane complexes presented in Chapter 2 readily undergo H/D exchange of the respective alkane when placed under an atmosphere of D_2. The complexes of **[1-*iso*butane][BAr$^F_4$]** and **[1-*iso*pentane][BAr$^F_4$]** were found to include isotopologues of maximum deuterium incorporation (*iso*butane-d_{10} and *iso*pentane-d_{12} respectively). For the σ-alkane complexes of **[1-propane][BAr$^F_4$]**, **[1-hexane][BAr$^F_4$]** and **[1-(3-methylpentane)][BAr$^F_4$]**, although H/D exchange was shown to have occurred, this was limited in comparison. This was explained by the poor stability of these alkane complexes under a D_2 / H_2 atmosphere before eventual solid-state decomposition to **[1-BAr$^F_4$]**.

H/D exchange of these complexes in the solid-state are also further proof of their production and stability. The solid-state environments of these complexes retains the coordination of alkane ligand to metal centre, which further allows for H/D exchange to occur. When conducted in solution, this supportive environment is removed, and the poorly co-ordinated alkane ligand is rapidly displaced by solvent or anion. This was confirmed by experimental attempts of H/D exchange upon these complexes in solution, which did not yield any isotopologues greater than addition of D_2 over their C=C bonds.

Chapter 4 also further highlights the relative ease of C–H activation processes. When starting from molecular σ-alkane complexes, by simple exposure to an atmosphere of D_2, all the alkane complexes exhibit a level of deuterium incorporation. The significant amount of incorporation within these relatively short times shows how facile the H/D exchange processes can be when starting from molecular σ-alkane complexes.

4.6. References

1 W. D. Jones, *Inorg. Chem.*, 2005, **44**, 4475–4484.
2 W. D. Jones, *Acc. Chem. Res.*, 2003, **36**, 140–146.
3 G. Parkin, *J. Label. Compd. Radiopharm.*, 2007, **50**, 1088–1114.
4 A. S. Weller, F. M. Chadwick and A. I. McKay, in *Advances in Organometallic Chemistry*, Academic Press, 2016, pp. 223–276.
5 K. R. Sawyer, J. F. Cahoon, J. E. Shanoski, E. A. Glascoe, M. F. Kling, J. P. Schlegel, M. C. Zoerb, M. Hapke, J. F. Hartwig, C. Edwin Webster and C. B. Harris, *J. Am. Chem. Soc.*, 2010, **132**, 1848–1859.
6 J. Atzrodt, V. Derdau, W. J. Kerr and M. Reid, *Angew. Chem. Int. Ed.*, 2018, **57**, 3022–3047.
7 W. H. Bernskoetter, S. K. Hanson, S. K. Buzak, Z. Davis, P. S. White, R. Swartz, K. I. Goldberg and M. Brookhart, *J. Am. Chem. Soc.*, 2009, **131**, 8603–8613.
8 N. M. Scott, R. Dorta, E. D. Stevens, A. Correa, L. Cavallo and S. P. Nolan, *J. Am. Chem. Soc.*, 2005, **127**, 3516–3526.
9 A. F. Dunlop-Brière, M. C. Baird and P. H. M. Budzelaar, *Organometallics*, 2015, **34**, 2356–2368.
10 R. G. Bergman, *Nature*, 2007, **446**, 391–393.
11 E. A. Cobar, R. Z. Khaliullin, R. G. Bergman and M. Head-Gordon, *Proc. Natl. Acad. Sci.*, 2007, **104**, 6963–6968.
12 T. J. Hebden, M. C. Denney, V. Pons, P. M. B. Piccoli, T. F. Koetzle, A. J. Schultz, W. Kaminsky, K. I. Goldberg and D. M. Heinekey, *J. Am. Chem. Soc.*, 2008, **130**, 10812–10820.
13 G. Alcaraz and S. Sabo-Etienne, *Coord. Chem. Rev.*, 2008, **252**, 2395–2409.
14 R. H. Crabtree, *Chem. Rev.*, 2016, **116**, 8750–8769.
15 M. Grellier, S. A. Mason, A. Albinati, S. C. Capelli, S. Rizzato, C. Bijani, Y. Coppel and S. Sabo-Etienne, *Inorg. Chem.*, 2013, **52**, 7329–7337.
16 J. C. Green, M. L. H. Green and G. Parkin, *Chem. Commun.*, 2012, **48**, 11481–11503.
17 M. Brookhart, M. L. H. Green and G. Parkin, *Proc. Natl. Acad. Sci.*, 2007, **104**, 6908–6914.
18 A. L. Pitts, A. Wriglesworth, X. Z. Sun, J. A. Calladine, S. D. Zarić, M. W. George and M. B. Hall, *J. Am. Chem. Soc.*, 2014, **136**, 8614–8625.
19 S. H. Lee, S. I. Gorelsky and G. I. Nikonov, *Organometallics*, 2013, **32**, 6599–6604.
20 R. A. Periana and R. G. Bergman, *J. Am. Chem. Soc.*, 1986, **108**, 7332–7346.
21 J. M. Buchanan, J. M. Stryker and R. G. Bergman, *J. Am. Chem. Soc.*, 1986, **108**, 1537–1550.
22 M. D. Walter, P. S. White, C. K. Schauer and M. Brookhart, *J. Am. Chem. Soc.*, 2013, **135**, 15933–15947.
23 A. Sattler, *ACS Catal.*, 2018, **8**, 2296–2312.
24 D. Balcells, E. Clot and O. Eisenstein, *Chem. Rev.*, 2010, **110**, 749–823.
25 M. Lersch and M. Tilset, *Chem. Rev.*, 2010, **110**, 749–823.
26 G. J. Kubas, *Metal Dihydrogen and sigma-Bond Complexes - Structure, Theory and Reactivity*, Plenum Publishers, 2001.
27 R. H. Crabtree, *Chem. Rev.*, 2016, **116**, 8750–8769.
28 R. H. Crabtree, *The Organometallic Chemistry of the Transition Metals*, John Wiley & Sons, Ltd, 4th edn., 2014.
29 R. Waterman, *Organometallics*, 2013, **32**, 7249–7263.
30 R. N. Perutz and S. Sabo-Etienne, *Angew. Chem. Int. Ed.*, 2007, **46**, 2578–2592.
31 B. A. Vastine and M. B. Hall, *J. Am. Chem. Soc.*, 2007, **129**, 12068–12069.
32 F. M. Chadwick, T. Krämer, T. Gutmann, N. H. Rees, A. L. Thompson, A. J. Edwards, G. Buntkowsky, S. A. Macgregor and A. S. Weller, *J. Am. Chem. Soc.*, 2016, **138**, 13369–13378.
33 A. I. McKay, A. J. Bukvic, B. E. Tegner, A. L. Burnage, A. J. Martínez-Martínez, N. H. Rees, S. A. Macgregor and A. S. Weller, *J. Am. Chem. Soc.*, 2019, **141**, 11700–11712.
34 G. A. Newsome, F. L. Steinkamp and B. C. Giordano, *J. Am. Soc. Mass Spectrom.*, 2016, **27**, 1789–1795.
35 A. J. Martínez-Martínez, C. G. Royle, S. K. Furfari, K. Suriye and A. S. Weller, *ACS Catal.*, 2020, **10**, 1984–1992.
36 T. M. Douglas, S. K. Brayshaw, R. Dallanegra, G. Kociok-Köhn, S. A. Macgregor, G. L. Moxham, A. S. Weller, T. Wondimagegn and H. P. Vadivelu, *Chem. - A Eur. J.*, 2008, **14**, 1004–1022.
37 T. M. Douglas and A. S. Weller, *New J. Chem.*, 2008, **32**, 966–969.
38 R. S. Rubins, A. Feldman and A. Honig, *Phys. Rev.*, 1968, **169**, 299–311.
39 *2-methylbutane -- AIST Spectr. Database Org. Compd. -- (SDBS No. 10633) -- Date Acc. 10-07-2020*.

Chapter 5:
Surface Modifcation of Solid-State σ-Alkane Complexes

5.1. Chapter Introduction

The previous work in this thesis focuses on solid/gas reactivity involving SMOM materials with relatively inert gases. The resulting bulk transformations observed are often only simple displacement or (de)hydrogenation reactions. If a more reactive substrate is used, this may allow for surface-specific reactivity to be explored. One such reactive substrate is ethyl vinyl ether.

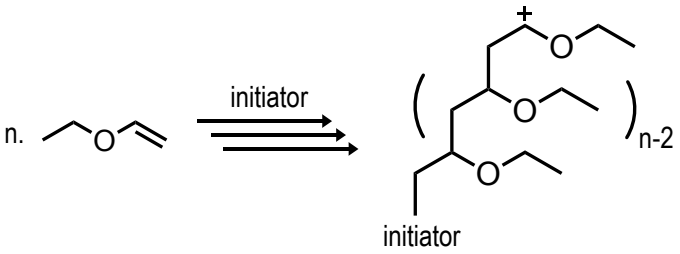

Scheme 5.1: Overview of ethyl vinyl ether polymerisation.

Vinyl ethers have been reported to undergo rapid, cationic polymerisation to form poly(vinylethers) (Scheme 5.1), where these poly(vinylethers) are typically deployed as lubricants and adhesives.[1] Typical initiators include simple Lewis acids, such as $BF_3 \cdot Et_2O$ $FeCl_3$ and $SnCl_2$,[2] as well as organometallic examples.[3,4] These follow a chain growth mechanism, where the chain propagates from the growing end of the polymer chain, away from the initiator.

Vinyl ethers are also employed in the polymer coating of support materials. This concept of forming a polymer layer around a material is described as graft polymerisation and is a well-established methodology in the surface modification of materials. By using either pre-formed polymer chains[5,6] (grafting-*to*) or a controlled polymerisation (grafting-*from*) reaction[7] (Scheme 5.2), these polymer coats can adapt a solid material towards a range of purposes. Notably, grafting-from reactions rely on the ability of a surface to initiate[8] and control a polymerisation reaction.

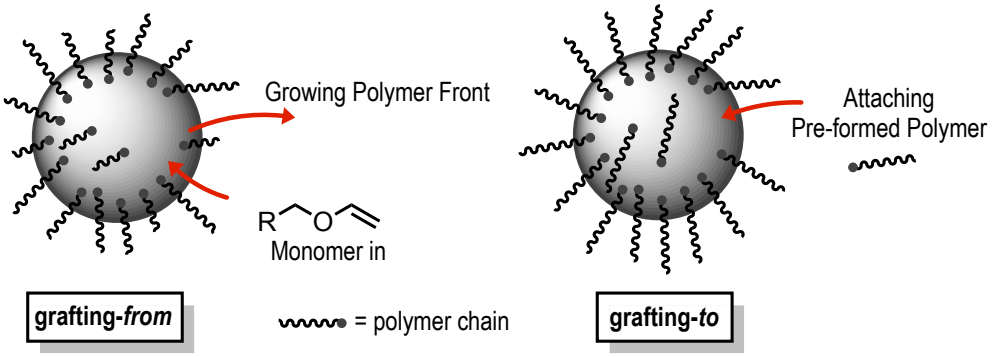

Scheme 5.2: Grafting-*from versus* grafting-*to* of a polymer chain to support material.

Examples of this process include support materials such as nanoparticles,[9–11] which can lead to a tuning of their magnetic properties, and grafting-from metal-organic frameworks,[12] which can allow for increased stability and conductivity of the MOF material. Supported molecular ruthenium catalysts towards the ring opening metathesis polymerisation of norbornene can also be coated, which can give control over the morphology of the poly(norbornene) produced.[13]

More specifically, grafting-from polymerisation towards *single-crystalline* materials is less established, with limited examples. These only include support materials such as MOFs,[14,15] organic materials[16,17] and polyoxometalate frameworks[18] to our knowledge, to which the polymer coat gave control over the guest-host exchange rate within these clusters. Work by the Blum group has also reported the polymerisation of ethylene oxide upon the surface of crystalline cobalt-ligand complexes, but this was limited to specific loci upon the surface of the crystal, and did not yield a uniform distribution of polymer covering.[19]

Applying this methodology to ideas presented in this thesis, it was postulated if SMOM materials could control a grafting-from polymerisation reaction. σ-Alkane complexes are viewed as masked, naked rhodium-complexes, which are Lewis acidic in nature. This makes them ideal for vinyl ether polymerisation when the alkane is removed.[20] Additionally, the surface of these molecular crystals can even be viewed as single-atom catalysts.[21,22] Therefore, if all sites are active towards polymerisation, a potential complete surface covering can be achieved.

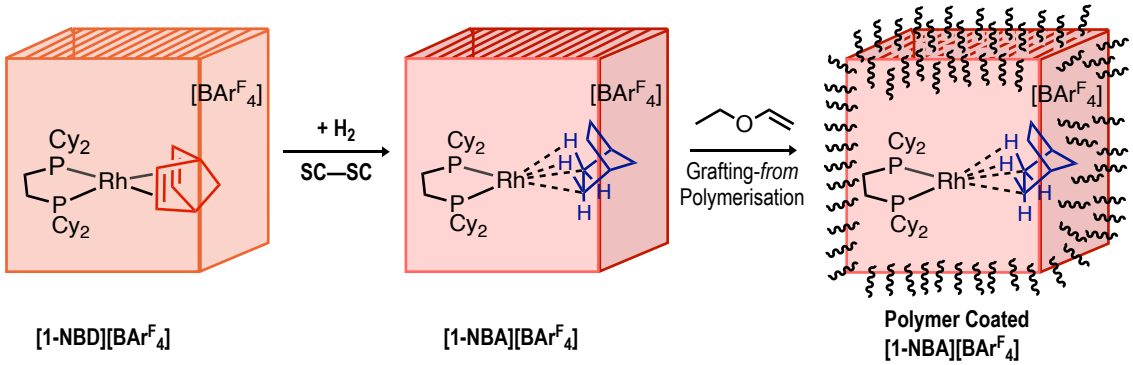

Scheme 5.3: Concept of using ethyl vinyl ether to polymerise upon, and therefore coat, the surface of the single crystals of **[1-NBA][BAr$^F_4$]**.

Chapter 5 aims to link a grafting-from polymerisation reaction to a SMOM system (Scheme 5.3). This would lead to a complete surface covering of polymer, which could modify the properties and stabilities of the bulk SMOM system. The SMOM material of **[1-NBA][BAr$^{F}_{4}$]** was chosen, due to its high stability under an inert atmosphere and relatively easy synthesis coupled with an aim of the polymer coat acting as a protective barrier towards detrimental reagents, such as oxygen gas and water vapour. This could potentially stabilise the highly reactive complex towards air.

5.2. SMOM@polymer

5.2.1. Synthesis of [1-NBA][BAr$^{F}_{4}$]@poly(EVE)

In previous SMOM reactions, only solid/gas studies have been reported. As no suitable gaseous vinyl ethers were available, ethyl vinyl ether (EVE) was chosen due to its high volatility (b.p. 33 ºC) and consequent ease in forming a vapour, gas-like, atmosphere. As the reactivity of volatile liquid substrates and SMOM materials have not been explored before either, a new experiment set-up had to be developed and optimised.

To achieve this, specialised reaction equipment had to be made. By attaching a needle to the base of a J. Youngs tap, multiple crystals of **[1-NBD][BAr$^{F}_{4}$]** (size of ~0.5 × 0.5 × 1.0 mm, ~1.0 mgs each) could be mounted to said pin (Figure 5.1a and b). Attachment of the crystals was aided by a small amount of silicon grease. These crystals can then be hydrogenated in an *in situ*, single-crystal to single-crystal reaction to yield crystals of **[1-NBA][BAr$^{F}_{4}$]**, the active polymerisation initiator (Figure 5.1c). Due to the fragile nature of the **[1-NBA][BAr$^{F}_{4}$]** crystals, they could not be easily handled and mounted, hence stronger crystals of **[1-NBD][BAr$^{F}_{4}$]** were mounted and hydrogenated *in situ*.

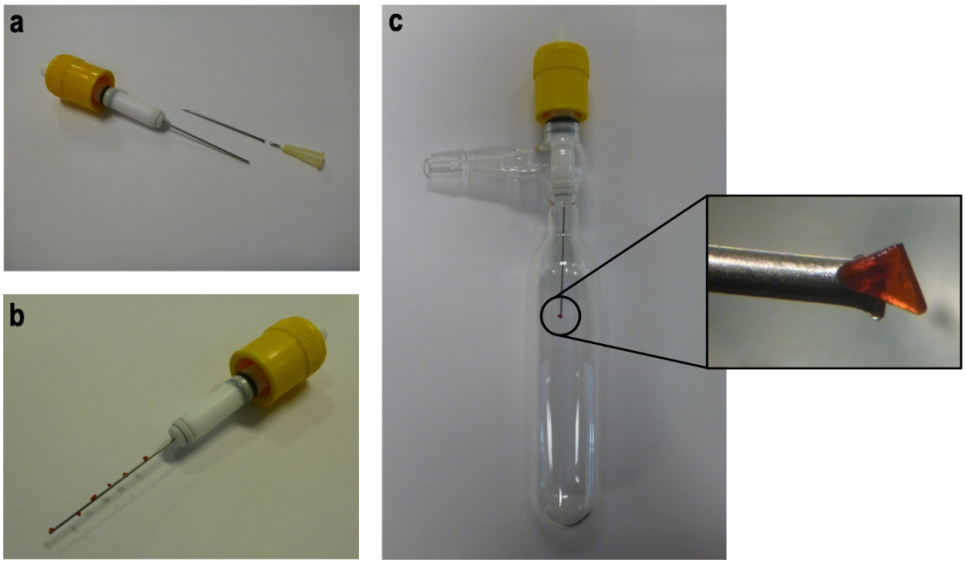

Figure 5.1: Glassware set up used in the formation of **[1-NBA][BAr$^{F}_{4}$]@poly(EVE)**. **a**) Set up of specially adapted J. Youngs tap, by inserting a cut needle into the base of a J. Youngs tap. **b**) Adapted tap with multiple crystals of **[1-NBD][BAr$^{F}_{4}$]** mounted to the needle. **c**) Full construction inserted into J. Youngs flask, with expansion showing a mounted, single crystal of **[1-NBA][BAr$^{F}_{4}$]**.

The EVE monomer was then vacuum transferred into the flask, the flask sealed under a static vacuum and warmed to room temperature. The static vacuum and volatile nature of EVE meant a vapour atmosphere of EVE was formed within the flask, surrounding the mounted crystals. The vapour then condensed upon the surface of the crystalline **[1-NBA][BAr$^{F}_{4}$]** initiating the polymerisation event in a solid / vapour reaction.

After either 30 seconds, 2.5 minutes or 15 minutes the flask was exposed to a dynamic vacuum, removing the excess vapour monomer and halting the polymerisation reaction. This yielded the polymer coated crystalline σ-alkane complex of [Rh($Cy_2PCH_2CH_2PCy_2$)(NBA)][BAr$^{F}_{4}$]@poly(ethylvinylether);**[1-NBA][BAr$^{F}_{4}$]@poly(EVE)** (Figure 5.2), with respect to the individual EVE exposure time. The exposure time was kept at either 30 seconds, 2.5 or 15 minutes throughout. Upon longer exposure times to EVE (> 15 minutes), further polymerisation events occurred, and are discussed in Section 5.5. As **[1-NBA][BAr$^{F}_{4}$]** was fully encapsulated in a polymer coat this becomes a material@polymer, more specifically SMOM@poly(EVE), adapted from MOF nomenclature.[15]

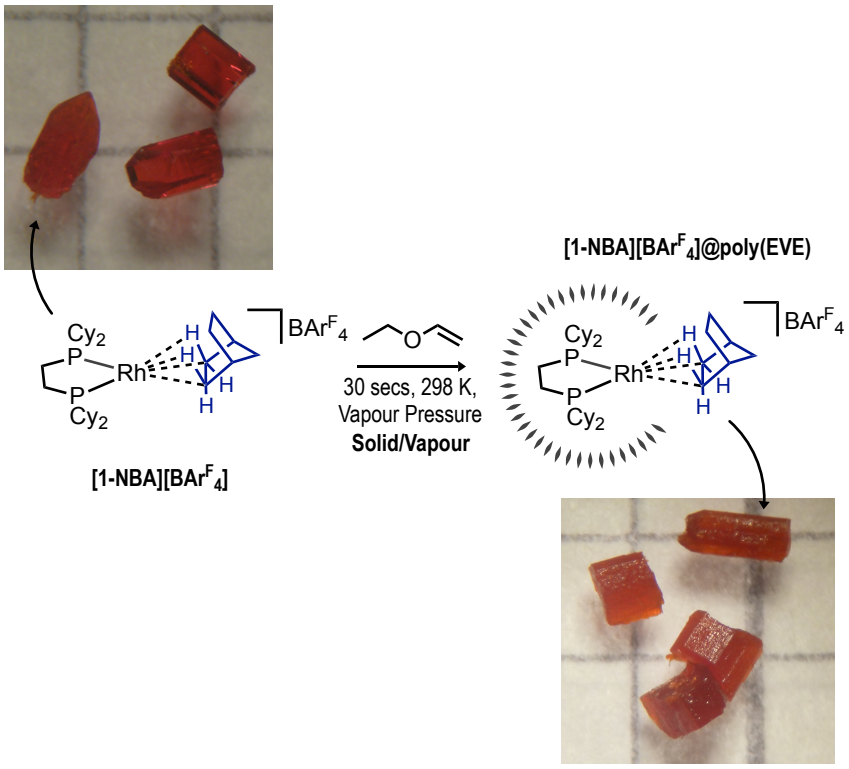

Figure 5.2: **a**) Synthetic route to **[1-NBA][BAr$^F_4$]@poly(EVE)**. Images are example crystals of uncoated **[1-NBD][BAr$^F_4$]** and **[1-NBA][BAr$^F_4$]@poly(EVE)** with 30 seconds EVE exposure removed from their mounts. This highlights the slight shine left upon the polymer coated crystals. Each grid marks 2 mm x 2 mm.

This grafting-from polymerisation coats individual crystals in a layer of poly(EVE), where the thickness of the polymer layer can be controlled through the exposure time to EVE. Vapour phase polymerisation reactions in other systems are well established, and are ideal for easy separation of monomer and initiator.[23] This separation of SMOM-initiator and liquid monomer is essential, as any direct contact between the two resulted in rapid dissolution and loss of crystallinity. Importantly, no reaction was observed between **[1-NBD][BAr$^F_4$]** and EVE, in either solid/vapour reaction or in CH_2Cl_2 solution. This suggests displacement of the weakly bound alkane fragment by EVE monomer is a key step in the polymerisation pathway.

5.2.2. Characterisation of the Bulk of [1-NBA][BAr$^F_4$]@poly(EVE)

After 30 seconds of EVE exposure, $^{31}P\{^1H\}$ SSNMR spectroscopy was used to probe the bulk of **[1-NBA][BAr$^F_4$]@poly(EVE)**, shown in Figure 5.3. The major signal at δ 110 is from unreacted **[1-NBA][BAr$^F_4$]**, that is assumed to be internal to the crystal.[24] New species at δ 105 and 80 are observed, which integrate to ~10 % of the total signals and are tentatively assigned to new surface, polymer bound species. Resonances at δ 71 at 42 can also be observed in the $^{13}C\{^1H\}$ SSNMR spectrum, consistent with that of the O**C**H$_2$ and O**C**H environments within the EVE polymer coat, labelled ⊹ in Figure 5.3.[25]

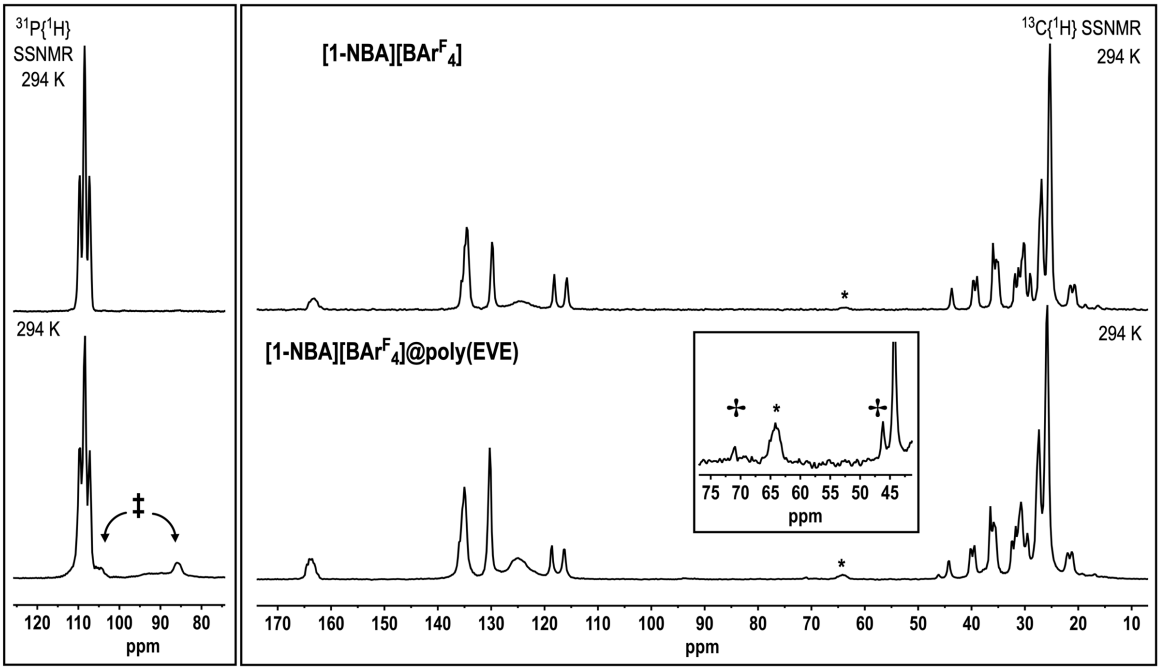

Figure 5.3: The $^{31}P\{^1H\}$ and $^{13}C\{^1H\}$ SSNMR (162 / 101 MHz, 10 kHz spin rate, 294 K) spectra of **[1-NBA][BAr$^F_4$]** and **[1-NBA][BAr$^F_4$]@poly(EVE)**. ‡ = signal assigned to ^{31}P environments associated with **[1-NBA][BAr$^F_4$]@poly(EVE)**. The inset is an enlargement of the signals between 75 and 45 ppm, where ⊹ = signals assigned to ^{13}C environments in the polymer coat. * = spinning sidebands.

In addition to this, single crystal x-ray diffraction studies confirmed the retention of crystallinity during the coating process. A structure of **[1-NBA][BAr$^F_4$]** was collected and refined (R_1 = 7.5 %) after 30 seconds EVE exposure whilst operating under strict anaerobic conditions. No structural differences could be observed between the crystal structures of **[1-NBA][BAr$^F_4$]** and **[1-NBA][BAr$^F_4$]@poly(EVE)**. This structure, combined with SSNMR spectroscopy, suggest the bulk crystalline material has remained unchanged during the polymerisation time of 30 seconds.

After 2.5 minutes EVE exposure however, although the shape and form of the crystals were visually unchanged, a solid-state structure of this complex by single-crystal x-ray diffraction could not be collected. The poor crystallographic quality of the crystal is shown by broad spots[26] in the diffraction frames shown in Figure 5.4. This suggests degradation of the crystal bulk during this longer exposure to an EVE atmosphere, most likely from the monomer beginning to polymerise throughout the crystal in this time. It is suggested that the polymerisation reaction is now not limited to a surface polymerisation reaction. After 15 minutes EVE exposure, complete loss of form and shape of the crystals had occurred, where no long-range order is confirmed by single-crystal x-ray diffraction.

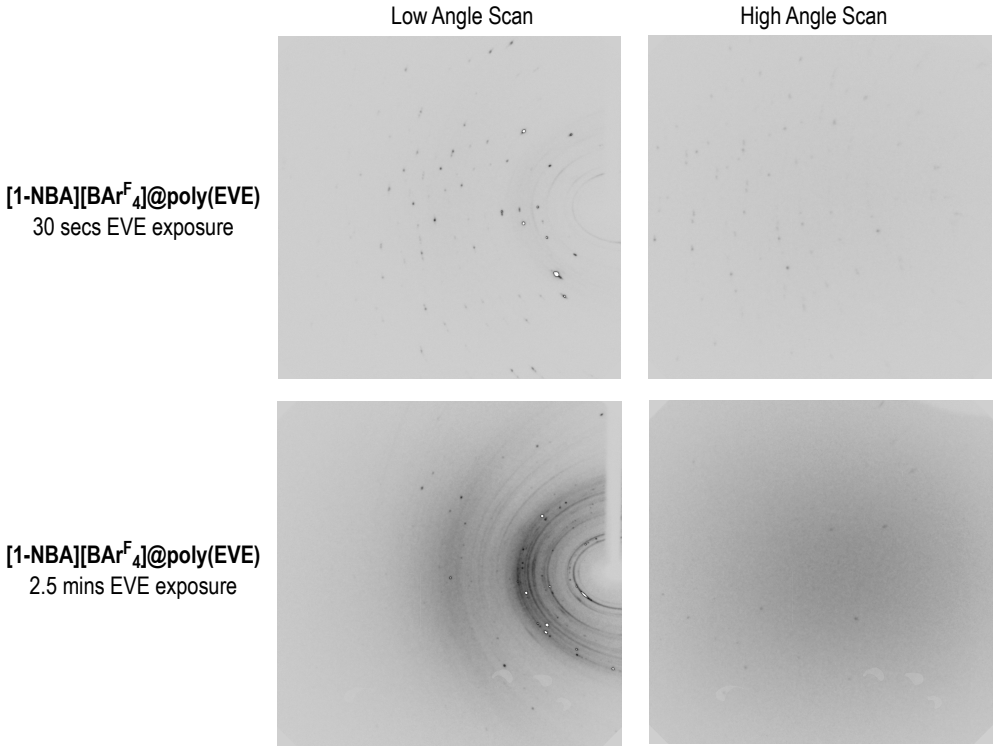

Figure 5.4: Selected high and low angle single-crystal x-ray frames of **[1-NBA][BAr$^F_4$]@poly(EVE)** after 30 seconds and 2.5 minutes.

The thickness of this poly(EVE) coat was quantified by solution ^{1}H NMR spectroscopy of the dissolved **[1-NBA][BAr$^F_4$]@poly(EVE)** after different EVE exposure times. Crystals of **[1-NBA][BAr$^F_4$]@poly(EVE)** with 30 seconds, 2.5 or 15 minutes EVE exposure times were dissolved in MeCN-d_3, which liberated the polymer coats and forms the organometallic fragment of the deuterated analogue of **[1-(MeCN)$_2$][BAr$^F_4$]**.[27] This was shown by free-polymer ether groups in the ^{1}H NMR spectrum (Figure 5.5), additionally proving poly(EVE) formation. The relative integrals of ^{1}H signals of [BAr$^F_4$]$^-$ anion to the OC**H** and OC**H$_2$**CH$_3$ signals of poly(EVE) [δ 3.75 – 3.25][25] can be calculated.

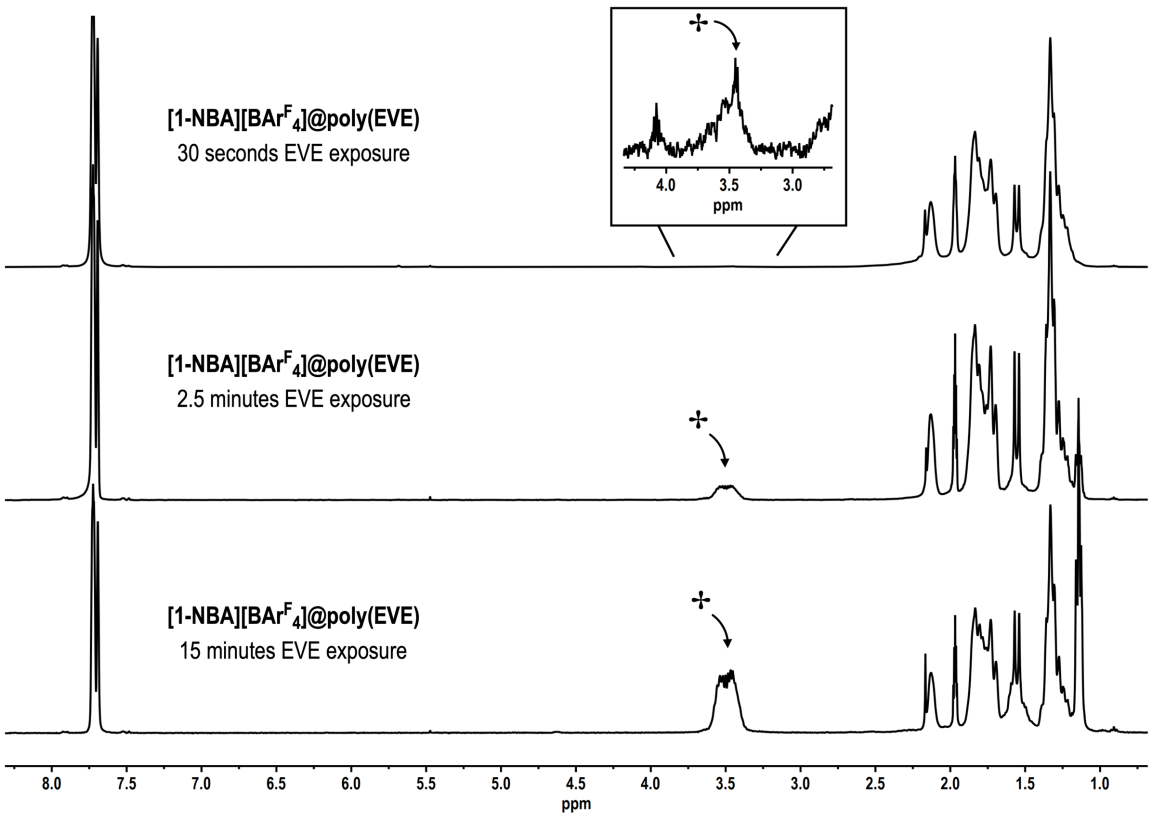

Figure 5.5: ^{1}H NMR spectra of **[1-NBA][BAr$^F_4$]@poly(EVE)** dissolved in MeCN-d_3. ✢ = signals assigned to overlapping –OC**H**– and –OC**H$_2$**CH$_3$ of the liberated polymer.

At 30 seconds, 2.5 and 15 minutes respectively, the relative integrals of EVE *versus* [BAr$^F_4$]$^-$ anion signals increase from 0.1: 1, 0.7: 1 to 4.4: 1. This shows that upon longer EVE exposure times, a greater amount of polymer is formed, and the coating layer is increasing in thickness with respect to time. Unfortunately, gel permeation chromatography (GPC) analysis could not be reliably conducted upon such a small volume of polymer. This would aid in the characterisation of the polymer length/structure and would show if the increase in polymer was from multiple chains of similar length, or one continual chain growth which is anchored to the SMOM platform.

5.2.3. Characterisation of the Surface of [1-NBA][BAr$^{F}_{4}$]@poly(EVE)

To probe just the surface of the **[1-NBA][BAr$^{F}_{4}$]@poly(EVE)** crystals, analysis by Scanning Electron Microscopy (SEM) and Energy-Dispersive X-ray (EDX) spectroscopy was conducted. To highlight the difference in polymer coating, **[1-NBD][BAr$^{F}_{4}$]**, **[1-NBA][BAr$^{F}_{4}$]** and **[1-NBA][BAr$^{F}_{4}$]@poly(EVE)** were also studied. As shown in Figure 5.6a, crystals of uncoated **[1-NBD][BAr$^{F}_{4}$]** have a metallic, polished look. The main composition of the surface was shown to be fluorine and carbon, suggesting the surface on this face is dominated by the -CF_3 groups in the [BAr$^{F}_{4}$]$^{-}$ anion. This was shown by relatively high C: F ratio (8.1: 1). In addition, no rhodium signals were located in the EDX of **[1-NBD][BAr$^{F}_{4}$]**.

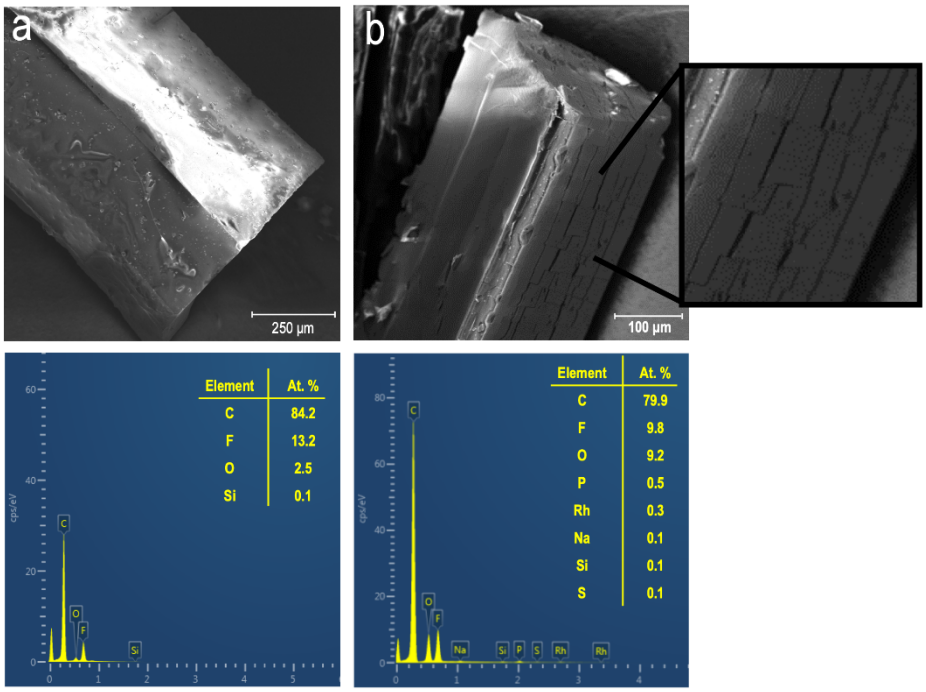

Figure 5.6: SEM image (top) and EDX sum spectrum (bottom) of a single crystal of **a**) **[1-NBD][BAr$^{F}_{4}$]** and **b**) **[1-NBA][BAr$^{F}_{4}$]**. Enlargement shows micro-cracking can also be seen upon the faces of the crystals. At. % = Atomic Percentage.

Upon hydrogenation to form **[1-NBA][BAr$^{F}_{4}$]**, cracking of the crystalline surface can be clearly seen in the crystals (Figure 5.6b). This has been previously proposed to enable a range of solid/gas transformations in SMOM materials[27,28] and in microcrystalline ruthenium complexes.[29] Small, but significant levels of rhodium and phosphorus can now be seen in the EDX of **[1-NBA][BAr$^{F}_{4}$]**, suggesting that this micro-cracking has also exposed internal cationic fragments. This can be linked to the high surface reactivity towards vinyl ether polymerisation, as active sites may have been exposed. This array of

exposed cations forms the single-atom type catalyst, pivotal in the formation of a polymer layer across the crystalline surface. This is unlike in the previously reported molecular system by the Blum group, where specific loci upon the crystal surface initiated reactions.[19]

In both the EDX spectra of **[1-NBD][BAr$^{F}_{4}$]** and **[1-NBA][BAr$^{F}_{4}$]**, 2.5 and 9.2 atomic % of oxygen is located respectively, (Figure 5.6). At this point, no polymer coating has been applied, and no oxygen containing species are within the complex. It is suggested that this is related to unavoidable contact with air when transferring the samples from argon filled glove box to vacuum chamber of the SEM machine. The 0.1 atomic % of silicon is attributed to the dab of silicon grease used in crystal mounting.

The surface of **[1-NBA][BAr$^{F}_{4}$]@poly(EVE)** with 30 seconds EVE exposure, shows a rougher, textured appearance (Figure 5.7a). The crystals' form and shape had remained intact, critical for further SC-SC reactions. The EDX shows a decrease in intensity of fluorine signals (C: F ratio of now 9.5: 1), and a significant increase in oxygen signals. As fluorine signals are still observed, this suggests only a partial coating of poly(EVE) has been applied to the surface, as some [BAr$^{F}_{4}$]$^{-}$ anions are still exposed. This coating is proposed to be 1–2 μm, as this is the typical penetration depth in EDX spectroscopy upon polymers.[30]

After 2.5 minutes and 15 minutes EVE exposure (Figure 5.7b and c respectively), the EDX only shows the elements of C and O, the intensities of which are consistent with the atomic percentage of neat polymer, (At.%$_{calc}$ of poly(EVE) = C: 80 %, O: 20 %). No fluorine signals can be observed, suggestive of a saturated surface of polymer beyond the significant EDX limit (> 2 μm). This build-up of polymer can be also linked to the visual inspection of the crystal surfaces after these times. After 2.5 minutes, the polymer coat can now be clearly seen by the oily nature of the crystal surface. After 15 minutes, liquid polymer coating can also be seen to be flowing away from the crystal exterior, suggestive of a further polymerisation reaction (see Section 5.5.).

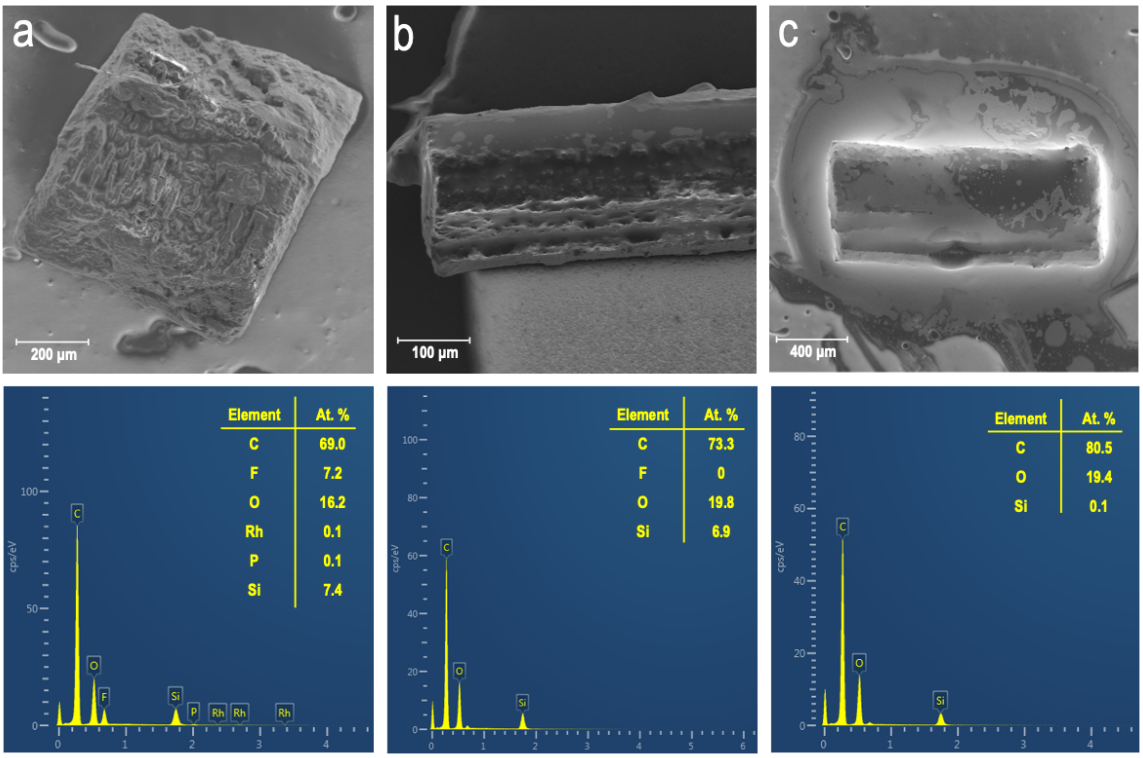

Figure 5.7: SEM image (top) and EDX sum spectrum (bottom) of a single crystal of **[1-NBA][BAr$^{F}_{4}$]@poly(EVE)** with of **a**) 30 seconds EVE exposure **b**) 2.5 minutes EVE exposure and **c**) 15 minutes EVE exposure. At. % = Atomic Percentage.

With this polymer coat synthesised and characterised, the next sub-sections explore if this enables any different reactivity compared to uncoated **[1-NBA][BAr$^{F}_{4}$]**. To explore this, the reactions of the SMOM materials were reacted in air or with propene gas.

5.3. Further Reactivity of SMOM@polymer

5.3.1. Stability of [1-NBA][BAr$^F_4$]@poly(EVE) in Air

This Section aims to explore if the polymer coat in **[1-NBA][BAr$^F_4$]@poly(EVE)** results in any differences in further reactivity compared to that of uncoated **[1-NBA][BAr$^F_4$]**. The first such reactivity to be explored was that with air (Scheme 5.4).

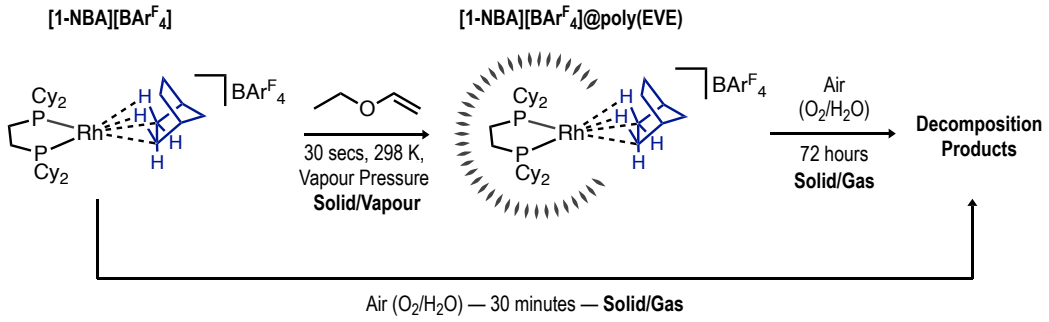

Scheme 5.4: Decomposition pathway of **[1-NBA][BAr$^F_4$]** and **[1-NBA][BAr$^F_4$]@poly(EVE)** when left in air.

When crystals of **[1-NBA][BAr$^F_4$]@poly(EVE)** that had undergone 30 seconds EVE exposure are exposed to air for 30 minutes, the bulk was found to have remarkably remained as **[1-NBA][BAr$^F_4$]**. This reaction was followed by SSNMR spectroscopy and single-crystal x-ray diffraction, where the solid-state structure collected after 30 minutes air exposure is shown in Figure 5.8a.

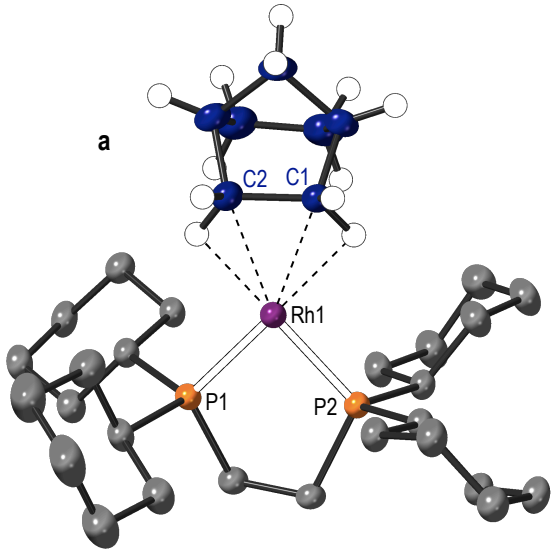

b

	[1-NBA][BAr$^F_4$]	[1-NBA][BAr$^F_4$]@poly(EVE)
Rh1-P1	2.1932(7)	2.1854(7)
Rh1-P2	2.1950(7)	2.1949(7)
Rh1-C1	2.389(3)	2.389(3)
Rh1-C2	2.400(3)	2.409(3)
C1-C2	1.552(5)	1.544(5)
R Factor	**4.2 %**	**4.9 %**

Figure 5.8: **a**) Isolated cation of **[1-NBA][BAr$^F_4$]@poly(EVE)** after 30 seconds EVE exposure and 30 minutes air exposure. Displacement ellipsoids set at 30%. Hydrogen atoms from bisphosphine ligand and [BAr$^F_4$]$^-$ anion removed for clarity. **b**) Table shows selected bond metrics of **[1-NBA][BAr$^F_4$]**[24] and **[1-NBA][BAr$^F_4$]@poly(EVE)**.

The collected structure was near identical to that of **[1-NBA][BAr$^{F}_{4}$]** prepared under an inert atmosphere. No structural differences or significant differences in bond metrics could be observed between the structures of **[1-NBA][BAr$^{F}_{4}$]** and **[1-NBA][BAr$^{F}_{4}$]@poly(EVE)** (Figure 5.8b). This shows how the crystallinity of **[1-NBA][BAr$^{F}_{4}$]** is retained not only during the surface polymerisation reaction, but also after 30 minutes air exposure.

The $^{31}P\{^{1}H\}$ SSNMR spectra of **[1-NBA][BAr$^{F}_{4}$]@poly(EVE)** after 30 seconds EVE exposure and 30 minutes air exposure exhibited a major sharp signal at δ 105 (Figure 5.9). This is consistent to that of **[1-NBA][BAr$^{F}_{4}$]** and shows how the bulk has remained intact during air exposure. The broad, low intensity features however between δ 105 and 80 present in the spectrum of **[1-NBA][BAr$^{F}_{4}$]@poly(EVE)** (Figure 5.3) are no longer present. Whether this is due to surface located species undergoing reactions with oxygen is not clear.

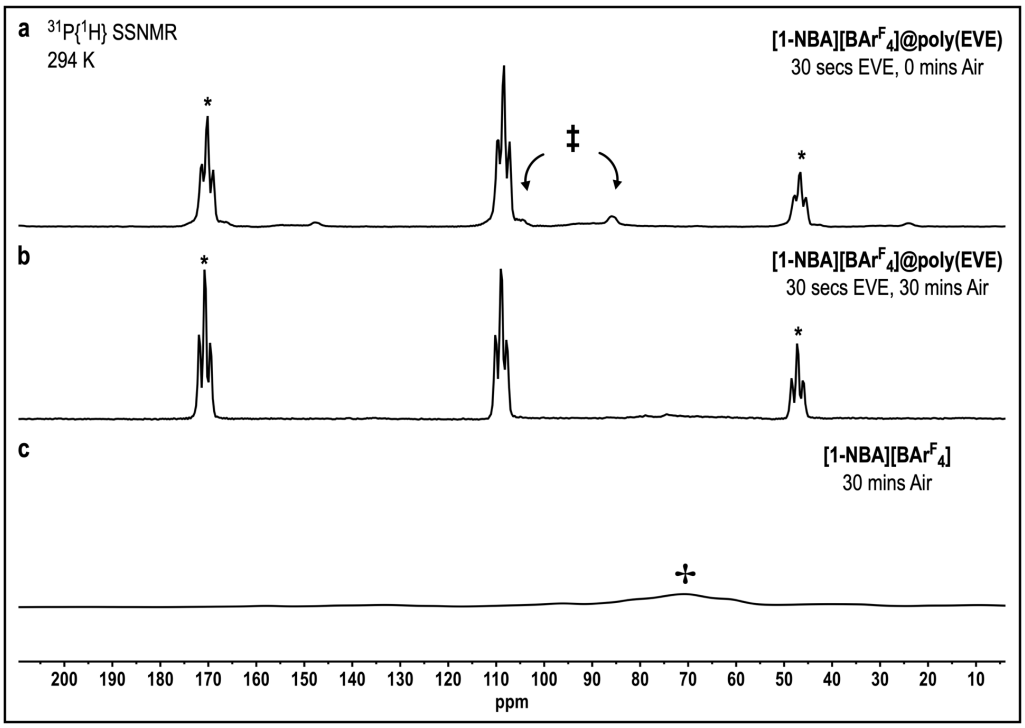

Figure 5.9: The $^{31}P\{^{1}H\}$ SSNMR (162 MHz, 10 kHz spin rate, 294 K) spectra of **a**) **[1-NBA][BAr$^{F}_{4}$]@poly(EVE)** exposed to EVE for 30 seconds, kept under an inert atmosphere. This is the same spectrum as Figure 5.3. **b**) **[1-NBA][BAr$^{F}_{4}$]@poly(EVE)** exposed to EVE for 30 seconds and a further 30 minutes in air. **c**) Uncoated **[1-NBA][BAr$^{F}_{4}$]** exposed to air for 30 minutes. ‡ = signal assigned to ^{31}P environments associated with **[1-NBA][BAr$^{F}_{4}$]@poly(EVE)**. ✢ = Solid-state decomposition product of **[1-NBA][BAr$^{F}_{4}$]** in air. * = spinning sidebands.

In contrast, uncoated crystals of **[1-NBA][BAr$^{F}_{4}$]** underwent complete decomposition within 30 minutes. No signals relating to that of **[1-NBA][BAr$^{F}_{4}$]** are observed in the $^{31}P\{^{1}H\}$

SSNMR spectra of this material after 30 minutes air exposure (Figure 5.9c). Crystals of this product were shown to be amorphous, shown by the complete loss of all Bragg peaks within this time. Furthermore, a colour change of the crystals (red to green) was also noted.

5.3.2. Reactions in Air – Visual Images

The further reactivity of **[1-NBA][BAr$^F_4$]** and **[1-NBA][BAr$^F_4$]@poly(EVE)** after times greater than 30 minutes in air was also studied. Shown in Figure 5.10 are images taken over a range of 72 hours of both uncoated **[1-NBA][BAr$^F_4$]** and **[1-NBA][BAr$^F_4$]@poly(EVE)** (with 30 seconds EVE exposure) crystals when left in air.

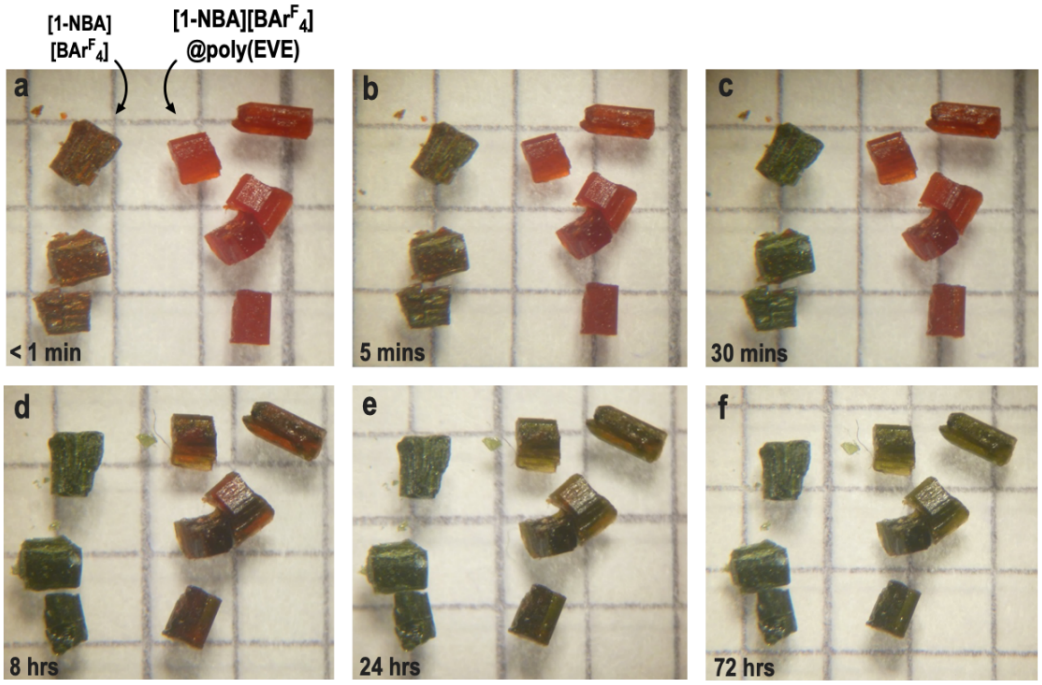

Figure 5.10: Optical images of samples of **[1-NBA][BAr$^F_4$]** and **[1-NBA][BAr$^F_4$]@poly(EVE)** exposed in air for varying times. The photos were taken after 1, 5, 30 minutes and 8, 24, 72 hours. Each grid marks 2 mm x 2 mm.

After just 30 minutes' exposure to air, clear differentiation between the two samples can be seen (Figure 5.10c). The green coloured, un-coated reacted **[1-NBA][BAr$^F_4$]** are shown next to the dark red crystals of **[1-NBA][BAr$^F_4$]@poly(EVE)**. Due to the very reactive nature of **[1-NBA][BAr$^F_4$]** even at time-of-measuring (< 1 min) some colour change can be seen. When under an argon atmosphere **[1-NBA][BAr$^F_4$]** is a dark-red colour. After 72 hours however, the products of both systems are of the same green colour, suggesting **[1-NBA][BAr$^F_4$]@poly(EVE)** is not stable in air indefinitely.

5.3.3. Reactions in Air – Diffraction Images

To quantify these colour changes, single-crystal x-ray diffraction was also used to follow the decomposition. The selected x-ray diffraction frames in Figure 5.11, shows how the crystallographic quality of crystals of **[1-NBA][BAr$^{F}_{4}$]@poly(EVE)** that had undergone 30 seconds exposure to EVE degrades over a period of 8 hours exposure to air. After this time, **[1-NBA][BAr$^{F}_{4}$]@poly(EVE)** was still exhibiting diffraction however, far weaker in intensity. A unit cell matching to that of **[1-NBA][BAr$^{F}_{4}$]** was collected, suggesting stability in air of at least 8 hours.

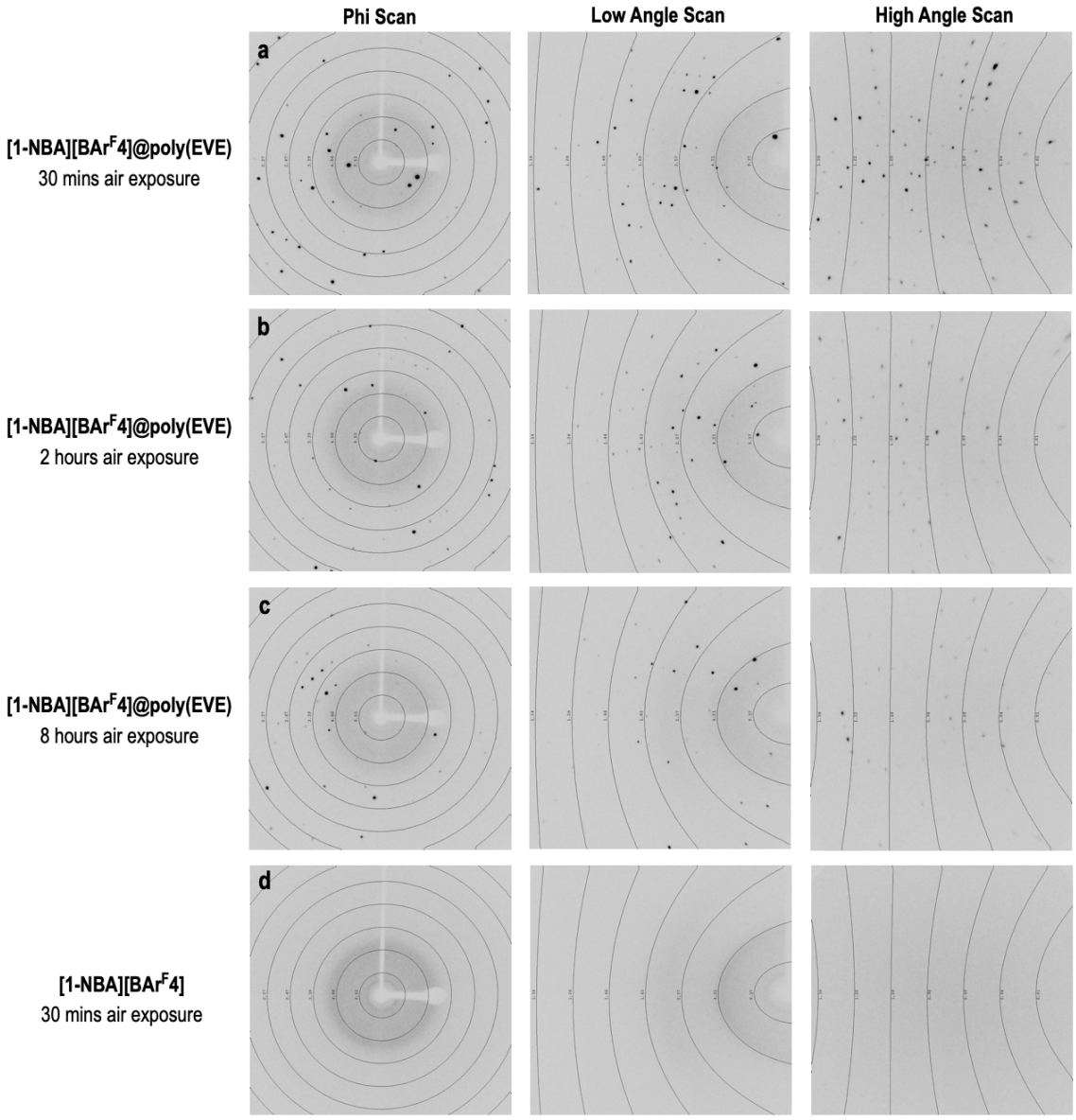

Figure 5.11: Example single frames of a Phi, Low and High angle scan of crystalline **[1-NBA][BAr$^{F}_{4}$]@poly(EVE)** when exposed to an air for **a**) 30 minutes **b**) 2 hours **c**) 8 hours. These spots could all be easily indexed to the unit cell of **[1-NBA][BAr$^{F}_{4}$]**. **d**) Example frames of **[1-NBA][BAr$^{F}_{4}$]** which has been exposed to air for 30 minutes. No spots could be located suggesting no long-range crystallinity.

Again, this is contrasted to **[1-NBA][BAr$^F_4$]** when exposed to air for 30 minutes, which shows no Bragg peaks in the single-crystal x-ray diffraction frames, Figure 5.11d. This suggests an amorphous material is present after this time, unlike for **[1-NBA][BAr$^F_4$]@poly(EVE)** (Figure 5.11a). This is consistent with the $^{31}P\{^1H\}$ SSNMR spectra after these times shown in Figure 5.9.

After 72 hours' air exposure however, no notable difference in colour can be observed between air-reacted **[1-NBA][BAr$^F_4$]** and **[1-NBA][BAr$^F_4$]@poly(EVE)** (Figure 5.10f). Both have been shown to turn green in colour and no Bragg peaks were observed by single-crystal x-ray diffraction in either system. This suggests that while the polymer layer acts as a barrier towards oxygen and water from the air, it only reduces the rate of decomposition, rather than completely preventing any decomposition. The next Section looks to characterise this product.

5.3.4. Reactions in Air – Decomposition Product

Attempts to fully characterise this air-reacted, green decomposition product were ultimately unsuccessful. This section however describes the range of possible products it may be. Notably, the reactions in this section were all conducted on uncoated, **[1-NBA][BAr$^F_4$]** after air exposure of 30 minutes. It was found that the same products were formed after **[1-NBA][BAr$^F_4$]@poly(EVE)** with 72 hours air exposure.

After **[1-NBA][BAr$^F_4$]** was exposed to air for 30 minutes, the green product was amorphous in nature, so could not be analysed by single-crystal x-ray diffraction (Figure 5.11d). As well, the $^{31}P\{^1H\}$ SSNMR spectrum shows multiple, broad features across a range of δ 100 to 40 (Figure 5.9c), suggestive of a paramagnetic material. This meant these solid-state characterisation techniques could not be fully utilised.

Dissolution of this air reacted product in dichloromethane (working under strict anaerobic and dry conditions) resulted in a yellow-coloured solution. The solution $^{31}P\{^1H\}$ NMR spectrum of this showed a major signal [δ 64.5, J_{RhP} = 117 Hz], assigned to $[Rh(Cy_2PCH_2CH_2PCy_2)(\mu_2\text{-}O)(H_2O)_2]_2[BAr^F_4]_2$, **[1-(H$_2$O)$_2$(μ-O)$_2$][BAr$^F_4$]$_2$**. This product was also crystallographically characterised, shown in Figure 5.12.

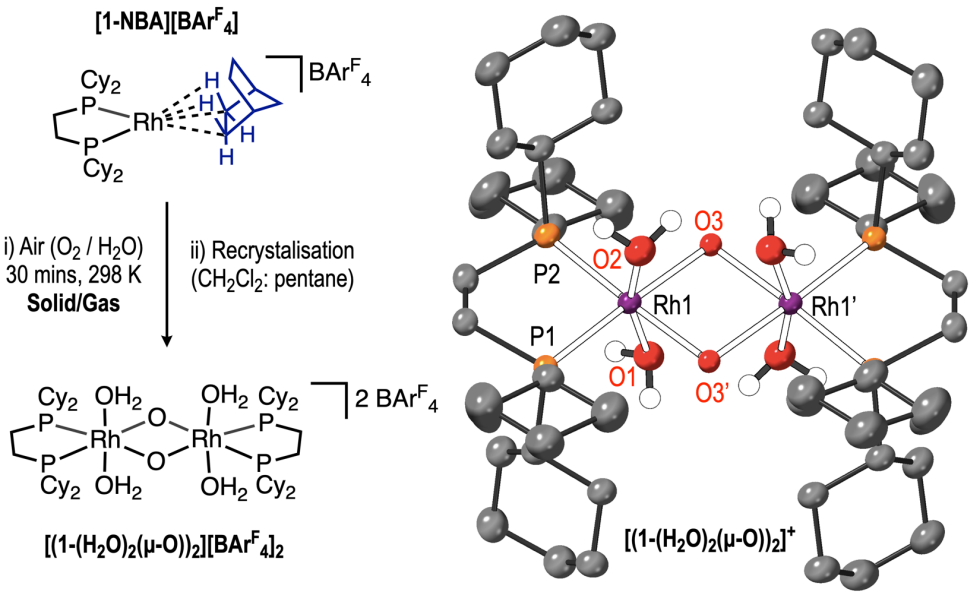

Figure 5.12: Cationic fragment of **[(1-(H_2O)$_2$(μ-O))$_2$][BAr$^F_4$]$_2$**.** Displacement ellipsoids set at 30%. Both equivalents of $[BAr^F_4]^-$ anions, three equivalents of CH_2Cl_2 within the lattice and hydrogen atoms from the bisphosphine ligand removed for clarity. Selected bond lengths (Å): Rh1–P1 2.2646(14), Rh1–P2 2.2644(13), Rh1–O1 2.013(4), Rh1–O2 2.095(4), Rh1–O3 2.113(3).

It is not suggested that **[(1-(H_2O)$_2$(μ-O))$_2$][BAr$^F_4$]$_2$** is the product of the initial solid-state decomposition reaction, however, it is a further product of this upon dissolution in solvent. As the dissolution step was conducted in dry/anaerobic solvent, this suggests the solid-state decomposition product is an O_2/H_2O rich species, where the source of O_2/H_2O would be from the air. This complex then rapidly dimerises in solution to form **[(1-(H_2O)$_2$(μ-O))$_2$][BAr$^F_4$]$_2$**, which is consistent with the green to yellow colour change observed.

To further explore this solid-state decomposition product, a sample of **[1-NBA][BAr$^F_4$]** was exposed to an atmosphere of dry, O_2 gas. After 6 hours, the sample had tuned a dark green colour. Dissolution in dry CD_2Cl_2 under an argon atmosphere results in a green solution, which was silent by solution $^{31}P\{^1H\}$ NMR spectroscopy across the range of δ + 1000 to – 1000. This is suggestive of a paramagnetic, super oxo Rh^{II} complex, postulated in Scheme 5.5.[31–34]

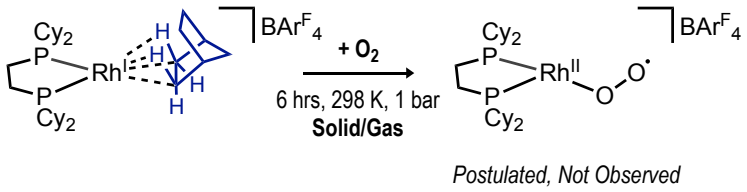

Scheme 5.5: Postulated reaction pathway of **[1-NBA][BAr$^F_4$]** with neat O_2.

Remarkably, addition of water to this dark green, paramagnetic solution resulted in the formation of **[(1-(H$_2$O)$_2$(μ-O))$_2$][BAr$^F_4$]$_2$**, shown by the growing in of the doublet at δ 64.5 in the solution $^{31}P\{^1H\}$ NMR spectrum, following the loss of paramagnetism. Therefore, a proposed decomposition pathway of **[1-NBA][BAr$^F_4$]** in air is shown in Scheme 5.6.

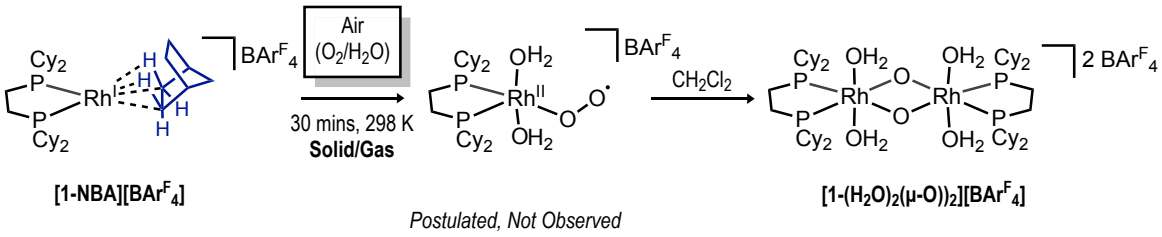

Scheme 5.6: Postulated reaction scheme of **[1-NBA][BAr$^F_4$]** to **[(1-(H$_2$O)$_2$(μ-O))$_2$][BAr$^F_4$]$_2$** when reacted with air and then dissolved in solvent.

When left in air, atmospheric O_2 and H_2O can displace the coordinated NBA in **[1-NBA][BAr$^F_4$]**, which forms a green, amorphous material, proposed to be a superoxo complex. Upon dissolution, this dimerises, resulting in the loss of paramagnetism and forms **[(1-(H$_2$O)$_2$(μ-O))$_2$][BAr$^F_4$]$_2$**. This pathway was found to occur whether the crystal of **[1-NBA][BAr$^F_4$]** is polymer coated or not however, it requires 72 hours air exposure for polymer coated material, rather than just 30 minutes for uncoated crystals. This is in line with the observation the polymer layer does not alter the reactivity, just attenuates the rate of which it occurs. This is also shown by the reaction with propene, described in the following section.

5.3.5. Reactivity of [1-NBA][BAr$^F_4$]@poly(EVE) with Propene

To show if the poly(EVE) coating was acting as a *selective* barrier to gases, **[1-NBA][BAr$^F_4$]@poly(EVE)** was placed under an atmosphere of propene. As described in Chapter 1, when single crystals of **[1-NBA][BAr$^F_4$]** are placed under propene, a SC-SC displacement of the weakly bound norbornane ligand occurs to form **[1-propene][BAr$^F_4$]** within 2 hours.[27]

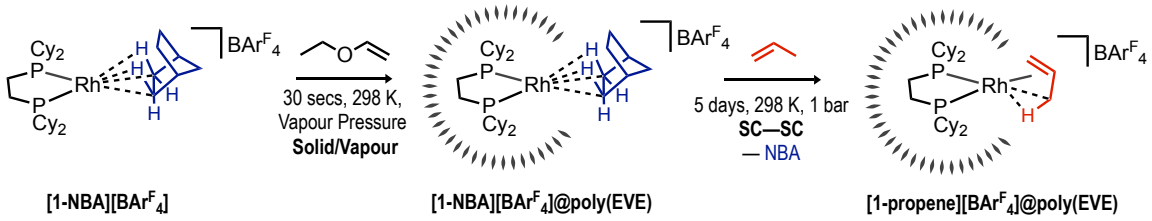

Scheme 5.7: Synthetic route to **[1-propene][BAr$^F_4$]@poly(EVE)**.

When crystals of **[1-NBA][BAr$^F_4$]@poly(EVE)** that had undergone 30 seconds EVE exposure were placed under a propene atmosphere for 2 days (under strict anaerobic conditions), only 50% conversion to **[1-propene][BAr$^F_4$]** was observed by solution $^{31}P\{^1H\}$NMR spectroscopy of the dissolved material in CD_2Cl_2. The remaining material was of the anion coordinated zwitterion complex of **[1-BAr$^F_4$]**, consistent with that of **[1-NBA][BAr$^F_4$]** upon dissolution in CD_2Cl_2.

Complete conversion to the polymer coated propene complex of **[1-propene][BAr$^F_4$]@poly(EVE)** was found to take 5 days. This was confirmed by solution and solid-state NMR spectroscopy, where the solution $^{31}P\{^1H\}$ NMR spectrum then only showed signals related to **[1-propene][BAr$^F_4$]** [δ 98, d., J_{RhP} = 201 Hz). The $^{31}P\{^1H\}$ SSNMR spectra of this material showed a major signal at δ 95, consistent with that reported for **[1-propene][BAr$^F_4$]**.[27]

Single-crystal x-ray diffraction could also be used to show this SC-SC transformation, consistent with the uncoated system. A solid-state structure of **[1-propene][BAr$^F_4$]@poly(EVE)** was collected, solved and refined (R = 10 %). No significant structural differences or bond metric differences in the solid-state structures were again observed between **[1-propene][BAr$^F_4$]** and **[1-propene][BAr$^F_4$]@poly(EVE)**, as shown in Figure 5.13.

a

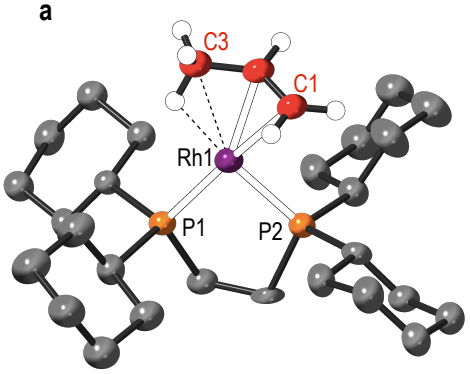

b

	[1-propene][BAr$^F_4$]	[1-propene][BAr$^F_4$]@poly(EVE)
Rh1-P1	2.235(3)	2.232(2)
Rh1-P2	2.240(3)	2.238(2)
Rh1-C1	2.24(2)	2.259(16)
Rh1-C3	2.29(2)	2.33(2)
C1-C2	1.24(3)	1.28(2)
C2-C3	1.36(3)	1.40(3)
R Factor	**12.7 %**	**10.0 %**

Figure 5.13: **a**) Isolated cation of **[1-propene][BAr$^F_4$]@poly(EVE)** after 30 seconds EVE exposure. Displacement ellipsoids set at 30%. Hydrogen atoms from the bisphosphine ligand, [BAr$^F_4$]$^-$ anion and disorder of propene ligand removed for clarity. **b**) Table shows selected bond metrics of **[1-propene][BAr$^F_4$]**[27] and **[1-propene][BAr$^F_4$]@poly(EVE)**.

This shows the polymer coating does not act as a selective barrier towards oxygen, water or propene, as all were shown to penetrate the polymer layer. These individual reactions however occurred at an attenuated rate compared to their uncoated counterparts, suggesting the coating polymer layer acts a semi-permeable barrier.

5.4. Mechanism of Polymer Coating

5.4.1. Suggested Mechanism of Polymer Growth

The mechanism of vinyl ether polymerisation using Lewis acid initiators[2] and transition metal variants[3] have been well reported. Adapting these, a proposed mechanism for the **[1-NBA][BAr$^F_4$]** initiated polymerisation is shown in Scheme 5.8b.

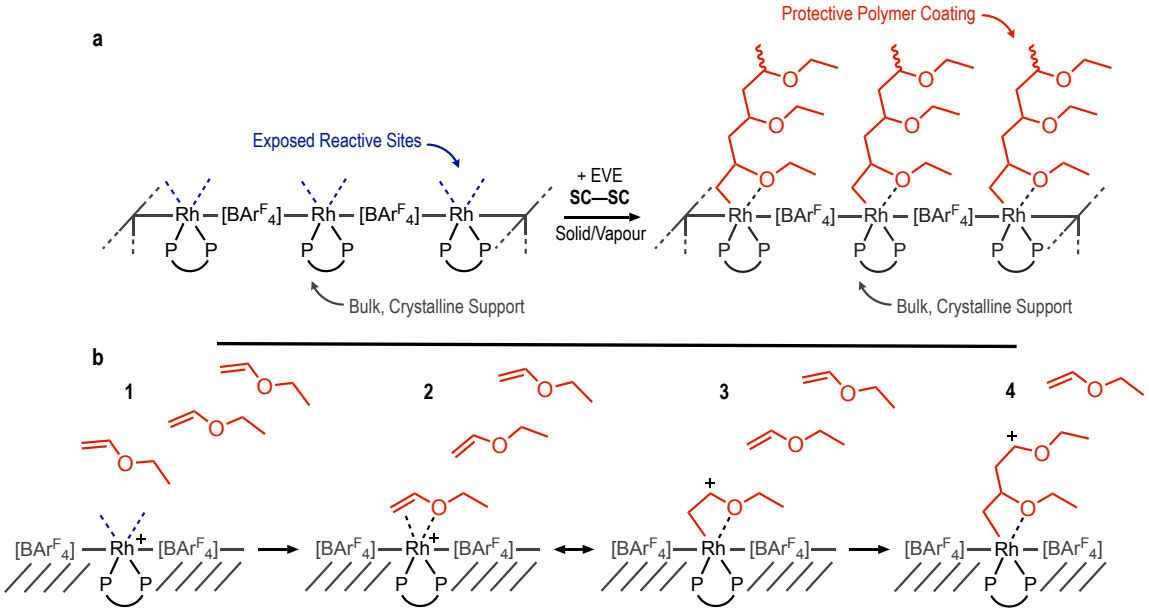

Scheme 5.8: Overview and proposed mechanism of the grafting-from polymerisation upon the surface of **[1-NBA][BAr$^F_4$]**.

The proposed mechanism shows initiation can occur from a surface, cationic species of **[1-NBA][BAr$^F_4$]** (**1**). The coordinated NBA is readily displaced by the incoming, coordinating EVE monomer (**2**), and activation of the initial EVE monomer forms a formally neutral, Rh(I) complex (**3**). In doing so, the cation is displaced onto the growing polymer chain and further propagation can then occur, following a cationic chain growth mechanism (**4**). This overall results in the grafted-from, polymer bound complex of **[1-NBA][BAr$^F_4$]@poly(EVE)** (Scheme 5.8a).

The termination step however could not be definitively determined. It is proposed that mechanical stress from the growing polymer chain may result in polymer detachment. In typical cationic polymerisation reactions, the positive charge is located upon the growing polymer chain.[2] As the counter charge is fixed upon the [BAr$^F_4$]$^-$ anion, this may result in these charges being separated and so, the polymer 'folds' over to keep these charges close. This added stress may be the driving force needed for detachment.

5.4.2. A Diethylether Complex

The proposed initiation step, shown in Scheme 5.8b (step 2), shows the initial coordination of EVE to the rhodium centre, before any polymerisation activity. To evidence this, a diethylether complex was targeted (Scheme 5.9). Diethylether is the saturated analogue of EVE and could be substituted to probe the bonding motif. This would model the initiation step but cannot withgo any propagation.

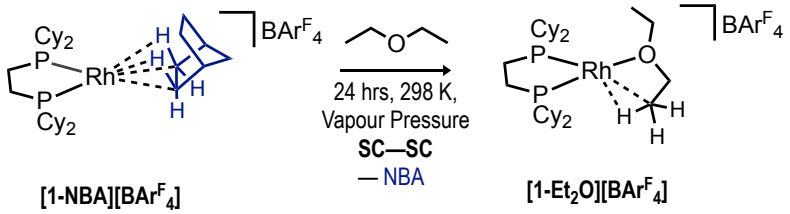

Scheme 5.9: Synthetic route to **[1-Et₂O][BAr^{F}₄]**.

When dark orange crystals of **[1-NBA][BAr^{F}₄]** were placed under a vapour atmosphere of diethylether, after 24 hours, the crystals had turned dark brown in colour. Analysis by single-crystal x-ray diffraction resulted in the structure shown in Figure 5.14a, of [Rh($Cy_2PCH_2CH_2PCy_2$)($C_4H_{10}O$)][BAr^{F}₄], **[1-Et₂O][BAr^{F}₄]**. It shows that diethyl ether is coordinated to the rhodium centre through a Rh–O and an γ-agostic interaction. This γ-agostic interaction can be shown by the relatively unconstrained O1-C26-C27 angle[35] (105.2° *versus* 109.5° in free diethyl ether).

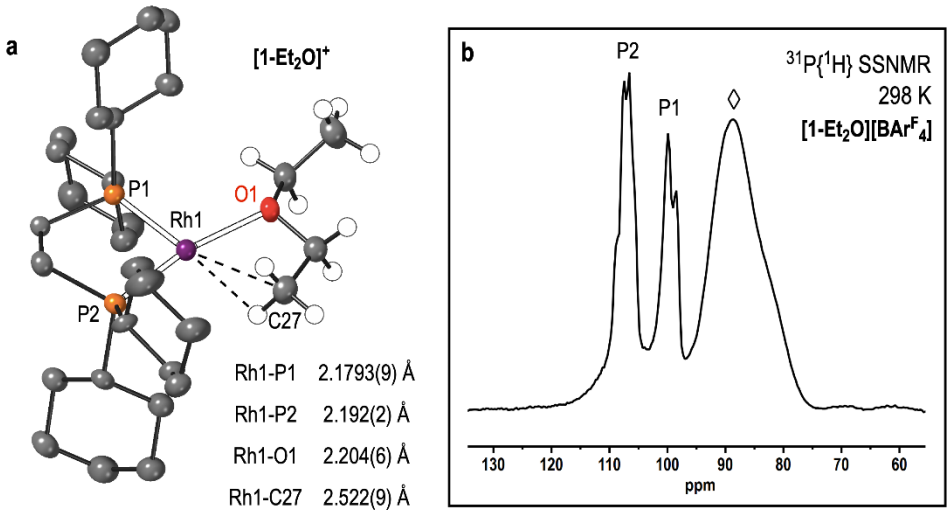

Figure 5.14: **a**) Cationic portion of **[1-Et₂O][BAr^{F}₄]** along with selected bond lengths. Displacement ellipsoids set at 30% and hydrogen atoms from bisphosphine ligand and [BAr^{F}₄]$^-$ anion removed for clarity. **b**) $^{31}P\{^1H\}$ SSNMR spectrum (162 MHz, 10 kHz spin rate, 298 K) of **[1-Et₂O][BAr^{F}₄]**. ◊ = **[1-BAr^{F}₄]**.

Selected bond metrics include the Rh–P bond distances, 2.192(2) and 2.1793(9) Å, where the difference in values arises from the respective *trans* influences of the oxygen and agostic interaction. Additionally, the shorter Rh1–O1 distance compared to the Rh•••C agostic interaction (2.204(6) and 2.522(9) Å respectively) reflects the greater donor strength of the oxygen lone pairs *versus* the C–H σ-orbital donation. **[1-Et$_2$O][BAr$^F_4$]** represents the first reported diethyl ether complex coordinated in this fashion, however other diethyl ether complexes are known. These solely coordinate through the oxygen lone pairs and no evidence for agostic interactions are presented.[36]

The $^{31}P\{^1H\}$ SSNMR spectrum of **[1-Et$_2$O][BAr$^F_4$]** exhibited two sharp signals [δ 107, J_{RhP} = 201 Hz; 99.2, J_{RhP} = 223 Hz], Figure 5.14b. These were attributed to the ^{31}P atoms trans to the oxygen[37] and agostic interactions[27] respectively. The larger Rh–P coupling constant present in the *trans* agostic interaction is consistent with a greater s-orbital character of this interaction. A new signal in the $^{13}C\{^1H\}$ SSNMR spectrum [δ 70] is assigned to the O**C**H$_2$CH$_3$ carbon from the coordinating diethyl ether.[25]

The spectroscopic yield for this complex is ~50 % however, where the remaining material was shown to be **[1-BAr$^F_4$]** by the broad resonance seen in Figure 5.14b. This low yield may be due to the high solubility of both **[1-Et$_2$O][BAr$^F_4$]** and **[1-NBA][BAr$^F_4$]** in diethyl ether. This may facilitate the alkane loss, and subsequent anion coordination to form **[1-BAr$^F_4$]**, during the formation of **[1-Et$_2$O][BAr$^F_4$]**. Any prolonged period under a dynamic vacuum also saw the removal of coordinated diethyl ether and complete formation of **[1-BAr$^F_4$]**, suggestive of the diethyl ether being extremely weakly coordinating.

Finally, any attempts to dissolve **[1-Et$_2$O][BAr$^F_4$]** in a range of solvents either led to the solvent bound complex or coordinated zwitterion complex of **[1-BAr$^F_4$]**. For example, dissolution in 1,2-F$_2$C$_6$H$_4$ or MeCN resulted in **[1-F$_2$C$_6$H$_4$][BAr$^F_4$]** or **[1-(MeCN)$_2$][BAr$^F_4$]** respectively, confirmed by solution $^{31}P\{^1H\}$ NMR spectroscopy. Dissolution in neat diethyl ether or CD_2Cl_2, either at 295 or 183 K, resulted in the formation of **[1-BAr$^F_4$]**. This suggests this complex is unique to the solid-state, only synthesisable using SMOM methodology.

5.5. Catalytic Polymerisation using SMOM@polymer

To probe if this solid/vapour polymerisation could be tuned to the synthesis of poly(EVE) in bulk, and not limited to the crystal surface, EVE exposure times of greater than 15 minutes were also explored.

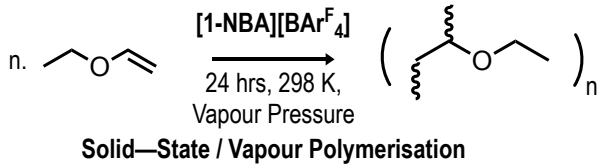

Scheme 5.10: Concept of Solid/Vapour polymerisation reaction.

Experimentally, by adapting the procedure for the synthesis of **[1-NBA][BArF4]@poly(EVE)**, crystal(s) of **[1-NBD][BArF4]** were mounted to the wall of a J. Youngs flask, shown in Figure 5.15, and hydrogenated *in situ* to form the active initiator of **[1-NBA][BArF4]**. An insert containing liquid EVE was added, which ensured the separation of liquid monomer and solid initiator. The flask was sealed and a vapour atmosphere of EVE began to form.

This results in EVE vapour beginning to polymerise upon the surface of the crystal, and after 15 minutes, pooling of liquid polymer can be seen around the crystal. This is alike to **[1-NBA][BArF4]@poly(EVE)** when mounted on a pin. After ~2 hours however, liquid polymer could be observed on the side of the flask, flowing away from the solid initiator, and began to pool at the bottom of the flask. Complete monomer consumption was achieved in 48 hours.

Easy separation of initiator / polymer could be achieved, as the remaining initiator remained bound at the side of the flask. This allowed for the easy characterisation of the polymer, confirmed to be poly(EVE) by ^{1}H NMR spectroscopy. The $^{13}C\{^{1}H\}$ NMR spectrum of the isolated polymer showed multiple signals assigned to both -**C**H- and -O**C**H_2CH_3 environments [δ ~40 and ~65]. These multiple diads and triads respectively are consistent with a polymer that is atactic in nature, and is well reported for the uncontrolled nature of cationic polymerisation reactions.[38,39]

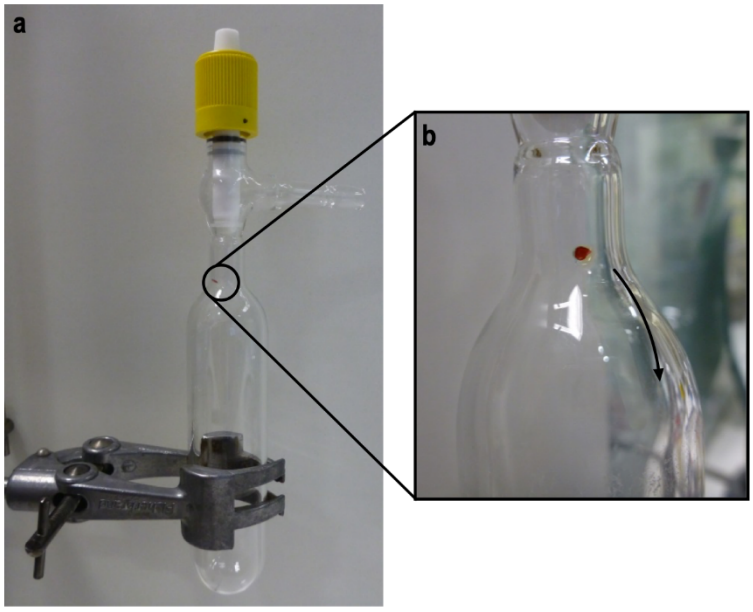

Figure 5.15: Image of the glassware set-up used in catalytic polymerisation reactions. Arrow added to indicate direction of polymer flow.

Interestingly, GPC analysis was used to show how changing the total surface area of the initiator results in a significant change in the number average molecular weight (M_n) and polydispersity index (PDI, $Đ$) of the resulting polymer. To show this, catalytic polymerisation reactions were conducted with one crystal (~ size of 1 × 1 × 2 mm, ~ 1.5 mgs) or three crystals (~ size of 0.5 × 1.0 × 1.0 mm, ~ 0.5 mgs *each*). Although this does not differ the initiator loading in terms of mass, the total initiator surface area has been increased.

GPC analysis resulted in an average M_n of 23,000 ($Đ$ = 2.5) and average M_n of 10,900 ($Đ$ = 3.6) respectively. This decrease in average M_n and increase in $Đ$ with respect to increased surface area is consistent with an increased number of active sites. As a greater number of propagating sites are exposed, the polymerisation reaction is less controlled, which leads shorter polymer chains on average with higher dispersities.

Although this bulk production of polymer is noted, it has not been explored further. Bulk production of poly(EVE) is well established, utilising far cheaper and accessible initiators,[2] and so this Chapter focussed on the reactivity of crystalline **[1-NBA][BAr$^F_4$]@poly(EVE)**.

5.6. Chapter Conclusions

This Chapter has shown it is possible to coat a highly reactive, discrete organometallic species in a protective polymer layering. Single-crystals of **[1-NBA][BAr$^{F}_{4}$]** could be reacted upon in a solid-vapour polymerisation, using ethyl vinyl ether monomer to form a poly(EVE) coating. This uniform, complete coating of polymer layer could be enhanced by increasing the exposure time of **[1-NBA][BAr$^{F}_{4}$]** to an EVE atmosphere. When crystals of **[1-NBA][BAr$^{F}_{4}$]** were left for times greater than 15 minutes, this resulted in further, catalytic production of polymer.

This SMOM@polymer material was confirmed by single-crystal x-ray diffraction, solution and solid-state NMR spectroscopy as well as SEM/EDX analysis upon the surface of this new material. The exposed reactive sites of σ-alkane complex were linked to single-atom catalysts and were shown to control a cationic polymerisation reaction and form an external, uniformly distributed layer of poly(EVE). This polymer layer was shown to act as an unselective, semi-permeable barrier towards reactivity of σ-alkane complexes, as it allowed for the slow diffusion of gases through the polymer layer, decreasing the rates of substitution and decomposition. It does not however selectively block either O_2 or alkene gases. The attenuated rate at which decomposition occurred in air allowed for the stability of **[1-NBA][BAr$^{F}_{4}$]** for at least 8 hours, greater than any solid-state σ-alkane complexes in air.

5.7. Future Work

Further work would ideally look into expanding the range vinyl ether monomers which are able to undergo surface polymerisation upon SMOM materials. If it were possible to tune said polymer coats, this may all for the coat to be selective towards certain gasses. For example, a more polar polymer (from such monomer with added ethereal groups) may favour oxygen transport, whilst more non-polar polymers (with longer alkyl chains) may favour non-polar gases such as propene. The latter idea would allow the SMOM material to be able to withstand degradation in air for even longer periods of time.

5.8. References

1 W. G. S. Reyntjens and E. J. Goethals, *Polym. Adv. Technol.*, 2001, **12**, 107–122.
2 A. Kanazawa, S. Kanaoka and S. Aoshima, *Chem. Lett.*, 2010, **39**, 1232–1237.
3 C. Chen, S. Luo and R. F. Jordan, *J. Am. Chem. Soc.*, 2010, **132**, 5273–5284.
4 A. Kanazawa, S. Kanaoka and S. Aoshima, *J. Am. Chem. Soc.*, 2007, **129**, 2420–2421.
5 M. Asai, D. Zhao and S. K. Kumar, *ACS Nano*, 2017, **11**, 7028–7035.
6 W. L. Chen, R. Cordero, H. Tran and C. K. Ober, *Macromolecules*, 2017, 50, 4089–4113.
7 N. Rubio, H. Au, H. S. Leese, S. Hu, A. J. Clancy and M. S. P. Shaffer, *Macromolecules*, 2017, **50**, 7070–7079.
8 C. M. Hui, J. Pietrasik, M. Schmitt, C. Mahoney, J. Choi, M. R. Bockstaller and K. Matyjaszewski, *Chem. Mater.*, 2014, 26, 745–762.
9 T. Uemura and S. Kitagawa, *J. Am. Chem. Soc.*, 2003, **125**, 7814–7815.
10 T. Uemura, M. Ohba and S. Kitagawa, *Inorg. Chem.*, 2004, **43**, 7339–7345.
11 S. Kango, S. Kalia, A. Celli, J. Njuguna, Y. Habibi and R. Kumar, *Prog. Polym. Sci.*, 2013, **38**, 1232–1261.
12 Y. Wang, W. Zhang, X. Wu, C. Luo, Q. Wang, J. Li and L. Hu, *Synth. Met.*, 2017, **228**, 18–24.
13 Q. T. Easter, V. Trauschke and S. A. Blum, *ACS Catal.*, 2015, **5**, 2290–2295.
14 L. Hou, L. Wang, N. Zhang, Z. Xie and D. Dong, *Polym. Chem.*, 2016, **7**, 5828–5834.
15 S. He, H. Wang, C. Zhang, S. Zhang, Y. Yu, Y. Lee and T. Li, *Chem. Sci.*, 2019, 1816–1822.
16 R. Muramatsu, Y. Oaki, K. Kuwabara, K. Hayashi and H. Imai, *Chem. Commun.*, 2014, **50**, 11840–11843.
17 S. S. Jeon, J. K. Park, C. S. Yoon and S. S. Im, *Langmuir*, 2009, **25**, 11420–11424.
18 Y. Takashima, H. N. Miras, S. Glatzel and L. Cronin, *Chem. Commun.*, 2016, **52**, 7794–7797.
19 A. Fast, N. M. Esfandiari and S. A. Blum, *ACS Catal.*, 2013, **3**, 2150–2153.
20 S. Aoshima and S. Kanaoka, *Chem. Rev.*, 2009, **109**, 5245–5287.
21 X. F. Yang, A. Wang, B. Qiao, J. Li, J. Liu and T. Zhang, *Acc. Chem. Res.*, 2013, **46**, 1740–1748.
22 A. Wang, J. Li and T. Zhang, *Nat. Rev. Chem.*, 2018, **2**, 65–81.
23 A. T. Lawal and G. G. Wallace, *Talanta*, 2014, **119**, 133–143.
24 S. D. Pike, F. M. Chadwick, N. H. Rees, M. P. Scott, A. S. Weller, T. Krämer and S. A. Macgregor, *J. Am. Chem. Soc.*, 2015, **137**, 820–833.
25 K. Matsuzaki, H. Ito, T. Kawamura and T. Uryu, *J Polym Sci Part A1 Polym Chem*, 1973, **11**, 971–987.
26 A. L. Thompson, *Crystallogr. Rev.*, 2019, **25**, 3–53.
27 F. M. Chadwick, A. I. McKay, A. J. Martinez-Martinez, N. H. Rees, T. Krämer, S. A. Macgregor and A. S. Weller, *Chem. Sci.*, 2017, **8**, 6014–6029.
28 A. J. Martínez-Martínez, C. G. Royle, S. K. Furfari, K. Suriye and A. S. Weller, *ACS Catal.*, 2020, **10**, 1984–1992.
29 M. Olivan, A. V. Marchenko, J. N. Coalter and K. G. Caulton, *J. Am. Chem. Soc.*, 1997, **119**, 8389–8390.
30 J. Bergström, *Experimental Characterization Techniques - Mechanics of Solid Polymers*, William Andrew Publishing, 2015.
31 M. P. García, M. V. Jiménez, L. A. Oro, F. J. Lahoz, J. M. Casas and P. J. Alonso, *Organometallics*, 1993, **12**, 3257–3263.
32 J. Cipot-Wechsler, D. Covelli, J. M. Praetorius, N. Hearns, O. V. Zenkina, E. C. Keske, R. Wang, P. Kennepohl and C. M. Crudden, *Organometallics*, 2012, **31**, 7306–7315.
33 X. Yi, B. Liu, K. Chen, W. Chen and W. Chen, *Dalton Trans.*, 2019, **48**, 3835–3839.
34 W. Cui and B. B. Wayland, *J. Am. Chem. Soc.*, 2006, **128**, 10350–10351.
35 A. S. Weller, F. M. Chadwick and A. I. McKay, in *Advances in Organometallic Chemistry*, Academic Press, 2016, pp. 223–276.
36 J. Ledford, C. S. Shultz, D. P. Gates, P. S. White, J. M. DeSimone and M. Brookhart, *Organometallics*, 2001, **20**, 5266–5276.
37 A. Kumar, N. A. Beattie, S. D. Pike, S. A. Macgregor and A. S. Weller, *Angew. Chem. Int. Ed.*, 2016, **55**, 6651–6656.
38 L. Lin, G. Zhang, K. Kodama, H. Shitara and T. Hirose, *J. Polym. Sci. Part A Polym. Chem.*, 2016, **54**, 861–870.
39 P. J. Albietz, K. Yang and R. Eisenberg, *Organometallics*, 1999, **18**, 2747–2749.

Chapter 6:
Thesis Conclusions

This thesis has reported the synthesis of the σ-alkane complexes of **[1-propane][BAr^F_4]**, **[1-butane][BAr^F_4]**, **[1-*iso*butane][BAr^F_4]**, **[1-*iso*pentane][BAr^F_4]**, **[1-hexane][BAr^F_4]** and **[1-(3-methylpentane)][BAr^F_4]**, all of which synthesised from single-crystal to single-crystal hydrogenation reactions upon their respective alkene or diene precursor complexes. This solid/gas reactivity allows for their formation to be definitively proven by single-crystal x-ray diffraction, revealing the structural coordination of each, and solid-state NMR spectroscopy, confirming the bulk transformations. This expands upon the range of structural characterised σ-alkane complexes utilising the SMOM methodology.

Previously reported, solution, σ-alkane complexes have had their formation and stabilities hindered by detrimental solvent coordination, resulting in lifetimes on the ns to second timeframes. By working in the solvent free, solid-state environment these complexes were shown to have vastly increased lifetimes of hours to days, achieved by completely biasing the pre-equilibrium towards that of alkane coordination.

As well as removing any possible solvent induced decomposition pathways, the solid-state also provides a robust framework structure of anions, surrounding the reactive cations, supporting such solid/gas reactivity and stabilising the σ-alkane product. This arrangement of anions results in number of C–H•••F–C solid-state interactions between the cation and neighbouring $[BAr^F_4]^-$ anions, shown to be pivotal in the kinetic stabilisation of such complexes.

These stabilising factors meant the reliable production of solid-state σ-alkane complexes can be produced, which enables the further reactivity studies starting from these. The forced alkane coordination allows for C–H oxidative cleavage by a relative low energy process. This is shown by the ease of which such C–H activation pathways can be induced upon these complexes, shown by the rapid alkane dehydrogenation when placed under a simple Schlenk line vacuum or rapid H/D exchange when placed under an atmosphere of D_2. These reactions were shown to occur at room temperature, with no other external factors required, exhibiting how facile these processes can be when starting from respective σ-alkane complexes.

Chapter 7:
Experimental Procedures and Data

7.1. Experimental Details

All manipulations (unless otherwise stated) were performed under an atmosphere of argon, using standard Schlenk techniques on a dual vacuum/inlet manifold or by employment of an MBraun glovebox. Glassware was dried in an oven at 130 °C overnight prior to use. Pentane, benzene and dichloromethane (abbreviated as CH_2Cl_2) were dried using an MBraun SPS-800 solvent purification system and degassed by three freeze-pump-thaw cycles. 1,2-$F_2C_6H_4$ (abbreviated as $F_2C_6H_4$) was stirred over Al_2O_3 for two hours then over CaH_2 overnight before being vacuum distilled and subsequently degassed by three freeze- pump-thaw cycles. Dichloromethane-d_2 (abbreviated to CD_2Cl_2) and acetonitrile-d_3 (abbreviated to MeCN-d_3) was dried by stirring over CaH_2 overnight before being vacuum distilled onto 3 Å molecular sieves and subsequently degassed by three freeze-pump-thaw cycles. Benzene-d_6 (abbreviated as C_6D_6) was stirred over Na pieces overnight before being vacuum distilled onto 3 Å molecular sieves and subsequently degassed by three freeze-pump-thaw cycles. Propene, *iso*butene and 1-butene gasses were purchased from CK Gases and used as received. All other chemicals were purchased from commercial vendors and used as received.

$[Rh(Cy_2PCH_2CH_2PCy_2)(C_6H_4F_2)][BAr^F{}_4]$ **[1-$C_6H_4F_2$][$BAr^F{}_4$]**[1], $[Rh(Cy_2PCH_2CH_2PCy_2)(NBD)][BAr^F{}_4]$ (NBD = norbornadiene) **[1-NBD][$BAr^F{}_4$]**[2] and $[Rh(Cy_2PCH_2CH_2PCy_2)(NBA)][BAr^F{}_4]$ (NBA = norbornane) **[1-NBA][$BAr^F{}_4$]**[2] were prepared by the literature procedures.

Solution NMR data were collected on either a Bruker AVD 500 MHz or a Bruker Ascend 400 MHz spectrometer at room temperature unless otherwise started. Non-deuterated solvents were locked to standard external CD_2Cl_2 solutions. Residual protio solvent resonances were

used as a reference for ^{1}H NMR spectra. ^{2}H NMR spectra were referenced to CD_2Cl_2 (δ 5.32). $^{31}P\{^{1}H\}$ NMR spectra were referenced externally to 85 % H_3PO_4 (D_2O). All chemical shifts (δ) are quoted in ppm and coupling constants in Hz.

Solid state NMR (SSNMR) samples were prepared packing powdered microcrystalline sample into either a 3.2 mm or 4 mm zirconia solid state rotor inside an argon filled glove box. SSNMR spectra were obtained on a Bruker Avance III HD spectrometer equipped with a 9.4 Tesla magnet, operating at 100.6 MHz for ^{13}C and 162 MHz for ^{31}P, respectively, and a MAS rate of 10 kHz. Relaxation time for ^{1}H and contact time for $^{31}P\{^{1}H\}$ CP/MAS, $^{13}C\{^{1}H\}$ CP/MAS, $^{13}C\{^{1}H\}$ NQS and FSLG-HETCOR NMR experiments were optimized for each compound as appropriate. All $^{13}C\{^{1}H\}$ CP/MAS spectra were referenced to adamantane (up field methine resonance, δ 29.5)[3] on a scale where δ (TMS) = 0 as a secondary reference. The temperature for Variable Temperature (VT) NMR experiments at low temperatures was externally calibrated using lead nitrate ($PbNO_3$). The ^{1}H chemical shifts obtained from $^{1}H/^{13}C$ Frequency Switched Lee-Goldburg HETCOR SSNMR spectra were referenced internally to the *p*-ArH resonance of the $[BAr^{F}{}_{4}]^{-}$ (δ = 7.12).[4]

Gas phase ^{1}H NMR spectroscopy was carried out using a Bruker Ascend 400 MHz spectrometer. The spectrometer was pre-locked and shimmed to a separate CD_2Cl_2 sample in a similar bore tube. The T1 delay was set to 1 s, and this has been previously shown to allow for the accurate comparison of integrals.[5]

Electrospray ionization mass spectrometry (ESI-MS) was carried out using a Bruker MicrOTOF instrument directly connected to a modified Innovative Technology glovebox.[6] Typical acquisition parameters were used (sample flow rate: 4 μL min^{-1}, nebulizer gas pressure: 0.4 bar, drying gas: Argon at 333 K flowing at 4 L min^{-1}, capillary voltage: 4.5 kV, exit voltage: 60 V). The spectrometer was calibrated using a mixture of tetraalkyl ammonium bromides $[N(C_nH_{2n+1})_4]Br$ (n = 2-8, 12, 16 and 18). Samples were diluted to a concentration of 1×10^{-6} M in the appropriate solvent before sampling by ESI-MS.

Gas Chromatography Electron Ionization-Mass Spectrometry (GC EI-MS) analyses were performed on an Agilent 7200 quadrupole time of flight (Q-ToF) instrument equipped with a 7890B gas chromatograph and a PAL auto-sampler fitted with a 2.5 mL headspaces syringe. Instrument control and data processing were performed using Agilent MassHunter software. The system was calibrated within 1 hour prior to the analysis and its mass accuracy with external calibration (as used for these experiments) is better than 5 ppm for 2 hours following calibration. Samples were prepared in 20 mL headspace vials. Vials were incubated at 35 °C

for 30 seconds before a 2.5 mL sample of the headspace was taken and injected into the GC inlet (headspace syringe was held at 40 °C). The GC-inlet was operated in split mode held at 300 °C with a 2:1 split. The column was a Restek RT Q-Bond 30 m x 320 µm with at 10 µm film thickness. The oven was held at 40 °C for 4 minutes then ramped at 20 °C min^{-1} to 300 and held for 3 min. Column flow rate was 1 mL min^{-1}. Mass spectrometer was operated in EI mode and with the ionization energy set to 20 eV.

Scanning electron microscopy (SEM) was performed using a Carl Zeiss Merlin– Analytical instrument, with an operating voltage of 5 kV. The samples were prepared by selecting crystals and mounting directly on carbon tape within an argon filled glove box. The samples were rapidly transferred to the main chamber of the instrument under air, then immediately placed under vacuum.
Energy dispersive X-ray spectroscopy (EDX), carried out on a Carl Zeiss Merlin– Analytical instrument with an operating voltage of 5 kV or 3 kV, was used to identify the elements found in the materials.

SEC (GPC) data was obtained using a Shimadzu LC-20AD instrument fitted with a refractive index (RI) detector. HPLC grade THF was used as the eluent, flowing at 1.0 mL/min at 30 °C and samples calibrated to monodisperse polystyrene standard.

Elemental analyses were conducted by Mr. Stephan Boyer at London Metropolitan University.

7.2. Synthetic Procedures

7.2.1. [Rh(Cy$_2$PCH$_2$CH$_2$PCy$_2$)(C$_3$H$_8$)][BAr$^F_4$], [1-propane][BAr$^F_4$]

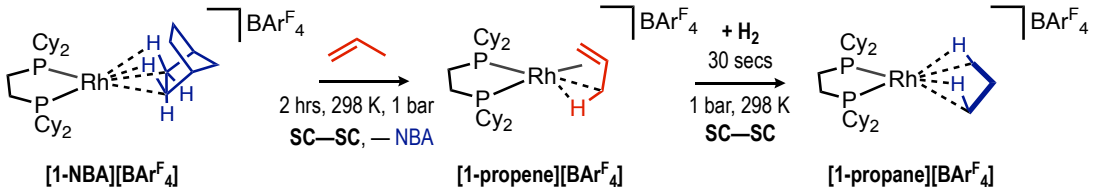

7.2.1.1. Synthesis of the Precursor Propene Complex, [1-propene][BAr$^F_4$]

Note: **[1-propene][BAr$^F_4$]** has been previously reported, and the synthesis is repeated below.[7]

A J. Young flask (~50 mL) was loaded with crystals of **[1-NBA][BAr$^F_4$]** (750 mgs), evacuated (< 2 × 10^{-2} mbar) and re-charged with propene gas (1 bar, 298 K). The flask was left to stand

for 4 hours. The excess propene and liberated norbornane could be removed under vacuum (< 2 × 10^{-2} mbar, 18 hours) to quantitively yield [Rh($Cy_2PCH_2CH_2PCy_2$)(C_3H_6)][BAr^F_4], **[1-propene][BAr^F_4]**. The crystalline material is stored in an argon filled glove box in a freezer operating at –25 °C.

7.2.1.2. Synthesis of a Propane-Complex, [1-propane][BAr^F_4]

For Single-Crystal X-Ray Diffraction: A single, orange crystals of **[1-propene][BAr^F_4]** was affixed upon a 50 μm MiTeGen Micromount using epoxy resin. The mount was inserted and affixed inside a 100 μm quartz capillary. This in turn was supported into a stainless-steel gas-line adapter fitted with Swagelok adapters, forming the gas cell. Each gas cell could be cycled onto the specially adapted gas-rig connected directly to the diffractometer upon Beamline I19 at Diamond Light Source synchrotron facility.[8] A unit-cell check was performed on each crystal to ensure the correct starting material had been mounted. Further details on this procedure and equipment is shown in Section 7.4

Crystals of **[1-propene][BAr^F_4]** were treated with H_2 (1 bar, 293 K) as the cyrostream was set to cool to 150 K at a rate of 360 K / hour. This gave an approximate time of ~3 minutes between 293 K and 275 K. Below this temperature no reactivity with H_2 was observed. The colour of the crystals slowly turned from orange to dark red in this time. When the cyrostream reached 150 K, an x-ray diffraction study was undertaken and the structure of [Rh($Cy_2PCH_2CH_2PCy_2$)(C_3H_8)][BAr^F_4], **[1-propane][BAr^F_4]** could be refined. For further details of structural refinement refer to Section 7.4.

For Solid-State NMR Spectroscopy: A powdered microcrystalline sample of **[1-propene][BAr^F_4]** (45 mgs) was packed in a 4.0 mm SSNMR rotor, inside an argon filled glove box. The rotor was then placed in a custom-built glass J. Young flask[7] and the flask was placed under a vacuum (< 2 × 10^{-2} mbar) then exposed to H_2 (1 bar, 298 K) and the rotor cap immediately fitted under a flush of H_2. The sample was placed into the bore of a SSNMR spectrometer at 298 K and rapidly cooled to 158 K (~10 minutes) before being analysed by $^{31}P\{^1H\}$ and $^{13}C\{^1H\}$ solid state NMR spectroscopy.

Note: In both the above cases, these conditions were optimized to form **[1-propane][BAr^F_4]**. The time period at 298 K (~10 minutes) in the solid-state NMR experiment was found to be the experimentally shortest time possible, but this still led to a significant amount of decomposition to **[1-BAr^F_4]** ($^{31}P\{^1H\}$ SSNMR: δ 91)[2] under an H_2 environment. Minor signals

assigned to **[1-propene][BAr$^F_4$]**, (^{31}P{^{1}H} SSNMR: δ 99, 93),[7] are also observed. At 158 K no reactivity with H_2 is observed.

^{31}P{^{1}H} SSNMR (162 MHz, 158 K, 10 kHz spin rate): δ 106.8 (br s) (~ 30% yield).
^{13}C{^{1}H} SSNMR (101 MHz, 158 K, 10 kHz spin rate): δ 163.4 (ArC), 133.8 (ArC), 129.3 (ArC), 124.5 (ArC), 116.5 (ArC), 34.6, 29.2, 25.1, 19.2, 15.5 (multiple aliphatic resonances).

7.2.2. [Rh(Cy$_2$PCH$_2$CH$_2$PCy$_2$)(*n*-C$_4$H$_{10}$)][BAr$^F_4$], [1-butane][BAr$^F_4$]

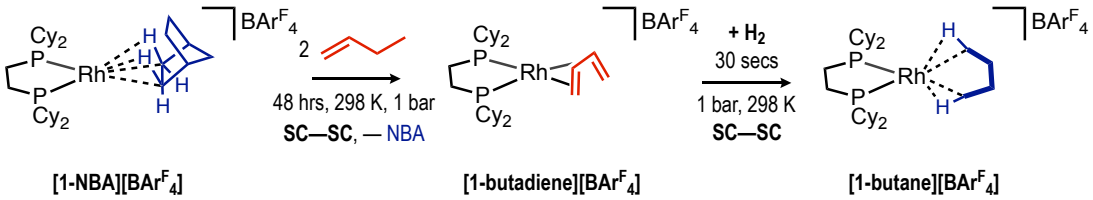

[1-NBA][BAr$^F_4$] [1-butadiene][BAr$^F_4$] [1-butane][BAr$^F_4$]

7.2.2.1. Synthesis of the Precursor Butadiene-Complex, [1-butadiene][BAr$^F_4$]

Note: **[1-butadiene][BAr$^F_4$]** has been previously reported,[7] where the synthesis is summarised below.

A J. Young flask (~50 mL) was loaded with crystals of **[1-NBA][BAr$^F_4$]** (750 mgs). The flask is evacuated (< 2 × 10^{-2} mbar) and 1-butene gas (1 bar, 298 K) was added and left to stand for 48 hours. The excess 1-butene, butane and liberated norbornane could be removed under vacuum (< 2 × 10^{-2} mbar, 18 hours) to quantitively yield [Rh(Cy$_2$PCH$_2$CH$_2$PCy$_2$)(C$_4$H$_8$)][BAr$^F_4$], **[1-butadiene][BAr$^F_4$]**. The crystalline material was stored in an argon filled glove box at room temperature.

Note: There has been no change in the synthetic route compared to that previously reported.[7] We now report the solid-state structure due to the improved quality of the single-crystals obtained. For further details of structural refinement refer to Section 7.4.

7.2.2.2. Synthesis of a *n*-butane Complex, [1-butane][BAr$^F_4$]

For Single-Crystal X-Ray Diffraction: A single, ruby red crystal of **[1-butadiene][BAr$^F_4$]** was affixed upon a 50 μm MiTeGen Micromount using epoxy resin. The mount was inserted and affixed inside a 100 μm quartz capillary. This in turn was supported into a stainless-steel gas-line adapter fitted with Swagelok adapters, forming the gas cell. Each gas cell could be cycled

onto the specially adapted gas-rig connected directly to the diffractometer upon Beamline I19 at Diamond Light Source synchrotron facility.[8] A unit-cell check was performed on each crystal to ensure the correct starting material had been mounted. Further details on this procedure and equipment is shown in Section 7.4.

The crystals of **[1-butadiene][BAr$^F_4$]** were treated with H_2 (1 bar, 293 K) as the cyrostream was set to cool to 150 K at a rate of 360 K / hour. This gave an approximate time of ~3 minutes between 293 K and 275 K, to which below this temperature, no reactivity or further reactivity with H_2 was observed, as confirmed by a separate experiment. The colour of the crystals turned from ruby to dark red in this time. When the cyrostream reached 150 K, an x-ray diffraction study was undertaken and the structure of [Rh($Cy_2PCH_2CH_2PCy_2$)(C_4H_{10})][BAr$^F_4$], **[1-butane][BAr$^F_4$]** could be refined. For further details of structural refinement refer to Section 7.4.

For Solid-State NMR Spectroscopy: A powdered microcrystalline sample of **[1-butadiene][BAr$^F_4$]** (45 mgs) was packed in a 4.0 mm SSNMR rotor, inside an argon filled glove box. The rotor was then placed in a custom-built glass J. Young flask[7] and the flask was placed under a vacuum (< 2 × 10^{-2} mbar) then exposed to H_2 (1 bar, 298 K) and the rotor cap immediately fitted under a flush of H_2. The sample was placed into the bore of a SSNMR spectrometer at 298 K and rapidly cooled to 158 K (~10 minutes) before being analysed by $^{31}P\{^1H\}$ and $^{13}C\{^1H\}$ solid state NMR spectroscopy.

Note: These conditions were optimized to form the maximum spectroscopic yield of **[1-butane][BAr$^F_4$]**. The time period at 298 K (~10 minutes) was found to be the experimentally shortest period possible, which still led to a significant mixture of products which include unreacted **[1-butadiene][BAr$^F_4$]** ($^{31}P\{^1H\}$ SSNMR: δ 81)[7] the partly-hydrogenated 2-butene bound complex, ([Rh($Cy_2PCH_2CH_2PCy_2$)(C_4H_8)][BAr$^F_4$], **[1-(2-butene)][BAr$^F_4$]** ($^{31}P\{^1H\}$ SSNMR: 158 K δ 95)),[7] the proposed butane complex of **[1-butane][BAr$^F_4$]** and the decomposition product of **[1-BAr$^F_4$]**.[2] At 158 K, no reactivity with H_2 is observed.

$^{31}P\{^1H\}$ SSNMR (162 MHz, 158 K, 10 kHz spin rate): δ 109.6 (br s) (~ 20% yield).

$^{13}C\{^1H\}$ SSNMR (101 MHz, 158 K, 10 kHz spin rate): δ 163.4 (ArC), 134.1 (ArC), 129.6 (ArC), 124.4 (ArC), 116.8 (ArC), 115.7 (ArC), 34.8, 29.7, 24.2, 19.9, 13.9 (multiple aliphatic resonances).

7.2.3. [Rh(Cy$_2$PCH$_2$CH$_2$PCy$_2$)(*iso*-C$_4$H$_{10}$)][BAr$^F_4$], [1-*iso*butane][BAr$^F_4$]

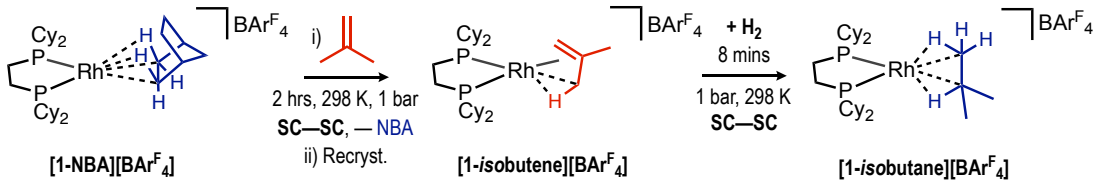

7.2.3.1. Synthesis of the Precusor *Iso*butene Complex, [1-*iso*butene][BAr$^F_4$]

To an orange sample of crystalline **[1-NBA][BAr$^F_4$]** (200 mgs, 135 μmol) in an evacuated (< 2 × 10^{-2} mbar) J. Young flask (~50 mL) *iso*butene gas (1 bar, 298 K) was added and left to stand for 2 hours, to form [Rh(Cy$_2$PCH$_2$CH$_2$PCy$_2$)(C$_4$H$_8$)][BAr$^F_4$], **[1-*iso*butene][BAr$^F_4$]**. After this time, working under an atmosphere of *iso*butene at –78 °C in an acetone/dry ice bath, the sample was dissolved in CH_2Cl_2 (3 mL) and filtered into a J. Youngs crystallisation flask and layered with pentane. The solution was warmed and kept at 4 °C to which after 3 days yielded orange block like crystals of [Rh(Cy$_2$PCH$_2$CH$_2$PCy$_2$)(*iso*-C$_4$H$_8$)][BAr$^F_4$], **[1-*iso*butene][BAr$^F_4$]** (Yield: 169 mgs, 86 %). The crystalline material is stored in a glove box in a freezer operating at –25 °C.

Note: CH_2Cl_2 and pentane used in this preparation were freeze-pump-thawed degassed three times and then saturated and stored with *iso*butene gas (1 bar) prior to use. When solvents were left under an argon atmosphere, ~50% decomposition of **[1-*iso*butene][BAr$^F_4$]** to **[1-BAr$^F_4$]**[2] occurs in 2 hours.

^{1}H NMR (CD_2Cl_2, 298 K, 400 MHz): δ 7.72 (s, 8H, ortho-ArH), 7.55 (s, 4H, para-ArH), 2.09-1.64 (br m, 28H, overlapping aliphatic CH), 1.61-1.42 (br s, 8H, aliphatic CH), 1.40-1.0.96 (br m, 20H, overlapping aliphatic CH).

^{1}H NMR (CD_2Cl_2, 183 K, 400 MHz): δ 7.75 (s, 8H, ortho-ArH), 7.56 (s, 4H, para-ArH), 3.75 (br s, ~2H, alkene CH), 2.09-1.64 (br m, ~30H, overlapping aliphatic CH), 1.40-1.09 (br m, ~20H, overlapping aliphatic CH), -0.15 (br, CH_3).

Note: The low temperature limit was not reached at 183 K in the ^{1}H NMR spectrum so integrated values are approximate. NMR samples prepared under argon, but immediately run after preparation.

^{31}P{^{1}H} NMR (CD_2Cl_2, 298 K, 162 MHz): δ 95.3 (d, J_{RhP} 179 Hz).

^{31}P{^{1}H} NMR (CD_2Cl_2, 183 K, 162 MHz): δ 97.6 (dd., J_{RhP} 201 Hz, J_{PP} 26 Hz *trans* to agostic interaction), 93.6 (d. of d., J_{RhP} 158 Hz, J_{PP} 26 Hz *trans* to alkene interaction).

$^{13}C\{^1H\}$ NMR (CD_2Cl_2, 298 K, 126 MHz): δ 161.1 (1:1:1:1 q, J_{CB} 50 Hz, ipso-ArC), 134.6 (s, ortho-ArC), 128.8 (q, J_{CF} 32 Hz, meta-ArC), 124.8 (q, J_{CF} 272 Hz, CF_3), 117.3 (s, para-ArC), 112.4 (br s, C=C), 53.8 (qu. CD_2Cl_2), 37.3 (s, cyclohexyl-CH), 30.9 (s, cyclohexyl-CH_2), 29.9 (s, cyclohexyl-CH_2), 29.6 (s, cyclohexyl-CH_2), 29.2 (s, cyclohexyl-CH_2), 26.5 (cyclohexyl-CH_2), 25.7 (cyclohexyl-CH_2), 25.3 (cyclohexyl-CH2), 22.1 (s, cyclohexyl-CH_2).

$^{13}C\{^1H\}$ NMR (CD_2Cl_2, 183 K, 126 MHz): δ 161.1 (1:1:1:1 q, J_{CB} 50 Hz, ipso-ArC), 134.6 (s, ortho-ArC), 128.8 (q, J_{CF} 32 Hz, meta-ArC), 124.8 (q, J_{CF} 272 Hz, CF_3), 117.3 (s, para-ArC), 111.5 (br s, C=C), 72.6 (br s, C=C, 53.8 (qu. CD_2Cl_2), 36.7 (br s.), 35.2 (br s.), 31.1 (s, cyclohexyl-CH_2), 29.4 (m, cyclohexyl-CH_2), 25.6 (s, cyclohexyl-CH_2), 24.9 (s, cyclohexyl-CH_2), 24.3 (s, cyclohexyl-CH_2), 22.2 (s, cyclohexyl-CH_2), 19.4 (br. s).

$^{19}F\{^1H\}$ NMR (CD_2Cl_2, 298 K, 377 MHz): δ -62.9 (s).

$^{31}P\{^1H\}$ SSNMR (162 MHz, 294 K, 10 kHz spin rate): δ 95.9 (br. triplet from coincident environments).

$^{31}P\{^1H\}$ SSNMR (162 MHz, 158 K, 10 kHz spin rate): δ 94.8 (br. triplet from coincident environments).

$^{13}C\{^1H\}$ SSNMR (101 MHz, 294K, 10 kHz spin rate): δ 162.4 (ipso-ArC), 134.1 (ortho-ArC), 130.9 (meta-ArC), 125.0 (br, CF_3), 119.4 (para-ArC), 118.9 (para-ArC), 112.6 (**C**=CH_2), 38.7, 36.3, 33.9, 32.1, 30.6, 27.5, 26.6, 25.9, 22.2.

$^{13}C\{^1H\}$ SSNMR (101 MHz, 158K, 10 kHz spin rate): δ 163.1 (ipso-ArC), 134.2 (ortho-ArC), 130.4 (meta-ArC), 124.9 (br, CF_3), 117.6 (para-ArC), 116.1 (para-ArC), 111.6 (**C**=CH_2), 73.6 (C=**C**H_2), 39.7, 34.3, 31.2, 29.8, 27.5, 24.1, 22.7, 21.9, 15.7.

Note: Signals at 111 and 73 disappeared upon addition of H_2, to form **[1-*iso*butane][BAr^F_4]**.

ESI-MS: Not stable under mass spectrometric conditions (20eV, 333K). Species with appropriate isotopic distributions at m/z found = 581.240, calculated to $[(Cy_2PCH_2CH_2PCy_2)Rh(N_2)_2]^+$ (581.242). There is no evidence for the nitrogen compound in bulk samples so it is assumed to form via an in-situ ESI-MS process.

Elemental Analysis (calc. for $C_{62}H_{68}BF_{24}P_2Rh$): C 52.39 (51.54), H 4.87 (4.74).

7.2.3.2. Synthesis of a *Iso*butane Complex, [1-*iso*butane][BAr^F_4]

For Single-Crystal X-Ray Diffraction: Orange crystals of **[1-*iso*butene][BAr^F_4]** (1.5 mgs) were treated with H_2 (1 bar, 298 K, 8 minutes) inside a J. Young NMR tube. The colour of the crystals rapidly turned dark red in this time. The crystalline material was then coated with Fomblin® Y oil under an argon-flush; a suitable crystal was rapidly selected and then transferred to the Cryostream of a diffractometer and an x-ray diffraction study was undertaken. For further details of structural refinement please refer to Section 7.4.

For Solid-State NMR Spectroscopy: A powdered microcrystalline sample of **[1-*iso*butene][BAr^F_4]** (35 mgs) was packed in a 4.0 mm SSNMR rotor, inside an argon filled glove box. The rotor was then placed in a custom-built glass J. Young flask[7] and the sample was then exposed to H_2 (1 bar, 298 K). After 12 minutes, the rotor cap was fitted under a flush of H_2. The sample was rapidly transferred to the bore of a SSNMR spectrometer, cooled to 158 K (~10 minutes) and analysed by $^{31}P\{^1H\}$ and $^{13}C\{^1H\}$ solid-state NMR spectroscopy.

These conditions were optimized to form **[1-*iso*butane][BAr^F_4]**. At 158K, no onward reactivity with H_2 is observed. When H_2 was replaced by argon at 298K, as so the rotor is packed under an argon atmosphere, dehydrogenation to re-form **[1-*iso*butene][BAr^F_4]** is observed before cooling to 158 K. Further exposure to H_2 (90 minutes) at 298 K results in complete decomposition to **[1-BAr^F_4]**.

$^{31}P\{^1H\}$ SSNMR (162 MHz, 298K, 10 kHz spin rate): δ 106.4 (br. triplet from coincident environments).

$^{31}P\{^1H\}$ SSNMR (162 MHz, 158 K, 10 kHz spin rate): δ 106.8 (br. triplet from coincident environments) (~ 80% yield).

$^{13}C\{^1H\}$ SSNMR (101 MHz, 158 K, 10 kHz spin rate): δ 160.5 (ArC), 132.9 (ArC), 127.1 (ArC), 121.6 (br, CF_3), 114.9 (ArC), 112.8 (ArC), 35.0, 32.1, 27.9, 22.8, 17.3, 15.9 (multiple aliphatic resonances).

^1H projection from $^1H/^{13}C$ FSLG HETCOR SSNMR (10 kHz spin rate, 158 K): δ 9.81 (br), 7.12 (br), 0.7 (br), -3.4 (br).

7.2.4. [Rh(Cy$_2$PCH$_2$CH$_2$PCy$_2$)(*iso*-C$_5$H$_{12}$)][BAr$^F{}_4$], [1-*iso*pentane][BAr$^F{}_4$]

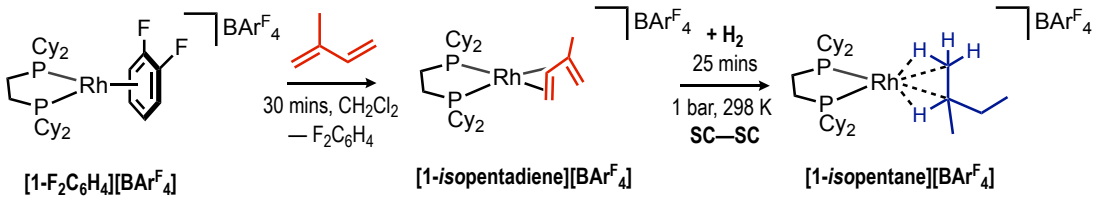

[1-F$_2$C$_6$H$_4$][BAr$^F{}_4$] [1-*iso*pentadiene][BAr$^F{}_4$] [1-*iso*pentane][BAr$^F{}_4$]

7.2.4.1. Synthesis of a *Iso*pentadiene Complex, [1-*iso*pentadiene][BAr$^F{}_4$]

A pale-yellow solution of **[1-C$_6$H$_4$F$_2$][BAr$^F{}_4$]** (600 mgs, 0.40 mmol) in CH_2Cl_2 (20 mL) was treated with 2-methyl-1,3-butadiene (50 µL, 0.5 mmol) at ambient temperature. The resultant deep red solution was stirred at ambient temperature for 30 minutes. Pentane (100 mL) was then added with vigorous stirring which resulted in the formation of a red precipitate. The solid was isolated by filtration and washed with pentane (2 × 20 mL). The solid was then dissolved in CH_2Cl_2 (~8 mL) and filtered into a J. Youngs crystallisation flask and layered with pentane. Deep red crystals were obtained after storage for 1 week at room temperature of [Rh(Cy$_2$PCH$_2$CH$_2$PCy$_2$)(*iso*-C$_5$H$_8$)][BAr$^F{}_4$], **[1-*iso*pentadiene][BAr$^F{}_4$]** (Yield: 551 mgs, 95 %).

^{1}H NMR (CD_2Cl_2, 298 K, 400 MHz): δ 7.73 (s, 8H, *ortho*-ArH), 7.57 (s, 4H, *para*-ArH), 5.16 (d. of d. of d., 1H, alkene-H, *J* = 13.8, 8.1, 1.6 Hz), 4.38 (d, 1H, alkene-H, *J* = 2.8), 4.32 (d. of d. of d., 1H, alkene-H, *J* = 7.8, 4.1, 1.3 Hz), 2.74 (d. of m., 1H, alkene-H, *J* = 14.1, 1.3 Hz), 2.70 (br. m., 1H, alkene-H), 2.23-1.52 (br m, 31H, multiple overlapping aliphatic CH), 1.42-0.84 (br m, 20H, multiple overlapping aliphatic CH).

^{31}P{^{1}H} NMR (CD_2Cl_2, 298 K, 162 MHz): δ 84.3 (d.d., J_{RhP} 163 Hz, J_{PP} 22 Hz), δ 79.5 (d.d., J_{RhP} 169 Hz, J_{PP} 22 Hz).

^{13}C{^{1}H} NMR (CD_2Cl_2, 298 K, 126 MHz): δ 162.4 (q, J_{CB} 50 Hz, *ipso*-ArC), 135.1 (s, *ortho*-ArC), 129.3 (q, J_{CF} 32 Hz, meta-ArC), 125.1 (q, J_{CF} 272 Hz, -CF_3), 120.0 (apparent triplet, C=C, *J* = 4.3 Hz), 117.8 (s, *para*-ArC), 101.2 (apparent triplet, C=C, *J* = 4.3 Hz), 63.7 (d. of d. of d., C=C, *J* = 14.4, 5.3, 1.5 Hz), 62.8 (d. of d. of d., C=C, *J* = 10.9, 7.6, 1.7 Hz), 38.4 – 22.6 (m, overlapping cyclohexyl-CH_2).

^{19}F{^{1}H} NMR (CD_2Cl_2, 298 K, 377 MHz): δ -62.9 (s).

^{31}P{^{1}H} SSNMR (162 MHz, 294 K, 10 kHz spin rate): Orientation 1**:** δ 86.2 (d, J_{RhP} 152 Hz), 75.5 (d, J_{RhP} 165 Hz). Orientation 2**:** δ 81.9 (d, J_{RhP} 147 Hz), 74.1 (d, J_{RhP} 150 Hz).

^{13}C{^{1}H} SSNMR (101 MHz, 294 K, 10 kHz spin rate): δ 164.7 (*ipso*-ArC), 134.5 (*ortho*-ArC), 129.7 (*meta*-ArC), 124.4 (br, -CF_3), 120.5 (C=C), 117.3 (*para*-ArC), 116.1 (*para*-ArC), 104.3 (C=C), 103.0 (C=C), 96.4 (C=C), 94.3 (C=C), 91.6 (C=C), 88.0 (C=C), 60.4 (C=C), 38.7 – 18.7 (m, overlapping cyclohexyl-CH_2).

Note: Peaks that are assigned (C=C) as they disappear upon hydrogenation of the sample.

ESI-MS (calc. for $[Rh(Cy_2PCH_2CH_2PCy_2)(C_5H_8)]^+$): m/z 593.2912 (593.2907).
Elemental Analysis (calc. for $C_{63}H_{68}BF_{24}P_2Rh$): C 52.06 (51.94), H 4.50 (4.70).

7.2.4.2. Synthesis of a *Iso*pentane Complex, [1-*iso*pentane][BAr^F_4]

For Single-Crystal X-Ray Diffraction: Ruby red crystals of **[1-*iso*pentadiene][BAr^F_4]** (1.5 mgs) were treated with H_2 (1 bar, 298 K, 25 minutes) inside a J. Young NMR tube. The colour of the crystals slowly turned a dark red over this time. The crystalline material was then coated with Fomblin® Y oil under an argon-flush; a suitable crystal was rapidly selected and then transferred to the cyrostream of a diffractometer and an x-ray diffraction study was undertaken. For further details of structural refinement please refer to Section 7.4.

For Solid-State NMR Spectroscopy: A powdered microcrystalline sample of **[1-*iso*pentadiene][BAr^F_4]** (45 mgs) was packed in a 4.0 mm SSNMR rotor, inside an argon filled glove box. The rotor was then placed in a custom-built glass J. Young flask[7] and the sample was then exposed to H_2 (1 bar, 298 K). After 20 minutes, the rotor cap was fitted under a flush of H_2. The sample was rapidly transferred to the bore of a SSNMR spectrometer, cooled to 158 K (~10 minutes) and analysed by $^{31}P\{^1H\}$ and $^{13}C\{^1H\}$ solid-state NMR spectroscopy.

Note: These conditions were optimized to form **[1-*iso*pentadiene][BAr^F_4]**. At 158K, no onward reactivity with H_2 is observed. When H_2 is replaced by argon at 298K, as so the rotor is packed under an argon atmosphere, rapid dehydrogenation to form **[1-*iso*pentenes][BAr^F_4]** was observed before cooling to 158 K. Further exposure to H_2 (90 minutes) at 298 K results in complete decomposition to **[1-BAr^F_4]**.[2]

$^{31}P\{^1H\}$ SSNMR (162 MHz, 158 K, 10 kHz spin rate): δ 106.9 (d, J_{RhP} 204 Hz), 104.1 (d, J_{RhP} 220 Hz) (~ 75% yield).
$^{13}C\{^1H\}$ SSNMR (101 MHz, 158 K, 10 kHz spin rate): δ 163.3 (*ipso*-ArC), 134.1 (*ortho*-ArC), 128.9 (*meta*-ArC), 123.7 (br, -CF_3), 116.6 (*para*-ArC), 39.9, 36.6, 34.8, 31.1, 30.1, 28.3, 25.0, 20.2, 17.3, 13.3, 10.1, 8.42 (multiple aliphatic resonances).

7.2.4.3. Synthesis of a *Iso*pentene Complex, [1-*iso*pentenes][BAr^F_4]

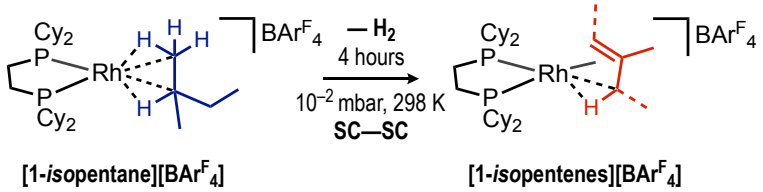

[1-*iso*pentane][BAr^F_4] [1-*iso*pentenes][BAr^F_4]

For Solid-State NMR Spectroscopy and Single-Crystal X-Ray Diffraction: Ruby red crystals of **[1-*iso*pentadiene][BAr^F_4]** (100 mgs) were placed under an atmosphere of H_2 (1 bar, 298 K, 25 minutes) inside a J. Young flask. The colour of this material slowly turned dark red within this time. The powder was then exposed to a dynamic Schlenk line vacuum (< 2 × 10^{-2} mbar), optimised at 4 hours) to yield [Rh($Cy_2PCH_2CH_2PCy_2$)(*iso*-C_5H_{10})][BAr^F_4], **[1-*iso*pentenes][BAr^F_4]**. The now yellow-orange powder was then taken into an argon filled glove box and stored at – 25 ºC. This dehydrogenation reaction was also found to occur under a flushing argon flow within 6 hours.

A single-crystal x-ray diffraction experiment was conducted on a sample of these crystals (for further details of the structural refinement please refer to Section 7.4.) as well as variable temperature solution NMR spectroscopy. A sample of this material (45 mgs) was further packed in a 4.0 mm SSNMR rotor, inside an argon filled glove box. The sample was transferred to the bore of a SSNMR spectrometer and analysed by $^{31}P\{^1H\}$ and $^{13}C\{^1H\}$ solid-state NMR spectroscopy at 294 and 158 K.

^{1}H NMR (CD_2Cl_2, 298 K, 400 MHz): δ 7.76 (s, 8H, *ortho*-ArH), 7.61 (s, 4H, *para*-ArH), 2.05-1.68 (br m, overlapping aliphatic CH), 1.61-0.85 (br m, aliphatic CH).
^{1}H NMR (CD_2Cl_2, 183 K, 400 MHz): δ 7.77 (s, 8H, *ortho*-ArH), 7.58 (s, 4H, *para*-ArH), 5.08 (s, 2H, C=C**H**CH_3 from *internal isomer*), 4.33 (s, 1H, C=C**H_2** from *terminal isomer*), 3.29 (s, 1H, C=C**H_2** from *terminal isomer*), 2.14-0.78 (br m, overlapping aliphatic CH), -0.25, (s, 3H, agostic from *terminal isomer*), –1.23 (s, 1H, agostic from *terminal isomer*).
$^{31}P\{^1H\}$ NMR (CD_2Cl_2, 298 K, 162 MHz): δ 94.4 (d, J_{RhP} 181.7 Hz).
$^{31}P\{^1H\}$ NMR (CD_2Cl_2, 183 K, 162 MHz): *Internal Isomer*: δ 96.6 (d of d, J_{RhP} 199.6 Hz, J_{PP} 25 Hz), 93.9 (d of d, J_{RhP} 155.9 Hz, J_{PP} 25 Hz). *Terminal Isomer:* δ 95.2 (d of d, J_{RhP} 152.6 Hz, J_{PP} 26 Hz), 93.9 (d of d, J_{RhP} 212.0 Hz, J_{PP} 26 Hz).

Note: The assignments for the above data have been made from ^{1}H / ^{1}H COSY analysis upon the same sample, as well as comparison to the similar, previously reported *iso*butene[9] and 2-butene complexes.[7] The low temperature limit was not reached at 183K in the ^{1}H NMR

spectrum, so integrated values are approximate. NMR samples prepared under argon, but immediately run after preparation.

$^{13}C\{^1H\}$ NMR (CD_2Cl_2, 183 K, 126 MHz): δ 161.6z (q, J_{CB} 50 Hz, *ipso*-ArC), 134.6 (s, *ortho*-ArC), 128.6 (q, J_{CF} 32 Hz, *meta*-ArC), 124.5 (q, J_{CF} 272 Hz, -CF_3), 119.1 (s, alkene-CH), 117.6 (s, *para*-ArC), 104.8 (s, alkene-CH), 86.4 (s, alkene-CH), 72 (br., alkene-CH), 37.4 to 19.8 (multiple aliphatic resonances from both isomers), 17.4, 17.2, 14.5, 13.7, 12.4, 11.7.
$^{19}F\{^1H\}$ NMR (CD_2Cl_2, 298 K, 377 MHz): δ -62.9 (s).

$^{31}P\{^1H\}$ SSNMR (162 MHz, 294 K, 10 kHz spin rate): δ 95.4 (br, apparent triplet).
$^{31}P\{^1H\}$ SSNMR (162 MHz, 158 K, 10 kHz spin rate): δ 94.6 (br, apparent triplet).
$^{13}C\{^1H\}$ SSNMR (101 MHz, 294 K, 10 kHz spin rate): δ 163.8 (*ipso*-ArC), 134.5 (*ortho*-ArC), 130.1 (*meta*-ArC), 124.6 (br, CF_3), 118.2 (*para*-ArC), 115.5 (*para*-ArC), 38.4 (CH), 35.9 (CH), 30.6 (CH_2), 21.7 (CH_2), 13.1 (CH_2).
$^{13}C\{^1H\}$ SSNMR (101 MHz, 158 K, 10 kHz spin rate): δ 163.9 (*ipso*-ArC), 133.9 (*ortho*-ArC), 129.4 (*meta*-ArC), 124.2 (br, CF3), 117.7 (*para*-ArC), 114.9 (*para*-ArC), 106.5 (C=C), 87.6 (C=C), 69.5 (C=C), 38.8 (CH), 36.6 (CH), 30.8 (CH_2), 26.6 (CH_2), 24.7 (CH_2), 19.2 (CH_2), 16.8 (CH_2), 12.6 (CH_2).

ESI-MS: Not stable under mass spectrometric conditions (20eV, 333K). Species with appropriate isotopic distributions at m/z found = 581.240, calculated to $[(Cy_2PCH_2CH_2PCy_2)Rh(N_2)_2]^+$ (581.242). There is no evidence for the nitrogen compound in bulk samples so it is assumed to form via an in-situ ESI-MS process.

7.2.4.4. Liberation of bound *iso*pentene from [1-*iso*pentenes][BAr^F_4]

A J. Young flask was charged with a sample of **[1-*iso*pentenes][BAr^F_4]** (30 mgs), as prepared from the method in Section 7.2.4.1. The flask was placed under vacuum (< 2 × 10^{-2} mbar) and backfilled with CO (1 bar, 298 K). After 18 hours, the orange crystalline material had turned a pale-yellow colour. The volatile component was then isolated by trap-to-trap distillation into CD_2Cl_2 and analysed by solution ^1H NMR spectroscopy. The resultant solid was confirmed to be **[1-$(CO)_2$][BAr^F_4]** by solution $^{31}P\{^1H\}$ NMR spectroscopy (δ 85.22, d, J_{RhP} = 116 Hz).

2-methylbut-1-ene: ^1H NMR ($CDCl_3$, 298 K, 400 MHz): δ 4.66 (s., 2H), 2.02 (quartet, 2H, J_{HH} = 7.5 Hz), 1.73 (s., 3H), 1.03 (triplet, 3H, J_{HH} = 7.5 Hz).

2-methylbut-2-ene: ^{1}H NMR (CH_2Cl_2, 298 K, 500 MHz): δ 5.18 (m., 1H), 1.67 (s., 3H), 1.60 (s., 3H), 1.55 (d., 3H, J_{HH} = 6.7 Hz)

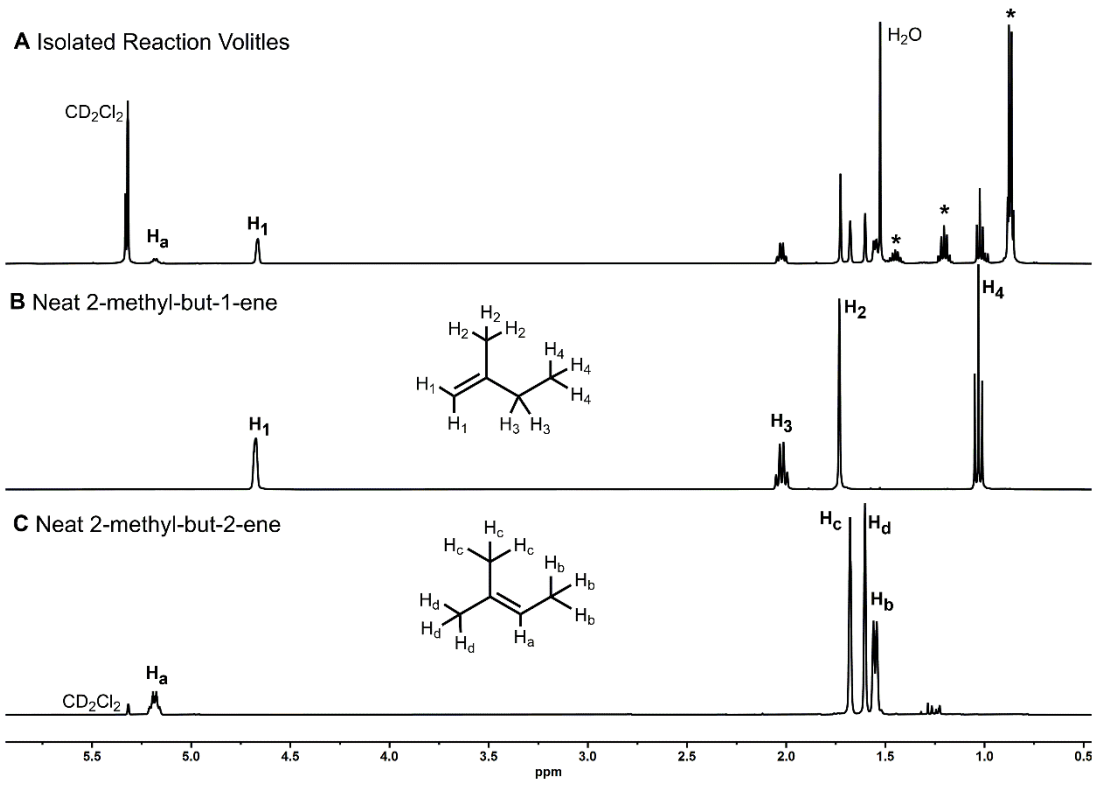

Figure 7.1: The solution ^{1}H NMR of: **A** (CD_2Cl_2, 298 K, 500 MHz) Liberated reaction volatiles, showing mix of *iso*pentene isomers. Peaks marked * are from *iso*pentane from alkane liberation from sample decomposition during the initial hydrogenation. **B** ($CDCl_3$, 298 K, 400 MHz) Neat 2-methyl-but-1-ene. **C** (CD_2Cl_2, 298 K, 400 MHz) Neat 2-methylbut-2-ene.

Note: The integration of the H_1: H_a resonances (from spectrum A) is **2.79: 1**. This suggests a **1.4: 1** ratio of coordinated terminal: internal isopentene.

7.2.5. [Rh(Cy$_2$PCH$_2$CH$_2$PCy$_2$)(*n*-C$_6$H$_{10}$)][BAr$^F_4$], [1-hexane][BAr$^F_4$]

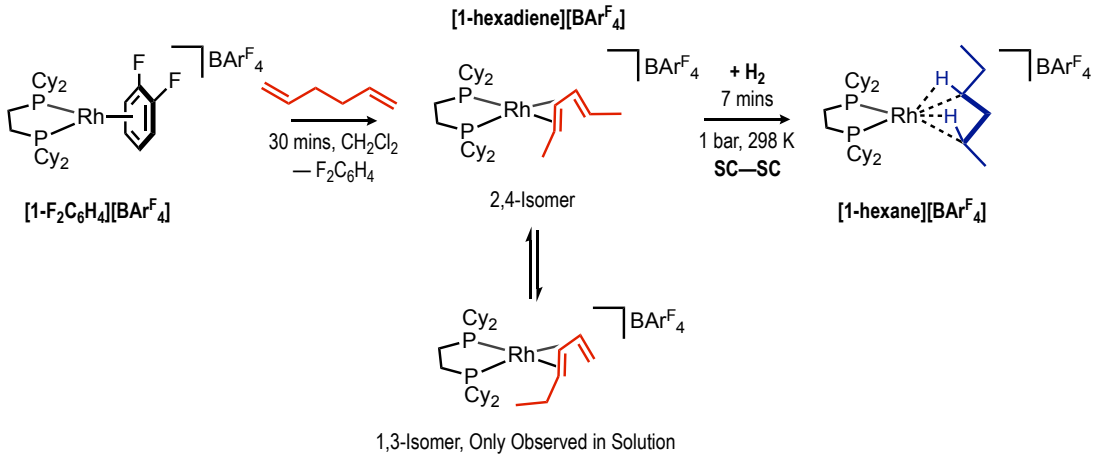

7.2.5.1. Synthesis of the Precursor Hexadiene Complex, [1-hexadiene][BAr$^F_4$]

A pale-yellow solution of **[1-C$_6$H$_4$F$_2$][BAr$^F_4$]** (600 mgs, 0.40 mmol) in CH_2Cl_2 (20 mL) was treated with 1,5-hexadiene (0.1 mL, 0.48 mmol) at ambient temperature. The resultant deep red solution was stirred at ambient temperature for 30 minutes. Pentane (100 mL) was then added with vigorous stirring which resulted in the formation of a red precipitate. The solid was isolated by filtration and washed with pentane (2 × 20 mL). The solid was then dissolved in 1,2-dichloroethane (~12 mL) and filtered into a J. Young crystallisation flask and layered with pentane. Ruby red crystals were obtained after storage for 1 week at room temperature of [Rh(Cy$_2$PCH$_2$CH$_2$PCy$_2$)(C$_6$H$_{10}$)][BAr$^F_4$], **[1-hexadiene][BAr$^F_4$]** (Yield: 404 mgs, 69 %).

Note: The 2,4-isomer was found to be the only isomer present in the solid-state. Taking single-crystals of the 2,4-isomer and re-dissolving in CH_2Cl_2 initially showed only the 2,4-isomer, where the mixture of isomers was observed to grow in within 2 hours.

^{1}H NMR (CD_2Cl_2, 298 K, 400 MHz): δ 7.82 (s, 8H, *ortho*-ArH), 7.67 (s, 4H, *para*-ArH), 5.68 (d. of d., alkene-H, J = 14.6, 3.8 Hz), 5.49 (d. of m., alkene-H, J = 12.5 Hz), 5.34 (m., alkene-H, J = 1.1 Hz), 4.25 (m., alkene-H), 4.12 (m., alkene-H), 2.88 (d., alkene-H, J = 14.4 Hz), 2.16 - 1.70 (br m, overlapping aliphatic CH), 1.52-0.98 (br m, aliphatic CH).

^{31}P{^{1}H} NMR (CD_2Cl_2, 298 K, 162 MHz): 2,4-isomer: δ 80.6 (d, J_{RhP} 179 Hz). The 1,3-isomer: δ 84.5 (d.d., J_{RhP} 174 Hz, J_{PP} 22 Hz), δ 77.3 (d.d., J_{RhP} 171 Hz, J_{PP} 22 Hz).
^{19}F{^{1}H} NMR (CD_2Cl_2, 298 K, 377 MHz): δ -62.9 (s).
^{13}C{^{1}H} NMR (CD_2Cl_2, 298 K, 126 MHz): δ 162.1 (q, J_{CB} 50 Hz, *ipso*-ArC), 135.1 (s, *ortho*-ArC), 129.2 (q, J_{CF} 32 Hz, meta-ArC), 125.0 (q, J_{CF} 272 Hz, -CF_3), 117.7 (s, *para*-ArC), 108.2, 109.2, 104.6, 101.0, 98.6, 97.5, 88.8, 61.8 (m, multiple alkene resonances from 2,4-isomer

and 1,3-isomers), 38.8, 38.5, 37.8, 37.0, 36.2, 35.5, 32.0 - 19.9 (m, overlapping cyclohexyl-CH_2 from isomers A and B).
ESI-MS (calc. for $[Rh(Cy_2PCH_2CH_2PCy_2)(C_6H_{10})]^+$): m/z 607.3086 (607.3063).
Elemental Analysis (calc. for $C_{64}H_{70}BF_{24}P_2Rh$): C 52.17 (52.26), H 4.83 (4.80).

$^{31}P\{^1H\}$ SSNMR (162 MHz, 298 K, 10 kHz spin rate): δ 82.5 (d, J_{RhP} 189 Hz), 74.5. (d, J_{RhP} 182 Hz).
$^{13}C\{^1H\}$ SSNMR (101 MHz, 298 K, 10 kHz spin rate): δ 164.7 (ArC), 161.3 (ArC), 134.8 (ArC), 129.0 (ArC), 124.4 (ArC), 117.7 (ArC), 115.1 (ArC), 99.3 (C=C), 98.6 (C=C), 88.6 C=C), 85.3 (C=C), 39.6, 38.1, 34.9, 32.5, 30.6, 29.2, 27.0, 26.0, 24.6, 22.6, 19.9, 17.0 (multiple aliphatic resonances).

7.2.5.2. Synthesis of a Hexane Complex, [1-hexane][BAr^F_4]

For Single-Crystal X-Ray Diffraction: Red crystals of **[1-hexadiene][BAr^F_4]** (1.5 mgs) were treated with H_2 (1 bar, 298 K, 7 minutes) inside a J. Young NMR tube. The colour of the crystals turned a dark red over this time. The crystalline material was then coated with Fomblin® Y oil under an argon-flush; a suitable crystal was rapidly selected and then transferred to the Cryostream of a diffractometer and an x-ray diffraction study was undertaken. For further details of structural refinement please refer to Section 7.4.

For Solid-State NMR Spectroscopy: A powdered microcrystalline sample of **[1-hexadiene][BAr^F_4]** (45 mgs) was packed in a 4.0 mm SSNMR rotor, inside an argon filled glove box. The rotor was then placed in a custom-built glass J. Young flask[7] and the sample was then exposed to H_2 (1 bar, 298 K). After 10 minutes, the rotor cap was fitted under a flush of H_2. The sample was rapidly transferred to the bore of a SSNMR spectrometer, cooled to 158 K (~10 minutes) and analysed by $^{31}P\{^1H\}$ and $^{13}C\{^1H\}$ solid state NMR spectroscopy.

Note: These conditions were optimized to form **[1-hexane][BAr^F_4]**. At 158K, no onward reactivity with H_2 is observed.

$^{31}P\{^1H\}$ SSNMR (162 MHz, 158 K, 10 kHz spin rate): δ 106.0 (d, J_{RhP} 226 Hz), 102.5. (d, J_{RhP} 216 Hz) (~ 80 % yield).
$^{13}C\{^1H\}$ SSNMR (101 MHz, 158 K, 10 kHz spin rate): δ 162.7 (ArC), 134.0 (ArC), 129.1 (ArC), 124.0 (ArC), 115.7 (ArC), 37.2, 34.9, 34.6, 32.5, 31.5, 30.7 , 28.1, 24.8, 22.6, 20.1, 18.1, 13.9, 13.1 (multiple aliphatic resonances).

7.2.6. [Rh(Cy$_2$PCH$_2$CH$_2$PCy$_2$)(C$_6$H$_{14}$)][BAr$^F_4$], [1-(3-methylpentane)][BAr$^F_4$]

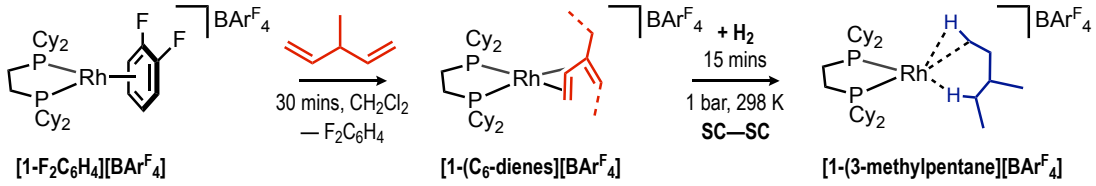

7.2.6.1. Synthesis of a hexadiene Complex, [1-(C$_6$-dienes)][BAr$^F_4$]

A pale-yellow solution of **[1-C$_6$H$_4$F$_2$][BAr$^F_4$]** (600 mgs, 0.40 mmol) in CH_2Cl_2 (20 mL) was treated with 3-methyl-1,4-pentadiene (0.1 mL, 0.78 mmol) at ambient temperature. The resultant deep red solution was stirred at ambient temperature for 30 minutes. Pentane (100 mL) was then added with vigorous stirring which resulted in the formation of a red precipitate. The solid was isolated by filtration and washed with pentane (2 × 20 mL). The solid was then dissolved in CH_2Cl_2 (~8 mL) and filtered into a J. Young crystallisation flask and layered with pentane. Deep red crystals were obtained after storage for 1 week at room temperature of [Rh(Cy$_2$PCH$_2$CH$_2$PCy$_2$)(C$_6$H$_{10}$)][BAr$^F_4$], **[1-(C$_6$-dienes)][BAr$^F_4$]** (Yield: 515 mgs, 88 %).

^{1}H NMR (CD_2Cl_2, 298 K, 400 MHz): δ 7.72 (s, 8H, *ortho*-ArH), 7.56 (s, 4H, *para*-ArH), 5.16 (d. of d. of d., alkene-H, *J* = 13.9, 8.6, 2.2 Hz), 5.01 (d. of d. of d., alkene-H, *J* = 13.7, 8.1, 2.1 Hz), 4.37-4.33 (broad m., alkene-H), 4.04 (d. of d. of d., alkene-H, *J* = 8.2, 4.3, 1.4 Hz), 3.90 (apparent quartet, alkene-H, *J* = 6.3 Hz), 2.31 -1.51 (br m, overlapping aliphatic CH), 1.44-0.82 (br m, aliphatic CH).

^{31}P{^{1}H} NMR (CD_2Cl_2, 298 K, 162 MHz): Isomer A: δ 85.6 (d.d., J_{RhP} 171 Hz, J_{PP} 24 Hz), 79.2 (d.d., J_{RhP} 169 Hz, J_{PP} 24 Hz). Isomer B: δ 84.0 (d.d., J_{RhP} 172 Hz, J_{PP} 23 Hz), 75.3 (d.d., J_{RhP} 163 Hz, J_{PP} 23 Hz).

^{19}F{^{1}H} NMR (CD_2Cl_2, 298 K, 377 MHz): δ -62.9 (s).

^{13}C{^{1}H} NMR (CD_2Cl_2, 298 K, 126 MHz): δ 162.7 (q, J_{CB} 50 Hz, *ipso*-ArC), 134.7 (s, *ortho*-ArC), 128.8 (q, J_{CF} 32 Hz, meta-ArC), 125.1 (apparent triplet, C=C, *J* = 4.3 Hz), 124.6 (q, J_{CF} 272 Hz, -CF_3), 119.3 (apparent triplet, C=C, *J* = 4.2 Hz), 117.4 (s, *para*-ArC), 99.6 (apparent triplet, C=C, *J* = 5.5 Hz), 98.4 (apparent triplet, C=C, *J* = 5.7 Hz), 86.0 (d. of d., C=C, *J* = 12.8, 3.3 Hz), 63.4 (d. of d. of d., C=C, *J* = 10.5, 7.8, 1.5 Hz), 62.8 (d. of d. of d., C=C, *J* = 14.2, 5.4, 1.6 Hz), 59.2 (d. of d. of d., C=C, *J* = 11.8, 8.2, 2.1 Hz), 38.3 – 21.1 (m, overlapping cyclohexyl-CH_2 from both isomers), 19.4, 15.9, 14.5, 13.8 (s, -ethyl/-methyl groups from co-ordinated isomers).

^{31}P{^{1}H} SSNMR (162 MHz, 294 K, 10 kHz spin rate): δ 84.8 (from two, coincident ^{31}P environments), 79.6, 74.9.

$^{13}C\{^1H\}$ SSNMR (101 MHz, 294 K, 10 kHz spin rate): δ 163.3 (*ipso*-ArC), 134.7 (*ortho*-ArC), 129.5 (*meta*-ArC), 124.4 (br, CF_3), 117.2 (*para*-ArC), 101.8 (C=C), 99.8 (C=C), 84.3 (C=C), 63.5 (C=C), 38.7 (CH), 36.0 (CH), 30.8 (CH_2), 26.2 (CH_2), 25.3 (CH_2), 21.2 (CH_2), 17.5 (CH_2), 14.5 (CH_2).

ESI-MS (calc. for $[Rh(Cy_2PCH_2CH_2PCy_2)(C_6H_{10})]^+$): m/z 607.3097 (607.3063).

Elemental Analysis (calc. for $C_{64}H_{70}BF_{24}P_2Rh$): C 52.38 (52.26), H 4.57 (4.80).

7.2.6.2. Liberation of bound C_6-dienes from [1-(C_6-dienes)][BAr^F_4]

A J. Young flask was charged with a crystalline sample of **[1-(C_6-dienes)][BAr^F_4]** (30 mgs), as prepared from the method in Section 7.2.6.1. The sample was dissolved in CD_2Cl_2 (0.5 mL, dark red solution) and MeCN-d_3 (0.05 mL) added to liberate the bound alkene products. After 2 minutes, the solution had turned a pale-yellow colour, and was confirmed to be $[Rh(Cy_2PCH_2CH_2PCy_2)(MeCN)_2][BAr^F_4]$ by solution $^{31}P\{^1H\}$ NMR spectroscopy (δ 91, d, J_{RhP} = 175 Hz).[7] The volatile components were then isolated by trap-to-trap distillation and analysed by solution ^1H NMR spectroscopy. A second batch was prepared in a similar fashion, however using neat MeCN, and analysed by solution $^{13}C\{^1H\}$ NMR spectroscopy.

$^{13}C\{^1H\}$ NMR (CD_2Cl_2, 298 K, 126 MHz): δ 148.2, 141.5, 139.0, 134.9, 133.4, 133.0, 127.3, 125.2, 114.4, 122.9, 122.8, 109.9, 23.8, 19.0, 13.0, 12.1, 11.2, 10.5.

^1H NMR (CD_2Cl_2, 298 K, 400 MHz): δ 6.84 (d. of d., *J* = 17.28, 10.55 Hz), 6.41 (d. of t., *J* = 18.18, 10.70 Hz), 5.60 (broad quartet, *J* = 6.46 Hz, H_4), 5.49 (broad quartet, *J* = 6.43 Hz, H_4), 5.26 (d., *J* = 18.6 Hz, H_4), 5.21 (d., *J* = 17.6 Hz), 5.08 (multiple overlapping signals), 5.04 (m.), 5.01 (m.), 4.92 (d., *J* = 11.85 Hz), 2.26 (quartet, *J* = 7.70 Hz, H_5), 1.82 (m.), 1.75 (m.), 1.12 (t., *J* = 7.70 Hz).

Note: Labelled signals have been assigned from $^1H/^1H$ COSY and $^1H/^{13}C$ HSQC analysis.

Literature Values: 2-ethylbutadiene[10]

$^{13}C\{^1H\}$ NMR (Neat, 298 K, 10 MHz): δ 112.9 [1], 148.3 [2], 139.6 [3], 114.7 [4], 24.6 [5], 12.6 [6].

Literature Values: (*E*)-3-methyl-1,3-pentadiene[11]

$^{13}C\{^1H\}$ NMR ($CDCl_3$, 298 K, 15.1 MHz): δ 133.5 [1], 133.2 [2], 125.0 [3], 113.0 [4], 19.71 [5], 12.9 [6].

Literature Values: (*Z*)-3-methyl-1,3-pentadiene[12]

$^{13}C\{^1H\}$ NMR ($CDCl_3$, 298 K, 15.1 MHz): δ 141.6 [1], 135.0 [2], 127.0 [3], 110.0 [4], 13.7 [5], 11.3 [6].

The solid-state structure was modelled to include both 2-ethylbutadiene and (*Z*)-3-methyl-1,3-pentadiene. (E)-3-methyl-1,3-pentadiene could not be modelled in the solid-state yet can be observed in the isolated dienes. We suggest a fast isomerisation event during the liberation of the bound dienes.

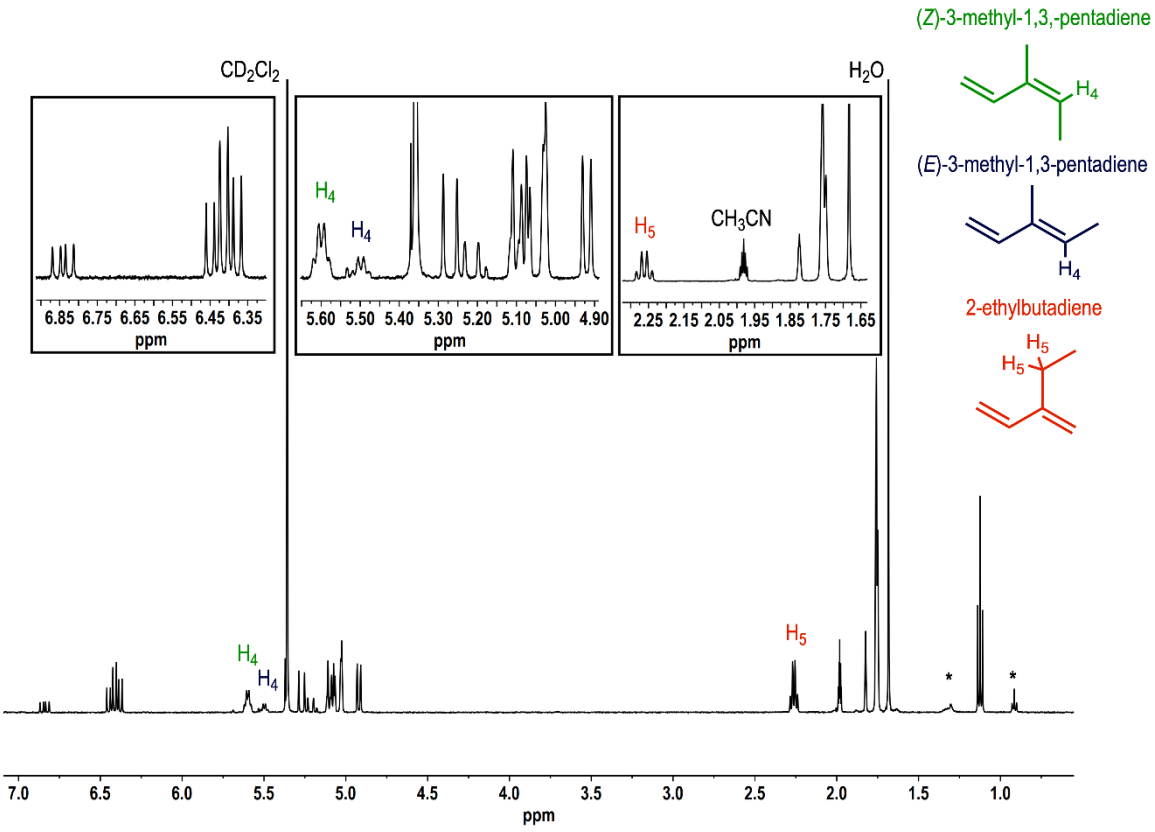

Figure 7.2: The solution ^{1}H NMR (CD_2Cl_2, 298 K, 500 MHz) spectrum of isolated isohexadiene volatiles. * = *n*-hexane impurity. The integration of the H_4: H_4: H_5 resonances is 0.70: 0.26 :1. This suggests an ~1: 1 ratio of coordinated (*Z/E*)-3-methyl-1,3-pentadiene and 2-ethylbutadiene.

7.2.6.3. Synthesis of a 3-methylpentane-Complex, [1-(3-methylpentane)][BAr$^F_4$]

For Single-Crystal X-Ray Diffraction: Red crystals of **[1-(C$_6$-dienes)][BAr$^F_4$]** (1.5 mgs) were treated with H_2 (1 bar, 298 K, 15 minutes) inside a J. Young NMR tube. The colour of the crystals slowly turned a dark red over this time. The crystalline material was then coated with Fomblin® Y oil under an argon-flush as a suitable crystal was rapidly selected, then transferred to the cyrostream of a diffractometer and an x-ray diffraction study was undertaken. For further details of structural refinement please refer to Section 7.4.

For Solid-State NMR Spectroscopy: A powdered microcrystalline sample of **[1-(C$_6$-dienes)][BAr$^F_4$]** (45 mgs) was packed in a 4.0 mm SSNMR rotor, inside an argon filled glove box. The rotor was then placed in a custom-built glass J. Young flask[7] and the sample was then exposed to H_2 (1 bar, 298 K). After 20 minutes, the rotor cap was fitted under a flush of argon. The sample was rapidly transferred to the bore of a SSNMR spectrometer (~10 minutes) and analysed by $^{31}P\{^1H\}$ and $^{13}C\{^1H\}$ solid-state NMR spectroscopy. These conditions were optimised to form **[1-(3-methylpentane)][BAr$^F_4$]**.

$^{31}P\{^1H\}$ SSNMR (162 MHz, 285 K, 10 kHz spin rate): δ 107.9 (d, J_{RhP} 188 Hz), 105.2 (d, J_{RhP} 236 Hz) (~ 70 % yield).
$^{13}C\{^1H\}$ SSNMR (101 MHz, 285 K, 10 kHz spin rate): δ 164.6 (ArC), 135.9 (ArC), 131.5 (ArC), 130.6 (ArC), 125.5 (ArC), 119.3 (ArC), 118.6 (ArC), 117.1 (ArC), 39.1, 37.8, 36.9, 34.5, 33.7, 32.2, 31.4, 30.8, 30.2, 28.2, 26.8, 21.9, 19.2, 11.9, 10.5, 7.63 (multiple aliphatic resonances).

7.2.7. [Rh(Cy$_2$PCH$_2$CH$_2$PCy$_2$)(C$_8$H$_{14}$)][BAr$^F_4$], [1-octadiene][BAr$^F_4$]

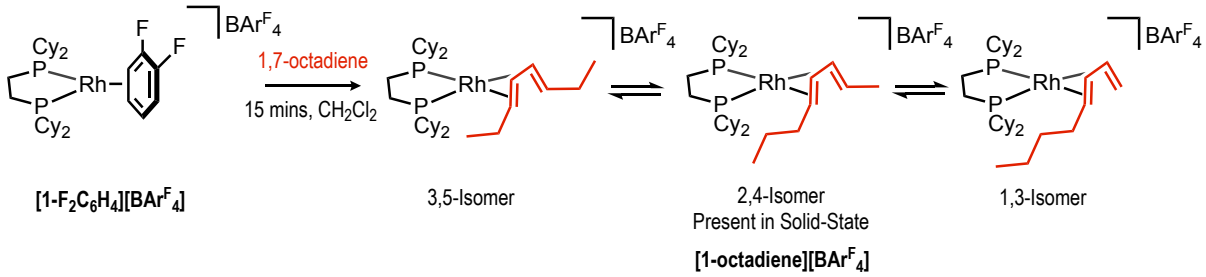

7.2.7.1. Synthesis of an Octodiene-Complex, [1-octadiene][BAr$^F_4$]

A pale-yellow solution of **[1-C$_6$H$_4$F$_2$][BAr$^F_4$]** (600 mgs, 0.40 mmol) in CH_2Cl_2 (20 mL) was treated with 1,7-octadiene (50 µL) at ambient temperature. The resultant deep red solution was stirred at ambient temperature for 15 minutes. Pentane (100 mL) was then added with vigorous stirring which resulted in the formation of a red precipitate. The solid was isolated by filtration and washed with pentane (2 × 20 mL). The solid was then dissolved in 1,2-dichloroethane (~12 mL) and filtered into a J. Young crystallisation flask and layered with pentane. Deep red crystals were obtained after storage for 1 week at room temperature of [Rh(Cy$_2$PCH$_2$CH$_2$PCy$_2$)(C$_8$H$_{14}$)][BAr$^F_4$], **[1-octadiene][BAr$^F_4$]** (Yield: 466 mgs, 78 %).

^{1}H NMR (CD$_2$Cl$_2$, 298 K, 400 MHz): δ 7.72 (s, 8H, *ortho*-ArH), 7.57 (s, 4H, *para*-ArH), 6.65, 6.30, 5.56, 5.36, 5.25, 4.16, 4.02, 2.78 (m, multiple alkene resonances from isomers *A, B* and *C*), 2.47-0.98 (br m, overlapping aliphatic CH).
^{31}P{^{1}H} NMR (CD$_2$Cl$_2$, 298 K, 162 MHz): Isomer *A*: δ 80.7 (d, J_{RhP} 178 Hz). Isomer *B*: δ 80.9 (d.d., J_{RhP} 178 Hz, J_{PP} 24.1 Hz), δ 80.6 (d.d., J_{RhP} 178 Hz, J_{PP} 24.1 Hz). Isomer *C*: δ 84.5 (d.d., J_{RhP} 175 Hz, J_{PP} 22.8 Hz), δ 77.3 (d.d., J_{RhP} 173 Hz, J_{PP} 22.8 Hz).
^{19}F{^{1}H} NMR (CD$_2$Cl$_2$, 298 K, 377 MHz): δ -62.9 (s).
ESI-MS (calc. for [Rh(Cy$_2$PCH$_2$CH$_2$PCy$_2$)(C$_8$H$_{14}$)]$^+$): m/z 635.3329 (635.3376).

7.2.7.2. Attempted Synthesis of a Octane-Complex

Following the previously stated procedures in Sections 7.2.3.3 and 7.2.4.3., addition of H_2 (1 bar, 298 K, 10 minutes) to crystals of **[1-octadiene][BAr$^F_4$]** resulted in a light-yellow colour change. It was found single-crystals of the yellow product did not diffract. Dissolution of this product in CD_2Cl_2 shows the complete hydrogenation of **[1-octadiene][BAr$^F_4$]** as no signals from this could be seen in the solution $^{31}P\{^1H\}$ NMR spectra and trap-to-trap distillation of the volatiles confirmed the formation of octane.

Any reduction in the time of hydrogenation (< 10 minutes) resulted in a mix of **[1-octadiene][BAr$^F_4$]** starting material and **[1-BAr$^F_4$]** product by solution $^{31}P\{^1H\}$ NMR spectroscopy.

7.3. Experimental Procedures for SMOM@Polymer

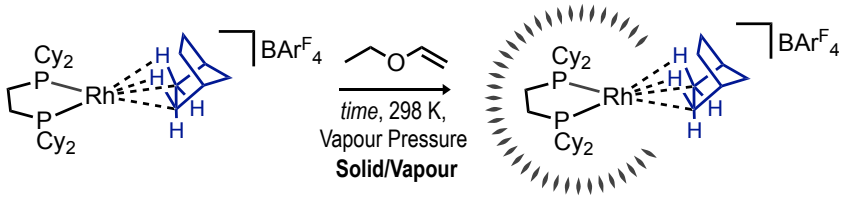

[1-NBA][BAr$^F_4$] **[1-NBA][BAr$^F_4$]@poly(EVE)**

7.3.1. Synthesis of [1-NBA][BAr$^F_4$]@poly(EVE)

To Mount: Inside an argon filled glove box, crystals of **[1-NBD][BAr$^F_4$]** (Typically 5 x crystals of approximately 1 mg each, with an approximate size of 1 x 1 x 1.5 mm) were mounted to a specially adapted J. Young tap. This was constructed from a cut needle gently pressed into the base of the J. Young tap and was lightly covered in silicon grease to aid attachment of the **[1-NBD][BAr$^F_4$]** crystals.

Once mounted: A J. Young flask (~50 mL) was sealed with the adapted J. Young tap with mounted crystals and evacuated (< 2 × 10^{-2} mbar) filled with H_2 gas (15 psi, 298 K) and left to stand for 15 minutes, to form **[1-NBA][BAr$^F_4$]** *in-situ*.[2] Care was taken to not dislodge any crystals from the mount during gas evacuation and addition. After this time, the H_2 was removed under vacuum (< 2 × 10^{-2} mbar) and flask cooled to 77 K using liquid nitrogen. Ethyl Vinyl Ether (EVE) (0.1 mL) was then vacuum distilled into the flask, and rapidly warmed to room temperature, at which the volatility of EVE (b.p. 33 ºC) allowed for an atmosphere of EVE to be formed as a timer was started. After set time periods of either 30 seconds, 2.5 minutes, or 15 minutes at ambient temperature, the flask was again placed under vacuum (< 2 × 10^{-2} mbar) to remove excess ethyl vinyl ether and back filled with argon to yield [Rh($Cy_2P(CH_2)_2PCy_2$)(NBA)][BAr$^F_4$]@polymer; **[1-NBA][BAr$^F_4$]@poly(EVE)**.

[1-NBA][BAr$^F_4$]@poly(EVE) was analysed by ^1H and $^{31}P\{^1H\}$ solution NMR spectroscopy, $^{31}P\{^1H\}$ and $^{13}C\{^1H\}$ Solid-State NMR spectroscopy, single crystal x-ray diffraction and SEM / EDX experiments.

Note: Due to the fragile nature of the crystals, it was found **[1-NBA][BAr$^F_4$]** could not be easily handled or mounted, hence stronger crystals of **[1-NBD][BAr$^F_4$]** were mounted and hydrogenated *in situ* to give **1-NBA][BAr$^F_4$]**. It was also found **[1-NBD][BAr$^F_4$]** does not initiate the polymerisation of ethyl vinyl ether. **[1-NBA][BAr$^F_4$]** was essential for initiation.

7.6.2. Synthesis of [1-propene][BAr$^F_4$]@poly(EVE)

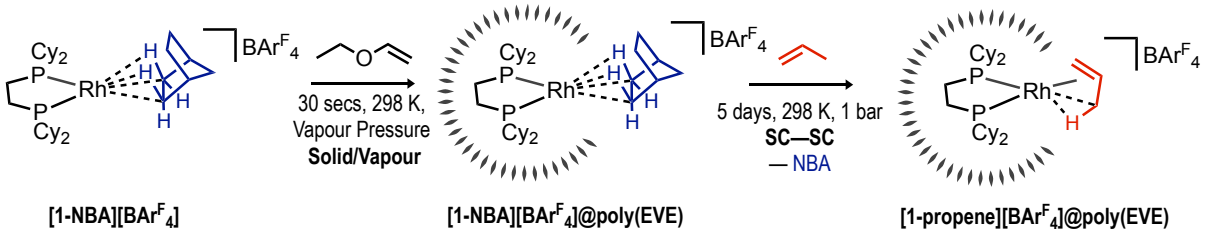

[1-NBA][BAr$^F_4$] [1-NBA][BAr$^F_4$]@poly(EVE) [1-propene][BAr$^F_4$]@poly(EVE)

Crystals of **[1-NBA][BAr$^F_4$]@poly(EVE) (**approximately 1 x 1 x 1.5 mm in size and 1.0 mg in mass) were prepared following the procedure in Section 7.3.1., with 30 seconds EVE exposure time. The flask was placed under vacuum (< 2 × 10^{-2} mbar) and propene (1 bar, 298 K) was added. After 5 days, the flasks was evacuated and re-filled with argon, to yield yellow/orange crystals of [Rh($Cy_2PCH_2CH_2PCy_2$)(C_3H_6)][BAr$^F_4$])@poly(ethylvinylether), **[1-propene][BAr$^F_4$]@poly(EVE)**. When dissolved in CD_2Cl_2 and analysed by solution ^{1}H and ^{31}P{^{1}H} NMR spectroscopy or analysed directly by solid-state ^{31}P{^{1}H} and ^{13}C{^{1}H} NMR spectroscopy and single-crystal x-ray diffraction showed the formation of **[1-propene][BAr$^F_4$]@poly(EVE)**. Further information about the single-crystal x-ray diffraction refinement structure can be found in Section 7.4.

^{1}H NMR (CD_2Cl_2, 400 MHz, 298 K): δ 7.71 (8H, s, BAr$^F_4$), 7.54 (4H, s, BAr$^F_4$), ~5.1 (br, propene), 2.02-0.94 (~60H, multiple overlapping aliphatic resonances).[7]
^{31}P{^{1}H} NMR (CD_2Cl_2, 126 MHz, 298 K): δ 95.1 (br d, J_{RhP} = 180 Hz). (Reported value of δ 95.2 (br d, J_{RhP} = 181 Hz)).[7]
^{31}P{^{1}H} SSNMR (162 MHz, 10 kHz spin rate, 298 K): δ 95.3 (br s.). (Reported value of δ 95.6 (br s.).[7]

Note: On a separate batch to that above **[1-NBA][BAr$^F_4$]@poly(EVE)** was left under propene for 2 days. When analysed by solution ^{31}P{^{1}H} NMR spectroscopy after this time, two complexes were observed in approximate 50: 50 ratio of **[1-propene][BAr$^F_4$]@poly(EVE)** and **[1-BAr$^F_4$]**, where **[1-BAr$^F_4$]** is the product of decomposition of **[1-NBA][BAr$^F_4$]** in solution.[2] After 2 hours under a propene atmosphere, un-coated **[1-NBA][BAr$^F_4$]** was fully converted to **[1-propene][BAr$^F_4$]**.

7.6.3. Synthesis of [1-Et$_2$O][BAr$^F_4$]

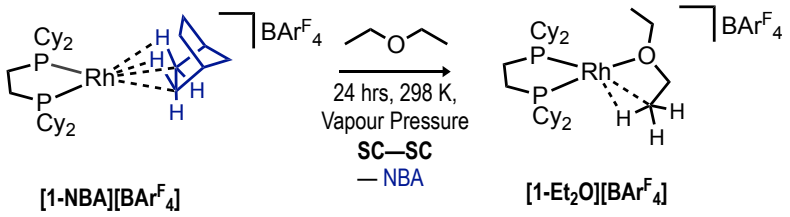

[1-NBA][BAr$^F_4$] [1-Et$_2$O][BAr$^F_4$]

Dark red crystals of **[1-NBD][BAr$^F_4$]** (50 mgs) were placed within a glass insert, which in turn was placed inside a J. Young flask (~50 mL). This insert was constructed by flame sealing the narrow end of a 150 mm glass Pasteur pipette. The flask was evacuated (< 2 × 10^{-2} mbar) filled with H_2 gas (15 psi, 298 K) and left to stand for 15 minutes, to form **[1-NBA][BAr$^F_4$]** *in-situ*.[2] After this time, the H_2 was removed under vacuum (< 2 × 10^{-2} mbar) backfilled with argon. Diethyl ether (0.05 mL) was then syringed into the flask, taking care for no liquid diethyl ether to be directly added inside the insert, and therefore come in contact with the crystals directly. The flask was then sealed and a vapour atmosphere of Et_2O was established.

After 24 hours, the colour of the crystals had turned a dark brown to yield [Rh($Cy_2PCH_2CH_2PCy_2$)(Et_2O)][BAr$^F_4$]; **[1-Et$_2$O][BAr$^F_4$]**. The crystals were placed under an argon flush for 15 minutes, to remove and excess diethyl ether and transferred to an argon filled glove box and stored at –25 °C.

[1-Et$_2$O][BAr$^F_4$] was analysed by single crystal x-ray diffraction and $^{31}P\{^1H\}$ / $^{13}C\{^1H\}$ Solid-State NMR spectroscopy. Any attempts to dissolve **[1-Et$_2$O][BAr$^F_4$]** in a range of solvents either led to the solvent bound complex (in $F_2C_6H_4$, to give **[1-F$_2$C$_6$H$_4$][BAr$^F_4$]**[1] or in MeCN to give [Rh($Cy_2PCH_2CH_2PCy_2$)($MeCN)_2$][BAr$^F_4$]).[7] When dissolved in neat Et_2O or CD_2Cl_2, either at 295 or 183 K, formation of the [BAr$^F_4$]$^-$ coordinated zwitterion complex **[1-BAr$^F_4$]**[2] was observed by solution $^{31}P\{^1H\}$ NMR spectroscopy.

$^{31}P\{^1H\}$ SSNMR (162 MHz, 10 kHz spin rate, 298 K): δ 107.0 (d., J_{RhP} 201 Hz, *trans*- to the oxygen)[13], 99.2 (d., J_{RhP} 223 Hz, *trans*- to the agostic interaction).[7]

$^{13}C\{^1H\}$ SSNMR (101 MHz, 10 kHz spin rate, 298 K): δ 163 (ipso-ArC), 134 (br, ortho-ArC), 129 (meta-ArC), 124 (CF_3), 116 (para-ArC), 113.1 (para-ArC), 70 (br, -O**C**H_2- of diethyl ether), 42 – 13 (br, multiple aliphatic environments).

Note: Regardless of synthetic method to this compound, a large amount (approximately 50 %) of decomposition to **[1-BAr$^{F}_{4}$]**[2] is observed. This may be due to the high solubility of both **[1-Et$_2$O][BAr$^{F}_{4}$]** and **[1-NBA][BAr$^{F}_{4}$]** in diethyl ether, which facilitates alkane loss and anion co-ordination in the solid-state during the reaction. Furthermore, any prolonged period under a dynamic vacuum saw the removal of coordinated Et_2O and formation of **[1-BAr$^{F}_{4}$]**.[2]

It was also found bound norbornadiene in **[1-NBD][BAr$^{F}_{4}$]** was not displaced by Et_2O. Therefore, **[1-NBA][BAr$^{F}_{4}$]** was essential for this reaction.

7.4. Crystallographic and Refinement Data

7.4.1. Crystal Structure Collection Methods

7.4.1.1. University of Oxford

The structures of **[1-*iso*butene][BAr$^{F}_{4}$]**, **[1-*iso*butane][BAr$^{F}_{4}$]** (100 K), **[1-*iso*pentadiene][BAr$^{F}_{4}$]**, **[1-*iso*pentane][BAr$^{F}_{4}$]**, **[1-hexadiene][BAr$^{F}_{4}$]**, **[1-hexane][BAr$^{F}_{4}$]**, **[1-(C_6-dienes)][BAr$^{F}_{4}$]**, **[1-(3-methylpentane)][BAr$^{F}_{4}$]**, **[1-octadiene][BAr$^{F}_{4}$]**, **[1-NBA][BAr$^{F}_{4}$]@poly(EVE)**, **[1-propene[BAr$^{F}_{4}$]@poly(EVE)** **[(1-(H_2O)$_2$(μ-O))$_2$][BAr$^{F}_{4}$]$_2$** and **[1-$C_4H_{10}O$][BAr$^{F}_{4}$]** (all at 150 K unless otherwise stated) were collected at the Oxford Chemical Crystallography Service from the University of Oxford, with an Agilent SuperNova diffractometer (Cu Kαradiation, λ = 1.54180 Å). Single crystal X-ray diffraction data for all samples were collected as follows: a selected crystal was mounted on a MiTeGen Micromounts using perfluoropolyether oil and cooled rapidly to the collection temperature in a stream of nitrogen gas using an Oxford Cryosystems Cryostream unit.[14]

7.4.1.2. Diamond Light Source

Gas cell: The I19 1mm quartz capillary gas cell comprises of a quartz capillary (Hampton research HR6-148, OD 1mm, ID 0.98 mm, L 25 mm) which is glued into a brass specimen pin (Hampton research HR4-661) using silver epoxy glue and the open end cut to length using a capillary cutting stone (Hampton research HR4-334). The other half of the cell is a 1/8 to 1/16 inch reducing union with 1/16-inch stainless steel capillary tubing (Swagelok SS-T1-S-014-6ME) to a miniature quick connector (Swagelok SS-QM2-D-100).

Due to the air sensitivity of the systems under investigation the mounting procedure occurs under an inert atmosphere within a glove box. Without the use of manipulation oil, a crystal is selected and mounted, using a minimal amount of epoxy glued, to the tip of a sample mount (mitogen M2-L25SP-30). The mount is then placed into the capillary and fixed in place with a small amount of glue. The two halves of the gas cell assembled creating a gas tight environment for the sample ready to be mounted on the diffractometer and connected to gas rig.

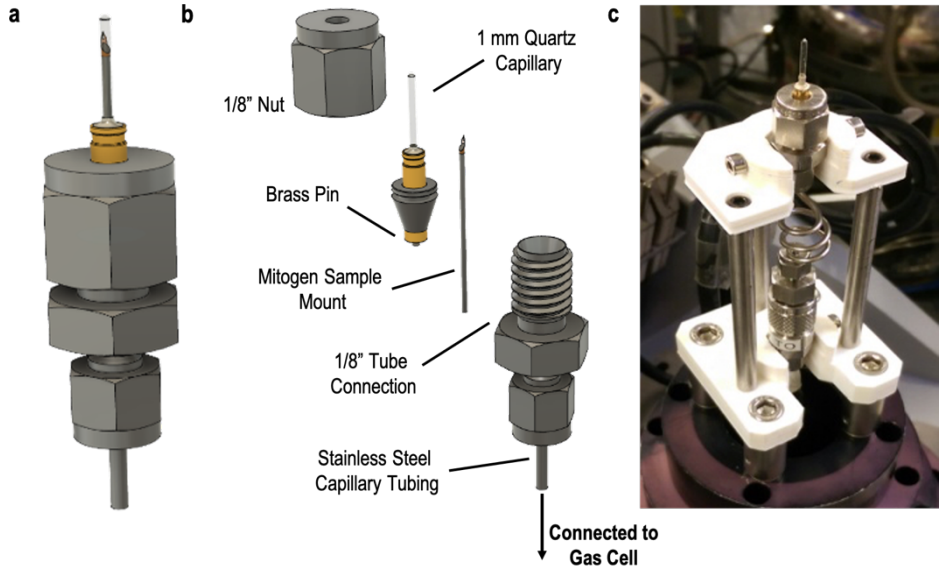

Figure 7.3: I19 Beamline 1mm quartz capillary gas cell equipment. **a**) Technical drawing of the head of the cell with **b**) showing the exploded view. **c**) Image of the diffractometer mounted cell. Image adapted with kind permission from Dr Mark Warren, Diamond Light Source.

Gas Rig: The I19 gas-cell control panel allows the users to operate the gas flow, gas pressure, gas mixture and vacuum remotely. The main rig has several pneumatic valves (V1-6), for connections to samples (S1), sample return (SR1), gases (G1-3), vacuum (Vac1), pressure transducers (PR1-2) and exhaust (EX1).

The vacuum pump is a scroll pump with a turbo attachment capable of reducing the pressure to 10^{-6} mbar at the pump transducer and 10^{-4} mbar at the sample position. Gas pressure, flows and mixtures can be controlled by the mass flow controllers (Alicat MC-200SCCM-D) and pneumatic valves (V1-3).

The gas-cell on the diffractometer is attached to the control apparatus via 1/16-inch tubing with quick release connectors. The quick release connectors allow users to rapidly and easily attach and remove the cell whilst maintaining the pressure in the cell. The setup of this

apparatus allows for the gas-cell to be subjected to vacuum, single gases or gas mixtures either under flow of the gas or with gas pressures up to 200 bar in-situ with the diffraction experiment. The alicat mass flow controllers, pneumatic valves and transducers can be controlled and read through the supporting control software.

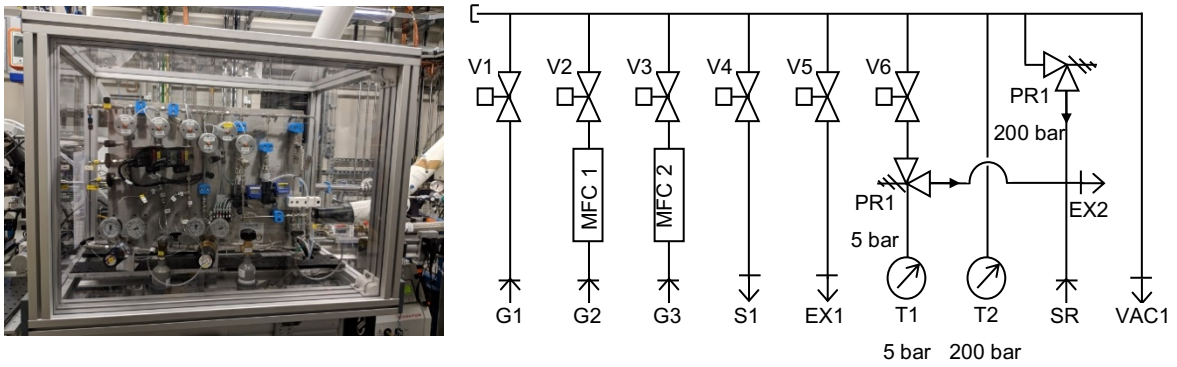

Figure 7.4: Gas-cell control apparatus schematic. Key: V1-6 pneumatic valves, MFC1-2 alicat mass flow controllers, G1-3 gas inlets, S1 sample connection, EX1-2 exhaust connection, T1-2 pressure transducers, PR1-2 pressure relief valves and VAC1 vacuum connection.

Using the above set-up, the structures of **[1-propane][BAr$^{F}_{4}$]**, **[1-butadiene][BAr$^{F}_{4}$]**, **[1-butane][BAr$^{F}_{4}$]** (150 K) were collected on a Pilatus 300K hybrid pixel diffractometer with synchrotron source Zr K-edge (17.998 keV which equates to λ = 0.6889 Å) on Station I19 at the Diamond Light Source (DLS).[8]

7.4.1.3. National Crystallography Service

[1-*iso*pentene][BAr$^{F}_{4}$] (150 K) was collected at the National Crystallography Service, University of Southampton, Southampton, UK, using a Rigaku 007HF diffractometer equipped with Varimax confocal mirrors (Cu K_{α} radiation, 1.54184 Å), an AFC11 goniometer, and HyPix 6000 detector.

7.4.2. Comments on Solved Structures

Regardless of collection method (Section 7.4.1.), all raw frame data were reduced using CrysAlisPro.[15] The structures were solved using SHELXT[16] and refined using full-matrix least squares refinement on all F^2 data using the SHELXL-18[17] using the interface OLEX2.[18] In all structures, disorder of the -CF_3 groups was treated by introducing a split site model and restraining geometries and displacement parameters. All non-hydrogen atoms were refined anisotropically and hydrogen atoms were geometrically placed and allowed to ride on their parent atoms. Notably, all hydrogen atoms involved in any Rh•••H–C interactions have also been placed in their geometric position, and not located in the Fourier maps. Distances and angles were calculated using the full covariance matrix.

Additionally, the structures of **[1-*iso*pentane][BAr^F_4]** and **[1-*iso*pentene][BAr^F_4]** were refined as a 2-componant twins; rotated by -179.9945° around 0.71 0.71 -0.00 (reciprocal space) or 0.73 0.69 0.05 (direct space) with BASF refined to 0.4997(13) for **[1-*iso*pentane][BAr^F_4]** and rotated by -179.9799° around 0.71 0.71 -0.00 (reciprocal space) or 0.72 0.69 0.03 (direct space) with BASF refined to 0.899(2) for **[1-*iso*pentene][BAr^F_4]**.

Any additional comments upon Alerts flagged during the CheckCIF process have been commented upon within the CheckCIF files submitted with the thesis. The CIF files for all structures reported can also be found within this submission.

7.4.3. Refinement Tables

Table 7.1: Selected crystallographic and refinement data.

	[1-propane] [BAr^F_4]	**[1-butadiene] [BAr^F_4]**	**[1-butane] [BAr^F_4]**	**[1-*iso*butene] [BAr^F_4] (Solution Grown)**
Chemical formula	$C_{61}H_{68}BF_{24}P_2Rh$	$C_{62}H_{66}BF_{24}P_2Rh$	$C_{62}H_{70}BF_{24}P_2Rh$	$C_{62}H_{68}BF_{24}P_2Rh$
Formula weight	1432.81	1442.80	1446.84	1444.82
Temperature (K)	150	150	150	150
Crystal system	triclinic	monoclinic	monoclinic	triclinic
Space group	P-1	C2/c	C2/c	P-1
a (Å)	12.9862(8)	19.2781(5)	19.4945(10	12.7477(3)
b (Å)	13.0857(8)	17.2067(5)	17.6563(17)	13.0092(3)
c (Å)	19.9409(11)	20.1614(8)	20.1777(15)	19.8574(4)
α (deg)	91.206(5)	90	90	92.3462(17)
β (deg)	90.367(5)	90.611(3)	90.530(6)	90.9972(16)
γ (deg)	96.291(5)	90	90	96.6033(17)
V (Å^3)	3367.3(4)	6687.4(4)	6944.9(9)	3267.70(13)
Z	2	8	4	2
ρ(calcd) (g cm^{-3})	1.413	1.433	1.384	1.468
μ (mm^{-1})	0.374	0.377	0.364	3.530
Reflections collected	16866	45286	45369	77320
Unique reflections	6569	10327	10465	12411
Restraints / Parameters	1212/1028	579/537	576/539	791/1014
R_{int}	0.0532	0.0435	0.0759	0.0406
R_1 [$I > 2\sigma(I)$]	0.1053	0.0754	0.1254	0.0511
wR_2 [all data]	0.2766	0.2774	0.4158	0.1509
GooF	1.086	1.059	1.161	1.096
Residual electron density (e Å^{-3})	2.25/-0.77	1.02/-1.14	0.86/-1.22	2.38/-1.12
CCDC no.	–	–	–	1916756

	[1-*iso*butane] [BAr^F_4]	**[1-*iso*butene] [BAr^F_4] (SC-SC-SC)**	**[1-*iso*pentadiene] [BAr^F_4]**	**[1-*iso*pentane] [BAr^F_4]**
Chemical formula	$C_{62}H_{70}BF_{24}P_2Rh$	$C_{62}H_{68}BF_{24}P_2Rh$	$C_{63}H_{68}BF_{24}P_2Rh$	$C_{63}H_{72}BF_{24}P_2Rh$
Formula weight	1446.84	1444.82	1456.83	1460.86
Temperature (K)	100	150	150	150
Crystal system	monoclinic	triclinic	triclinic	triclinic
Space group	$P2_1/n$	P-1	P-1	P-1
a (Å)	19.1238(3)	12.7582(16)	12.7425(3)	12.7559(6)
b (Å)	34.6204(5)	12.9595(15)	12.9552(3)	13.1978(5)
c (Å)	19.5735(3)	19.8097(8)	20.0752(4)	19.7970(5)
α (deg)	90	92.028(6)	92.435(2)	93.734(2)
β (deg)	90.624(2)	90.685(7)	91.227(2)	92.418(3)
γ (deg)	90	96.2300(10)	97.363(2)	95.556(3)
V (Å^3)	12958.3(3)	3253.5(6)	3282.54(13)	3306.2(2)
Z	8	2	2	2
ρ(calcd) (g cm^{-3})	1.483	1.475	1.474	1.467
μ (mm^{-1})	3.561	3.545	3.519	3.494
Reflections collected	160559	11700	51527	26345
Unique reflections	24598	11700	13739	26345
Restraints / Parameters	1706/1939	1171/1029	399/999	571/975
R_{int}	0.0943	0.0555	0.0512	
R_1 [$I > 2\sigma(I)$]	0.0949	0.1095	0.0575	0.0930
wR_2 [all data]	0.2543	0.2956	0.1679	0.2622
GooF	1.059	1.139	1.019	0.997
Residual electron density (e Å^{-3})	3.42/-1.76	1.99/-1.41	1.32/-0.71	3.40/-1.02
CCDC no.	1916755	–	–	–

	[1-*iso*pentenes] [BAr^F_4]	**[1-hexadiene] [BAr^F_4]**	**[1-hexane] [BAr^F_4]**	**[1-(C_6-dienes)] [BAr^F_4]**
Chemical formula	$C_{63}H_{70}BF_{24}P_2Rh$	$C_{64}H_{70}BF_{24}P_2Rh$	$C_{64}H_{74}BF_{24}P_2Rh$	$C_{64}H_{70}BF_{24}P_2Rh$
Formula weight	1458.85	1470.86	1474.89	1470.86
Temperature (K)	100	150	150	150
Crystal system	triclinic	triclinic	triclinic	triclinic
Space group	P-1	P-1	P-1	P-1
a (Å)	12.7343(2)	12.8807(3)	13.1078(2)	12.3717(7)
b (Å)	13.0256(2)	13.3277(4)	13.6868(3)	13.1412(6)
c (Å)	19.8332(4)	20.1295(6)	19.1309(3)	20.1179(7)
α (deg)	92.6533(16)	101.803(2)	99.0834(15)	94.535(5)
β (deg)	91.1282(16)	97.376(2)	95.1697(2)14	92.043(4)
γ (deg)	96.6525(15)	100.681(2)	99.1623(15)	96.288(4)
V ($Å^3$)	3263.06(11)	3273.92(16)	3322.42(10)	3331.9(3)
Z	2	2	2	2
ρ(calcd) (g cm^{-3})	1.485	1.492	1.474	1.466
μ (mm^{-1})	3.540	3.543	3.483	3.473
Reflections collected	13689	35413	36508	28618
Unique reflections	13689	13553	13707	13907
Restraints / Parameters	508/956	571/1010	597/1003	1491/1112
R_{int}		0.0356	0.0320	0.0376
R_1 [$I > 2\sigma(I)$]	0.0861	0.0402	0.0408	0.0726
wR_2 [all data]	0.2666	0.1064	0.1108	0.2144
GooF	1.145	1.030	1.021	1.047
Residual electron density (e $Å^{-3}$)	0.93/-1.74	1.42/-0.95	0.92/-0.91	1.49/-1.33
CCDC no.	–	–	–	–

	[1-(3-methyl pentane)][BAr$^F_4$]	**[1-octadiene] [BAr$^F_4$]**	**[1-NBA][BAr$^F_4$] @poly(EVE)***	**[1-propene][BAr$^F_4$] @poly(EVE)**
Chemical formula	$C_{64}H_{74}BF_{24}P_2Rh$	$C_{66}H_{74}BF_{24}P_2Rh$	$C_{65}H_{72}BF_{24}P_2Rh$	$C_{61}H_{66}BF_{24}P_2Rh$
Formula weight	1474.89	1498.91	1484.88	1430.79
Temperature (K)	150	150	150.01(10)	150.1(2)
Crystal system	triclinic	monoclinic	Monoclinic	Triclinic
Space group	P-1	$P2_1/c$	$P2_1/n$	P-1
a (Å)	12.6885(2)	22.8949(2)	19.0553(10)	12.8015(10)
b (Å)	13.2056(2)	13.1174(1)	18.0135(2)	12.9012(7)
c (Å)	20.0728(3)	90	19.5654(2)	19.8814(9)
α (deg)	94.5410(10)	114.565(1)	90	91.347(4)
β (deg)	91.6930(10)	90	91.6800(10)	90.717(5)
γ (deg)	95.6740(10)	96.2300(10)	90	96.597(6)
V (Å^3)	3334.03(9)	6945.67(13)	6712.99(11)	3260.5(3)
Z	2	4	4	2
ρ(calcd) (g cm^{-3})	1.469	1.433	1.469	1.457
μ (mm^{-1})	3.471	3.342	3.453	3.532
Reflections collected	62097	84898	137418	29822
Unique reflections	13909	14458	13967	29822
Restraints / Parameters	710/983	601/1016	267/894	785 / 971
R_{int}	0.0337	0.0357	0.0660	0.0535
R_1 [$I > 2\sigma(I)$]	0.0483	0.0477	0.0490	0.1003
wR_2 [all data]	0.1295	0.1387	0.1399	0.3209
GooF	1.048	1.018	1.044	1.160
Residual electron density (e Å^{-3})	1.29/-1.05	1.38/-0.70	1.65/-0.56	2.27 / -1.75
CCDC no.	–	–	–	1983128

* Structure collected after 30 seconds exposure to EVE atmosphere followed by 30 minutes exposure to air. The CCDC number for the previously published collection of **[1-NBA][BAr$^F_4$]** is 1022726.[2]

	[(1-$(H_2O)_2$(μ-O))$_2$] [$BAr^F{}_4$]$_2$	**[1-$C_4H_{10}O$][$BAr^F{}_4$]**
Chemical formula	$C_{119}H_{134}B_2Cl_6F_{48}O_3P_4Rh_2$	$C_{62}H_{70}BOF_{24}P_2Rh$
Formula weight	3136.28	1462.84
Temperature (K)	150.01(18)	150.01(10)
Crystal system	Triclinic	Triclinic
Space group	P-1	P-1
a (Å)	14.1321(5)	12.8770(13)
b (Å)	14.3678(4)	13.5514(7)
c (Å)	19.2696(5)	19.2488(13)
α (deg)	73.605(3)	91.699(5)
β (deg)	70.883(3)	95.671(7)
γ (deg)	81.874(3)	98.347(6)
V (Å^3)	3541.4(2)	3303.8(4)
Z	2	2
ρ(calcd) (g cm^{-3})	1.471	1.470
μ (mm^{-1})	4.353	3.510
Reflections collected	91821	36581
Unique reflections	14710	13564
Restraints / Parameters	965 / 1052	595 / 989
R_{int}	0.0750	0.0943
R_1 [$I > 2\sigma(I)$]	0.0845	0.0900
wR_2 [all data]	0.2672	0.3020
GooF	1.048	1.011
Residual electron density (e Å^{-3})	3.10 / -0.67	1.58 / -1.38
CCDC no.	–	1983126

7.5. References

1 F. M. Chadwick, N. H. Rees, A. S. Weller, T. Krämer, M. Iannuzzi and S. A. Macgregor, *Angew. Chem. Int. Ed.*, 2016, **55**, 3677–3681.

2 S. D. Pike, F. M. Chadwick, N. H. Rees, M. P. Scott, A. S. Weller, T. Krämer and S. A. Macgregor, *J. Am. Chem. Soc.*, 2015, **137**, 820–833.

3 W. L. Earl and D. L. Vanderhart, *J. Magn. Reson.*, 1982, **48**, 35–54.

4 A. I. McKay, T. Krämer, N. H. Rees, A. L. Thompson, K. E. Christensen, S. A. Macgregor and A. S. Weller, *Organometallics*, 2017, **36**, 22–25.

5 S. D. Pike, T. Krämer, N. H. Rees, S. A. Macgregor and A. S. Weller, *Organometallics*, 2015, **34**, 1487–1497.

6 A. T. Lubben, J. Scott McIndoe and A. S. Weller, *Organometallics*, 2008, **27**, 3303–3306.

7 F. M. Chadwick, A. I. McKay, A. J. Martinez-Martinez, N. H. Rees, T. Krämer, S. A. Macgregor and A. S. Weller, *Chem. Sci.*, 2017, **8**, 6014–6029.

8 H. Nowell, S. A. Barnett, K. E. Christensen, S. J. Teat and D. R. Allan, *J. Synchrotron Radiat.*, 2012, **19**, 435–441.

9 A. I. McKay, A. J. Bukvic, B. E. Tegner, A. L. Burnage, A. J. Martínez-Martínez, N. H. Rees, S. A. Macgregor and A. S. Weller, *J. Am. Chem. Soc.*, 2019, **141**, 11700–11712.

10 K. Hasegawa, R. Asami and K. Takahashi, *Bull. Chem. Soc. Jpn.*, 1978, **51**, 916–920.

11 *(E)-3-methyl-1,3-pentadiene -- AIST Spectr. Database Org. Compd. -- (SDBS No. 293) -- Date Acc. 25-06-2020*.

12 *(Z)-3-methyl-1,3-pentadiene -- AIST Spectr. Database Org. Compd. -- (SDBS No. 292) -- Date Acc. 25-06-2020*.

13 A. Kumar, N. A. Beattie, S. D. Pike, S. A. Macgregor and A. S. Weller, *Angew. Chem. Int. Ed.*, 2016, **55**, 6651–6656.

14 B. J. Cosier and A. M. Glazer, *J. Appl. Crystallogr.*, 1986, **19**, 105–107.

15 *Oxford Diffraction Ltd.*, 2011.

16 G. M. Sheldrick, *Acta Crystallogr. Sect. A Found. Crystallogr.*, 2008, **64**, 112–122.

17 G. M. Sheldrick, *Acta Crystallogr. Sect. A Found. Crystallogr.*, 2015, **71**, 3–8.

18 O. V. Dolomanov, L. J. Bourhis, R. J. Gildea, J. A. K. Howard and H. Puschmann, *J. Appl. Crystallogr.*, 2009, **42**, 339–341.